Detection of Electrooxidation Products Using Microfluidic Devices and Raman Spectroscopy

by

Tianyu Li
B.Sc., Nanjing University, 2016

A Dissertation Submitted in Partial Fulfillment of the
Requirements for the Degree of

DOCTOR OF PHILOSOPHY

in the Department of Chemistry

Detection of Electrooxidation Products Using Microfluidic Devices and Raman Spectroscopy

by

Tianyu Li

B.Sc., Nanjing University, 2016

Supervisory Committee

Dr. D. A. Harrington, Supervisor (Department of Chemistry)

Dr. A. G. Brolo, Departmental Member (Department of Chemistry)

Dr. K. S. Elvira, Departmental Member (Department of Chemistry)

Dr. R. B. Bhiladvala, Outside Member (Department of Mechanical Engineering)

Supervisory Committee

Dr. D. A. Harrington, Supervisor (Department of Chemistry)

Dr. A. G. Brolo, Departmental Member (Department of Chemistry)

Dr. K. S. Elvira, Departmental Member (Department of Chemistry)

Dr. R. B. Bhiladvala, Outside Member (Department of Mechanical Engineering)

Abstract

Microfluidic flow devices coupled with quantitative Raman spectroscopy are able to provide a deep insight into the reaction mechanism and kinetics of electrocatalytic reactions. With a microfluidic flow device made with glass microscope slides and polymer building blocks, the feasibility of this technique was examined by methanol electrooxidation reaction with a Pt working electrode. Pre-calibration of the Raman peak area was done with solutions of known concentrations of methanol and its major oxidation product, *i.e.*, formate, which enabled the time-dependent Raman spectra taken during the reaction to be converted to time-dependent concentrations. These were interpreted in terms of a model with one-dimensional convection and the reaction kinetics.

An improved version of this technique was then applied to a comparative study of different alcohols with Ni-based electrodes. This showed the production of formate as the major product from the oxidation of alcohols with vicinal OH groups, leading to the discovery that C-C bond dissociation is a major reaction pathway for vicinal diols and triols if Ni electrocatalysts are used. It is also suggested that the cleavage of C-C bonds is the rate-determining step. The potential use of printed circuit boards (PCB) in the next generation of a novel microfluidic device was explored, as PCB

have advantages over regular electrochemical microfluidic substrates, such as simpler electrode fabrication strategies, more wiring layers, and customization of size and shape of electrodes. Pretreatments and electrodeposition protocols of nickel, silver, palladium and platinum on PCB were successfully developed, together with four types of PCB-based microfluidic devices designed with an open-source PCB design software. This work establishes a new electrochemical microfluidic platform for online and *in-situ* monitoring of electrocatalytic reactions, which can quickly determine the reaction mechanism and kinetics.

Table of Contents

List of Tables

List of Figures

Nomenclature

Γ_{m}	Number of active sites on the electrode surface
ε	Nature of the crystal plane
η	Overpotential, V
θ	Coverage of Adsorbate B
ρ	Electrolyte resistivity, Ω m
ρ_{bulk}	Bulk density of Toray paper 090, g cm^{-3}
ρ_{fiber}	Density of carbon fiber, g cm^{-3}
ρ_{w}	Density of water, kg m^{-3}
τ	Time constant, s
A_{c}	Cross-sectional area of channel, m^2
ads	Adsorbed
Ag|AgCl	Silver silver chloride electrode
ATR	Attenuated total reflectance
b_i	Intercept of regression line
2-BuOH	2-Butanol
1,4-BuOH	1,4-Butanol
$C_{\mathrm{ads\_eff}}$	Effective pseudo-capacitance of the adsorbed species, F cm^{-2}
$C_{\mathrm{dl\_eff}}$	Effective double layer capacitance, F cm^{-2}
C_{p}	Heat capacity of water, J mol^{-1} K^{-1}
c^{b}	Initial concentration, mol dm^{-3}
c_i	Concentration of species i, mol dm^{-3}

c_{min}	Concentration detection limit, mol dm^{-3}
CB	Carbon balance
CE	Counter electrode
CNT	Carbon nanotube
$\mathrm{CO_B}$	Bridge-bonded CO
$\mathrm{CO_L}$	Linearly-bonded CO
CV	Cyclic voltammogram
D	Diffusion coefficient, $\mathrm{m}^2\ \mathrm{s}^{-1}$
D_{fiber}	Thickness of carbon fibers, μm
d	Distance from the detection point to working electrode, mm
$d_{\mathrm{WE\text{-}CE}}$	Distance between working and counter electrode, mm
ds	downstream
DAFC	Direct alcohol fuel cell
DEMS	Differential electrochemical mass spectrometry
DFT	Density functional theory
DHA	Dihydroxyacetone
E	Potential, V
EB	Electron balance
ECSA	Electrochemical Surface Area
EGOH	1,2-Ethanediol
EIS	Electrochemical Impedance Spectroscopy
Ethylene glycol	1,2-Ethanediol
EtOH	Ethanol
F	Faraday's constant, $\mathrm{C\ mol}^{-1}$
f	Frequency, Hz
FA	Formate
FTIR	Fourier-transform infrared spectroscopy
GEOR	Glycerol electrooxidation

Glycerol	1,2,3-Propanetriol
GlyOH	1,2,3-Propanetriol
h	Thickness of the channel of the microfluidic flow cell, mm
HER	Hydrogen evolution reaction
Hg|HgO	Mercury mercury oxide electrode
HPLC	High-performance liquid chromatography
I	Current, A
I_{ave}	Current average, A
IRE	Internal reference electrode
j	Current density, A cm^{-2}
k	Rate constant
L	Characteristic linear dimension, m
L_{fiber}	Total length of carbon fiber in a unit volume of Toray paper 090, cm
M_{w}	Molar mass of water, g mol^{-1}
m	Slope of regression line, dm^3 mol^{-1}
m_{KOH}	Molality of KOH, mol kg^{-1}
MeOH	Methanol
n	Coefficient of surface heterogeneity
NiCP	Ni electrodeposited on carbon paper
OER	Oxygen evolution reaction
PCB	Printed circuit board
PDMS	Polydimethylsiloxane
1-PrOH	1-Propanol
1,2-PrOH	1,2-Propanediol
1,3-PrOH	1,3-Propanediol
2-PrOH	2-Propanol
PTFE	Polytetrafluoroethylene
Q_{ads}	Constant phase element of adsorbed species

Q_{dl}	Constant phase element of double layer
Q_{i}	Heating source, W
R^2	Coefficient of determination
$R_{\mathrm{ads\_eff}}$	Effective resistance of adsorbed species, Ω cm^2
R_{ct}	Charge transfer resistance, Ω cm^2
$R_{\mathrm{ct\_eff}}$	Effective charge transfer resistance, Ω cm^2
R_{i}	Source or sink of the species, mol m^{-3} s^{-1}
R_{s}	Solution resistance, Ω cm^2
Re	Reynolds number
RE	Reference electrode
RHE	Reversible hydrogen electrode
S_i	Area of Raman characteristic peaks
S_{fiber}	Specific surface area, cm^2
S/N ratio	Signal-to-noise ratio
SEM	Scanning electron microscopy
SERS	Surface enhanced Raman scattering
T	Temperature, K
t_{diff}	Diffusion time for a molecule to travel half the width of the channel, s
t_{exp}	Experiment duration, s
t_{flow}	Time for a molecule to be flowed downstream for detection, s
U_{j}	Radiation efficiency, W
us	Upstream
UV-Vis	Ultraviolet–visible
v	Reaction rate
V_{bulk}	Bulk volume of carbon paper 090, cm^3
V_{f}	Volumetric flow rate, μL min^{-1}
V_{fiber}	Volume of carbon fiber, cm^3
w	Length of the working electrode, mm

WE	Working electrode
z	Number of electrons transferred per molecule
Z	Impedance, Ω cm^2
Z_{real}	Real part of impedance, Ω cm^2
Z_{imag}	Imaginary part of impedance, Ω cm^2

Acknowledgements

This work was financially supported by the Natural Sciences and Engineering Research Council of Canada through its Discovery Frontiers program (Engineered Nickel Catalysts for Electrochemical Clean Energy project ("Ni Electro Can") administered from Queen's University), Discovery Grants program and CREATE program (Materials for Enhanced Energy Technologies ("MEET") project), and by the Research Council of Norway through its International Partnerships Program (Canada-Norway Partnership in Electrochemical Energy Technologies ("CANOPENER") project). The financial support from the above-mentioned funding agencies is highly appreciated. Apart from that, I want to express my gratitude to my supervisor and role model, Prof. David Harrington, for his guidance, support and the knowledge imparted to me. I would also like to say thanks to my colleagues: Mr. Tory Borsboom-Hanson, Ms. Natalie Stubb, Mr. Victor Aiyejuro, Mr. Mohammad Alikarami and Dr. Thomas Holm, as their help and encouragement give me faith over these years. I would like to thank Prof. Alexander Brolo, Prof. Jeremy Wulff and their group members for their help and company during my four-year PhD life. I would like to thank the chemistry department of the University of Victoria for providing me a very good atmosphere for doing research. In the end, I want to thank my parents for their understanding, patience, and financial supports.

To My Parents.

Chapter 1

Introduction

In this dissertation, the design and testing of a novel electrocatalytic microfluidic platform coupled with confocal Raman spectroscopy for online *in-situ* detection of downstream products are presented. This tool was established with three components (*i.e.* internal three-electrode system, microfluidic devices and Raman spectroscopy) for investigating the kinetics and reaction mechanisms of certain electrocatalytic systems. The reaction mechanisms of glycerol electrooxidation (GEOR), as well as other small alcohols at Ni-based electrocatalysts, were investigated, showing the feasibility of this methodology. To make a second type of microfluidic device, printed circuit boards (PCB) were used as a novel substrate material with surface-mounted Cu pads. These customizable (size and shape) pads were electroplated with different metals to become microfluidic electrodes, which is a strategy that innovates the field of lab-on-a-chip as the electrode fabrication processes do not need clean-room conditions. In addition to the experimental works, a literature review was done, which surveys previously reported GEOR studies with Pt, Pd and Au and proposes a new reaction mechanism based on the reported experimental results.

In the following paragraphs of this chapter, the advantages of using microfluidic devices combined with Raman spectroscopy for determining electrochemical reaction

mechanisms, and in particular oxidation of glycerol and related alcohols, are presented.

Electrocatalytic reactions of small organic molecules by metal electrodes can be used to generate energy with low pollution (from alcohols, glucose, *etc.*) in fuel cells [1–3] and to produce valuable organic chemicals (*e.g.* CO_2 electroreduction [4]) efficiently, safely and economically [5, 6]. As a pre-requisite for choosing appropriate electrocatalytic systems for commercialization, reaction mechanisms and kinetics of those electrochemical systems must be determined. To do this, it requires studies of reactions occurring under well-controlled conditions such as mass transport or surface conditions and quantification of the consumed and generated species.

In the most recent decades, microfluidic flow devices have been extensively used in electrochemical studies, either as reactors (*e.g.* microfluidic fuel cells [7, 8], hydrogen generators [9], sea water desalinators [10]) which outperform large-scale competitors in the efficiency of conversion / energy output or as highly sensitive electrochemical detectors [11–13].

Electrochemical microfluidic flow devices have great potential in studying kinetics of many electrocatalytic systems for several reasons. Firstly, many experimental works have revealed that the reaction pathways and kinetics depend on convective mass transport to the surface of catalysts [14], which can only be studied with accurate flow pattern control. Secondly, well-controlled mass transport enables researchers to quantify efficiency of conversion of reagents to electric signals such as current density and transferred charge, which directly reveals kinetic information. Thirdly, since electrocatalytic reactions are very much localized and well-distributed in a microfluidic channel, the effect of external conditions (*e.g.* temperature [15], pressure [16], *etc.*) on the kinetics can be more easily investigated. Fourthly, other physical techniques such as microscopy [17], spectroscopy [18], and electrochemical impedance spectroscopy (EIS) [19–21] can be easily applied to identify the species involved in the kinetic studies. So far, both "flow-over" and "flow-through" configurations are

extensively used in the design of electrochemical microfluidic devices. The configuration of "flow-over" involves planar electrodes (whose thickness is usually negligible compared to the thickness of the channel) deposited on top of the substrate, and the fluid flows over the electrodes when the electrochemical reaction occurs [22, 23]. A "flow-through" design means that the cross-section of the channel is fully filled by a three-dimensional electrode that is usually a porous or network-like structure, and this configuration is commonly seen in microfluidic fuel cells [24, 25]. These two configurations can be used for studying the kinetics of electrocatalytic reactions with 1D/3D ("flow-through") and 2D ("flow-over") mass-transport models [19].

Vibrational spectroscopies are promising methods for online detection in microfluidic devices. They have a high detection sensitivity for molecules and can quantify their concentrations after locating their vibrational modes in a finger-print region from 1100 to 1400 cm^{-1} [26], exemplified by the C-O stretching mode of formate centering at 1352 cm^{-1}. One advantage over other product identification tools like HPLC is the measurement speed, which makes it suitable for soluble products that are unstable and can be slowly converted to other species [27]. Many *in-situ* Fourier-Transform Infrared (FTIR) spectroscopy studies have been conducted to investigate reaction mechanisms of complicated electrocatalytic systems (*e.g.* glycerol electrooxidation) [28–30]; however, IR spectroscopy is inferior when used to detect aqueous samples, as water strongly absorbs IR radiation (bending mode at 1600 cm^{-1}) and masks the fingerprint region. One way to address this issue involves a special cell that brings the working electrode close enough to the CaF_2 window, thereby minimizing the amount of water in between [31]. However, this makes kinetic studies difficult as the thin liquid region makes the mass convection difficult and uncontrolled. Also, the electrolyte resistance makes it difficult to determine the actual potential at the electrode surface accurately. To resolve this issue, Attenuated Total Reflectance – Fourier Transform Infrared (ATR-FTIR) spectroscopy is adopted by researchers [32, 33]. In that case, the incident infrared waves go through a prism to

reach the boundary between the prism and the electrolyte, and the reflective waves carrying the IR absorption information are detected after bouncing within the prism. The advantage is that a thicker layer of electrolyte is allowed, as the evanescent waves only penetrate several hundreds of nanometers, and therefore the absorption of IR by water is significantly reduced. However, it usually works with thin film electrodes, which limits its wide applicability to many reaction systems.

Recently, confocal Raman spectroscopy, an advanced spectroscopic tool that provides similar functions (sister spectra) compared with FTIR, has received increasing attention [34, 35]. It outperforms FTIR although the bending mode of water at 1600 cm^{-1} is Raman-active, it is very weak. Therefore, it is suitable for the identification and quantification of aqueous species. Also, as it has a very high spatial resolution due to the shorter wavelength of the visible laser light (usually 532 nm, 633 nm or 785 nm) compared with infrared wavelengths, it is highly compatible with microfluidic systems [26]. Moreover, it can directly probe the liquid at or near the electrode surface under the flow conditions relevant for the kinetics. So far, for the majority of microfluidic designs, channels for mass transport are made of polymers blocks such as PDMS, PMMA and PTFE, sandwiched by a substrate and a cover [36, 37]. A transparent cover of glass or polymeric materials allows a laser beam to penetrate in order to measure Raman spectra. Many biological and biochemical studies using quantitative Raman spectroscopy combined with microfluidic devices have been presented by researchers for decades [26]. However, their combined use in the investigation of soluble species of electrochemical reactions is just beginning.

Combining the merits of Raman spectroscopy and microfluidics, this project is aimed at presenting a more advanced and efficient technology to determine the kinetics and reaction mechanisms of electrocatalytic reactions. An electrocatalytic microfluidic platform has been developed, which can provide *in-situ* and quantitative product analysis using Raman spectroscopy and therefore was used for investigating the oxidation of small alcohols. This device can be used for "flow-through" experi-

ments, which outperforms the conventional microfluidic devices that have electrodes made on top of glass substrates by photolithography, as these devices usually involves channels made with PDMS. For these devices, PDMS is usually casted on top of the substrate to make channels, but it strongly absorbs small alcohols like methanol and ethanol, which jeopardizes the study of alcohol oxidation. Also, photolithography only makes planar electrodes whose thickness is usually in sub-micrometer scale, which cannot operate stably to provide large oxidation currents.

With the devices introduced in Chapter 3 and 4, the Raman peak area of the targeted molecules (reactants and products) were pre-calibrated with solutions of known concentrations, and time-dependent Raman spectra were taken as a way of monitoring the reaction processes. A kinetic study of methanol electrooxidation at Pt mesh electrode showed the feasibility of this microfluidic platform, while a comparative study of ten different alcohols conducted using this device suggested different reaction mechanisms of alcohols with different structures, combined with potentiostatic electrochemical impedance spectroscopy results.

In the field of novel microfluidic devices, potential breakthroughs lie in the area of efficient electrode fabrication and rapid prototyping to meet the increasing demand of researchers. Among a number of candidates, PCB is taken as a promising substrate material which supports customization of electrode pads mounted on top and multiple wiring layers. Most importantly, the electrode fabrication by electrodeposition is a key feature that outperforms the traditional photolithography method applied to glass substrates. Therefore, microfluidic devices that involve PCB substrates are deemed as a promising technique for studying electrocatalysis with "flow-over" configuration. In this dissertation, electrodeposition protocols of nickel, silver, palladium and platinum were successfully developed to make smooth coating layers on Cu pads. Four types of microfluidic devices were designed and printed out in factory.

References

[1] E. Kjeang, N. Djilali, and D. Sinton, *Journal of Power Sources*, 2009, **186**(2), 353–369.

[2] S. D. Minteer, *International Materials Reviews*, 2018, **63**(4), 241–256.

[3] M. Guerra-Balcázar, F. M. Cuevas-Muñiz, L. Álvarez-Contreras, L. G. Arriaga, and J. Ledesma-García, *Journal of Power Sources*, 2012, **197**, 121–124.

[4] O. Scialdone, E. Corrado, A. Galia, and I. Sirés, *Electrochimica Acta*, 2014, **132**, 15–24.

[5] J. F. Gomes, V. L. Oliveira, P. M. Pratta, and G. Tremiliosi-Filho, *Electrocatalysis*, 2014, **6**(1), 7–19.

[6] C. Coutanceau, S. Baranton, and R. S. Kouamé, *Frontiers in Chemistry*, 2019, **7**, 1–15.

[7] J. C. Abrego-Martínez, A. Moreno-Zuria, F. M. Cuevas-Muñiz, L. G. Arriaga, S. Sun, and M. Mohamedi, *Journal of Power Sources*, 2017, **371**, 10–17.

[8] O. Scialdone, A. Galia, S. Sabatino, D. Mira, and C. Amatore, *ChemElectroChem*, 2015, **2**(5), 684–690.

[9] S. Rarotra, T. K. Mandal, and D. Bandyopadhyay, *Energy Technology*, 2017, **5**(8), 1208–1217.

[10] J. F. Pérez, J. Llanos, C. Sáez, C. López, P. Cañizares, and M. A. Rodrigo, *Electrochemistry Communications*, 2017, **82**, 85–88.

[11] Y. Li, C. Sella, F. Lemaître, M. GuilleCollignon, L. Thouin, and C. Amatore, *Electroanalysis*, 2013, **25**(4), 895–902.

[12] A. Gencoglu and A. R. Minerick, *Microfluidics and Nanofluidics*, 2014, **17**(5), 781–807.

[13] D. Ye, Y. Yang, J. Li, X. Zhu, Q. Liao, and B. Zhang, *20th World Hydrogen Energy Conference, WHEC 2014*, 2014, **1**, 522–527.

[14] X. Shi, D. E. Simpson, and D. Roy, *Physical Chemistry Chemical Physics*, 2015, **17**(17), 11432–11444.

[15] L. S. Ribeiro, E. G. Rodrigues, J. J. Delgado, X. Chen, M. F. R. Pereira, and J. J. Órfão, *Industrial and Engineering Chemistry Research*, 2016, **55**(31), 8548–8556.

[16] T. Holm, P. K. Dahlstrøm, O. S. Burheim, S. Sunde, D. A. Harrington, and F. Seland, *Electrochimica Acta*, 2016, **222**, 1792–1799.

[17] R. R. Unocic, R. L. Sacci, G. M. Brown, G. M. Veith, N. J. Dudney, K. L. More, F. S. Walden, D. S. Gardiner, J. Damiano, and D. P. Nackashi, *Microscopy and Microanalysis*, 2014, **20**(2), 452–461.

[18] T. Yuan, L. Le Thi Ngoc, J. Van Nieuwkasteele, M. Odijk, A. Van Den Berg, H. Permentier, R. Bischoff, and E. T. Carlen, *Analytical Chemistry*, 2015, **87**(5), 2588–2592.

[19] T. Holm, S. Sunde, F. Seland, and D. A. Harrington, *Journal of Electroanalytical Chemistry*, 2015, **745**, 72–79.

[20] T. Holm, M. Ingdal, J. R. Strobl, E. V. Fanavoll, S. Sunde, F. Seland, and D. A. Harrington, *Electrochimica Acta*, 2017, **229**, 452–457.

[21] T. Holm, M. Ingdal, E. V. Fanavoll, S. Sunde, F. Seland, and D. A. Harrington, *Electrochimica Acta*, 2016, **202**, 84–89.

[22] M. Fighera, P. D. Van Der Wal, and H. Shea, *Journal of the Electrochemical Society*, 2017, **164**(12), H836–H845.

[23] Y. H. Kwok, A. C. H. Tsang, Y. Wang, and D. Y. C. Leung, *Journal of Power Sources*, 2017, **349**, 75–83.

[24] C. A. Martins, O. A. Ibrahim, P. Pei, and E. Kjeang, *Chemical Communications*, 2017, **54**(2), 192–195.

[25] C. A. Martins, O. A. Ibrahim, P. Pei, and E. Kjeang, *Electrochimica Acta*, 2018, **271**, 537–543.

[26] A. F. Chrimes, K. Khoshmanesh, P. R. Stoddart, A. Mitchell, and K. Kalantar-Zadeh, *Chemical Society Reviews*, 2013, **42**(13), 5880–5906.

[27] Y. Kwon, K. J. P. Schouten, and M. T. Koper, *ChemCatChem*, 2011, **3**(7), 1176–1185.

[28] J. F. Gomes, F. B. C. De Paula, L. H. S. Gasparotto, and G. Tremiliosi-Filho, *Electrochimica Acta*, 2012, **76**, 88–93.

[29] C. A. Martins, P. S. Fernández, H. E. Troiani, M. E. Martins, and G. A. Camara, *Journal of Electroanalytical Chemistry*, 2014, **717-718**, 231–236.

[30] J. L. Bott-Neto, A. C. Garcia, V. L. Oliveira, N. E. De Souza, and G. Tremiliosi-Filho, *Journal of Electroanalytical Chemistry*, 2014, **735**, 57–62.

[31] T. Iwasita and F. C. Nart, *Progress in Surface Science*, 1997, **55**(4), 271–340.

[32] W. Chen, J. Cai, J. Yang, M. M. Sartin, and Y. X. Chen, *Journal of Electroanalytical Chemistry*, 2017, **800**, 89–98.

[33] L. L. de Souza, A. O. Neto, and C. A. O. Forbicini, *International Journal of Electrochemical Science*, 2017, **12**(12), 11855–11874.

[34] N. I. Andersen, K. Artyushkova, I. Matanović, D. P. Hickey, S. D. Minteer, and P. Atanassov, *ChemElectroChem*, 2019, **6**(1), 246–251.

[35] N. I. Andersen, K. Artyushkova, I. Matanović, M. Seow Chavez, D. P. Hickey, S. Abdelloui, S. D. Minteer, and P. Atanassov, *ChemElectroChem*, 2019, **6**(9), 2448–2455.

[36] D. Kaluza, W. Adamiak, T. Kalwarczyk, K. Sozanski, M. Opallo, and M. Jönsson-Niedziolka, *Langmuir*, 2013, **29**(51), 16034–16039.

[37] F. T. G. van den Brink, W. Olthuis, A. van den Berg, and M. Odijk, *TrAC - Trends in Analytical Chemistry*, 2015, **70**, 40–49.

[38] L. Du, Y. Shao, J. Sun, G. Yin, C. Du, and Y. Wang, *Catalysis Science and Technology*, 2018, **8**(13), 3216–3232.

[39] A. Kara, A. Reitz, J. Mathault, S. Mehou-Loko, M. A. Amirdehi, A. Miled, and J. Greener, *Lab on a Chip*, 2016, **16**(6), 1081–1087.

[40] A. Déctor, J. P. Esquivel, M. J. González, M. Guerra-Balcázar, J. Ledesma-García, N. Sabaté, and L. G. Arriaga, *Electrochimica Acta*, 2013, **92**, 31–35.

[41] C. J. Huang, J. L. Lin, P. H. Chen, M. J. Syu, and G. B. Lee, *Electrophoresis*, 2011, **32**(8), 931–938.

[42] E. Sinkala, J. E. McCutcheon, M. J. Schuck, E. Schmidt, M. F. Roitman, and D. T. Eddington, *Lab on a Chip*, 2012, **12**(13), 2403–2408.

[43] S. Gu, Y. Lu, Y. Ding, L. Li, H. Song, J. Wang, and Q. Wu, *Biosensors and Bioelectronics*, 2014, **55**, 106–112.

[44] E. V. Fanavoll, D. A. Harrington, S. Sunde, G. Singh, and F. Seland, *Electrochimica Acta*, 2017, **225**, 69–77.

[45] Y. Li, W. Van Roy, P. M. Vereecken, and L. Lagae, *Microelectronic Engineering*, 2017, **181**, 47–54.

[46] S. Kang, A. F. Nieuwenhuis, K. Mathwig, D. Mampallil, and S. G. Lemay, *ACS Nano*, 2013, **7**(12), 10931–10937.

Chapter 2

An Overview of Glycerol Electrooxidation and Parallel Pathways Proposed for Carboxylate Products Generated on Platinum, Palladium and Gold.

Abstract

In the most recent decade, glycerol electrooxidation (GEOR) has attracted extensive research interest for valorization of glycerol, *i.e.*, the conversion of glycerol to value-added products. These reactions at platinum, palladium, and gold electrodes have a lot of uncertainty in their reaction mechanisms, which has generated some controversies. This review gathers many reported experimental results, observations and proposed reaction mechanisms in order to draw a full picture of GEOR. A particular focus is the clarification of two arguments: Pd is inferior to Pt in cleaving the C-C

bonds of glycerol during the electrooxidation and the massive production of CO_2 at high overpotentials is due to the oxidation of the already-oxidized carboxylate products. It is concluded that the inferior C-C bond cleavability with Pd electrodes, as compared with Pt electrodes, is due to the inefficiency of deprotonation, and the massive generation of CO_2 as well as other C1/C2 side products is partially caused by the consumption of OH^- at the anodes, as a lower pH reduces the amount of carboxylates and favors the C-C bond scission. A reaction mechanism is proposed in this review, in which the generation of side products are directly from glycerol ("competition" between each side product) rather than from the further oxidation of C2/C3 products. Additionally, GEOR results and associated interpretations for Ni electrodes are presented, as well as a brief review on the performances of multi-metallic electrocatalysts (most of which are nanocatalysts) as an introduction to these future research hotpots.

2.1 Introduction

Glycerol is produced on a large scale as a byproduct of biodiesel production, in the transterification of triglycerides with alcohols [1]. This makes it a cheap and useful starting point for conversion into value-added products ("valorization") such as dihydroxyacetone (DHA), glyceraldehyde, glyceric acid, glycolic acid, lactic acid, hydroxypyruvic acid, and *etc* [2] (see Figure 2.1). Previously, glycerol oxidation for valorization and energy generation has been implemented with many non-electrochemical methods. However, most of these have disadvantages such as requiring high temperature, high pressure, an external oxygen supply, or even use of heavy metals [3]. Compared with those harsh reaction conditions that are hard to maintain or toxicity that poses a threat to human health, electrooxidation of glycerol (GEOR) occurs under mild conditions and avoids those requirements.

There has been a rapid increase in the number of GEOR studies since 2010 (Figure 2.2a). Among the Scientific-Citation-Indexed studies on GEOR, most of which were done with highly catalytically active noble metals (*e.g.* platinum, palladium, and gold) for high efficiencies. However, as a non-noble metal abundant on earth, nickel has been receiving more and more attention (see Figure 2.2b). Nickel used to be utilized synergistically with noble metals [4–6], but, its high activity of electro-catalyzing GEOR alone has made it a promising substitute for noble metals. [7–9] With metallic electrocatalysts offering high efficiency in GEOR, studies conducted by researchers worldwide have covered all aspects related to GEOR, including novel nanocatalysts enhancing the efficiency and selectivity of GEOR towards certain products [10–12], product distribution analysis for the determination of the reaction mechanisms and kinetics [13, 14], and fuel cell fabrications (theoretically generating 1.01 V) [15–17], as shown in Figure 2.2c. Among them, the selectivity of glycerol oxidation products (usually reported with HPLC or FTIR data as illustrated in Figure 2.2d) is of great interest as it directly influences the potential for commericial production of

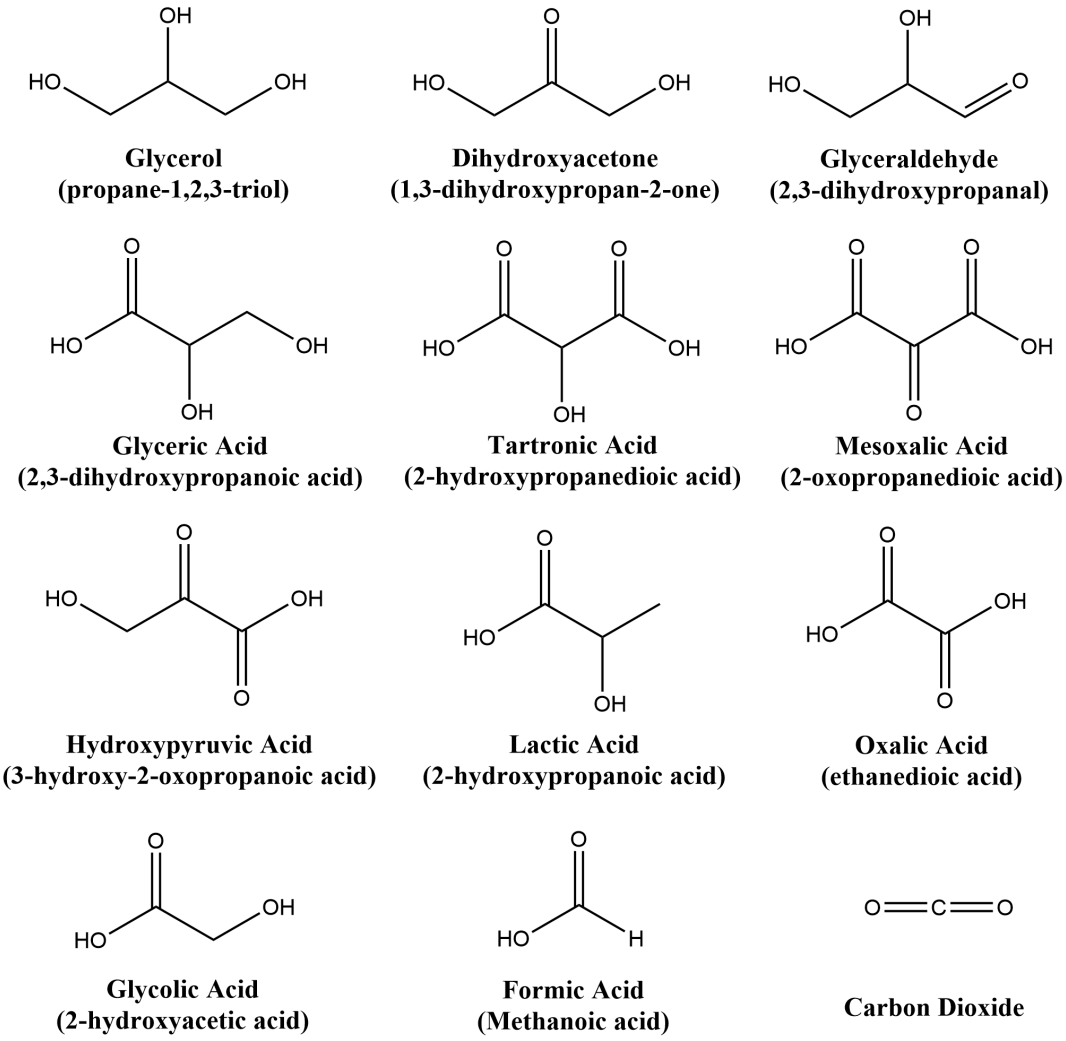

Figure 2.1: Molecular structures of glycerol and its oxidation products.

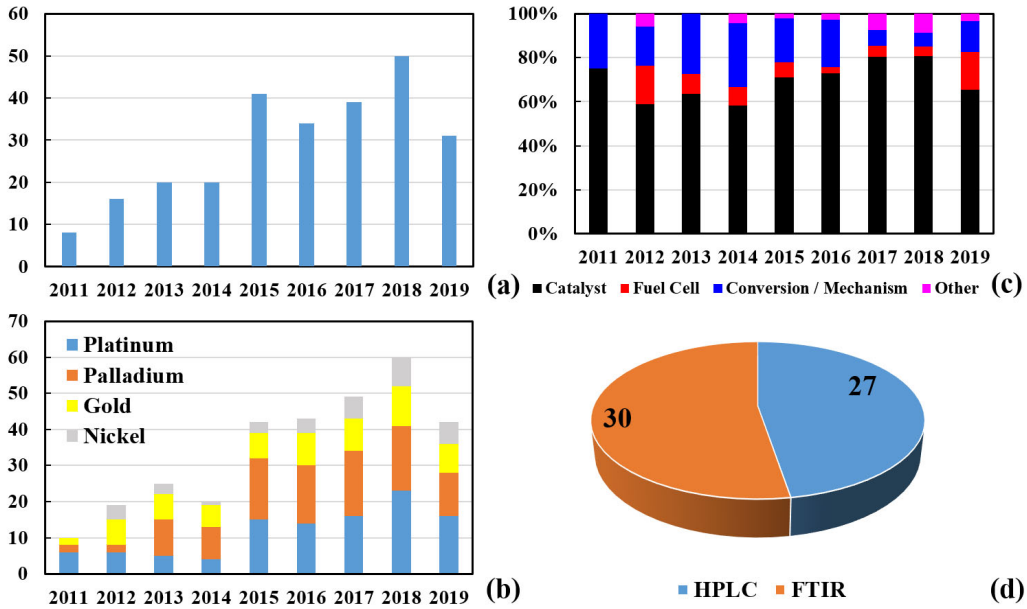

Figure 2.2: Statistical data of Scientific-Citation-Indexed (SCI) publications about glycerol electrooxidation since 2011. (a) Numbers of Scientific-Citation-Indexed (SCI) publications from 2011 to Jul 2019 found on Web of Science using the keyword "glycerol electrooxidation". (b) Numbers of GEOR studies conducted with Pt-based, Pd-based, Au-based, and Ni-based electrocatalysts from 2011 to Jul 2019. (c) Portions of GEOR studies focusing on catalysts, fuel cells, conversion / mechanism and *etc*, from 2011 to Jul 2019. (d) Portions of mechanism or conversion studies using HPLC or FTIR.

value-added products.

To obtain a high selectivity towards certain value-added products, reaction mechanism studies should be a prerequisite, but they are considerably outnumbered by papers describing empirical discoveries of novel electrocatalysts [1,18]. Moreover, the previously reported GEOR mechanisms with Pt, Pd, and Au are plagued by the fact that many hypotheses, observations and results are contradictory to each other. The innovations in new catalysts has somewhat worsened this issue as their preparation processes are under disparate conditions, and reporting of elemental compositions, morphologies and crystal planes have not been standardized [18].

An overview of these hypotheses and controversies is therefore timely, and should be used to direct the future works. It is an area that has not yet been emphasized in previously published reviews [19–21]. The reaction mechanism of GEOR was partially reviewed by Gomes et al. [22] together with other C3 alcohols. Different chemisorption assumptions are covered, including the adsorption via both terminal carbon atoms, or through one terminal carbon atom and the secondary carbon atom. In recently published reviews, Coutanceau et al. [23] categorized GEOR processes into two categories, that is, acidic and alkaline electrolytes, together with the performances of different metal catalysts. Du et al. [3] reviewed Pt-based, Pd-based and Au-based catalysts and proposed that higher pH and overpotentials tend to generate more highly oxidized products. Those reviews have nicely summarized the reported product distributions, but a comprehensive understanding of the mechanism remains elusive. A noteworthy overview was given by Martins et al. [18] as a chapter of the book *Increased Biodiesel Efficiency*. The overview ranges from reaction mechanisms to the types of electrocatalysts, and to the performances of glycerol-based fuel cells. Instead of giving detailed experimental conditions and comparing product distributions, only a few widely recognized observations and explanations are mentioned (*e.g.* enhanced selectivity towards DHA by adding Bi atoms to (111) planes). They concluded that the reaction mechanisms of GEOR are still far from fully understood.

Herein, an overview of GEOR conducted with Pt, Pd and Au catalysts is presented as an attempt to elucidate GEOR more comprehensively by presenting a comprehensive mechanistic scheme based on previously reported GEOR results by researchers worldwide. The content of this review includes: (1) summaries of the observations, hypotheses and controversies of GEOR brought by researchers in the most recent decade, (2) elucidations and clarifications of two propositions that prevail in the field of GEOR at Pt and Pd electrodes, (3) a proposed reaction mechanism arguing that the generation of C1/C2 products are directly from glycerol rather than from the electrooxidation of C2/C3 side products, and therefore the generation of a C1/C2

product is competing with other products generated through parallel pathways. For completeness, mechanisms for Ni-based GEOR and properties of nanocatalysts are also discussed.

2.2 Summary of Observed Glycerol Oxidation Results and Reported Reaction Mechanisms

Benefitting from the high reactivity induced by the adjacent hydroxyl groups [24–26], glycerol enjoys the potential of being oxidized into multiple intermediates/products, most of which are favored in industry because of the added commercial value. Pt, Pd and Au are noble metallic catalysts commonly used for electrocatalytically oxidizing glycerol [27, 28]. Based on hundreds of experimental observations, reaction mechanisms have been proposed by researchers worldwide to elucidate the oxidation processes. In this section, controversies and hypotheses are reviewed to give a comprehensive elucidation of GEOR mechanisms presented so far.

2.2.1 Platinum

In general, the electrocatalytic oxidation of alcohol can be divided into four steps: dissociative adsorption, bond breaking, reaction between oxygenated species and functional groups of adsorbed species on the surface, and intermediate/final product desorption [22]. Different adsorption pathways may lead to different adsorbates (*e.g.* alkoxide, acyl, aldehydes, etc. [29]), and presumably different products. Among all noble metallic catalysts, Pt is considered as the most active one due to its low d-band center (-2.25 eV) [30] which favors deprotonation. According to researchers, the reaction pathways of GEOR with Pt can be categorized into two groups: O-adsorption (happening at higher overpotentials through the coordination of a lone pair of oxygen

electrons in the hydroxyl group) and C-adsorption (major pathway at lower overpotentials) whose adsorbates are reportedly more stable than O-adsorbates in acidic medium [31].

O-adsorption (Figure 2.3a) involves the deprotonation of the primary or the secondary hydroxyl group to produce alkoxide. Kwon et al. [32] reported that strong alkali can promote this deprotonation step, since glycerol behaves as a weak acid in a strong alkaline solution whose pH is close to the pKa of glycerol (14.15). Once chemisorbed, a second deprotonation from the carbon atom occurs, which oxidizes glycerol into glyceraldehyde or DHA [19]. If OH^- exists in the electrolyte, Pt-OH(ads) (reportedly produced at 0.5 V – 0.6 V vs RHE [20]) can subsequently oxidize the chemisorbed glyceraldehyde into glyceric acid or glycerate. It is also known that under strong alkaline conditions, the Canizzaro reaction can convert aldehyde to carboxylic acid (or to carboxylate in alkali) and alcohol. However, no scission of the C-C bond occurs in either sub-pathway.

In the case of C-adsorption (Figure 2.3b), Koper et al. [31] and Sieben et al. [33] showed that Pt(100) only chemisorbs a terminal carbon atom of glycerol and oxidizes it into glyceraldehyde with partial deprotonation, whereas Pt(111) chemisorbs both types of carbon atoms for the oxidation to DHA [34] and glyceraldehyde. Also, both low and high overpotentials may completely deprotonate the terminal carbon atom and generate Pt-$CH_2OHCHOHCO$(ads). Similarly, two sub-pathways exist and take effect based on whether there is Pt-OH(ads). If not, since the C-C bond has been weakened by adsorption [35], the breaking of the C-C bond can generate Pt-CO(ads) (surface-poisoning species) and Pt-R(ads) (C2 or C1 products), as shown in Eq. (2.1). Without extensive production of Pt-OH(ads) at higher overpotentials, Pt-CO(ads) ends up slowing down the oxidation [12]. In alkaline conditions, with the help of Pt-OH(ads), Pt-CO(ads) can react with Pt-OH(ads) to give CO_2 (Langmuir-Hinshelwood mechanism, Eq. (2.2)) or Pt-COOH(ads) (subsequently converted into carbonate, Eqs. (2.3)-(2.5)). It is widely hypothesized that the removal of CO is the

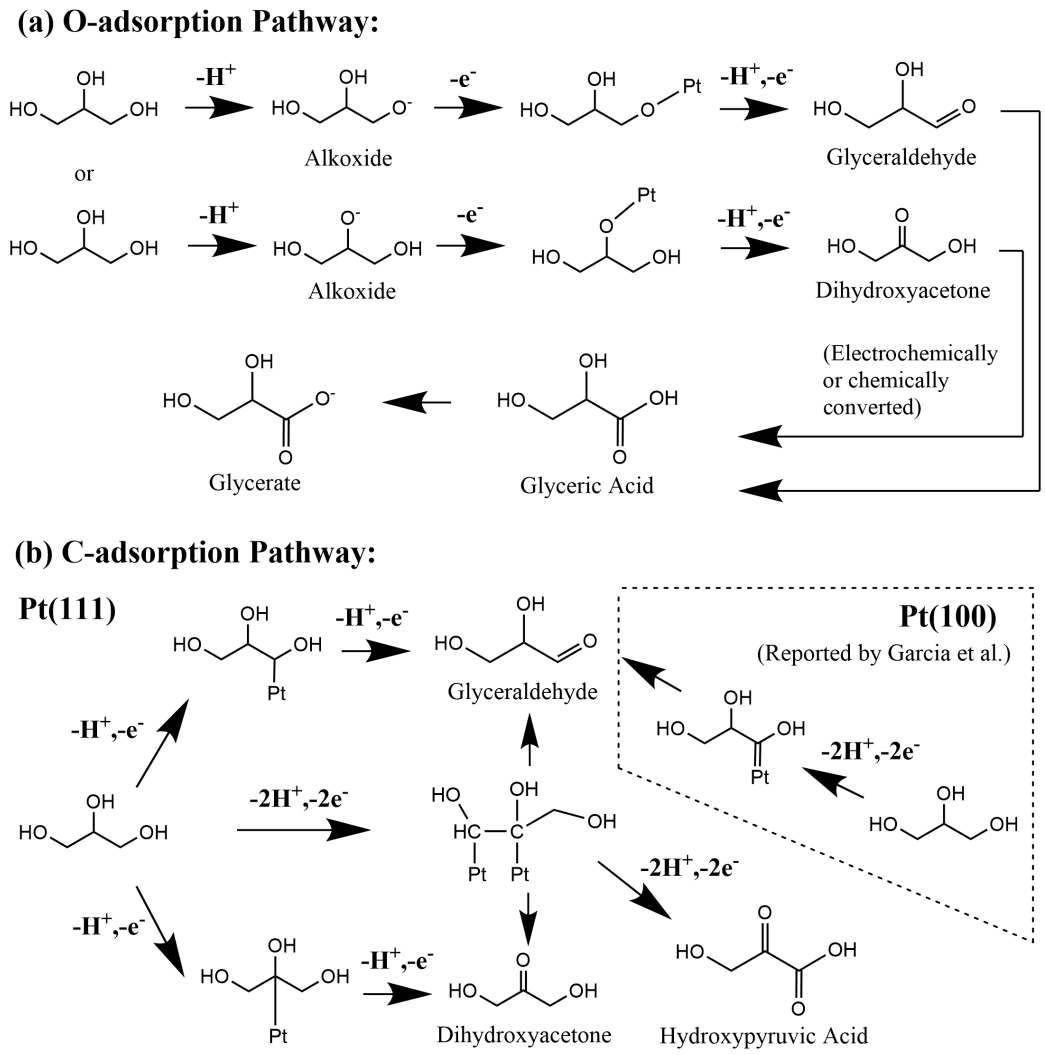

Figure 2.3: Pathways of glycerol electrooxidation at Pt electrodes. (a) O-adsorption, and (b) C-adsorption (adapted from Ref [31]).

rate-determining step of GEOR [16], and therefore higher OH^- concentration leads to better catalytic activity because of the higher OH(ads) coverage and greater OH^- diffusion. Therefore, it is believed that the onset potential of OH adsorption has a negative correlation with pH, which also applies to Pd and Au [15].

$$\mathrm{Pt-RCO(ads)} \rightarrow \mathrm{Pt-R(ads)} + \mathrm{Pt-CO(ads)} \tag{2.1}$$

$$\mathrm{Pt-CO(ads)} + \mathrm{Pt-OH(ads)} \rightarrow 2\mathrm{Pt} + \mathrm{CO_2}{+}\mathrm{H^+}{+}\mathrm{e^-} \tag{2.2}$$

$$\mathrm{Pt-CO(ads)} + \mathrm{Pt-OH(ads)} \rightarrow \mathrm{Pt} + \mathrm{Pt-COOH(ads)} \tag{2.3}$$

$$\mathrm{Pt-COOH(ads)} + \mathrm{Pt-OH(ads)} + 2\mathrm{OH^-} \rightarrow \mathrm{CO_3^{2-}}{+}2\mathrm{H_2O} \tag{2.4}$$

$$\mathrm{Pt-CO(ads)} + 2\mathrm{Pt-OH(ads)} + 2\mathrm{OH^-} \rightarrow \mathrm{CO_3^{2-}}{+}2\mathrm{H_2O} \tag{2.5}$$

In a hypothesis proposed by Roquet et al. [36], C-adsorption may happen with both types of carbon atoms, implying the existence of multiple adsorbates. It is widely observed that glyceraldehyde and DHA are the two major intermediates, which indicates two major oxidation pathways, either through the primary alcohols or the secondary alcohol [37]. Dai et al [38] measured the product distribution of GEOR in alkali with Au-Pt nanoparticles using NMR spectra and HPLC. Their results show that the secondary alcohol oxidation occurs preferentially at lower overpotentials (0.45 V vs RHE) leading to DHA, whereas primary alcohol oxidation starts at higher overpotentials (0.9 V vs RHE), and generates mainly glyceric acid and tartronic acid. However, with both Pt and Pt-Cu electrodes, Ribeiro et al. [39] illustrated that glyceraldehyde was identified as the major oxidation product under acidic conditions, together with DHA and glyceric acid. These results derived by different research groups seem contradictory, but can be reconciled by assuming two co-existing effects. Firstly, a structural effect (two primary OH groups to one secondary OH group) makes the hydroxyl group on terminal carbon atoms more easily oxidized [2, 40]. Secondly, secondary alcohol groups oxidizes through simpler deprotonation steps [41]. Cur-

rently, the only mechanism extensively proven is the high selectivity towards DHA if metals like Bi, Ru and Sb are introduced on Pt(111) [42–45], as the reaction through primary alcohol oxidation requires three adjacent Pt sites to proceed (see Section 2.5).

The ease of C-C bond cleavage is a controversial area that is still under debate and needs further investigation. The capability of an electrocatalyst to dissociate C-C bonds is usually estimated by calculating the ratio of C1/C2 products to C3 products [2]. The presence of CO(ads) can be taken as an indicator of bond cleavage [46]. Some observations suggest that this cleavage is favored at low overpotentials [16] and in acidic conditions [38, 47], which may be explained by the remarkable effect of oxygenated species on converting intermediates into carboxylates rather than breaking C-C bonds [13], together with a possibly higher barrier for C-C cleavage in the presence of more OH(ads)/O(ads) at such overpotentials. Other researchers argue that large overpotentials overcome the energy barrier of C-C cleavage, as they observed massive production of CO_2 at potentials higher than 1.1 V vs RHE [48, 49].

Aside from pH and overpotential, other factors affecting the C-C bond dissociation have also been examined. A higher temperature can generally promote the oxidation of adsorbed species by enabling the energy barrier crossing, which is then followed by desorption of adsorbates. Ribeiro et al. [39] tested the effect of high temperature on C-C bond cleavage and concluded that high-temperature acts positively on this process as glycolic acid was found at the expense of glyceric acid. However, researchers have also reported a barely affected DHA selectivity over a range of temperatures up to 70°C using a Sb-modified Pt catalyst [42].

Investigations of GEOR with Pt electrodes have involved both polycrystalline and monocrystalline (specifically Pt(111), Pt(110), and Pt(100)) electrodes. Two CV peaks are shown during the anodic scan of GEOR at Pt(111) in acidic solution, which can be ascribed to the deprotonation of glycerol towards CO(ads) (0.56 V, broad and decreasing during continuous cycling) and the removal of CO(ads) with

OH(ads) (0.78 V, sharp) [50]. Spectroscopic (FTIR) studies show that bridge-bonded CO (CO_B) only exists on Pt(100) above 0.05 V vs RHE, and linearly bonded CO (CO_L) appears at higher overpotential, while Pt(111) and Pt(110) have only linearly absorbed CO [31, 49, 51]. Pt(111) was proven to be the most active plane for removal of CO and other intermediates [16]. Gomes et al. [52] reported that the dissociative adsorption and the breaking of C-C bonds are much easier on Pt(110) and Pt(100) than Pt(111), from which they argued that RCO(ads) is more stable on Pt(111). Angelucci et al. [53] also reported that acyl (Pt-RCO(ads)) groups are stable on Pt(111), and therefore O-adsorption is thought to be the major oxidation pathway through which the adsorbates generated are relatively more unstable.

On polycrystalline Pt, GEOR occurs by various reaction pathways, which occur at different overpotentials [54]. Also, it is believed that the reaction processes on polycrystalline Pt are just the total of the reaction processes on the three different low index single-crystal faces. According to Fernandez et al. [54], the oxidation peak of GEOR below 0.8 V vs RHE is associated with defects in the (111) and (110) planes, whereas another peak at higher overpotentials (above 0.8 V vs RHE) is ascribed to the effect of Pt(100) defects.

At higher potential, Pt is oxidized to PtO, which is also regarded as an GEOR-active catalyst [36]. Dissociative adsorption of glycerol happens at the surface of PtO, with which both the primary carbon and secondary carbon are adsorbed onto two PtO sites. Nevertheless, only one proton is removed from each carbon adsorbed. The simultaneous reduction of PtO and oxidation of hydroxyl groups lead to Pt and a dissociated C-C bond, *i.e.* C1 or C2 products.

2.2.2 Palladium

Pd has a higher d-band center (-1.83 eV [30]) than Pt. Also, a difference between Pd and Pt is that on low index planes like (111) and (110), spectroscopic studies only

show the existence of CO_B [55, 56]. Pd only has linearly adsorbed CO at step and kink sites with low coordination numbers [57, 58].

One reaction mechanism proposed [59] is very much like the C-adsorption pathway in Pt-GEOR. However, Pd requires a more basic electrolyte as a promotor of this deprotonation process compared with Pt [39]. Nevertheless, excessive OH(ads) occupying the active sites may reduce the efficiency of GEOR [60]. Therefore, efficient GEOR on Pd depends on the presence of both Pd-OH(ads) and free Pd sites [61]. The reaction of Pd-RCO(ads) with Pd-OH(ads) is usually assumed to be the rate-determining step as on Pt (Eqs. (2.6) and (2.7), [62, 63]), but other researchers have hypothesized that the rate-determining step is the desorption of reaction intermediates (*e.g.* DHA at a low overpotential [64]).

$$\mathrm{Pd-(RCH_2OH)(ads)} + 3\mathrm{OH^-} \rightarrow \mathrm{Pd-RCO(ads)} + 3\mathrm{H_2O} + 3\mathrm{e^-} \tag{2.6}$$

$$\mathrm{Pd-RCO(ads)} + \mathrm{Pd-OH(ads)} \rightarrow \mathrm{Pd} + \mathrm{Pd-RCOOH(ads)} \tag{2.7}$$

Similar to Pt-GEOR, the production of CO_2 is usually seen at high overpotentials [65]. However, C-C bond dissociation is reportedly more difficult on Pd than Pt and Au [15, 66], which is supported by the observation that glyceric acid is more commonly produced on Pd than Pt [39]. In addition, oxygenated species are believed to facilitate C-C cleavage [67, 68], which is strongly contrasted by the negative role OH(ads) plays on C-C bond cleavage with Pt catalysts. Fortunately, the influence of the functional groups and the surface sites of Pd on C-C bond dissociation are much more deeply studied than on Pt catalysts. For example, Miller et al. [69] compared the C-C cleavability of ethanol and glycerol with Au@Pd nanoparticles (Pd shell covering Au core) and hypothesized that adjacent alcohol groups are needed for this bond cleavage. According to Coutanceau et al. [43], the cleavage of C-C bonds is subject to the adjacent sites on Pd terraces, as both the primary and secondary carbon atoms are supposed to be adsorbed on the crystal plane for this process.

The preferential deposition of Bi on Pd(111) rather than Pd(100) remarkably reduces the vicinity of Pd atoms, therefore lowering the ability of C-C cleavage. With the change in the amount of deposited Bi, the surface rearrangement from Bi monomers to islands leads to fluctuation of Pd atom vicinity and consequently affects the C1/C2 selectivity [14]. Presumably, this phenomenon also applies to Pt, since it has the same fcc crystal structure.

Additionally, a large number of studies have been directed to the catalytic activities of specific crystal planes. For example, Pd(100), which is prominent in some nanostructured Pd catalysts [45], is found to outperform Pd(111) in terms of the catalytic efficiency [43, 70, 71], as it can adsorb glycerol more easily [43, 45]. Furthermore, GEOR through the primary carbon on Pd(100) has been demonstrated in studies showing high selectivity towards glycerate [72] and tartronate [73]. Besides, Pd(520), as a high-index plane with lots of kinks and steps which promote bond dissociation of glycerol, was found to have a higher catalytic activity compared to low-index planes [11, 74].

2.2.3 Gold

According to Roy et al [75] and other researchers [76], deprotonation (C-H scission) is the rate-determining step of GEOR on Au, which differs completely from Pt and Pd. It is hypothesized that the dissociative adsorption of glycerol occurs only if Au-OH(ads) is present, which is based on the fact that GEOR has the same onset potential as the formation of Au-OH(ads), and the vast majority of GEOR studies with Au are done in alkaline conditions. Also, DFT studies showed that the adsorbed OH on Au surfaces lowers the activation barrier and thus facilitates the dissociation of C-H and O-H bonds [77]. Moreover, it was shown that the deprotonation process happens to H_α (scission of O-H) ahead of H_β (C-H) [77], which may also apply to Pd [78] as they both rely on the promotional effect of OH(ads). In fact, researchers found

that glycerol anchors to Au-OH(ads) for deprotonation and subsequent adsorption [79–81], which leads to the production of glyceraldehyde at lower overpotentials (Eq. (2.8)) [75], and therefore both OH(ads)-covered and free surface sites of Au must be present for the dissociative adsorption to proceed [82]. Fortunately, free sites of Au without adsorbed OH are always available, as the maximum OH(ads) coverage on Pt (at 0.85 V) and Au (at 1.3 V) is estimated to be around 0.4-0.5 monolayer [83]. Besides, some researchers believed that glycerol can be oxidized directly to glycerate rather than via glyceraldehyde under alkaline condition [84], which implies the existence of another reaction pathway.

$$\mathrm{Au-RCH_2OH(ads)+Au-OH(ads)+OH^-\rightarrow Au+RCHO+2H_2O+e^-} \quad (2.8)$$

The Au(111), Au(100) and Au(110) surfaces are all reportedly GEOR-active [85, 86], among which Au(111) has the lowest surface energy and highest catalytic activity [87, 88]. However, a study comparing the onset potential of OH(ads) formation on (111), (100) and (110) facets of Au showed that Au(110) is the most active one for OH(ads) formation as it has the lowest onset potential of GEOR, followed by (100) and lastly (111) [89].

It is still unclear whether GEOR in acidic conditions can occur on Au electrodes [90], although researchers have proposed that the loss of electrocatalytic activity is due to the absorption of sulfate or perchlorate ions from the acidic electrolytes on the surface of Au. (Sulfate is more easily adsorbed onto the surface compared to perchlorate.) A combined cyclic voltammetry and DFT study [90] has revealed that Au has catalytic activity in acidic medium. Interestingly, the catalytic activity is more obvious during the cathodic scan, which is possibly explained by the active sites made available by the removal of adsorbed sulfate/perchlorate.

The fully filled d-band of Au is believed to hinder the bond formation with free radicals of dissociated alcohols, which is one of the explanations of the reduced cat-

alytic activity of Au [91, 92]. Nevertheless, this feature prevents both the poisoning effect (CO existing as CO_B [93]) and the formation of Au-OH(ads) [94]. It is noticeable that the poisoning effect reportedly plays a positive role on the efficiency of Au-GEOR (possibly due to the promotion of OH(ads) formation on Au(111) and Au(100) by CO(ads) in order to deprotonate H_β), while the mechanism has not yet been comprehensively illustrated [95–98].

GEOR on Au is able to highly oxidize glycerol into C1 products, or highly oxidize glycerol into di-carboxylates. Researchers found that Au can adsorb both primary and secondary carbon atoms [68] and it favors C-C bond cleavage towards CO_2 at potentials higher than 0.9 V vs RHE [38, 99, 100]. The ability to cleave C-C bonds has also been reported by Ottoni et al. [79] using $Pd_{50}Au_{50}$/C, and only C1 products (formate and carbonate) are identified. Similarly, Yongprapat et al. [101] reported a higher selectivity towards formate (>60%) at potentials from 0.2 to 0.4 V vs Hg|HgO. Highly oxidized GEOR products are also commonly identified, which is attributed to a possible mechanism of simultaneous adsorption of either both of the terminal carbon atoms [80] or all three carbon atoms. Oxalate and formate are identified as main oxidation products (>0.95 V vs RHE) by Garcia et al [81]. Tartronate was reported to be produced at a low overpotential (lower than 0.45 V vs RHE) [102] or with a low ratio of glycerol concentration to the surface area, while the secondary hydroxyl group can be oxidized between 0.45 and 0.9 V [103, 104]. The reported generation of other products includes DHA and 2,3-dihydroxy-2-propanal, which were produced at 0.39 V vs RHE, whereas glyceraldehyde can be produced at 0.6 V vs RHE, which means that secondary alcohol oxidation is facile at low overpotentials [90, 105]. One possible explanation is that Au(100)-OH(ads) favors the deprotonation of secondary carbon atoms [86].

2.2.4 Nickel

The demand for new catalysts with lower cost of production has stimulated the development of Ni-based catalysts which exhibit a decent activity compared with noble metals [7]. Fundamental studies have shown that the catalytically active β-NiOOH (generated at 1.3 V vs RHE from β-$Ni(OH)_2$) is responsible for the oxidation of glycerol as well as other alcohols. The mechanism proposed by Fleischmann et al. (also called the indirect electron transfer pathway, see Eqs. (2.9) and (2.10)) described the oxidation of hydroxyl groups by the reduction of β-NiOOH, which is demonstrated by the observation that no reduction peak appears during the cathodic scan. By contrast, other researchers argue that the alcohol diffuses through the surface and reacts with OH^- on the surface to get oxidized (direct electron transfer pathway) [106, 107].

Existing reports show that Ni is capable of cleaving the C-C bond [9, 108], and it is very likely to convert glycerol into C1 products and produce CO_2 (carbonate) [109]. Oliveira et al. [9] reported that formate was produced as the major product at 1.6 V vs RHE, while glycolate and glycerate were identified as minor products. Additionally, they also found that switching potentials between 1.6 V and 1.9 V did not strongly affect the selectivity, since glycerate, glycolate and formate were produced in both cases, except the production of CO_2 above 1.70 V [110]. So far, the reaction pathway of C-C bond cleavage (*e.g.* towards to production of formate [9, 111]) is still unclear.

$$\beta\text{-NiOOH} + \mathrm{R-CH_2OH} + \mathrm{OH^-} \rightarrow \beta\text{-Ni(OH)}_2 + \mathrm{H_2O} + \mathrm{R-CHO} + \mathrm{e^-} \tag{2.9}$$

$$\mathrm{R-CHO} + 3\mathrm{OH^-} \rightarrow \mathrm{R-COO^-} + 2\mathrm{H_2O} + 2\mathrm{e^-} \tag{2.10}$$

In the presence of glycerol, oxygen evolution on NiOOH is shifted to a higher potential [9], which indicates that NiOOH prefers generating intermediates of GEOR instead of generating OH(ads) [111].

2.2.5 Summary

In general, many observations with respect to GEOR under various conditions have implied that the oxidation of a primary alcohol group into a primary carboxylate or carboxylic acid is likely to inhibit the oxidation of other alcohol groups [99]. As evidence, the production of glyceraldehyde/glyceric acid and glycolic acid, is favoured over production of tartronic acid, mesoxalic acid and oxalic acid. Also, compared with the easily produced DHA and glyceraldehyde, the production of hydroxypyruvic acid is rarely found, which could be because the oxidation of either a primary alcohol group or a secondary alcohol group would make it more difficult for the oxidation of the remaining group. A second explanation could be the lower possibility of having both terminal carbon atoms and secondary carbon atom simultaneously adsorbed on (111) planes for the oxidation to occur. Similar observations include the one illustrated by Miller et al. [69] that diols with two alcohol groups on adjacent carbon atoms tend to be oxidized into mono-carboxylates, while diols without this adjacency can be oxidized into di-carboxylates or ketones.

2.3 General Discussion

Detailed analysis of the reaction mechanisms of GEOR is always hindered by the uncertain interpretations of observed results. This issue is worsened by vaguely using words such as "favor" and "improve", because in some cases these words describe the efficiency of GEOR reactions, and in other cases they mean a higher selectivity towards certain products. Many of the controversies might have been resolved if the exact meaning of these descriptions were given.

Since the 1990s, *in-situ* FTIR has been used for monitoring electrochemical interfaces [112]. In the last decade, this method has been applied to the identification of the adsorbates and intermediates during GEOR. So far, many peaks / bands of

IR spectra have been assigned to specific vibrational modes [43, 113]. Nevertheless, controversies of peak identification still exist as the convolution of peaks may mask weak bands or shift the center of peaks. Overall, several facts can be confirmed by interpreting IR spectroscopic results.

In many GEOR studies by FTIR, Pt and Pd electrodes show three "stages" (denoted as **Stage I, II and III** here) as the overpotential is increased [31, 48, 52, 55]. Initially in Stage I, at low overpotentials which do not facilitate the formation of OH(ads), a complete oxidation of glycerol can occur, which is confirmed by characteristic peaks of CO_L (mostly at Pt(111) and Pt(110)) and CO_B (mostly at Pd and Pt(100)) (see Figure 2.4a-2.4c), together with the parallel production of glyceraldehyde [49]. Another proof of complete oxidation is that an experiment using isotope-labelled terminal carbon atoms show that CO(ads) are generated from both terminal and secondary carbon atoms (see Figure 2.4d) [48]. When the potential is above approximately 0.6 V into Stage II, the bands of CO(ads) disappear (see Figure 2.4e-2.4h), shrink or remain unchanged (rarely seen), indicating that the amount of CO adsorbed on the surfaces of Pt and Pd stop increasing [49]. Meanwhile, carboxylates are rapidly produced and accumulate, as revealed by the complexity of spectra in the range of 1100-1600 cm^{-1}. The beginning of the last stage is characterized by a steeply rising peak at 2343-2345 cm^{-1} (usually above 1.0-1.1 V vs RHE), which translates into the evolution of CO_2. At the same time, the peaks of carboxylates stop rising. The staging demonstrated in this paragraph can be clearly indicated by the change in the IR intensities of CO(ads) and CO_2 (see Figure 2.4e-2.4h).

Au is a special case as it very rarely produces CO(ads), and therefore CO_2 production is also limited (even though a short peak at 2343 cm^{-1} can be seen for some cases). Carboxylate peaks are usually seen, and are the only features in the FTIR spectra for Au [68, 81].

It is believed by many researchers that the capacity of Pd to cleave C-C bonds of glycerol is weaker than Pt (referred to here as **Proposition A**). This proposi-

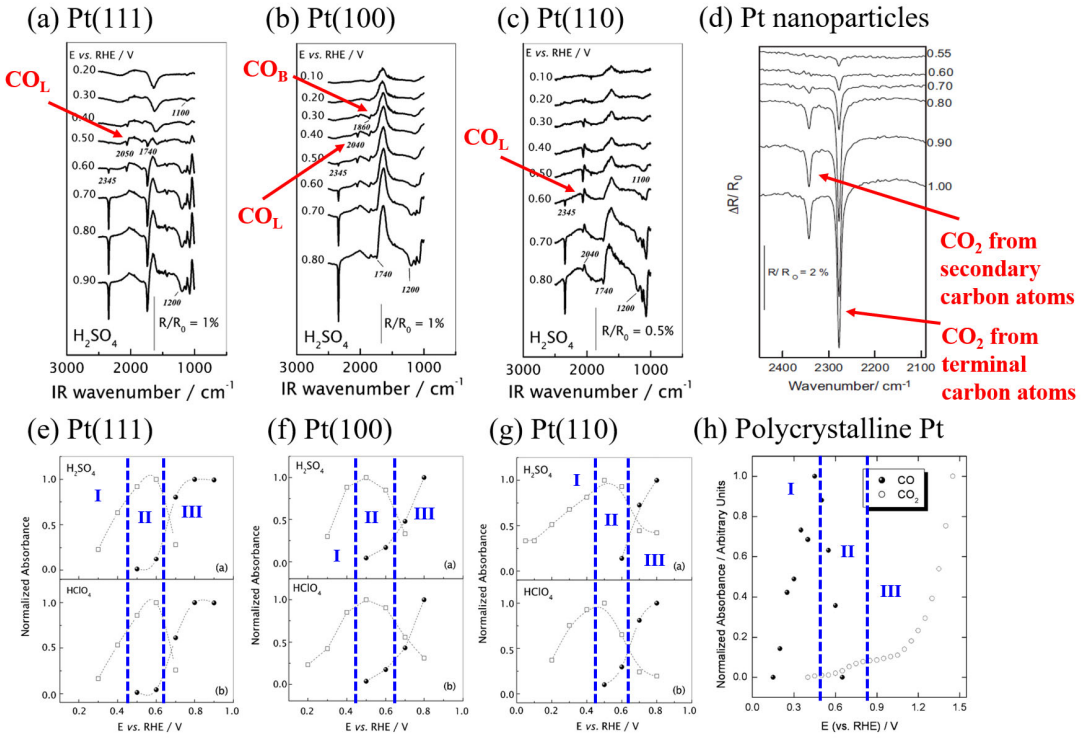

Figure 2.4: *In-Situ* FTIR spectra of glycerol electrooxdation with Pt catalysts and the analyses of adsorbed CO on Pt. (a-c) *In-situ* FTIR spectra of GEOR on Pt monocrystalline in 0.1 M glycerol with 0.1 M $HClO_4$ or H_2SO_4. (Reprinted with permission from Ref [52], with annotations in red. Copyright © 2012 Elsevier Ltd. All rights reserved.) (d) *In-situ* FTIR spectra in the presence of 0.255 M $^{13}CH_2OH$–$^{12}CHOH$–$^{13}CH_2OH$ + 0.1 M $HClO_4$. (Reprinted with permission from Ref [48], with annotations in red. Copyright © 2012 Elsevier Ltd. All rights reserved.) (e-g) Normalized absorbance of linear CO (white squares) and CO_2 (filled circles) for GEOR at different potentials with Pt monocrystalline in 0.1 M glycerol with 0.1 M $HClO_4$ or H_2SO_4. (Reprinted with permission from Ref [52], with annotations in blue. Copyright © 2012 Elsevier Ltd. All rights reserved.) (h) Normalized absorbance of CO and CO_2 for GEOR at different potentials (0.1 M glycerol with 0.1 M $HClO_4$) (Reprinted with permission from Ref [49], with annotations in blue. Copyright © 2011 Elsevier Ltd. All rights reserved.)

Table 2.1: Reported onset potentials of GEOR, OH adsorption, and surface oxide formation with Pt and Pd electrodes. Potentials vs RHE unless otherwise stated

	Onset Potentials	
	Pt	Pd
GEOR	0.05 V for (110),(100) [28]	0.4 V [55], 0.6 V [65]
OH(ads)	0.4 V [50], 0.5-0.6 V [20]	0.15 V vs HgO [117]
Oxide	0.5 V [83]	0.5 V [118], 0.67 V [119], 0.7 V [65]

tion is usually supported by two empirical observations: (1) a larger portion of C3 intermediates is often reported from Pd catalysts than Pt [39], and (2) the current density of Pd obtained in cyclic voltammetry is much lower than Pt [27] (see Figure 2.5a). In fact, this conclusion is doubtful, as there are many spectra comparing Pt and Pd catalysts showing that the onset potentials at which CO(ads) is formed on the surface of Pt and Pd are very close (see Figure 2.5b-2.5c), and both Pt and Pd can catalyze glycerol oxidation to produce large amounts of CO_2 at high potentials in Stage III (see Figure 2.6) [43, 50, 53, 55, 114, 115]. Comparative DFT studies are strongly needed to justify this proposition. A DFT study conducted by Rangarajan et al. [116] investigated the energetically favored reaction pathways of GEOR at Pt and Pd electrodes and found that both Pt and Pd favor C-C bond scission (after three deprotonation steps) over C-O bond scission.

Proposition A becomes clearer if it is combined with three other observations: (1) higher overpotentials and alkaline electrolytes lower the cleavability of C-C bonds on Pt [16, 38], whereas they improve the C-C bond dissociation on Pd [65, 67, 68]. (2) GEOR occurring on the surface of Pd is usually in alkaline conditions as its activity (current density) is very limited in acidic solutions compared with Pt [15]. (3) The difference between the onset potentials of rapid GEOR and OH(ads) formation are much closer in the cases of Pd than Pt (see Table 2.1).

Based on these three widely reported observations, an interpretation is that the lower cleavability of C-C bonds with Pd catalysts is due to the very limited efficiency of GEOR in Stage I, rather than the poor selectivity towards C1/C2 products. In

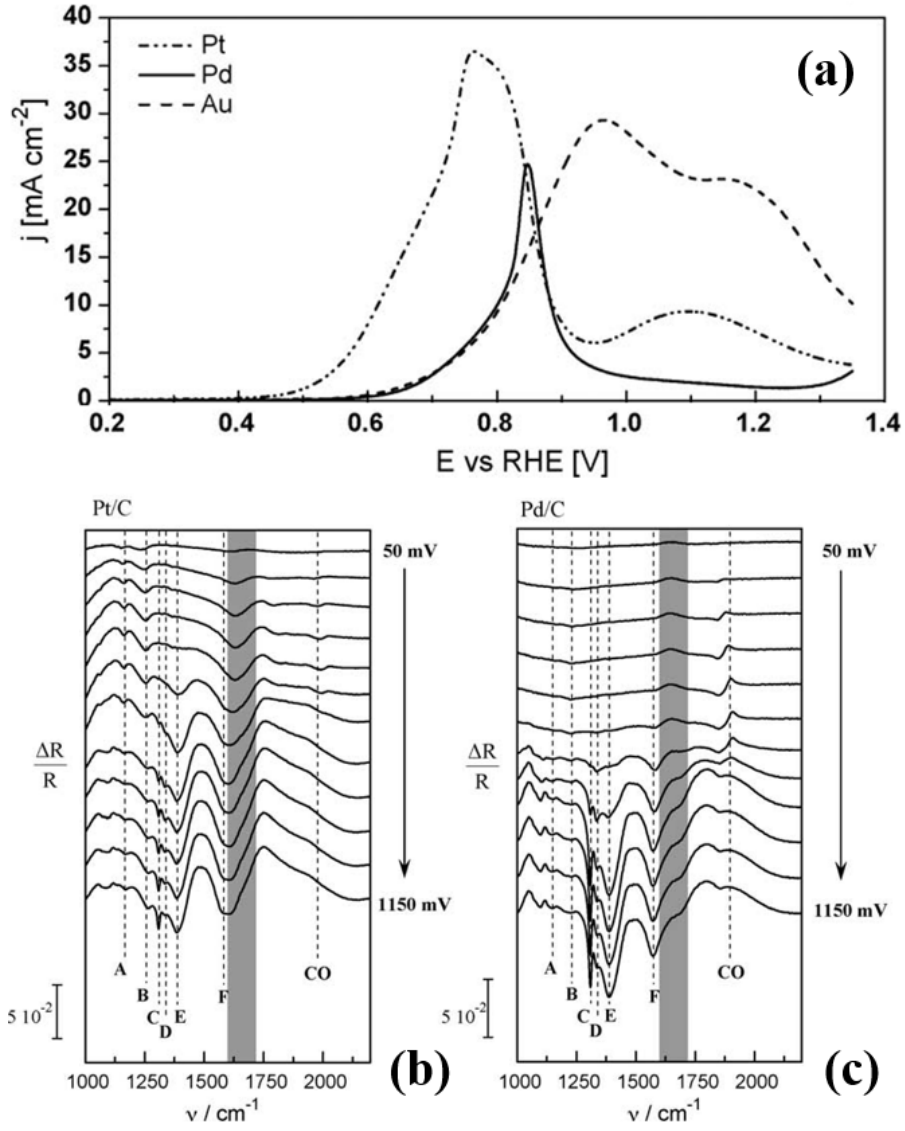

Figure 2.5: Cyclic voltammograms and *In-Situ* FTIR spectra and of glycerol electrooxidation with Pt and Pd electrocatalysts. (a) Cyclic voltammetry showing GEOR with Pt, Pd, and Au at room temperature (0.1 M glycerol + 1.0 M NaOH electrolyte). (b-c) *In-situ* infrared spectra of GEOR with Pt/C and Pd/C working electrodes (Reprinted with permission from Ref [27], Copyright © 2009 Elsevier B.V. All rights reserved.).

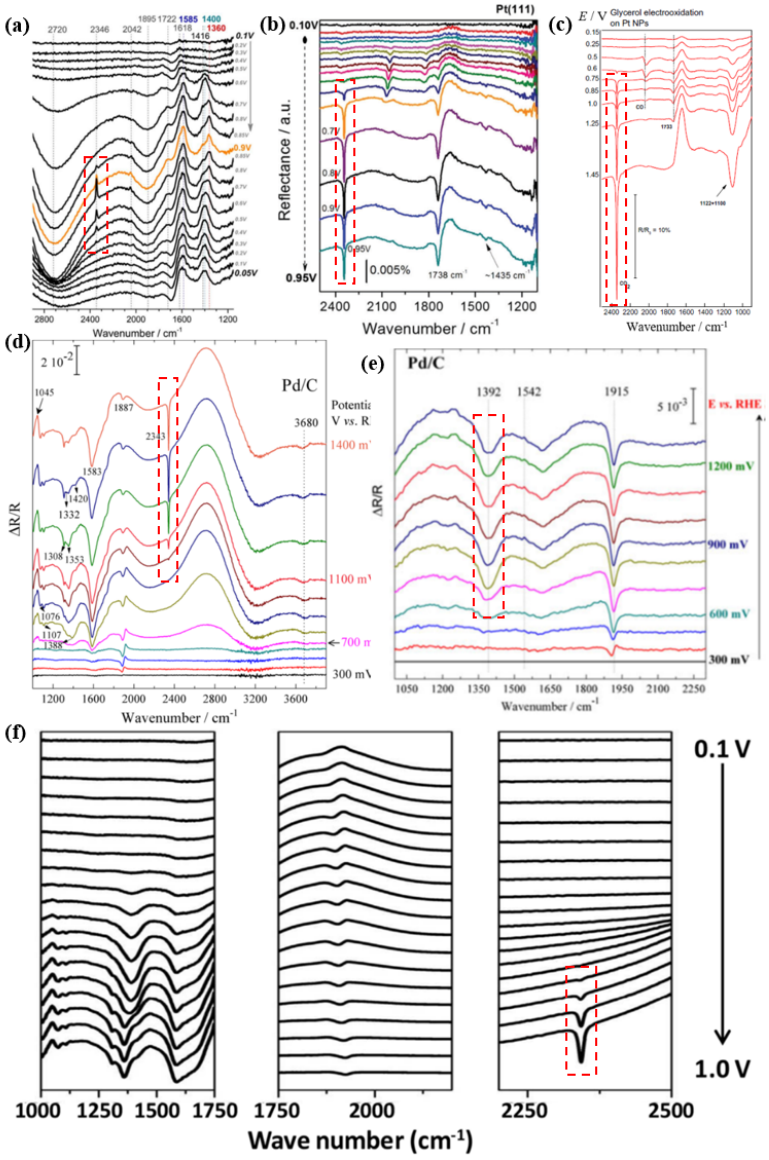

Figure 2.6: *In-situ* FTIR potential-dependent spectra of GEOR with Pt and Pd catalysts. (a) 0.5 M glycerol in 0.1 M NaOH on Pt(111). Potential: 0.05 to 0.9 V; (Reprinted with permission from Ref [53], © 2017 Elsevier B.V. All rights reserved.) (b) 0.2 M glycerol in 0.5 M H_2SO_4 solution with Pt(111) (Reprinted with permission from Ref [50], © the Owner Societies 2016) (c) 0.05 M glycerol & 0.1 M $HClO_4$ with Pt nanoparticles (Reprinted with permission from Ref [114], Copyright © 2014 Elsevier B.V.) (d) 0.1 M glycerol in 0.1 M NaOH electrolyte at 1 mV s^{-1} on Pd/C (Reprinted with permission from Ref [55], Copyright © 2013 American Chemical Society) (e) 0.1 M glycerol in 0.1 M NaOH on Pd/C (Reprinted with permission from Ref [115], © Springer Science+Business Media New York 2013) (f) 0.1 M glycerol in 0.1 M NaOH at Pd. Scan rate: 1 mV s^{-1} (Reprinted with permission from Ref [43], Copyright © 2015 Elsevier Ltd. All rights reserved.) IR bands of CO_2 (2343 cm^{-1}) or carbonate (1398 cm^{-1}) are highlighted by dashed rectangles in red.

Stage I, as the dissociative adsorption of glycerol on Pd is very slow, only a few researchers detected CO(ads) signals at a low overpotential (*e.g.* 0.3 V vs RHE) at which there is no OH adsorption. Under circumstances OH(ads) are generated and promote the dissociative adsorption of glycerol, Pd catalysts share a similar selectivity towards C2/C1 products with Pt. Higher overpotentials and alkalinity of electrolytes can bring both Pd and Pt to a stage where OH(ads) acts as a major reactant with glycerol. On one hand, as illustrated by Eq. (2.5), OH(ads) is able to convert poisoning species CO(ads) into CO_2 via a Langmuir-Hinshelwood mechanism. On the other hand, glyceric acid, glycolic and formic acid can be produced via the production of carboxylates (Eq. (2.7)), which means that a large portion of oxidized glycerol is directed to carboxylate (mainly glycerate [34, 49, 120, 121]), rather than completely oxidized into CO(ads). As the current density under such circumstances is much higher than for low-overpotential / acidic conditions, it is uncertain whether the exact amount of CO_2 / carbonate produced on Pt increases or not. However it is much more plausible that the amount of CO_2 evolved from Pd catalysts increases, which justifies **Proposition A**.

As the potential increases from Stage II to Stage III, the peak intensities of carboxylates basically remain unchanged after rapidly rising in the beginning of Stage II, while evolution of CO_2 becomes a major feature. Another proposition proposed by researchers (**Proposition B**) is that the massive production of CO_2 in Stage III (usually above 1.0-1.1 V vs RHE) is due to the electrooxidation of carboxylate intermediates. This proposition is usually developed into a reaction mechanism that attributes the production of C1/C2 products to the electrooxidation of C2/C3 intermediates [17, 28, 38, 55] (see Figure 2.7). A cautious verification of Proposition B requires two aspects: (1) showing that these C3/C2 intermediates have a relatively higher probability to be further oxidized than glycerol, and (2) how CO_2 / formate / C2 intermediates are produced at high overpotentials in Stage II and Stage III.

Exemplified by a Pd and a PdAg electrodes, at a constant potential (*e.g.* 0.8

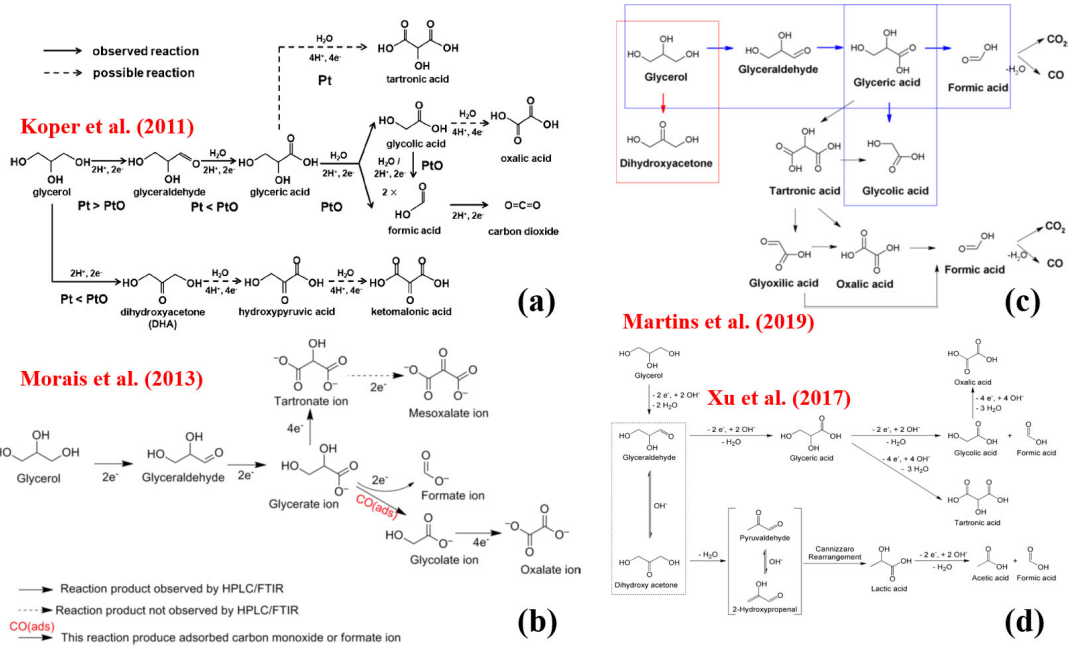

Figure 2.7: Previously reported reaction pathways of glycerol electrooxidation. (a) The glycerol oxidation mechanism on a Pt electrode in acidic media. (Reprinted with permission from Ref [28], Copyright © 2011 WILEY-VCH Verlag GmbH & Co. KGaA, Weinheim) (b) Proposed reaction scheme for glycerol electrooxidation on PdNi/C and PdAg/C nanocatalysts in alkaline medium. (Reprinted with permission from Ref [55], Copyright © 2013 American Chemical Society) (c) Schematic suggested pathways for glycerol electrooxidation on Pt surfaces in acid medium (Reprinted with permission from Ref [17], © Springer Science+Business Media, LLC, part of Springer Nature 2018) (d) Proposed reaction pathways for glycerol oxidation in alkaline solution on AuPt catalysts. (Reprinted with permission from Ref [38], © 2017 Elsevier Inc. All rights reserved.)

V vs RHE [55]) where there is no CO_2 production observed, the peak intensities of carboxylates increase versus time, but the ratio of the intensities remains the same (see Figure 2.8a-2.8b). Also, many HPLC results with various Pt-based electrodes shown in Figure 2.8c-d [38, 122] reveal that no side product shows a higher preference to be oxidized than glycerol or other side products. As shown in Figure 2.8d (PtFe composites oxidizing glycerol towards tartronic acid under alkaline conditions [38]), the rapid conversion from glycerate into tartronate and other side products occurs only after the complete depletion of glycerol. This strongly supports the fact that C3 intermediates can be oxidized into other highly oxidized products, but only in the absence of glycerol. Also, Koper et al. [31] compared the current densities of oxidizing glycerol, glyceraldehyde and DHA using Pt(111) and Pt(100) under acidic conditions. The results (Figure 2.8e) reveal that the current densities of glyceraldehyde and DHA oxidation are approximately one order of magnitude smaller than the current density of GEOR, which indicates that glycerol has higher reactivity than glyceraldehyde and DHA. (Very few researchers have ever reported C-C bond cleavage of tartronic acid and mesoxalic acid. Also, no studies have compared the current densities of C2 intermediates with that of glycerol.) Considering the massive production of CO_2 monitored by *in-situ* FTIR, it is unlikely that the majority of CO_2 originates from intermediates, as they are outnumbered by glycerol.

Generally, the rapid generation of CO_2 at higher overpotentials is regarded as a sign that the cleavage of C-C bonds is accelerated at such potentials. However, inspecting the spectra (Figure 2.9a-2.9b) obtained by Camara et al. [118] at PdRh electrodes, the peak at 1574 cm^{-1} (carboxylate) kept rising (although slowly) as the potential increased from 0.63 V to 1.3 V when 1 M KOH was used to better maintain the pH of the electrolyte at the interface. This observation shows that the levelling off of peak intensities of carboxylates at potentials above which the signal of CO_2 is detected is due to the complete consumption of hydroxide in the interface region, rather than the higher overpotentials favoring (a higher selectivity) C-C bond cleavage

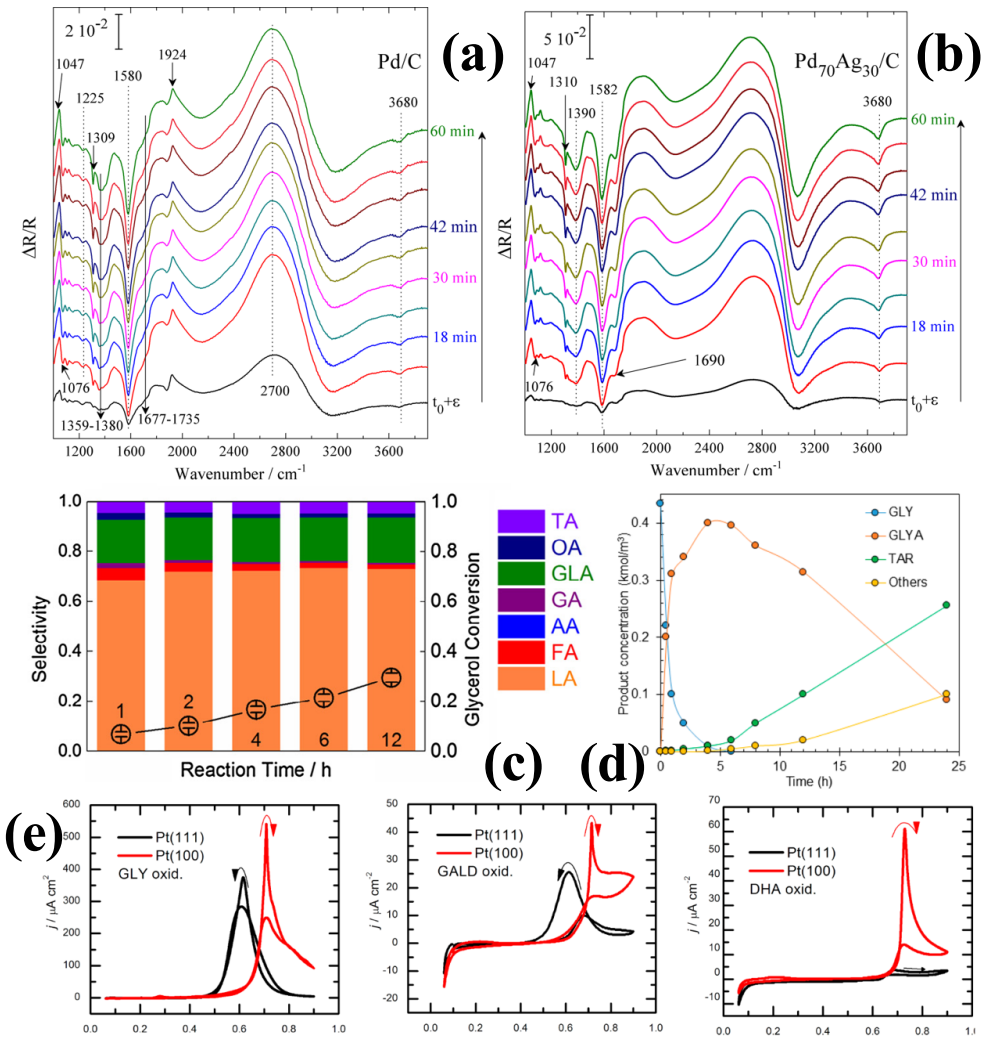

Figure 2.8: *In-situ* FTIR spectra, HPLC results and cyclic voltammograms showing the results of glycerol electrooxidation with various electrocatalysts. (a-b) FTIR spectra recorded during chronoamperometry in 0.1 M NaOH + 0.1 M glycerol on Pd/C and $Pd_{70}Ag_{30}/C$ catalysts at 0.8 V vs RHE. (Reprinted with permission from Ref [55], Copyright © 2013 American Chemical Society) (c) AuPt (15% Pt_{surf}) with applied potential of 0.45 V vs RHE in 0.5 M glycerol & 1 M KOH solution in 12 h. (Reprinted with permission from Ref [38], © 2017 Elsevier Inc. All rights reserved.) (d) concentration-time profiles on the annealed $PtFe_{4.5}$ catalyst (GLY: glycerol, GLYA: glyceric acid, TAR: tartronic acid, Others: lactic acid, formic acid, etc) in 0.43 M glycerol + 1.2 M KOH solution (Reprinted with permission from Ref [122], Copyright © 2017 American Chemical Society) (e) Cyclic voltammograms for 0.1 M of glycerol, glyceraldehyde, and DHA oxidation on Pt(111) (black line) and Pt(100) (red line) electrodes in $HClO_4$, respectively. (Reprinted with permission from Ref [31], Copyright © 2016 American Chemical Society)

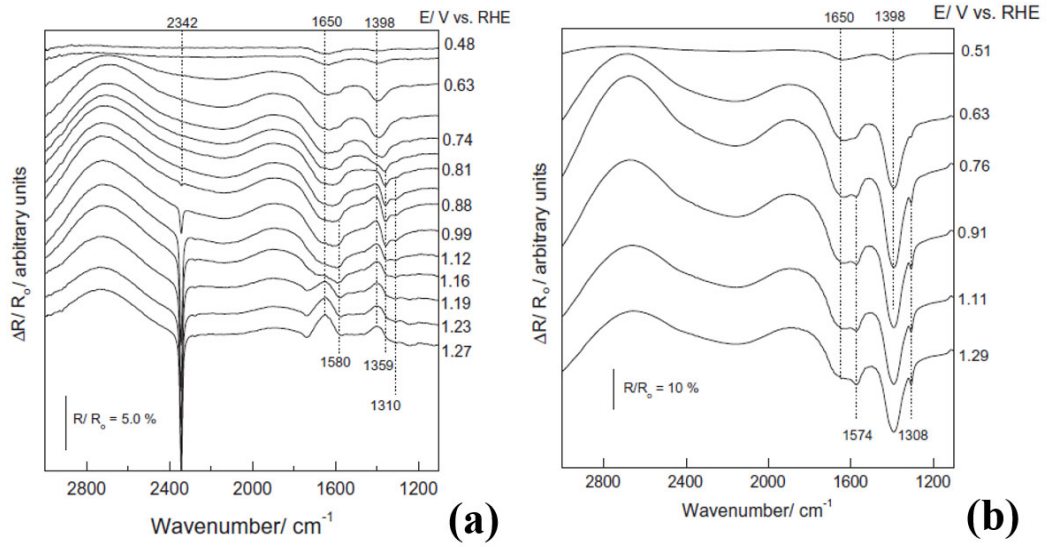

Figure 2.9: *In-situ* FTIR spectra in (a) 0.1 M and (b) 1.0 M KOH + 0.1 M glycerol on PdRh. (Reprinted with permission from Ref [118], © 2013 Elsevier B.V. All rights reserved.)

of glycerol and C3 intermediates. However, since the complete oxidation of glycerol into carbonate consumes 20 hydroxide ions per molecule of glycerol, the alkalinity of the electrolyte cannot be easily maintained if the applied potential facilitates a fast oxidation. It is also observed that the peak of CO(ads) vanishes at different potentials (or not at all throughout the whole potential range) in various studies [48, 49]. A widely accepted explanation is that the band intensity of CO(ads) depends on the rate of its generation and consumption [49], thereby a fast consumption of CO(ads) would lead to an earlier disappearance of the CO(ads) peak. In acidic conditions, only Pt(100) exhibits more C-C bond cleavage in Stage II and conversion into CO_2 (see Figure 2.4b) [52].

Based on the explanation given in the above paragraphs, Proposition B is unlikely to be true. Combining both propositions that are discussed in this section, a full picture of GEOR with Pt and Pd catalysts can now be presented. It is most

likely that C3/C2/C1 "intermediates" (or side products) of GEOR are generated from both resources, that is, directly generated from glycerol (mainstream) and indirectly generated from intermediates that are lightly oxidized (minor). The overpotentials and the alkalinity of the electrolytes are the most important factors controlling the portion of each. Therefore, a new reaction mechanism that differs from previously presented reaction pathways (exemplified by reaction pathways shown in Figure 2.7a-d) is proposed in Section 2.4.

2.4 Parallel Pathways Proposed as the Major Reaction Mechanism of Glycerol Electrooxidation

Recent GEOR studies have generated many proposed reaction mechanisms and pathways, contributed by, among others, the groups of Koper, Garcia, Coutanceau and Martin. Nevertheless, a well-established and widely accepted mechanism of GEOR has not yet been presented. Based on the experimental results from many GEOR studies, a comprehensive reaction mechanism interpreting the behavior of Pt, Pd and Au is proposed below, which awaits reliable experimental results for full validation. It explains how a high selectivity towards C-C bond cleavage, glycerate, or DHA is achieved, and also explains many common observations and hypotheses.

2.4.1 Dual Pathways of Deprotonation Processes on Pt, Pd, and Au

Different from the model shown in Figure 2.10a presented by Camara et al. [48], DFT studies [31,90,120,123–125] have shown that glycerol molecules can contact the (111) facet of Pt, Pd, and Au through carbon atom and / or oxygen atom (as shown in

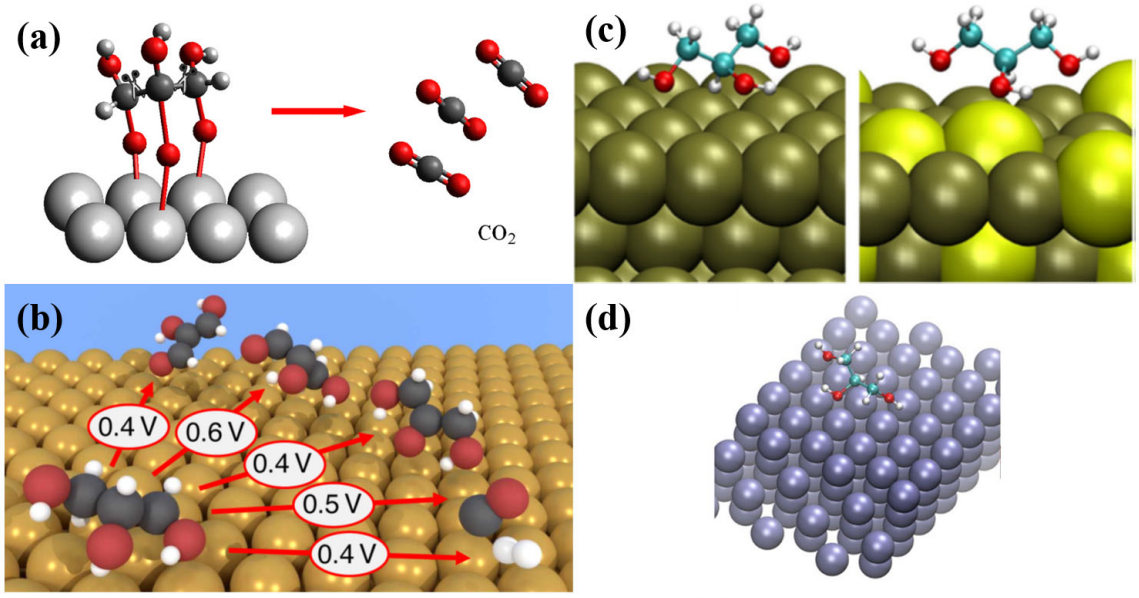

Figure 2.10: Schematic illustration and DFT studies of GEOR on various metallic electrocatalysts. (a) Schematic illustration of GEOR on Pt nanoparticles towards the production of CO_2 (reprinted with permission from Ref [48], Copyright © 2012 Elsevier Ltd. All rights reserved.). (b) Schematic illustration of DFT results of GEOR on gold in alkaline medium (reprinted with permission from Ref [90], Copyright © 2018 American Chemical Society). (c) Glycerol adsorbed on Pd(111) (left) and $Pd_{0.77}Pb_{0.23}$(111) (right) using DFT calculations (reprinted with permission from Ref [123], © Springer Science+Business Media, LLC, part of Springer Nature 2018). (d) Schematic illustration of DFT results of glycerol binding on Pt in acidic medium (reprinted with permission from Ref [120], © 2017 Wiley-VCH Verlag GmbH & Co. KGaA, Weinheim).

Figure 2.10b-d). Based on the DFT studies and the reports that GEOR generates mostly glyceraldehyde, DHA and glycerate, the O-adsorption pathway is more likely to occur than C-adsorption. However, the C-adsorption pathway is more involved in C-C bond cleavage, as M-CO(ads) is commonly seen in GEOR, and has been widely accepted as the main poisoning species generated from C-adsorption pathway for the electrooxidation of methanol, and formic acid.

It has been clearly and extensively proven that Pt(111), Pt(100) and Pt(110) are

able to catalytically oxidize glycerol in acidic solutions at potentials which cannot generate OH(ads) (*e.g.* below 0.5 V vs RHE) [48, 49, 52]. This complete oxidation of glycerol triggers the widely recognized poisoning effect caused by adsorbed species. This observation indicates that base catalysis is not the only way through which O-H cleavage and dehydrogenation can occur. Instead, it is more likely to be one of several possible ways. In acidic conditions, on the Pt(111) facet, both primary and secondary alcohols may oxidize through Eqs. (2.11)-(2.14) or Eqs. (2.15)-(2.16) (the adsorbed secondary carbon atom is highlighted in bold). The partial deprotonation at a primary carbon produces glyceraldehyde and deprotonation at the secondary carbon leads to DHA [31]. In addition, complete deprotonation at a primary carbon generates $CH_2OHCHOHCO$(ads) [126], which is an intermediate leading to C-C bond cleavage. This cleavage is shown by the production of CO(ads) in acidic conditions and the subsequent evolution of CO_2. This pathway from glycerol to glyceraldehyde, DHA and CO(ads) is called here the **acidic pathway**:

Acidic pathway:

$$\mathrm{M} + \mathrm{CH_2OHCHOHCH_2OH} \rightarrow \mathrm{M} - \mathrm{CH_2OHCHOH}\mathbf{C}\mathrm{HOH(ads)} + \mathrm{H^+ + e^-} \quad (2.11)$$

$$\mathrm{M} - \mathrm{CH_2OHCHOH}\mathbf{C}\mathrm{HOH(ads)} + \mathrm{M} \rightarrow \mathrm{M_2} - \mathrm{CH_2OHCHOH}\mathbf{CHO}\mathrm{(ads)} + \mathrm{H^+ + e^-} \quad (2.12)$$

$$\mathrm{M_2} - \mathrm{CH_2OHCHOH}\mathbf{CHO}\mathrm{(ads)} + \mathrm{M} \rightarrow \mathrm{M_3} - \mathrm{CH_2OHCHOH}\mathbf{CO}\mathrm{(ads)} + \mathrm{H^+ + e^-} \quad (2.13)$$

$$\mathrm{M_3} - \mathrm{CH_2OHCHOH}\mathbf{CO}\mathrm{(ads)} \rightarrow \mathrm{M} - \mathrm{CH_2OHCHOH}\mathbf{C}\mathrm{O(ads)} + 2\mathrm{M} \quad (2.14)$$

$$\mathrm{M} + \mathrm{CH_2OHCH(OH)CH_2OH} \rightarrow \mathrm{M} - \mathrm{CH_2OH}\mathbf{C}\mathrm{OHCH_2OH(ads)} + \mathrm{H^+ + e^-} \quad (2.15)$$

$$\mathrm{M} - \mathrm{CH_2OH}\mathbf{C}\mathrm{OHCH_2OH(ads)} + \mathrm{M} \rightarrow \mathrm{M_2} - \mathrm{CH_2OH}\mathbf{CO}\mathrm{CH_2OH(ads)} + \mathrm{H^+ + e^-} \quad (2.16)$$

Reaction mechanisms differ a lot when OH^- is present under alkaline condition

or at high overpotentials in an acidic solution. Pt-OH(ads), which is produced via Eq. (2.17) and Eq. (2.18) in basic and acidic solution, respectively, promotes the deprotonation of glycerol. From Eq. (2.19) to Eq. (2.22), $CH_2OHCHOHCO$(ads) can also form on the Pt surface. However, instead of removing this adsorbate through C-C bond cleavage, a reaction between $CH_2OHCHOHCO$(ads) and OH(ads) can occur rapidly to convert this intermediate into glyceric acid / glycerate (Eq. (2.23)), followed by its desorption. Behm et al. [51] has shown that in the potential range of 0.6-0.7 V, over 95% of the current goes to incomplete oxidation of glycerol. Presumably, this **OH-present pathway** tends to oxidize glycerol all the way to glyceric acid while also producing glyceraldehyde and DHA (Eqs. (2.24)-(2.25)).

OH-present pathway:

$$M + OH^- \rightarrow M - OH(ads) + e^- \tag{2.17}$$

$$M + H_2O \rightarrow M - OH(ads) + H^+ + e^- \tag{2.18}$$

$$M - OH(ads) + CH_2OHCHOHCH_2OH \rightarrow M - CH_2OHCHOH\mathbf{C}HOH(ads) + H_2O \tag{2.19}$$

$$M - CH_2OHCHOH\mathbf{C}HOH(ads) + M - OH(ads) \rightarrow M_2 - CH_2OHCHOH\mathbf{C}HO(ads) + H_2O \tag{2.20}$$

$$M_2 - CH_2OHCHOH\mathbf{C}HO(ads) + M - OH(ads) \rightarrow M_3 - CH_2OHCHOH\mathbf{C}O(ads) + H_2O \tag{2.21}$$

$$M_3 - CH_2OHCHOH\mathbf{C}O(ads) \rightarrow M - CH_2OHCHOH\mathbf{C}O(ads) + 2M \tag{2.22}$$

$$M - CH_2OHCHOH\mathbf{C}O(ads) + M - OH(ads) \rightarrow M - CH_2OHCHOH\mathbf{C}OOH(ads) + M \tag{2.23}$$

$$M - OH(ads) + CH_2OHCH(OH)CH_2OH \rightarrow M - CH_2OH\mathbf{C}OHCH_2OH(ads) + H_2O \tag{2.24}$$

$$M - CH_2OH\mathbf{C}OHCH_2OH(ads) + M - OH(ads) \rightarrow M_2{-}CH_2OH\mathbf{C}OCH_2OH(ads) + H_2O \quad (2.25)$$

However, the generation of glyceraldehyde can be suppressed as glyceraldehyde deprotonates again by reacting with OH(ads) to give $CH_2OHCHOHCO$(ads) via an Eley-Rideal mechanism [48]. Given the observation that the removal of CO(ads) with OH(ads) is the rate-determining step, the deprotonation steps are faster, which leads to a higher rate of $CH_2OHCHOHCOOH$(ads) and $CH_2OHCOCH_2OH$(ads) generation. Also, this interpretation successfully matches the mainstream observations that C-C cleavage is favored in acidic solution and at low overpotentials in Stage I, because the pathway towards $CH_2OHCHOHCOOH$(ads) competing with the pathway of C-C bond cleavage does not exist under such conditions.

According to many GEOR studies, Pd has a much higher d-band center and lower catalytic activity compared to Pt [30]. Also, it is observed that the catalytic activity of Pd is much inferior to Pt without base-catalyzed deprotonations [126]. In addition, from cyclic voltammetry under alkaline condition, the onset potential of observable GEOR is very close to the formation of OH(ads) (*e.g.* within 100 mV) (see Table 2.1). These correlated results translate into a hypothesis that the acidic pathway does exist in the case of Pd but is very limited [61]. Instead, the OH-present pathway is definitely the main pathway for GEOR occurring on Pd, supported by the fact that very few GEOR studies with Pd were conducted under acidic condition. This proposition perfectly explains the positive role OH^- plays in Pd catalysts in cleaving C-C bonds, because the formation of Pd-$CH_2OHCHOHCO$(ads) can only be promoted by OH^- through the OH-present pathway, in contrast to its negative impacts in the case of Pt.

With the addition of adatoms like Bi and Sb, two observations are usually obtained with Pd and Pt catalysts, that is, higher selectivity towards DHA and reduced ability to dissociate C-C bonds (detailed in Section 2.5). Researchers have presented the theory that oxidation through a primary carbon relies on the presence of three

adjacent Pt(111)/Pd(111) sites, and the introduction of Bi can disturb this vicinity and thus disable this pathway. This explanation is consistent with the mechanism proposed here, as the reduced number of vicinal Pt/Pd atoms affects both acidic and OH-present pathways towards $CH_2OHCHOHCO$(ads), and therefore the intermediates (glyceraldehyde, glyceric acid, C1/C2 products) produced via these processes are suppressed.

Distinct from Pt and Pd, Au shows no catalytic activity through the acidic pathway as the vast majority of researchers reported. This is supported by the fact that the onset potential of GEOR matches the onset potential of Au-OH(ads) formation under alkaline conditions [75, 81, 127]. Compared with bare Au, Au-OH(ads) has a much higher ability to break C-H bonds and O-H bonds, and therefore a high activity of GEOR (large current density) is commonly reported [77]. $CH_2OHCHOHCO$(ads) on the surface of Au(111) can be converted very easily into C1/C2 products [81], which is possibly due to the lowest d-band center among the three noble metals (-3.56 eV) [30] destabilizing RCO(ads). Besides, it has been widely reported that CO(ads) can further lower the d-band center of Au (*e.g.* 3 eV for Au monomer [128]), as the 5d bands narrows and the number of states reduces near E_F(Fermi level), which implies a promoting effect of CO(ads) on the catalytic activity of Au. A lower d-band center would increase the filling of the anti-bonding orbital of the adsorbed molecule and therefore facilitates the dissociation. The inexistence of the acidic pathway may be a result of a surface covered by sulfate / perchlorate in acidic solution, disabling the oxidation of glycerol [90].

2.4.2 Cleavage of C-C Bonds and Selectivity towards C1/C2 Products

The mechanism of dissociation of C-C bonds of $CH_2OHCHOHCO$(ads) on the surface of metals still remains unclear as there are few mechanistic studies. However, it is

clear that the further reaction of M-$CH_2OHCHOHCO$(ads) has two directions, either through a cleaved C-C bond, or through the reaction with M-OH(ads) to give glyceric acid / glycerate (as illustrated above in Eq. (2.23) and below in Eq. (2.26)). Considering that glycerol can be adsorbed onto Pt(100) with only one terminal carbon atom adsorbed and still generate CO(ads) [31], two Pt-C chemisorption bonds are presumably not a prerequisite for C-C bond cleavage. According to the previously reported reaction mechanism of ethanol and propanol electrooxidation with respect to bond cleavage ($CH_3CO(ads) \rightarrow\ CH_3(ads) + CO(ads), CH_3CH_2CO(ads) \rightarrow CH_3CH_2(ads) + CO(ads)$) [22], poly-ols with adjacent hydroxyl groups should have a much better reactivity as the newly adsorbed species bear hydroxyl groups for further deprotonation and bond cleavage. Please note that after deprotonation steps (Eq.(2.27)), the C-C bond dissociation proposed here (Eq. (2.28)) does not involve OH(ads) and electron transfer. As a result of this cleavage, a poisoning species (M-CO(ads) or M_2-CO(ads)) is formed, together with the generation of a new and shorter adsorbate with one fewer carbon (*i.e.* CH_2OHCO(ads)), waiting for conversion into glycolic acid (Eq. (2.29)). Under this circumstance, after deprotonation (Eq. (2.30)), C-C bond cleavage may occur the second time (see Eq. (2.31)), generating more M-CO(ads) and C1 intermediates. It is clearly shown in many studies on methanol electrooxidation at Pt that C1 intermediates can either be reacted into formic acid (Eqs. (2.32)) or deprotonated and left on the surface as the poisoning species CO(ads) (Eq. (2.33)).

GEOR to various products:

$$M - CH_2OHCHOH\mathbf{C}O(ads) + M - OH(ads) \rightarrow M - CH_2OHCHOH\mathbf{C}OOH(ads) + M \quad (2.26)$$

$$M - CH_2OHCHOH\mathbf{C}O(ads) + 2M \rightarrow M_3{-}CH_2OH\mathbf{COC}O(ads) + 2H^+ + 2e^- \quad (2.27)$$

$$\text{Or } M - CH_2OHCHOH\mathbf{C}O(ads) + 2M - OH(ads) \rightarrow M_3{-}CH_2OH\mathbf{COC}O(ads) + 2H_2O$$

$$M_3{-}CH_2OH\mathbf{COC}O(ads) \rightarrow M - CH_2OH\mathbf{C}O(ads) + M - CO(ads) + M \quad (2.28)$$

$$\text{Or } M_3{-}CH_2OH\mathbf{CO}\mathbf{C}O(ads) \rightarrow M - CH_2OH\mathbf{C}O(ads) + M_2{-}CO(ads)(CO_B)$$

$$M - CH_2OH\mathbf{C}O(ads) + M - OH(ads) \rightarrow M - CH_2OH\mathbf{C}OOH(ads) \text{ (glycolic acid)}{+}M \quad (2.29)$$

$$M - CH_2OH\mathbf{C}O(ads) + 2M \rightarrow M_3{-}\mathbf{C}H\mathbf{O}\mathbf{C}O(ads) + 2H^+{+}2e^- \quad (2.30)$$

$$\text{Or } M - CH_2OH\mathbf{C}O(ads) + 2M - OH(ads) \rightarrow M_3{-}\mathbf{C}H\mathbf{O}\mathbf{C}O(ads) + 2H_2O$$

$$M_3{-}\mathbf{C}H\mathbf{O}\mathbf{C}O(ads) \rightarrow M - H\mathbf{C}O(ads) + M - \mathbf{C}O(ads) + M \quad (2.31)$$

$$\text{Or } M_3{-}\mathbf{C}H\mathbf{O}\mathbf{C}O(ads) \rightarrow M - H\mathbf{C}O(ads) + M_2{-}\mathbf{C}O(ads)(CO_B)$$

$$M - H\mathbf{C}O(ads) + M - OH(ads) \rightarrow M - H\mathbf{C}OOH(ads) \text{ (formic acid)}{+}M \quad (2.32)$$

$$M - H\mathbf{C}O(ads) \rightarrow M - \mathbf{C}O(ads) + H^+{+}e^- \quad (2.33)$$

$$\text{Or } M - H\mathbf{C}O(ads) + M \rightarrow M_2{-}\mathbf{C}O(ads)(CO_B) + H^+{+}e^-$$

In summary, it is hypothesized that the $R^{(n)}CO(ads)$ intermediates, can react in two ways: either reacting with OH(ads) to **monocarboxylic acid / monocarboxylate**, or degrading to $\mathbf{R^{(n-1)}CO}(ads)$ until they are fully oxidized to C1 products and intermediates (*i.e.* CO_2 / carbonate or formic acid / formate), as shown in Figure 2.11. This proposition is based on the fact that glycerol can be fully oxidized to CO_2 on Pt, Pd and Au, together with the observation that glyceric acid and glycolic acid are the most commonly seen products beside DHA [10–12, 42, 129]. This proposed mechanism also matches the fact that oxalic acid, tartronic acid, and mesoxalic acid are not easily obtained unless a lower ratio of glycerol concentration to the concentration of OH^- is used [2, 38, 39, 102, 130], which is likely to involve the electrooxidation of DHA, glyceric acid and glycolic acid. Furthermore, this model also supports the fact that glyoxylic acid, glycoaldehyde and formaldehyde are rarely found in most of the studies.

Looking at FTIR results obtained with Pt and Pd (spectra in Figure 2.5 and

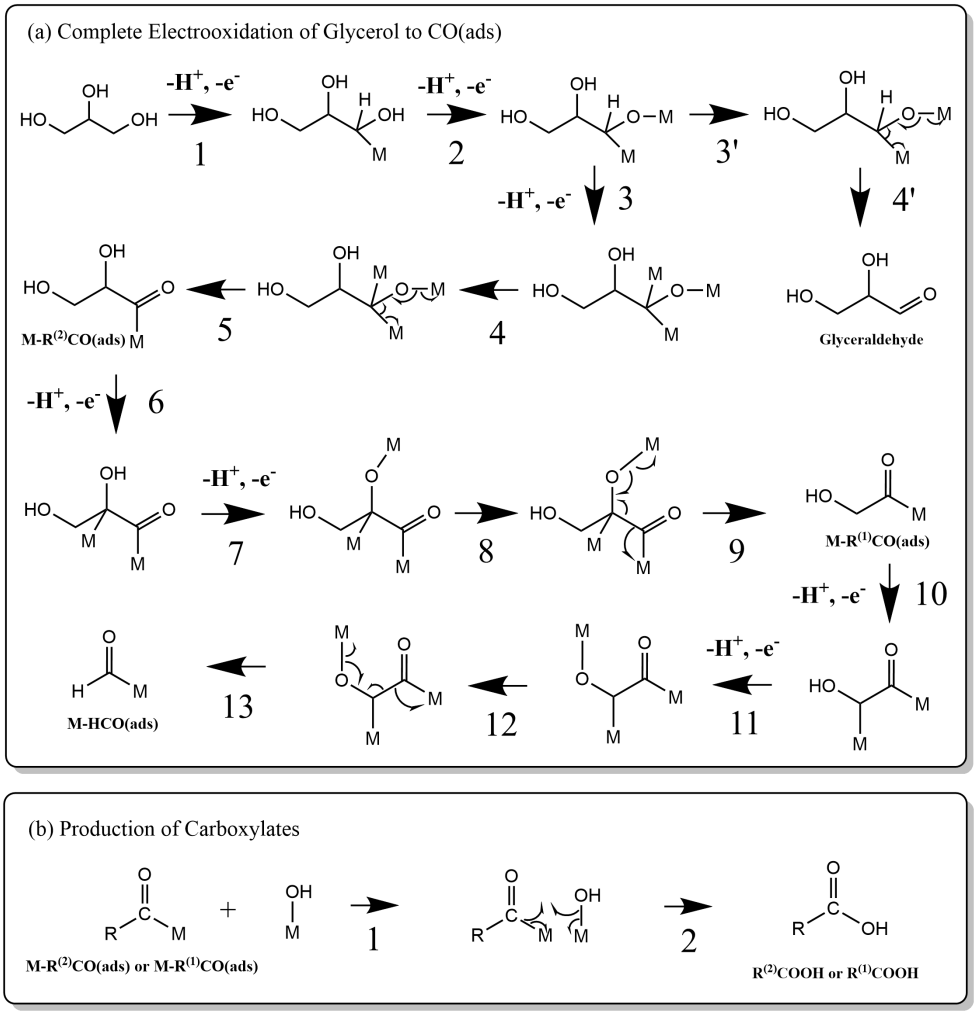

Figure 2.11: Schematic illustration of GEOR processes (deprotonation, C-C bond cleavage, and production of carboxylates) via (a) Acidic pathway (only for Pt and Pd electrodes), and (b) OH-present pathway.

2.6), CO(ads) and glyceraldehyde are generated in Stage I as a result of complete / partial deprotonation of a terminal carbon atom in the absence of OH(ads) (as in acidic solutions, or at very low overpotentials in alkaline solutions) [48, 49, 51]. A trend towards carboxylic acid / carboxylate (mainly glyceric acid) is initiated when OH(ads) is generated (in Stage II), which strongly directs the reaction pathway towards carboxylate and therefore reduces the proportion of products from cleaved C-C bond [65]. (This reduction is enhanced by the alkalinity of the electrolyte.) As the overpotential progresses up, a rapid consumption of hydroxide (up to 20 times of the amount of glycerol molecules consumed) tends to re-direct the reaction pathway back to the acidic case [118]. Therefore, more C1/C2 products and CO_2 are generated in Stage III, which is synergized by the high overpotential applied to overcome the energy barrier of C-C cleavage (not yet confirmed because of the uncertain local pH). To sum up, a table (Table 2.2) lists the conditions for preferentially producing certain products from GEOR, and a diagram summarizing the reaction mechanism proposed in this paper is shown in Figure 2.12.

Table 2.2: Conditions for glycerol valorization with Pt, Pd and Au

No. of Carbon atoms	**Product**	**Produced directly / indirectly from glycerol?**	**Acidic / Alkaline**	**OH(ads) needed for direct production?**	**Remarks**
3	Glyceraldehyde	Directly	Acidic	No	low overpotentials and more (100) planes
3	Dihydroxyacetone	Directly	Acidic	No	(111) planes with Sb and Bi deposited
3	Glyceric Acid	Both (indirectly from glyceraldehyde)	Both	Yes	low overpotentials and strong alkaline electrolyte for massive production
3	Tartronic Acid	Indirectly from glyceric acid	Both	N/A	long term oxidation
3	Mesoxalic Acid	Indirectly from hydroxypyruvic acid	Unknown	N/A	
3	Hydroxypyruvic Acid	Both (indirectly from DHA, glyceric acid)	Both	Yes	(111) planes
3	Lactic Acid	Indirectly from glyceraldehyde	Acidic	N/A	deaerated
2	Glycolic Acid	Both (indirectly from glyceric acid)	Both	Yes	strong alkaline electrolyte for massive production
2	Oxalic Acid	Both (indirectly from glycolic acid)	Both	Yes	
2	Glyoxylic Acid	Unknown			
1	Formic Acid	Both (from glyceric acid, glycolic acid)	Both	Yes	strong alkaline electrolyte for massive production
1	CO_2 / Carbonate	Both (indirectly from glyceric acid, glycolic acid, formic acid)	Both	Yes	high overpotentials (>1.0 V vs RHE) for massive production

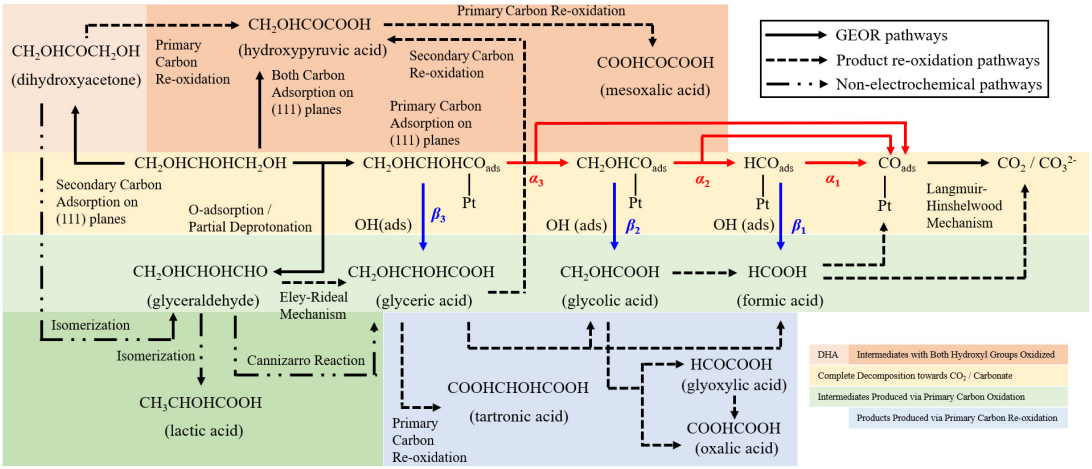

Figure 2.12: Proposed reaction mechanism of glycerol electrooxidation on Pt, Pd, and Au.

In this model, since the reaction of $R^{(n)}CO(ads)$ into the degraded $R^{(n-1)}CO(ads)$ is competing with other pathways towards carboxylates, α_n (C-C cleavage) and β_n (conversion into $R^{(n)}COOH$) are defined as the probabilities of these two processes, with the sum of α_n and β_n to be 1. The quantities α_n and β_n describe the preference of RCO(ads) towards each product, and therefore are a function of overpotential η, pH and the type of crystal plane ε, *i.e.*, α_n (η, pH, ε). The quantity β_n can be written as 1- α_n. Other factors possibly affecting α_n include but are not limited to temperature and pressure.

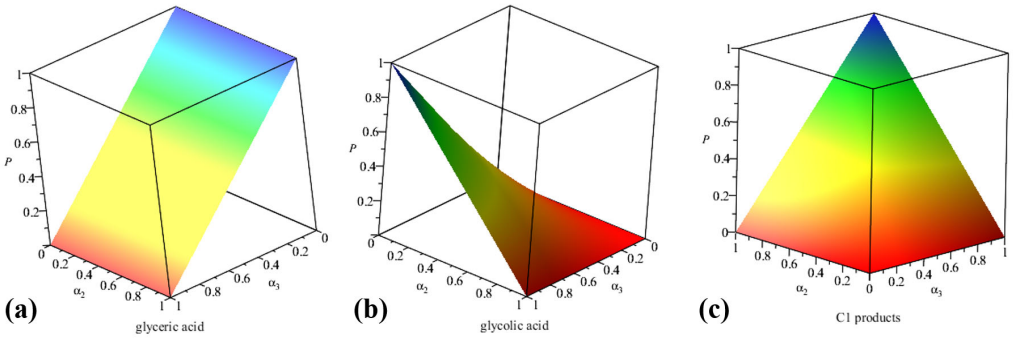

Figure 2.13: 3D plots showing the selectivity of GEOR towards (a) glyceric acid, (b) glycolic acid and (c) C1 products (formic acid + CO_2/carbonate) under different C-C bond cleavabilities (α_3 and α_2).

The probability of generating $R^{(m)}CO(ads)$ from $R^{(n)}CO(ads)$ can be expressed as $\prod_{m+1}^{n} \alpha_n$ (η, pH, ε) (m+1 $\leq$ n). Similarly, the probability of generating $R^{(m)}COOH$ with m carbon atoms from $R^{(n)}CO(ads)$ can be expressed as $\prod_{m+1}^{n} \alpha_n$ (η, pH, ε)-$\prod_{m}^{n} \alpha_n$ (η, pH, ε) (m+1 $\leq$ n). In the case of GEOR, two C-C cleavage processes and three carboxylate production processes are involved. Figure 2.13 illustrates the probability p of GEOR towards glyceric acid, glycolic acid, and C1 products (formic acid + CO_2) with different α_3 and α_2. From the 3D plot, it is clearly shown that a large α_3 and a small α_2 lead to a large portion of glycolic acid (glycolate) produced. If the aim is to produce as much formic acid as possible, both α_3 and α_2 need to be large, and α_1 needs to be small . An empirical estimation of α_3 and α_2 according to the existing HPLC results presented by various researchers suggests a large α_3 (around 0.6-0.8) and a small α_2 (around 0.2) [131–137]. However, this estimation is suspect, as the product distributions reported are based on different standards and calculations.

2.4.3 A Sample Analysis of the Proposed Reaction Mechanism

The model proposed in the above subsection involves α_3 and α_2 numbers different from each other, which needs to be verified by a real sample. Figure 2.14a displays a group of α_3 and α_2 numbers versus applied overpotentials calculated from Wang et al. (2015) [133]. In this work, Pd nanoparticles were reacted with different substrates and overpotentials ranged from 0 to 0.4 V vs SCE. The original selectivity results are shown in Figure 2.14b. As the reported selectivity towards tartronic acid and oxalic acid is very low (below 10%, mostly below 5%), these highly oxidized products are assumed to be generated from the oxidation of glycolic acid and glyceric acid, respectively. It is clearly shown that for all three Pd nanocatalysts tested within the potential range, there was a gap between α_3 and α_2, indicating that the first C-C bond was more easily cleaved than the second one. With increasing potential, the gap between α_3 and α_2 decreased, as the possibility of first C-C bond cleavage decreased while the possibility of second C-C bond cleavage increased. It is therefore important to notice that researchers should make separate statements on the cleavability of the two C-C bonds rather than simply stating that C-C bond cleavage is favored under certain conditions or by certain electrocatalysts.

2.5 Electrocatalysts for Enhanced Efficiency and Selectivity of GEOR

There has been significant recent research on bi-/tri-/multi-metallic nanocatalysts and composites aimed at improving the efficiency of glycerol conversion and the selectivity towards certain products. This section summarizes the achievements and also controversies with respect to the performances of metallic catalysts reported so far. As Martins et al. [122] have commented, the properties of electrocatalysts

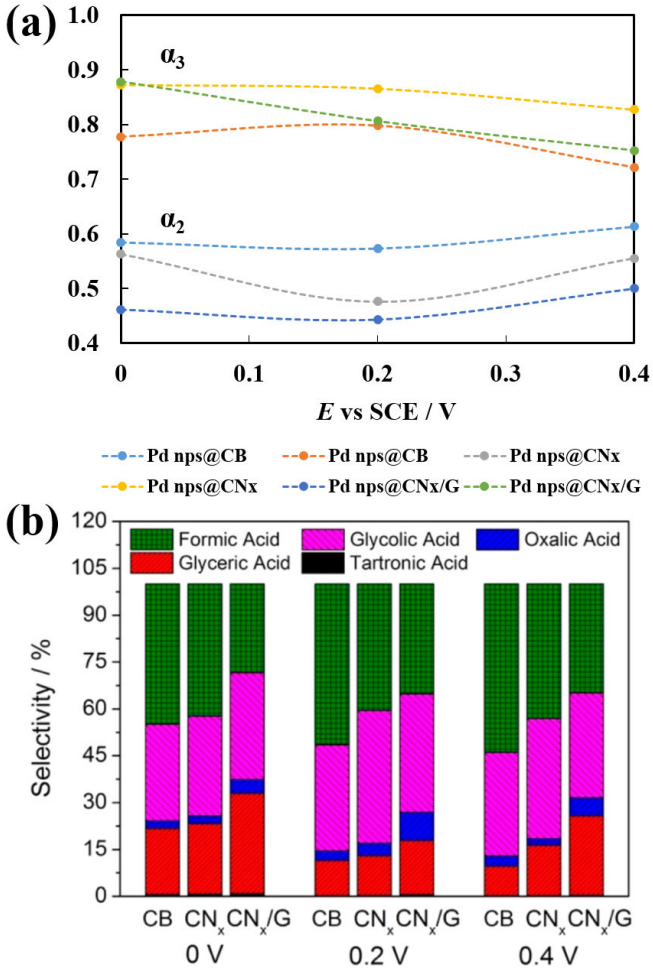

Figure 2.14: Calculated C-C bond cleavabilities for GEOR catalyzed by Pd nanoparticles and the original HPLC results. (a) Calculated C-C bond cleavabilities for GEOR catalyzed by Pd nanoparticles on different supports at different overpotentials versus SCE. (b) Original HPLC results of GEOR showing the product distributions. (Reprinted with permission from Ref [133], © 2015 American Chemical Society)

used for GEOR are subject to preparation processes which vary significantly between studies and between groups who conduct them. Also, conditions under which GEOR occurs lack uniformity, including even the choice of reference electrodes. It is barely possible to draw many conclusions under such circumstances, and future researchers are strongly urged to standardize their experimental conditions and give more mechanistic interpretations with tools like isotopic-labelling studies.

As illustrated in Figure 2.15, many nanocatalysts with novel structures have been synthesized [7, 74, 138–144]. Nanostructured catalysts (*e.g.* nano-dendrites [81, 145], nano-flowers) possess not only a higher specific surface area, but also the preferential growth on certain crystal planes. Also, they usually enjoy a large number of step and kink sites, as well as high-index planes that have a higher activity for catalysis. For example, Pd(520) has a higher catalytic activity compared with low-index planes. The reason is that it has a higher density of kinks (with dangling bonds) and steps which weaken the strength of C-C and C-H bonds [11, 74].

The catalytic performance of metallic electrocatalysts can be enhanced by alloying, introducing skin or shell overlayers, or introducing ad-atoms. In general, many studies have proven that adding other metals (*e.g.* oxophilic metals like Rh, Sn and Ni [146]) which have a lower onset potential of OH adsorption can efficiently prevent the CO poisoning effect on the modified metal surface [99]. Like metallic catalysts, metal oxides (*e.g.* NiO [147], CeO_2 [148]), especially those with oxygen defects [74], are also able to provide OH(ads) at a lower potential than the catalyst they modify.

Catalytic activities also depend on the electronic structures of the metallic substrates. With a downshifted d-band center, a metallic catalyst tends to adsorb more alcohol [33] (presumably the ability to cleave the C-H bond is improved) and form more M-OH(ads) which facilitates the oxidation of CO to CO_2. In this case, an overlap of the electronic orbitals of substrate metals (*e.g.* Pt (5d)) and transition metals (3d/4d) can occur [149], which leads to a lowered d-band center. Researchers have revealed that amphoteric metals (*e.g.* Al and Ga) have similar effects as their 3p

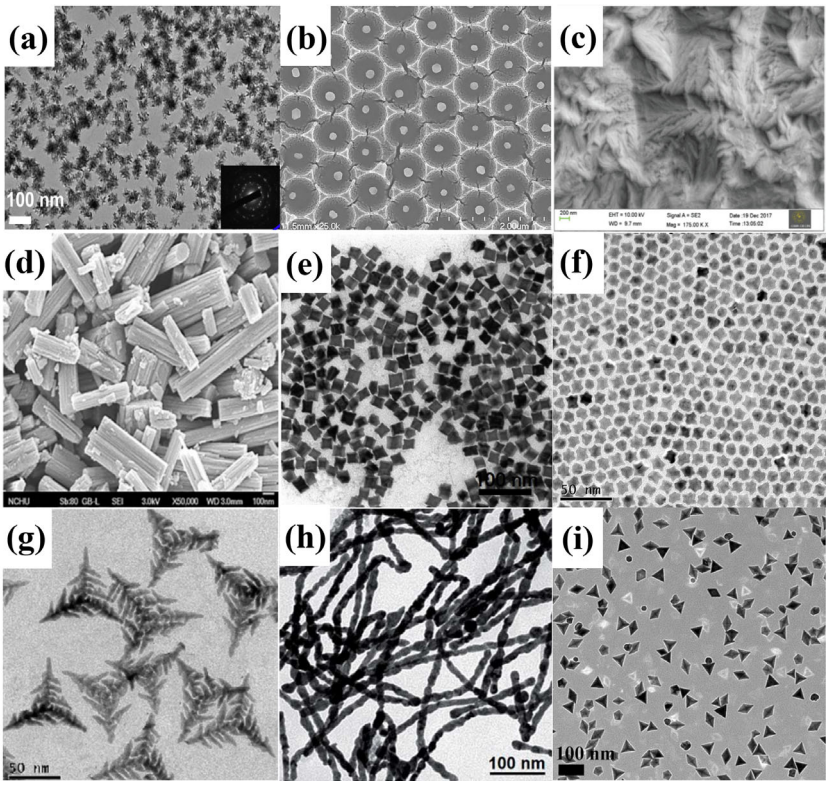

Figure 2.15: SEM pictures of various nanometallic electrocatalysts for GEOR. (a) Pd nanodendrites@rGO (Reprinted with permission from Ref [138], Copyright © 2013, Hydrogen Energy Publications, LLC. Published by Elsevier Ltd. All rights reserved.), (b) Au single nanoparticle@SiO_2 (Reprinted with permission from Ref [139], Copyright © 2014 Elsevier B.V. All rights reserved.), (c) Ni nanosponges (Reprinted with permission from Ref [7], © The Royal Society of Chemistry and the Centre National de la Recherche Scientifique 2019), (d) Pd@WO_x nanobundles (Reprinted with permission from Ref [74], Copyright © 2019 American Chemical Society), (e) PtSn nanocubes (Reprinted with permission from Ref [140], © 2018 Hydrogen Energy Publications LLC. Published by Elsevier Ltd. All rights reserved.), (f) PtCuCo hexagonal nanocrystals (Reprinted with permission from Ref [141], © 2018 Taiwan Institute of Chemical Engineers. Published by Elsevier B.V. All rights reserved.), (g) PtCu nano-tripods (Reprinted with permission from Ref [142], © The Royal Society of Chemistry 2018), (h) Pt nanowires (Reprinted with permission from Ref [143], © The Royal Society of Chemistry 2017), (i) Pd trigonal/pyramidal nanocrystals (Reprinted with permission from Ref [144], © 2017 Wiley-VCH Verlag GmbH &Co. KGaA, Weinheim).

orbitals can mix with the Pt(5d) orbitals [150]. This downshift can also be induced by ad-atoms with a different work function, because they can induce electron transfer from substrate metals (*e.g.* Pt) to them, lowering of density of states near Fermi level of the substrate metals to reach an equilibrium between two metals [2, 151], and this electron transfer can prevent the oxidation of substrate metals [34]. In addition, the lattice strain generated by ad-atoms can also downshift the d-band center of the metal they modify, and the effectiveness of lattice strain depends on the difference between their lattice parameters [152]. This downshift would cause the back-donation of electrons from Pt (5d) to CO(ads) (2p*), which reduces the bond strength of M-CO and promotes the CO removal [2, 126]. It is also reported that the position of the d-band center can be modulated by the morphology and shape of metallic nanoparticles [153]. The introduction of a second metal into the lattice may lead to the lattice distortion. In the case of PtFe nanocomposites [122], a sublayer of Pt atoms is generated, which transfers electrons to the surface of Pt. As a result, the d-band electron density of surface Pt increases and promotes the cleavage of C-H bonds.

The ratio of metal A to metal B needs to be carefully determined since the introduced metal atoms may rearrange the locations and distribution of surface atoms. On one hand, the coverage of certain active sites [14] / crystal planes with a non-active metal (*e.g.* Ru preferentially deposited on Pt(111) [154]) can decrease the efficiency of oxidation. On the other hand, it is noteworthy that the product selectivity strongly depends on the type of metal introduced, as preferential deposition can restructure the surface atoms. For example, a study on the "ensemble effect" with different ratios of Ag to Pd yields Pd with different structures and properties with respect to adsorption [24]. Some atoms favor the defective sites with higher energy, whereas others prefers to deposit on a certain facet [43]. It is well known that three vicinal sites (*i.e.* atoms) on (111) facets are required to oxidize primary alcohols in the case of Pt and Pd. The reason is that the oxidation through primary carbon atom involves the cleavage of two C-H bonds and one O-H bond. Each bond dissociation requires an

interaction with a surface atom [43]. Reducing the number of these ensembles lowers the efficiency of primary alcohol conversion, whereas secondary alcohol conversion is not affected as it only requires one Pt/Pd atom [33]. Benefitting from that, high selectivity towards DHA (partially converted to glyceraldehyde via isomerization [113] and further to glycerate if in strong alkali [110]) through the preferential oxidation of the secondary carbon can be achieved, as exemplified by Bi-modified [155], Ru-modified [129] and Sb-modified Pt [14,156]. Moreover, researchers have reported that Sb has a remarkably higher selectivity towards DHA (61.4%, obtained at 0.797 V vs RHE) than Bi (usually between 10-20%) and a higher potential of oxidation towards its oxide [42].

Ag is a special ad-metal that can oxidize glycerol on its own (producing formate, glycolate and glycerate at 1.125 V vs RHE [157]). It can upshift the d-band center of the substrate metals (Pt, Pd and Au) to promote the adsorption between substrate metals and glycerol [55,158]. As a noble metal with similar lattice parameters to Au, it is found to promote the C-C bond cleavability of Pd and Au [31,159,160]. With the help of Ag, GEOR occurs on Au through C-C bond cleavage to produce formate and glycolate in alkaline media [11]. Ag-OH(ads) produced in strong alkaline media (pH $>$ 11) has been shown to be the catalytic species, and not Ag [161] or Ag_2O (previously taken as a catalytic species [82], but regarded as an inhibitor at present).

The tailoring of GEOR with different ad-metals has been extensively studied. Rh shows little promotion on the catalytic efficiency [12] and C-C bond cleavage [162,163] when alloyed with Pt (still under debate [2,164]), whereas it facilitates the C-C bond cleavage on Pd [118]. Additionally, Rh shows reactivity through primary carbon oxidation and C-C bond dissociation on its own [165]. Ru can provide OH(ads) at lower potentials to promote GEOR [12], facilitate the dissociation of C-C bonds on Pd, and increase the selectivity towards glycerate (with Pd) or DHA (with Pt) in alkaline condition [129, 132], while it has no capability of oxidizing glycerol by itself [166]. Other reported observations include the production of DHA and glycolic acid with

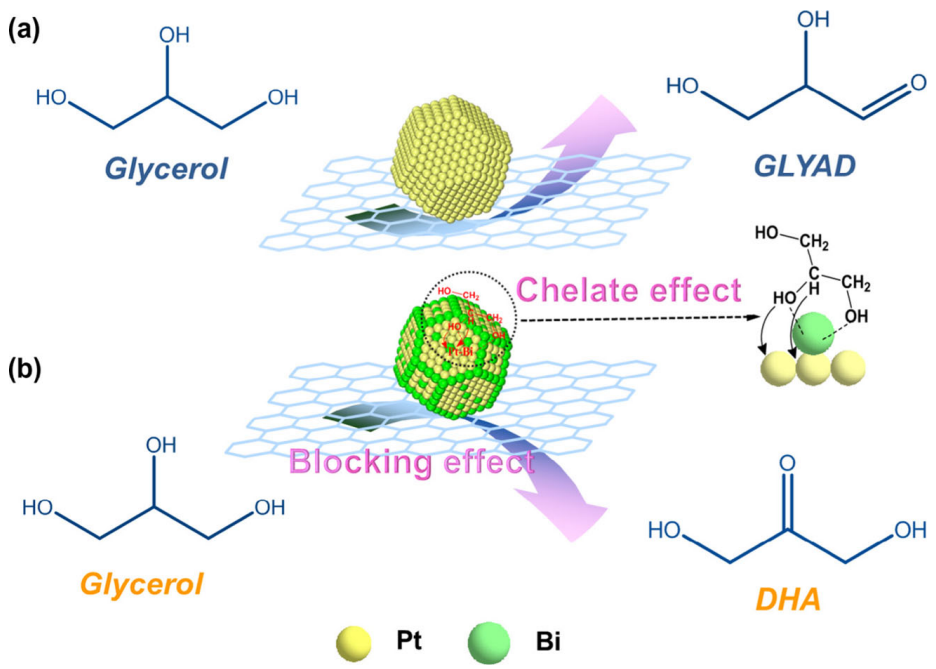

Figure 2.16: Scheme showing the blocking and chelate effects of Bi adatoms to Pt/NCNT electrocatalyst. (Reprinted with permission from Ref [14], © 2016 Elsevier Inc. All rights reserved.).

a Pt-Ru electrocatalyst, and the weakened binding energy of glycerol onto the PtRu surface in acidic solutions [120].

Other commonly investigated ad-metals include Sb, Bi, Pb, In and Sn. Sb and Bi tend to oxidize the secondary hydroxyl groups (via chelating and blocking effects as shown in Figure 2.16, as Bi chelates with secondary alcohol groups), while Pb and In promote the primary alcohol oxidation [156]. Sb is believed to facilitate C-C bond breakage at Pt under alkaline condition [113], while others discovered an inhibiting effect in an acidic solution [148]. Whether Sn can promote the dissociation of C-C bonds with Pt catalysts is still under debate [167, 168].

The conversion to CO_2 from glycerol with Ni electrodes can be increased by involving elements from the same group (*e.g.* Co and Fe). The enhancement can be attributed to CoOOH converted from $Co(OH)_2$, which occurs at a lower overpotential

compared with the conversion of $Ni(OH)_2$ to NiOOH [110].

To make multi-metallic catalysts, electrodeposition is a method commonly adopted. The epitaxial relationship of the deposit to the substrate is strongly influenced by the potential used for electrodeposition. It is also believed that the attachment of metallic catalysts onto carbon supports can change the electronic structure of metals, and consequently change the bonding strength with adsorbates. This modified electronic structure improves the adsorption of glycerol onto metals [169]. In addition, the interaction between metallic catalysts (*e.g.* nanoparticles) and carbon supports can leave defects on the metal surfaces, which are highly active sites for catalysis [170]. The defects on a carbon support are deemed as high-energy sites which could facilitate nucleation of metallic nanostructures and their further growth [2]. Taking single-wall carbon nanotube (SWNT) as an example, the preferential decoration of defect sites rather than sp^2-bonded lattice sites can be achieved by modulating the electrodeposition potentials [171].

2.6 Summary and Outlook

Glycerol electrooxidation has been shown to be a very promising way of generating value-added products. High selectivity towards certain products has been reported, including but not limited to DHA, glyceric acid and glycolic acid. However, the investigation of mechanism of glycerol valorization is still an open area of research. One of the key reasons is that the complete oxidation of glycerol into CO_2 consumes 20 OH^- ions per molecule, causing a significant change in the pH at the electrode, which may re-direct the reaction to other products and eventually affect the interpretation of reaction mechanisms [172]. Moreover, uncertainty is introduced by the diversity of catalysts used for GEOR. Unlike most studies arguing that C1/C2 products are generated from the oxidation of C2/C3 products, this review provides a perspective in which all side products are generated directly from glycerol via $CH_2OHCHOHCO$(ads),

CH_2OHCO(ads), and HCO(ads), supported by the observations that no side products have shown a higher electrochemical reactivity than glycerol. Based on the GEOR model proposed in this review, statements regarding C-C bond cleavability should be re-assessed because the cleavabilities of two C-C bonds are obviously different under the same conditions. Also, the proposition that Pd has a weaker ability to cleave C-C bonds than Pt has been clarified: this weaker ability is due to the lack of deprotonation efficiency without Pd-OH(ads). As Martins et al. [18] commented, more studies on multi-metallic catalysts should be carried out, with detailed reporting and standard conditions of catalyst preparations to better reveal the real reaction mechanisms. However, as many differences exist in the experimental conditions which cannot be easily unified, great efforts should be made by future researchers into fundamental studies of GEOR using advanced surface characterization methods and isotopic-labelling studies.

Examples of other interesting observations which are worthy to be further investigated include:

- Coutanceau et al. [173] reported that hydroxypyruvate and C2/C1 products were produced simultaneously with Pd-Sn nanoparticles, as hydroxypyruvate is a rarely found product.

- The conversion of glyceric acid to lactic acid as a byproduct of GEOR is a special case, as it is either not found in the mixture of products (mostly reported) or found to be a large amount [38].

- Ni has been found as an effective catalyst for GEOR which has the potential of replacing noble metals. The oxidation of alcohol to aldehyde and furthur to carboxylate has been widely recognized. Also, the cleavage of C-C bonds of glycerol with β-NiOOH to produce formate and carbonate are commonly observed. Throwing lights on this issue is a promising research hotspot.

References

[1] S. D. Minteer, *International Materials Reviews*, 2018, **63**(4), 241–256.

[2] Y. Zhou, Y. Shen, and J. Piao, *ChemElectroChem*, 2018, **5**(13), 1636–1643.

[3] L. Du, Y. Shao, J. Sun, G. Yin, C. Du, and Y. Wang, *Catalysis Science and Technology*, 2018, **8**(13), 3216–3232.

[4] P. Song, H. Xu, J. Wang, Y. Zhang, F. Gao, F. Ren, Y. Shiraishi, C. Wang, and Y. Du, *Journal of the Taiwan Institute of Chemical Engineers*, 2018, **93**, 616–624.

[5] T. Nitaya, Y. Cheng, S. Lu, K. Poochinda, K. Pruksathorn, and S. P. Jiang, *Chemical Communications*, 2018, **54**(87), 12404–12407.

[6] Y. Wang, T. Kou, H. Gao, J. Niu, J. Zhang, L. Lv, Z. Peng, and Z. Zhang, *Journal of Materials Chemistry A*, 2018, **6**(22), 10525–10534.

[7] P. Sivasakthi and M. V. Sangaranarayanan, *New Journal of Chemistry*, 2019, **43**(21), 8352–8362.

[8] G. Y. Hou, Y. Y. Xie, L. K. Wu, H. Z. Cao, Y. P. Tang, and G. Q. Zheng, *International Journal of Hydrogen Energy*, 2016, **41**(22), 9295–9302.

[9] V. L. Oliveira, C. Morais, K. Servat, T. W. Napporn, P. Olivi, K. B. Kokoh, and G. Tremiliosi-Filho, *Electrocatalysis*, 2015, **6**(5), 447–454.

[10] J. Han, Y. Kim, D. H. K. Jackson, K. E. Jeong, H. J. Chae, K. Y. Lee, and H. J. Kim, *Electrochemistry Communications*, 2018, **96**(July), 16–21.

[11] L. Thia, M. Xie, D. Kim, and X. Wang, *Catalysis Science and Technology*, 2017, **7**(4), 874–881.

[12] L. Huang, J. Y. Sun, S. H. Cao, M. Zhan, Z. R. Ni, H. J. Sun, Z. Chen, Z. Y. Zhou, E. G. Sorte, Y. Y. J. Tong, and S. G. Sun, *ACS Catalysis*, 2016, **6**(11), 7686–7695.

[13] E. Ferreira Frota, V. V. Silva de Barros, B. R. S. de Araújo, Â. Gonzaga Purgatto, and J. J. Linares, *International Journal of Hydrogen Energy*, 2017, **42**(36), 23095–23106.

[14] X. Ning, Y. Li, H. Yu, F. Peng, H. Wang, and Y. Yang, *Journal of Catalysis*, 2016, **335**, 95–104.

[15] B. Wang, L. Tao, Y. Cheng, F. Yang, Y. Jin, C. Zhou, H. Yu, and Y. Yang, *Catalysts*, 2019, **9**(4), 387.

[16] Y. Liu, W. Yu, D. Raciti, D. H. Gracias, and C. Wang, *Journal of Physical Chemistry C*, 2019, **123**(1), 426–432.

[17] A. A. Nascimento, L. M. Alencar, C. R. Zanata, E. Teixeira-Neto, A. P. Mangini, G. A. Camara, M. A. Trindade, and C. A. Martins, *Electrocatalysis*, 2019, **10**(1), 82–94.

[18] M. Trindade, *Increased Biodiesel Efficiency*, 2018.

[19] C. S. Lee, M. K. Aroua, W. A. Wan Daud, P. Cognet, Y. Pérès, and M. A. Ajeel, *Frontiers in Chemistry*, 2019, **7**(MAR), 1–11.

[20] C. Coutanceau and S. Baranton, *Wiley Interdisciplinary Reviews: Energy and Environment*, 2016, **5**(4), 388–400.

[21] M. Simões, S. Baranton, and C. Coutanceau, *ChemSusChem*, 2012, **5**(11), 2106–2124.

[22] J. F. Gomes, V. L. Oliveira, P. M. Pratta, and G. Tremiliosi-Filho, *Electrocatalysis*, 2014, **6**(1), 7–19.

[23] C. Coutanceau, S. Baranton, and R. S. Kouamé, *Frontiers in Chemistry*, 2019, **7**(FEB), 1–15.

[24] N. Cai, C. Jin, C. Wan, and R. Dong, *Journal of the Electrochemical Society*, 2017, **164**(7), H437—-H442.

[25] O. Enea and J. P. Ango, *Electrochimica Acta*, 1989, **34**(3-4), 391–397.

[26] A. Hilmi, E. M. Belgsir, J. M. Le ÌĄger, and C. Lamy, *Journal of Electroanalytical Chemistry*, 1995, **380**(1-2), 177–184.

[27] M. Simões, S. Baranton, and C. Coutanceau, *Applied Catalysis B: Environmental*, 2010, **93**(3-4), 354–362.

[28] Y. Kwon, K. J. P. Schouten, and M. T. Koper, *ChemCatChem*, 2011, **3**(7), 1176–1185.

[29] J. R. McManus, E. Martono, and J. M. Vohs, *Catalysis Today*, 2014, **237**, 157–165.

[30] I. Takigawa, K. I. Shimizu, K. Tsuda, and S. Takakusagi, *RSC Advances*, 2016, **6**(58), 52587–52595.

[31] A. C. Garcia, M. J. Kolb, C. Van Nierop Y Sanchez, J. Vos, Y. Y. Birdja, Y. Kwon, G. Tremiliosi-Filho, and M. T. Koper, *ACS Catalysis*, 2016, **6**(7), 4491–4500.

[32] Y. Kwon, S. C. Lai, P. Rodriguez, and M. T. Koper, *Journal of the American Chemical Society*, 2011, **133**(18), 6914–6917.

[33] R. M. Castagna, J. M. Sieben, A. E. Alvarez, and M. M. E. Duarte, *International Journal of Hydrogen Energy*, 2019, **44**(12), 5970–5982.

[34] Y. Zhou, Y. Shen, and J. Xi, *Applied Catalysis B: Environmental*, 2019, **245**(December 2018), 604–612.

[35] J. Schnaidt, M. Heinen, Z. Jusys, and R. J. Behm, *Electrochimica Acta*, 2013, **104**, 505–517.

[36] L. Roquet, E. M. Belgsir, J. M. Léger, and C. Lamy, *Electrochimica Acta*, 1994, **39**(16), 2387–2394.

[37] P. Saila and M. Hunsom, *Korean Journal of Chemical Engineering*, 2015, **32**(12), 2412–2417.

[38] C. Dai, L. Sun, H. Liao, B. Khezri, R. D. Webster, A. C. Fisher, and Z. J. Xu, *Journal of Catalysis*, 2017, **356**, 14–21.

[39] L. S. Ribeiro, E. G. Rodrigues, J. J. Delgado, X. Chen, M. F. R. Pereira, and J. J. M. Órfão, *Industrial and Engineering Chemistry Research*, 2016, **55**(31), 8548–8556.

[40] F. Frusteri, F. Arena, G. Bonura, C. Cannilla, L. Spadaro, and O. Di Blasi, *Applied Catalysis A: General*, 2009, **367**(1-2), 77–83.

[41] J. González-Cobos, S. Baranton, and C. Coutanceau, *Journal of Physical Chemistry C*, 2016, **120**(13), 7155–7164.

[42] S. Lee, H. J. Kim, E. J. Lim, Y. Kim, Y. Noh, G. W. Huber, and W. B. Kim, *Green Chemistry*, 2016, **18**(9), 2877–2887.

[43] A. Zalineeva, S. Baranton, and C. Coutanceau, *Electrochimica Acta*, 2015, **176**, 705–717.

[44] M. Hunsom and P. Saila, *International Journal of Electrochemical Science*, 2013, **8**(9), 11288–11300.

[45] A. Zalineeva, S. Baranton, and C. Coutanceau, *Electrochemistry Communications*, 2013, **34**, 335–338.

[46] M. Simões, S. Baranton, and C. Coutanceau, *Applied Catalysis B: Environmental*, 2011, **110**, 40–49.

[47] J. F. Gomes and G. Tremiliosi-Filho, *Electrocatalysis*, 2011, **2**(2), 96–105.

[48] P. S. Fernández, M. E. Martins, and G. A. Camara, *Electrochimica Acta*, 2012, **66**, 180–187.

[49] C. A. Martins, M. J. Giz, and G. A. Camara, *Electrochimica Acta*, 2011, **56**(12), 4549–4553.

[50] P. S. Fernández, P. Tereshchuk, C. A. Angelucci, J. F. Gomes, A. C. Garcia, C. A. Martins, G. A. Camara, M. E. Martins, J. L. F. Da Silva, and G. Tremiliosi-Filho, *Physical Chemistry Chemical Physics*, 2016, **18**(36), 25582–25591.

[51] J. Schnaidt, M. Heinen, D. Denot, Z. Jusys, and R. Jürgen Behm, *Journal of Electroanalytical Chemistry*, 2011, **661**(1), 250–264.

[52] J. F. Gomes, F. B. C. De Paula, L. H. S. Gasparotto, and G. Tremiliosi-Filho, *Electrochimica Acta*, 2012, **76**, 88–93.

[53] R. M. L. M. Sandrini, J. R. Sempionatto, E. Herrero, J. M. Feliu, J. Souza-Garcia, and C. A. Angelucci, *Electrochemistry Communications*, 2018, **86**(November 2017), 149–152.

[54] P. S. Fernández, C. A. Martins, C. A. Angelucci, J. F. Gomes, G. A. Camara, M. E. Martins, and G. Tremiliosi-Filho, *ChemElectroChem*, 2015, **2**(2), 263–268.

[55] Y. Holade, C. Morais, K. Servat, T. W. Napporn, and K. B. Kokoh, *ACS Catalysis*, 2013, **3**(10), 2403–2411.

[56] A. Kabbabi, R. Faure, R. Durand, B. Beden, F. Hahn, J. M. Leger, and C. Lamy, *Journal of Electroanalytical Chemistry*, 1998, **444**(1), 41–53.

[57] S. Zou, R. Gómez, and M. J. Weaver, *Journal of Electroanalytical Chemistry*, 1999, **474**(2), 155–166.

[58] S. Zou, R. Gómez, and M. J. Weaver, *Surface Science*, 1998, **399**(2-3), 270–283.

[59] K. I. Ozoemena, *RSC Advances*, 2016, **6**(92), 89523–89550.

[60] O. Muneeb, J. Estrada, L. Tran, K. Nguyen, J. Flores, S. Hu, A. M. Fry-Petit, L. Scudiero, S. Ha, and J. L. Haan, *Electrochimica Acta*, 2016, **218**, 133–139.

[61] E. Habibi and H. Razmi, *International Journal of Hydrogen Energy*, 2012, **37**(22), 16800–16809.

[62] L. Su, W. Jia, A. Schempf, and Y. Lei, *Electrochemistry Communications*, 2009, **11**(11), 2199–2202.

[63] A. Kahyaoglu, B. Beden, and C. Lamy, *Electrochimica Acta*, 1984, **29**(10), 1489–1492.

[64] A. Zalineeva, A. Serov, M. Padilla, U. Martinez, K. Artyushkova, S. Baranton, C. Coutanceau, and P. Atanassov, *Electrochemistry Communications*, 2015, **57**, 48–51.

[65] A. Zalineeva, A. Serov, M. Padilla, U. Martinez, K. Artyushkova, S. Baranton, C. Coutanceau, and P. B. Atanassov, *Journal of the American Chemical Society*, 2014, **136**(10), 3937–3945.

[66] C. Bianchini and P. K. Shen, *Chemical Reviews*, 2009, **109**(9), 4183–4206.

[67] T. Hu, Y. Wang, Q. Liu, L. Zhang, H. Wang, T. Tang, W. Chen, M. Zhao, and J. Jia, *International Journal of Hydrogen Energy*, 2017, **42**(41), 25951–25959.

[68] G. A. B. Mello, C. Busó-Rogero, E. Herrero, and J. M. Feliu, *Journal of Chemical Physics*, 2019, **150**(4).

[69] H. A. Miller, M. Bellini, F. Vizza, C. Hasenöhrl, and R. D. Tilley, *Catalysis Science and Technology*, 2016, **6**(18), 6870–6878.

[70] C. Jin, X. Sun, and Z. Chen, *Chemical Engineering and Technology*, 2012, **35**(6), 1064–1068.

[71] W. Hong, P. Bi, C. Shang, J. Wang, and E. Wang, *Journal of Materials Chemistry A*, 2016, **4**(12), 4485–4489.

[72] Y. Zhou and Y. Shen, *Electrochemistry Communications*, 2018, **90**(April), 106–110.

[73] K. E. Guima, L. M. Alencar, G. C. Da Silva, M. A. G. Trindade, and C. A. Martins, *ACS Sustainable Chemistry and Engineering*, 2018, **6**(1), 1202–1207.

[74] L. Karuppasamy, C. Y. Chen, S. Anandan, and J. J. Wu, *ACS Applied Materials and Interfaces*, 2019, **11**(10), 10028–10041.

[75] X. Shi, D. E. Simpson, and D. Roy, *Physical Chemistry Chemical Physics*, 2015, **17**(17), 11432–11444.

[76] Y. Chen, L. Zhuang, and J. Lu, *Chinese Journal of Catalysis*, 2007, **28**(10), 870–874.

[77] B. N. Zope, D. D. Hibbitts, M. Neurock, and R. J. Davis, *Science*, 2010, **330**(6000), 74–78.

[78] R. Kannan, A. R. Kim, and D. J. Yoo, *Journal of Applied Electrochemistry*, 2014, **44**(8), 893–902.

[79] C. A. Ottoni, S. G. da Silva, R. F. B. De Souza, and A. O. Neto, *Ionics*, 2016, **22**(7), 1167–1175.

[80] Z. Zhang, L. Xin, and W. Li, *International Journal of Hydrogen Energy*, 2012, **37**(11), 9393–9401.

[81] J. L. Bott-Neto, A. C. Garcia, V. L. Oliveira, N. E. De Souza, and G. Tremiliosi-Filho, *Journal of Electroanalytical Chemistry*, 2014, **735**, 57–62.

[82] M. Avramov-Ivić, V. Jovanović, G. Vlajnić, and J. Popić, *Journal of Electroanalytical Chemistry*, 1997, **423**(1-2), 119–124.

[83] C. A. Angelucci, H. Varela, G. Tremiliosi-Filho, and J. F. Gomes, *Electrochemistry Communications*, 2013, **33**, 10–13.

[84] S. C. Lai, S. E. Kleijn, F. T. Öztürk, V. C. Van Rees Vellinga, J. Koning, P. Rodriguez, and M. T. Koper, *Catalysis Today*, 2010, **154**(1-2), 92–104.

[85] X. Cui, Y. Li, M. Zhao, Y. Xu, L. Chen, S. Yang, and Y. Wang, *Nano Research*, 2019, **12**(2), 351–356.

[86] M. Mougenot, A. Caillard, M. Simoes, S. Baranton, C. Coutanceau, and P. Brault, *Applied Catalysis B: Environmental*, 2011, **107**(3-4), 372–379.

[87] J. Monzó, Y. Malewski, F. J. Vidal-Iglesias, J. Solla-Gullon, and P. Rodriguez, *ChemElectroChem*, 2015, **2**(7), 958–962.

[88] D. L. Zhou, R. Z. Wang, M. Zhang, X. Weng, J. R. Chen, A. J. Wang, and J. J. Feng, *Electrochimica Acta*, 2013, **108**, 390–397.

[89] R. R. Adžić and M. Avramov-Ivić, *Journal of Catalysis*, 1986, **101**(2), 532–535.

[90] M. Valter, M. Busch, B. Wickman, H. Grönbeck, J. Baltrusaitis, and A. Hellman, *Journal of Physical Chemistry C*, 2018, **122**(19), 10489–10494.

[91] I. T. Schwartz, A. P. Jonke, M. Josowicz, and J. Janata, *Catalysis Letters*, 2013, **143**(8), 777–782.

[92] P. Ocón, C. Alonso, R. Celdrán, and J. González-Velasco, *Journal of Electroanalytical Chemistry*, 1986, **206**(1-2), 179–196.

[93] K. N. Heck, B. G. Janesko, G. E. Scuseria, N. J. Halas, and M. S. Wong, *ACS Catalysis*, 2013, **3**(11), 2430–2435.

[94] N. Yahya, S. K. Kamarudin, N. A. Karim, M. S. Masdar, K. S. Loh, and K. L. Lim, *Energy Conversion and Management*, 2019, **188**(March), 120–130.

[95] P. Rodriguez, N. Garcia-Araez, and M. T. Koper, *Physical Chemistry Chemical Physics*, 2010, **12**(32), 9373–9380.

[96] P. Rodríguez, A. A. Koverga, and M. T. Koper, *Angewandte Chemie - International Edition*, 2010, **49**(7), 1241–1243.

[97] P. Rodriguez, Y. Kwon, and M. T. Koper, *Nature Chemistry*, 2012, **4**(3), 177–182.

[98] Y. Zhang, X. Zhu, J. Guo, and X. Huang, *ACS Applied Materials and Interfaces*, 2016, **8**(32), 20642–20649.

[99] N. Benipal, J. Qi, Q. Liu, and W. Li, *Applied Catalysis B: Environmental*, 2017, **210**, 121–130.

[100] C. A. Ottoni, S. G. da Silva, R. F. B. De Souza, and A. O. Neto, *Electrocatalysis*, 2016, **7**(1), 22–32.

[101] S. Yongprapat, A. Therdthianwong, and S. Therdthianwong, *Journal of Applied Electrochemistry*, 2012, **42**(7), 483–490.

[102] J. Qi, L. Xin, D. J. Chadderdon, Y. Qiu, Y. Jiang, N. Benipal, C. Liang, and W. Li, *Applied Catalysis B: Environmental*, 2014, **154-155**, 360–368.

[103] Z. Zhang, L. Xin, J. Qi, D. J. Chadderdon, K. Sun, K. M. Warsko, and W. Li, *Applied Catalysis B: Environmental*, 2014, **147**, 871–878.

[104] Z. Zhang, L. Xin, J. Qi, Z. Wang, and W. Li, *Green Chemistry*, 2012, **14**(8), 2150–2152.

[105] E. G. Rodrigues, M. F. Pereira, X. Chen, J. J. Delgado, and J. J. Órfão, *Industrial and Engineering Chemistry Research*, 2013, **52**(49), 17390–17398.

[106] G. Vértes and G. Horányi, *Journal of Electroanalytical Chemistry*, 1974, **52**(1), 47–53.

[107] A. A. El-Shafei, *Journal of Electroanalytical Chemistry*, 1999, **471**(2), 89–95.

[108] J. H. Sinfelt, *Advances in Catalysis*, 1973, **23**(C), 91–119.

[109] X. Liang, M. Xiao, M. Xu, D. Yang, Y. Yan, Y. Tian, and Y. Miao, *Journal of Applied Electrochemistry*, 2016, **46**(1), 1–8.

[110] V. L. Oliveira, C. Morais, K. Servat, T. W. Napporn, G. Tremiliosi-Filho, and K. B. Kokoh, *Journal of Electroanalytical Chemistry*, 2013, **703**, 56–62.

[111] V. L. Oliveira, C. Morais, K. Servat, T. W. Napporn, G. Tremiliosi-Filho, and K. B. Kokoh, *Electrochimica Acta*, 2014, **117**, 255–262.

[112] T. Iwasita and F. C. Nart, *Progress in Surface Science*, 1997, **55**(4), 271–340.

[113] T. P. Scachetti and A. C. D. Angelo, *Electrocatalysis*, 2015, **6**(5), 472–480.

[114] C. A. Martins, P. S. Fernández, H. E. Troiani, M. E. Martins, and G. A. Camara, *Journal of Electroanalytical Chemistry*, 2014, **717-718**, 231–236.

[115] Y. Holade, C. Morais, S. Arrii-Clacens, K. Servat, T. W. Napporn, and K. B. Kokoh, *Electrocatalysis*, 2013, **4**(3), 167–178.

[116] S. Rangarajan, R. R. Brydon, A. Bhan, and P. Daoutidis, *Green Chemistry*, 2014, **16**(2), 813–823.

[117] B. T. X. Lam, M. Chiku, E. Higuchi, and H. Inoue, *Journal of Power Sources*, 2015, **297**, 149–157.

[118] R. S. Ferreira, M. Janete Giz, and G. A. Camara, *Journal of Electroanalytical Chemistry*, 2013, **697**, 15–20.

[119] T. S. D. Almeida, K. E. Guima, R. M. Silveira, G. C. Da Silva, M. A. U. Martines, and C. A. Martins, *RSC Advances*, 2017, **7**(20), 12006–12016.

[120] Y. Kim, H. W. Kim, S. Lee, J. Han, D. Lee, J. R. Kim, T. W. Kim, C. U. Kim, S. Y. Jeong, H. J. Chae, B. S. Kim, H. Chang, W. B. Kim, S. M. Choi, and H. J. Kim, *ChemCatChem*, 2017, **9**(9), 1683–1690.

[121] L. M. Palma, T. S. Almeida, V. L. Oliveira, G. Tremiliosi-Filho, E. R. Gonzalez, A. R. De Andrade, K. Servat, C. Morais, T. W. Napporn, and K. B. Kokoh, *RSC Advances*, 2014, **4**(110), 64476–64483.

[122] X. Jin, H. Yan, C. Zeng, P. S. Thapa, B. Subramaniam, and R. V. Chaudhari, *Industrial and Engineering Chemistry Research*, 2017, **56**(45), 13157–13164.

[123] T. Asset, A. Serov, M. Padilla, A. J. Roy, I. Matanovic, M. Chatenet, F. Maillard, and P. Atanassov, *Electrocatalysis*, 2018, **9**(4), 480–485.

[124] A. Serov, T. Asset, M. Padilla, I. Matanovic, U. Martinez, A. Roy, K. Artyushkova, M. Chatenet, F. Maillard, D. Bayer, C. Cremers, and P. Atanassov, *Applied Catalysis B: Environmental*, 2016, **191**, 76–85.

[125] J. Han, Y. Kim, H. W. Kim, D. H. K. Jackson, D. Lee, H. Chang, H. J. Chae, K. Y. Lee, and H. J. Kim, *Electrochemistry Communications*, 2017, **83**(September), 46–50.

[126] N. Yahya, S. K. Kamarudin, N. A. Karim, S. Basri, and A. M. Zanoodin, *Nanoscale Research Letters*, 2019, **14**.

[127] Z. Zhang, L. Xin, J. Qi, D. J. Chadderdon, and W. Li, *Applied Catalysis B: Environmental*, 2013, **136-137**, 29–39.

[128] T. Pabisiak, M. J. Winiarski, and A. Kiejna, *Journal of Chemical Physics*, 2016, **144**(4), 044704.

[129] L. M. Palma, T. S. Almeida, C. Morais, T. W. Napporn, K. B. Kokoh, and A. R. de Andrade, *ChemElectroChem*, 2017, **4**(1), 39–45.

[130] Z. Chen, C. Liu, X. Zhao, H. Yan, J. Li, P. Lyu, Y. Du, S. Xi, K. Chi, X. Chi, H. Xu, X. Li, W. Fu, K. Leng, S. J. Pennycook, S. Wang, and K. P. Loh, *Advanced Materials*, 2019, **31**(2), 1–8.

[131] L. M. Alencar and C. A. Martins, *Electroanalysis*, 2018, **30**(9), 2167–2175.

[132] R. G. Da Silva, S. Aquino Neto, K. B. Kokoh, and A. R. De Andrade, *Journal of Power Sources*, 2017, **351**, 174–182.

[133] H. Wang, L. Thia, N. Li, X. Ge, Z. Liu, and X. Wang, *ACS Catalysis*, 2015, **5**(6), 3174–3180.

[134] D. Prasanna and V. Selvaraj, *RSC Advances*, 2015, **5**(120), 98822–98833.

[135] O. O. Fashedemi, H. A. Miller, A. Marchionni, F. Vizza, and K. I. Ozoemena, *Journal of Materials Chemistry A*, 2015, **3**(13), 7145–7156.

[136] A. Marchionni, M. Bevilacqua, C. Bianchini, Y. X. Chen, J. Filippi, P. Fornasiero, A. Lavacchi, H. Miller, L. Wang, and F. Vizza, *ChemSusChem*, 2013, **6**(3), 518–528.

[137] S. Yongprapat, S. Therdthianwong, and A. Therdthianwong, *Electrochimica Acta*, 2012, **83**, 87–93.

[138] S. S. Li, Y. Y. Hu, J. J. Feng, Z. Y. Lv, J. R. Chen, and A. J. Wang, *International Journal of Hydrogen Energy*, 2014, **39**(8), 3730–3738.

[139] N. Li, Q. Zhou, X. Li, W. Chu, J. Adkins, and J. Zheng, *Sensors and Actuators, B: Chemical*, 2014, **196**, 314–320.

[140] Z. Li, G. Qiu, Z. Jiang, W. Zhuang, J. Wu, and X. Du, *International Journal of Hydrogen Energy*, 2018, **43**(50), 22538–22547.

[141] C. Zhai, J. Hu, H. Gao, L. Zeng, M. Xue, Z. Q. Liu, and M. Zhu, *Journal of the Taiwan Institute of Chemical Engineers*, 2018, **93**, 477–484.

[142] H. Xu, P. Song, F. Gao, Y. Shiraishi, and Y. Du, *Nanoscale*, 2018, **10**(17), 8246–8252.

[143] N. Zhang, Y. Zhu, Q. Shao, X. Zhu, and X. Huang, *Journal of Materials Chemistry A*, 2017, **5**(36), 18977–18983.

[144] C. Shang, W. Hong, Y. Guo, J. Wang, and E. Wang, *Chemistry - A European Journal*, 2017, **23**(24), 5799–5803.

[145] Y. Zuo, L. Wu, K. Cai, T. Li, W. Yin, D. Li, N. Li, J. Liu, and H. Han, *ACS Applied Materials and Interfaces*, 2015, **7**(32), 17725–17730.

[146] H. Lv, L. Sun, D. Xu, S. L. Suib, and B. Liu, *Green Chemistry*, 2019, **21**(9), 2367–2374.

[147] M. C. Moraes, G. G. Junco, T. F. M. Moreira, C. J. G. Pinheiro, P. Olivi, D. Profeti, and L. P. R. Profeti, *Journal of Environmental Chemical Engineering*, 2019, **7**(1), 102922.

[148] Q. He, Y. Shen, K. Xiao, J. Xi, and X. Qiu, *International Journal of Hydrogen Energy*, 2016, **41**(45), 20709–20719.

[149] X. Y. Lang, G. F. Han, B. B. Xiao, L. Gu, Z. Z. Yang, Z. Wen, Y. F. Zhu, M. Zhao, J. C. Li, and Q. Jiang, *Advanced Functional Materials*, 2015, **25**(2), 230–237.

[150] Y. Wang, Z. Wang, J. Zhang, C. Zhang, H. Gao, J. Niu, and Z. Zhang, *Nanoscale*, 2018, **10**(36), 17070–17079.

[151] O. Muneeb, J. Estrada, T. Tran, S. Hu, B. Khorasani, A. Fry-Petit, L. Scudiero, S. Ha, and J. L. Haan, *ChemistrySelect*, 2017, **2**(29), 9261–9266.

[152] C. Jin, J. Zhang, R. Dong, and Q. Huo, *International Journal of Electrochemical Science*, 2014, **9**(10), 5743–5750.

[153] C. Wang, P. Song, F. Gao, T. Song, Y. Zhang, C. Chen, L. Li, L. Jin, and Y. Du, *Journal of Colloid and Interface Science*, 2019, **544**, 284–292.

[154] B. Tam, M. Duca, A. Wang, M. Fan, S. Garbarino, and D. Guay, *ChemElectroChem*, 2019, (100), 1784–1793.

[155] Y. Kwon, Y. Birdja, I. Spanos, P. Rodriguez, and M. T. Koper, *ACS Catalysis*, 2012, **2**(5), 759–764.

[156] Y. Kwon, T. J. P. Hersbach, and M. T. M. Koper, *Topics in Catalysis*, 2014, **57**(14-16), 1272–1276.

[157] N. Y. Suzuki, P. V. B. Santiago, T. S. Galhardo, W. A. Carvalho, J. Souza-Garcia, and C. A. Angelucci, *Journal of Electroanalytical Chemistry*, 2016, **780**, 391–395.

[158] A. G. Garcia, P. P. Lopes, J. F. Gomes, C. Pires, E. B. Ferreira, R. G. M. Lucena, L. H. S. Gasparotto, and G. Tremiliosi-Filho, *New Journal of Chemistry*, 2014, **38**(7), 2865–2873.

[159] N. Benipal, J. Qi, R. F. McSweeney, C. Liang, and W. Li, *Journal of Power Sources*, 2018, **375**, 345–350.

[160] H. Xu, J. Wang, B. Yan, K. Zhang, S. Li, C. Wang, Y. Shiraishi, Y. Du, and P. Yang, *Nanoscale*, 2017, **9**(35), 12996–13003.

[161] C. Jin, Z. Zhang, Z. Chen, and Q. Chen, *International Journal of Electrochemical Science*, 2013, **8**(3), 4215–4224.

[162] N. Erini, R. Loukrakpam, V. Petkov, E. A. Baranova, R. Yang, D. Teschner, Y. Huang, S. R. Brankovic, and P. Strasser, *ACS Catalysis*, 2014, **4**(6), 1859–1867.

[163] R. F. De Souza, L. S. Parreira, D. C. Rascio, J. C. Silva, E. Teixeira-Neto, M. L. Calegaro, E. V. Spinace, A. O. Neto, and M. C. Santos, *Journal of Power Sources*, 2010, **195**(6), 1589–1593.

[164] M. M. S. Pupo, F. E. López-Suárez, A. Bueno-López, C. T. Meneses, K. I. B. Eguiluz, and G. R. Salazar-Banda, *Journal of Applied Electrochemistry*, 2015, **45**(2), 139–150.

[165] M. V. Pagliaro, M. Bellini, M. Bevilacqua, J. Filippi, M. G. Folliero, A. Marchionni, H. A. Miller, W. Oberhauser, S. Caporali, M. Innocenti, and F. Vizza, *RSC Advances*, 2017, **7**(23), 13971–13978.

[166] S. Dash and N. Munichandraiah, *Electrochimica Acta*, 2015, **180**, 339–352.

[167] F. Colmati, E. Antolini, and E. R. Gonzalez, *Journal of Power Sources*, 2006, **157**(1), 98–103.

[168] C. Wang, Y. Rong, and T. Y. Hsu, *Materials Science- Poland*, 2006, **24**(21), 351–356.

[169] D. Lee, Y. Kim, Y. Kwon, J. Lee, T. W. Kim, Y. Noh, W. B. Kim, M. H. Seo, K. Kim, and H. J. Kim, *Applied Catalysis B: Environmental*, 2019, **245**(September 2018), 555–568.

[170] B. Ran, S. Liu, J. Zhao, T. Tan, B. Liang, and W. Wang, *Journal of Materials Science*, 2019, **54**(6), 4579–4588.

[171] Y. Fan, B. R. Goldsmith, and P. G. Collins, *Nature materials*, 2005, **4**(12), 906–911.

[172] D. Hiltrop, S. Cychy, K. Elumeeva, W. Schuhmann, and M. Muhler, *Beilstein Journal of Organic Chemistry*, 2018, **14**, 1428–1435.

[173] A. Zalineeva, A. Serov, M. Padilla, U. Martinez, K. Artyushkova, S. Baranton, C. Coutanceau, and P. B. Atanassov, *Applied Catalysis B: Environmental*, 2015, **176-177**, 429–435.

Chapter 3

A Method for Quantitative Detection of Oxidation Products Using a Microfluidic Device and Raman Spectroscopy

Abstract

A method for detecting oxidation products using quantitative Raman spectroscopy and a microfluidic device is described. This technique was demonstrated by methanol oxidation under controlled conditions. It was shown that the relevant oxidation products, formate and carbonate, can be detected online and quantified using Raman spectroscopy. Lower flow rates or higher overpotentials yielded a higher ratio of complete oxidation products, *i.e.*, CO_2 or carbonate, while high flow rates and low overpotentials yielded a higher ratio of partial oxidation products, *i.e.*, formate. This work provides a new, widely applicable and highly versatile method that uses low-cost materials for quantitative detection of oxidation products.

3.1 Introduction

Efficient determination of kinetics and reaction mechanisms of electrocatalytic reactions is of great research interest in electrochemistry studies. As microfluidic devices facilitate well-controlled mass transport conditions [1–3], many approaches have been attempted to couple analytical instruments with microfluidic devices for quantitatively detecting products of electrocatalytic reactions in real time [4, 5]. Among those techniques, confocal Raman spectroscopy is quantitative [6, 7], and can deliver spectra with high S/N ratio in minutes, or even seconds, which outperforms many chromatography methods in terms of the efficiency. Also, as the structural information of analytes is carried by photons, *in-situ* detection is therefore available [8, 9], which enables the capturing of intermediates with a very short lifespan. Compared with *in-situ* IR spectroscopy [10], Raman spectroscopy is much less hindered by the water molecules, as water strongly absorbs infrared photons but is a weak Raman scatterer [11]. Therefore, for electrochemical systems, Raman spectroscopy coupled with microfluidic devices has a great potential of being a cheap, easily implemented, and efficient method for quantitative analysis of reaction products.

In recent years, quantitative analysis using Raman spectroscopy and microfluidics has largely been limited to nanoparticles [12] and biological applications [13–18] due to the challenge in implementing an electrochemical system with microfluidics. For example, to satisfy the detection limit of Raman spectroscopy, a high reaction rate for the production of organic analytes within the microfluidic devices is required. When attempting to have high conversion rates in electrochemical microfluidic systems, the electrolyte resistance can give high uncertainties when determining the potential at the working electrode. To minimize the influence of electrolyte resistance, a highly concentrated and conductive electrolyte, and a short distance between the working, counter and reference electrodes are always adopted. Besides, a practical compromise is a large channel, which is at the expense of quickly achieving steady-state conditions,

and small sample volumes.

Methanol oxidation is a suitable system for assessing the method for quantitative detection of reaction products because it is widely studied [19–21], and has a limited number of reaction products. Many online spectroscopic methods have been performed to study the products from methanol oxidation, exemplified by differential electrochemical mass spectrometry (DEMS) [10,22–30] and infrared spectroscopy or more commonly attenuated total reflectance – Fourier transform infrared spectroscopy (ATR-FTIR) [31–39] for the identification of surface adsorbates. The reaction mechanism has been discussed in detail in some excellent reviews [40,41], which illustrated that it oxidizes by a dual-pathway mechanism either through surface CO to CO_2 or through short-lived adsorbates to HCOOH, HCHO, or CO, to CO_2 as a final product [42]. In alkaline systems, the oxidation products are only two: formate and carbonate [41, 43]. In addition, the reaction rate is faster in alkaline systems than in acidic systems [44], thus making methanol oxidation in alkaline solution a suitable test system. So far, the application of Raman spectroscopy in studying the electrochemical oxidation of small molecules has been limited to Surface-Enhanced Raman spectroscopy (SERS) to monitor the surface adsorbates [45–48], as Raman signals of surface adsorbates can be enhanced by the rough microstructures of Ag or Au electrodes. An exception is the work by de Souza and co-workers [49] where ethanol oxidation on platinum was studied using *in-situ* Raman spectroscopy and the possibility of using the method quantitatively is hinted at.

In this work, a microfluidic flow cell was designed and optimized for quantitative Raman spectroscopy studies. Being a low-cost device (less than 10 US dollars to make each device), it can provide online monitoring of alcohol electrooxidation (*e.g.* methanol electrooxidation) in an alkaline environment, which can be used for kinetic and mechanistic studies of electrocatalytic reactions of small organic species. Through quantitative analysis, the yield of the different oxidation products was calculated. High overpotentials and low flow rates yielded more of the complete oxidation

product, carbonate, while low overpotentials and high flow rate yielded more partial oxidation product, *i.e.*, formate. The method can be adapted to systems where i) the number of possible oxidation products is limited, ii) the products are detectable with Raman spectroscopy and can be uniquely identified (either through separate peaks or through peak deconvolution techniques), and iii) high conversion rates are possible in an electrochemical cell.

3.2 Experimental

3.2.1 Chemicals and Materials

Potassium hydroxide (Sigma Aldrich, $\geq$ 99.9%, semiconductor grade), potassium chloride (Caledon, 99%) and methanol (Caledon, 99.9%, reagent grade) were used to make the electrolytes. SYLGARD Silicone Elastomer Base and Curing Agent were supplied by Dow Corning Corporation. All chemicals were used without further purification. Silver wire (99%), platinum wire (99%), and platinum mesh (99%) were obtained from Sigma Aldrich. LePage® Epoxy Steel Syringe Glue was purchased from Henkel Canada Corporation. PTFE sheets (1 mm thick) were obtained from Goodfellow. Glass microscope slides and and cover slips (100 μm thick) were purchased from Fisher Scientific. Millipore Milli-Q water with a resistivity of 18 MΩ cm was used for all solutions.

3.2.2 Design of Microfluidic Flow Cell

The microfluidic device was fabricated in-house and is illustrated in Figure 3.1. The bottom of the cell was made by a teflon sheet on top of a 74 mm $\times$ 50 mm glass slide. The channel was made by placing two 1 mm thick teflon spacers (5 mm wide and 30 mm long, cut from PTFE sheets) on each side and covering it with a 0.1 mm thick

cover slip (22 mm×30 mm). To avoid etching of the glass when in contact with the strongly alkaline electrolyte, the glass cover slip (32 mm × 24 mm) was coated with PDMS. The PDMS layer was made by silicone elastomer mixed with its curing agent at weight ratio of 10:1, spin-coated on the cover slip at 1000 rpm, and cured at 80 °C for 2 hours. The thin cover slip (with a thin PDMS layer) design used was chosen to minimize the influence of the glass on the Raman measurements while allowing for the lens to come sufficiently close to the channel to enable bulk measurements of the solution.

The width of the channel was 6 mm to accommodate the 6 mm wide working electrode (WE, Pt wire with Pt mesh spot welded on top). Inlet tubing (1 mm O.D. Teflon Tube) and the working electrode were fitted in one end creating the inlet. A reservoir (1 cm wide) for collection of electrolyte and containing the reference electrode (RE) was fixed at the outlet. The reference electrode was a 1 mm diameter Ag|AgCl electrode submerged into saturated KCl solution (measured as 0.972 V vs RHE, molality of KOH $m_{\mathrm{KOH}} \approx 5.53$ mol kg^{-1}). All potentials measured are reported versus RHE if not otherwise stated. A Pt wire was used as the counter electrode (CE) and placed in the reservoir downstream of the channel. The length of the channel was 25 mm, of which 10 mm was occupied by the working electrode. All edges were sealed by Epoxy. This device was resistive to 5 M KOH and 5 M methanol over the duration of the experiment.

The inlet tubing was connected to Harvard PHD 2000 syringe pump with pre-set flow rates (5, 10, and 20 μL min^{-1}). Reynolds numbers for the three cases are calculated using Eq. 3.1-3.3, where u indicates flow rate in the unit of m s^{-1}, $L = 4A_{\mathrm{c}}/(2(h + A_{\mathrm{c}}/h))$ is the characteristic linear dimension (A_{c} and $2(h + A_{\mathrm{c}}/h)$ are the area and perimeter of the cross-section of the channel), and v is the kinematic viscosity of the fluid. Assuming the kinematic viscosity of the fluid is the same as water, Reynolds numbers are calculated to be 2.38, 4.76 and 9.53. To avoid small leaks, the edges of the device were sealed with epoxy before use, and the seal was

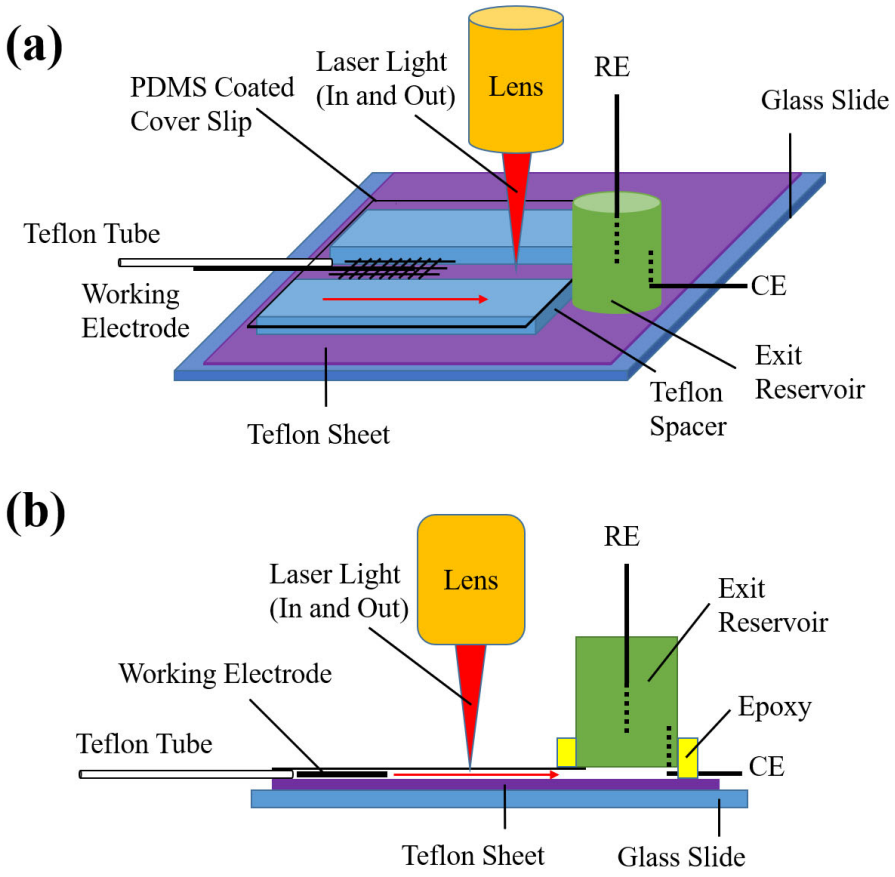

Figure 3.1: The Raman electrochemistry flow cell (not to scale). (a) Perspective view and (b) side view. Liquid enters through the Teflon tube (1 mm O.D.) and flows to the right (as indicated by the direction of a red arrow), exiting through the reservoir (green). The thickness and width of the channel are 1 mm and 6 mm. The length and width of the working electrode are 1 cm and 6 mm. Laser was focused at 8 mm downstream of the electrode. A 1 cm dia. glass reservoir was connected to the outlet of the channel, accommodating a Ag|AgCl reference electrode and a Pt wire counter electrode.

stable for the duration of the experiments.

$$Re_1 = \frac{u_1 L}{v} = \frac{4u_1 A_c}{2v(h + \frac{A_c}{h})} = \frac{4 \times 1.39 \times 10^{-5} \text{ m s}^{-1} \times 6 \times 10^{-4} \text{ m}^2}{2 \times 1 \times 10^{-6} \text{ m}^2 \text{ s}^{-1} \times 7 \times 10^{-3} \text{ m}} = 2.38 \quad (3.1)$$

$$Re_2 = \frac{u_2 L}{v} = \frac{4u_2 A_c}{2v(h + \frac{A_c}{h})} = \frac{4 \times 2.78 \times 10^{-5} \text{ m s}^{-1} \times 6 \times 10^{-4} \text{ m}^2}{2 \times 1 \times 10^{-6} \text{ m}^2 \text{ s}^{-1} \times 7 \times 10^{-3} \text{ m}} = 4.76 \quad (3.2)$$

$$Re_3 = \frac{u_3 L}{v} = \frac{4u_3 A_c}{2v(h + \frac{A_c}{h})} = \frac{4 \times 5.56 \times 10^{-5} \text{ m s}^{-1} \times 6 \times 10^{-4} \text{ m}^2}{2 \times 1 \times 10^{-6} \text{ m}^2 \text{ s}^{-1} \times 7 \times 10^{-3} \text{ m}} = 9.53 \quad (3.3)$$

3.2.3 Raman Detection

A confocal Raman spectrometer (Renishaw InVia Raman Microscope) was used with a HeNe laser (633 nm, laser power around 10 mW, laser power density = 0.38 W μm^{-3}) and detected with a Renishaw (horizontal) camera. Prior to each experiment, the Raman spectrometer was calibrated with a Si wafer to ensure similar conditions. A 50 times magnification lens for long working distances (Olympus IC50, N.A.=0.55) was used for the experiments, and the laser beam was focused at the center of the channel by first focusing on the channel bottom and manually moving the focus into the channel until a maximum in intensity was obtained for the electrolyte solution for quantitative study (5 M methanol with 5 M KOH). Each spectrum was collected for a total of 40 s in static mode from 970 cm^{-1} to 1530 cm^{-1}. These steady-state measurements were averaged to improve the signal to noise ratio. Each quantitative data point was based on 10 measurements for 5 μL min^{-1}, 5 measurements for 10 μL min^{-1}, and 3 measurements for 20 μL min^{-1} at the same conditions. The focal point was 8 mm downstream of the WE. The scattered light path is back through the lens to the detector.

3.2.4 Identification of Peaks and Quantification of Corresponding Peak Areas

The Raman spectra of solutions of 1 mol dm^{-3} methanol, formate, and carbonate in 5 mol dm^{-3} KOH are shown in Figure 3.2. Methanol, carbonate and formate have unique peaks that make it easy to qualitatively distinguish between the molecules without peak deconvolution. To ensure that all the main oxidation products were captured, calibration experiments with formaldehyde and methyl formate were conducted, as they are Raman-active species. These measurements confirmed that in strong base, formaldehyde (its original Raman spectrum is displayed in Figure S1) can decompose via a base-promoted self-disproportionation (Cannizzarro reaction) to formate and methanol, and this conversion was observably completed within seconds. Similarly, methyl formate hydrolyzes to formate and methanol in several seconds. No Raman spectrum showing these conversions was taken, as it was significantly shorter than the timescale of Raman measurements, *i.e.* 40 seconds in this work. Besides, carbon dioxide, a Raman-active product of methanol electrooxidation, is not able to be detected within the microfluidic flow cell by Raman due to the low solubility and conversion to carbonate in strong alkaline conditions. Thus, formate and carbonate were the only possible oxidation products that are Raman-detectable.

Concentrations were determined from Raman peak areas by calibration with solutions of known concentrations. The acquisition time for each concentration measured was 400 seconds. The obtained spectra were normalized to 40 seconds, as an average of ten consecutive measurements (40 seconds each). Figure 3.3 shows the calibration curve for (a) methanol, (b) formate and (c) carbonate. The area of the characteristic peaks were determined by least-square fitting to Gaussian functions (OriginLab 2018). The reliable detection limit of methanol, formate and carbonate is estimated to be 0.32 M, 0.05 M and 0.04 M, based on a criterion of $S/N > 3$. The fitting results are shown in Table 3.1, and the uncertainty ($\pm$) indicates 68% confidence intervals.

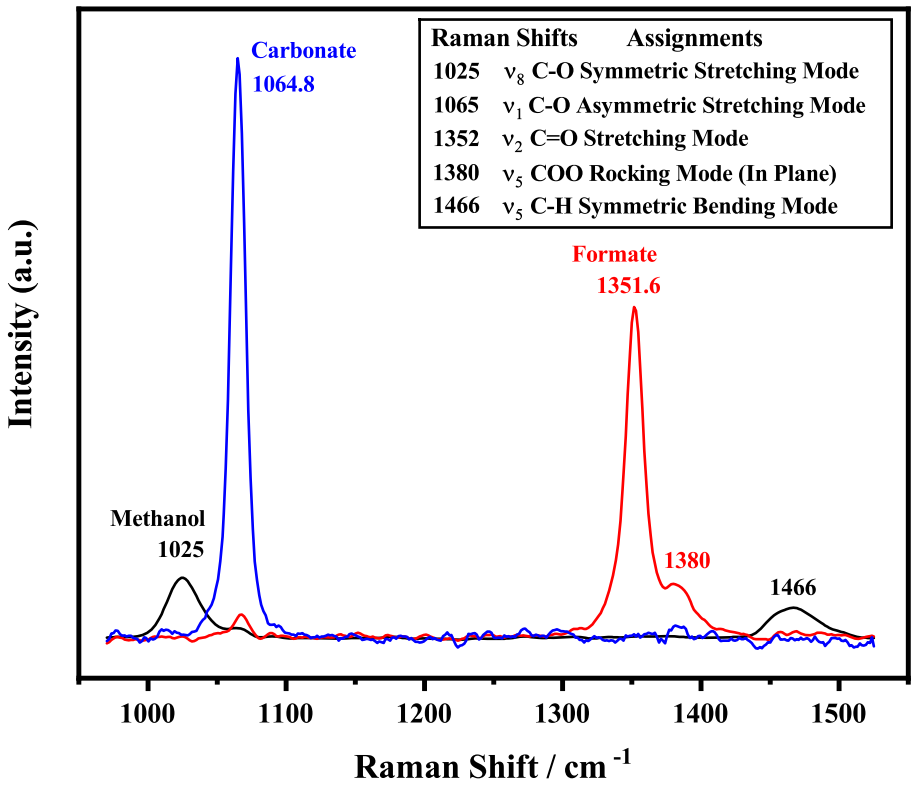

Figure 3.2: Example Raman spectra of 1 M methanol (black), 1 M formate (red), and 1 M carbonate (blue) in 5 M KOH. The peaks are marked by the wavenumber and the three main peaks, 1025 cm^{-1} (methanol), 1065 cm^{-1} (carbonate) and 1351 cm^{-1} (formate) are used for concentration calibration.

Table 3.1: Linear fit of concentration calibration curves for methanol, formate, and carbonate

	Slope / 10^4 M	**Intercept / 10^4** M	$\mathbf{R}^2$
Methanol	1.94 ± 0.05	0.21 ± 0.07	0.999
Formate	4.96 ± 0.09	0.02 ± 0.04	0.999
Carbonate	4.61 ± 0.04	0.17 ± 0.01	0.999

The linearity and good fit of the regression line indicates that methanol, formate, and carbonate can be quantitatively detected.

3.2.5 Electrochemical Measurements

The electrochemical measurements were performed with a Gamry Reference 600 potentiostat. Figure S2 shows a sample cyclic voltammogram recorded in the microfluidic device. Prior to the flow measurements, a series of cyclic voltammograms were recorded at zero flow rate between the region of the hydrogen evolution reaction (HER) and the oxygen evolution reaction (OER) until several consecutive cycles overlapped.

To ensure stable oxidation conditions and due to the well-known decay in oxidation currents during methanol oxidation, a procedure consisting of short potential holds (0.5 s at -0.03 V vs RHE) and long potential holds (20 s at oxidation potentials 1.37 V, 10 s at 1.97 V and 5 s at 2.77 V) was used to ensure a steady current through the whole experiment. Figure S3 shows a representative example of the chronoamperometry sequence used in this work. The possible formation of platinum oxide on the electrode surface and poisoning effect happening during the long potential holds can be removed by the cathodic currents during the following short potential holds. The reported currents, I_{ave}, were the average over the measurement duration. As the linearity of methanol oxidation CV revealed that the channel has a high resistance (around 45 Ω determined by EIS measurements), the three overpotentials used here were corrected to 1.06 V, 0.98 V and 0.70 V vs RHE by subtracting the iR-

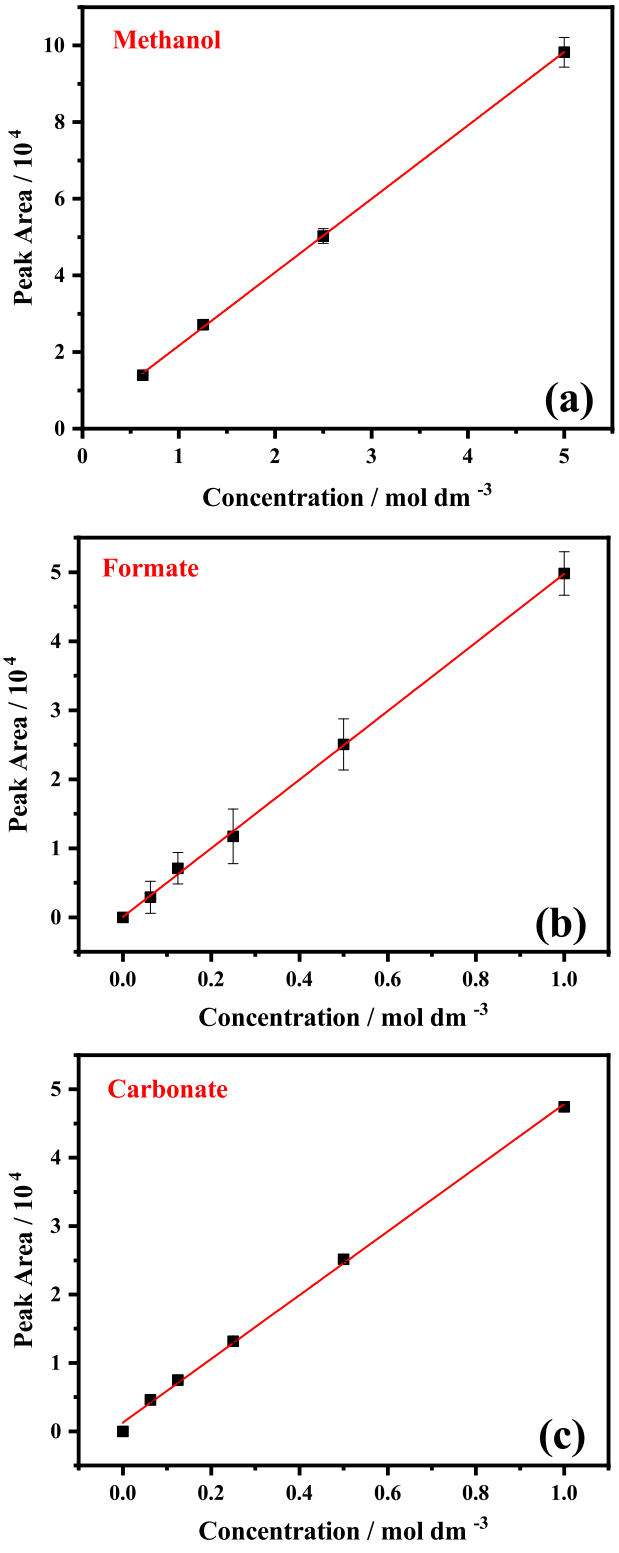

Figure 3.3: The calibration curves of (a) methanol, (b) formate, and (c) carbonate. The peaks used are 1025 cm^{-1} for methanol, 1065 cm^{-1} for carbonate and 1351 cm^{-1} for formate. Error bars are the standard deviation (σ_1) of the normalized characterisitic peaks. The data for the regression line are shown in Table 3.1.

loss. The currents were converted to current density based on the integrated hydrogen adsorption peaks in a separate measurement with 0.5 mol dm^{-3} H_2SO_4, assuming a true hydrogen underpotential deposition (UPD) charge of 220 μC cm^{-2}.

A full set of measurements consisted of flowing a total amount of 400 μL of electrolyte through the channel. This amount is about 4 times the total channel volume.

3.3 Results

A representative time sequence of the Raman spectra as the oxidation reaction proceeded (at 0.70 V vs RHE, 5 μL min^{-1}) is shown in Figure 3.4. The peak indicating the C=O stretching mode of formate centered at 1352 cm^{-1} showed up after several mins (Eq. 3.4), which means that electrolyte carrying oxidization products had reached the detection point. This peak kept increasing as the reaction went on, and reached steady-state after about 40 minutes. For trials at lower flow rates, a peak centered beside the major peak of methanol (at 1065 cm^{-1}) appeared after several minutes, which indicates that carbonate was produced (Eq. 3.5). The integrated area of the carbonate peak quickly reached a steady value.

$$CH_3OH + 5OH^- \rightarrow HCOO^- + 4H_2O + 4e^- \tag{3.4}$$

$$CH_3OH + 8OH^- \rightarrow CO_3^{2-} + 6H_2O + 6e^- \tag{3.5}$$

Figure 3.5 shows the concentration of methanol and formate versus time, as quantitatively converted from the peak areas of Raman spectra. The concentrations of all detected products stabilized after 10-70 minutes for cases with different flow rates, where the experiments at higher flow rates reached a steady value in less time. The decay of methanol concentration and increase of formate concentration manifested

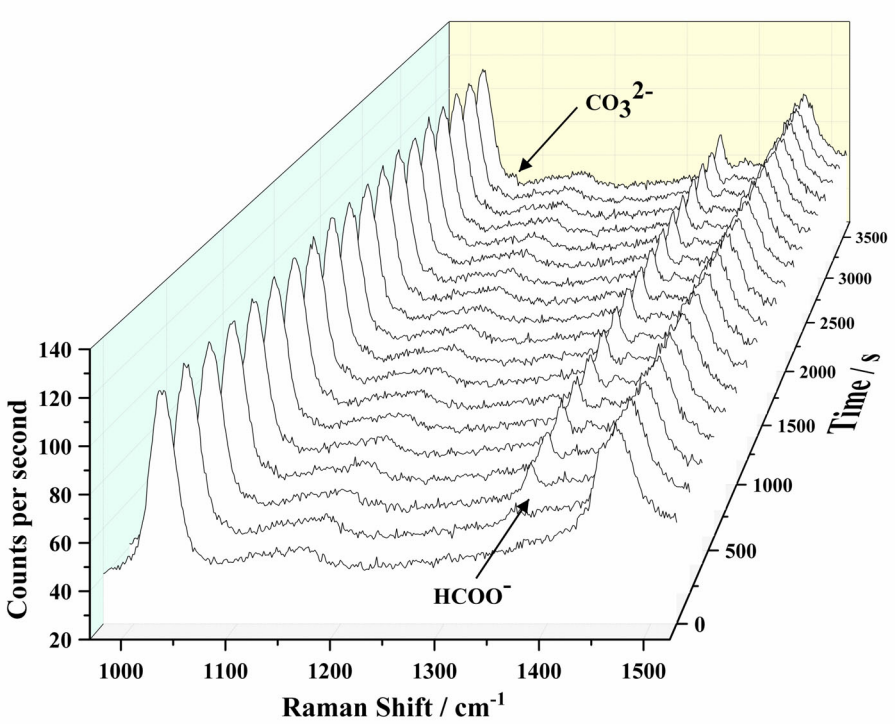

Figure 3.4: Time-dependent Raman spectra of methanol electrooxidation.

an exponential-like behavior, which suggests first-order kinetics. Thus, exponential fits of the decrease of methanol concentration and the increase of formate concentration were done, and the fitting outputs are shown in Table S1-S2. The concentration of carbonate is not shown here because although the concentration was above the detection limit, it was too low to be reliably quantified.

3.4 Discussion

3.4.1 Analysis of the Concentration Plot

One-dimensional Convection Flow Model

To model the concentration decay displayed in Figure 3.5, geometry of the channel and flow conditions are considered. The calculation of Reynolds numbers (< 10) shows that the flow pattern was laminar along the channel, so that it can be assumed that there is only convection in the flow direction (x direction), and the velocity vectors in the y and z directions are zero. Also, as infinite diffusion (perfect mixing) can be assumed in the y and z directions due to the small cross-sectional area, the one dimensional convection-diffusion equation (Eq. 3.6) can be used, where i is the chemical species that is consumed or produced. In this equation, $R_i(x,t)$ is defined as the source (positive) or sink (negative) of the species (mol m^{-3} s^{-1}), u describes average flow velocity, and D is the diffusivity of methanol or formate. In the timeframe of Figure 3.5, the approximate diffusion length from $\sqrt{Dt}$ assuming a diffusion coefficient, D, of approximately 10^{-9} m^2 s^{-1} is 1-2 mm, from which it can be concluded that convection is much faster than diffusion in the x direction. Therefore, the term for diffusion in the x direction can be neglected and only the term for convection is considered. Therefore, the time-dependent concentration profile within the channel can be simplified into a 1D convection model (Eq. 3.7).

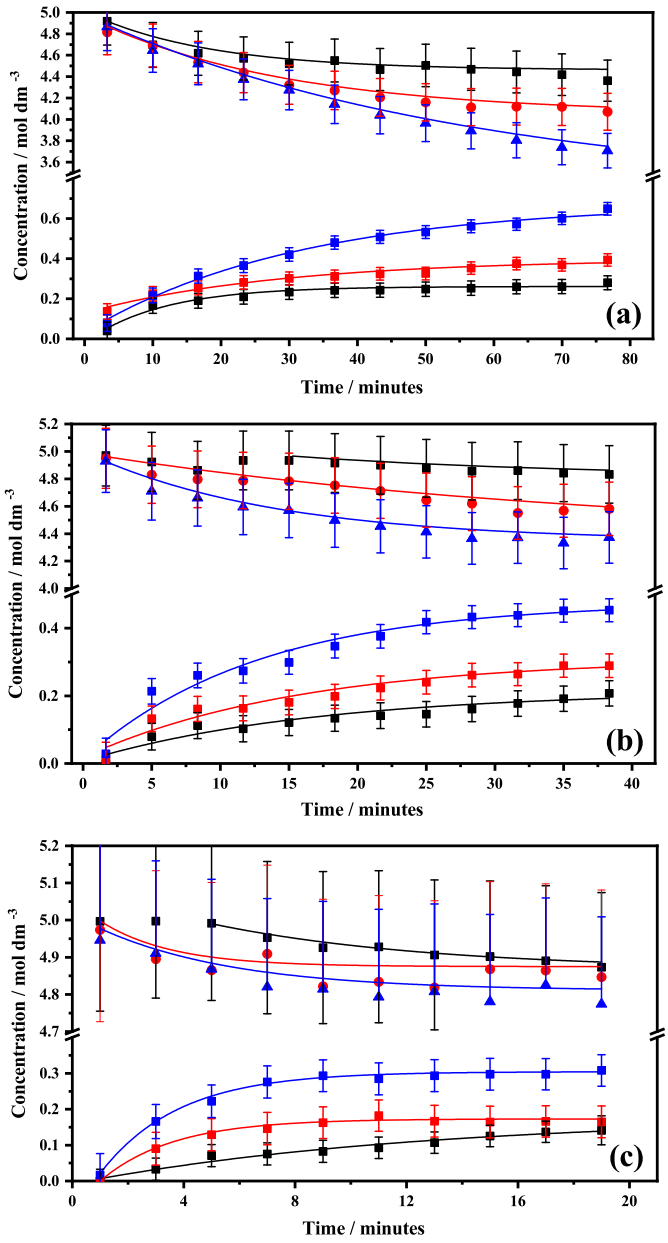

Figure 3.5: Evolution of concentrations of methanol and formate during methanol electrooxidation. Concentration of methanol (upper halves) and formate (lower halves) calculated from peak areas on Raman spectra versus time at (a) 5μL·min^{-1}, (b) 10 μL·min^{-1}, (c) 20 μL·min^{-1} and at 0.70 V (black), 0.98 V (red) and 1.06 V (blue). Data fitted with exponential decay curve. The fitting of characteristic peaks from online measurements was done using least squares fitting to Gaussian functions (OriginLab 2018) and the reported standard deviation (propagated with the uncertainty in Table 3.1) was used as the uncertainty. The calculation of error bars are introduced in the Supporting Information. The experiment was repeated three times using the same device, and the results were validated by the their consistency.

$$\frac{\partial c_i(x,t)}{\partial t} = D\frac{\partial}{\partial x}\cdot(\frac{\partial c_i(x,t)}{\partial x}) - u\frac{\partial}{\partial x}\cdot(c_i(x,t)) + R_i(x,t) \tag{3.6}$$

$$\frac{\partial c_i(x,t)}{\partial t} = -u\frac{\partial c_i(x,t)}{\partial x} + R_i(x,t) \tag{3.7}$$

The kinetics of methanol electrooxidation is assumed to be first-order in methanol, zero order in other species and irreversible, *i.e.* $R_i(x,t) = -\tau^{-1}c_i(x,t)$. Then a solution of Eq. 3.7 can be found as Eq. 3.8, with the initial concentration to be c^{b}. The methanol concentration at the detection point is displayed as in Eq. 3.9. When $d/u \leq t \leq (w+d)/u$ (where d is the distance from the downstream edge of the electrode to the detection point and w is the length of the electrode), the methanol concentration can be expressed as an exponential decay, *i.e.*, $c^{\mathrm{b}}\exp(-t/\tau)$. At steady-state, *i.e.*, $t \geq (w+d)/u$, the methanol concentration at the detection point is $c^{\mathrm{b}}\exp(-\frac{w}{\tau u})$, and therefore a higher flow rate would result in a smaller concentration decay.

$$c(x,t) = \begin{cases} c^{\mathrm{b}}\exp(-x/\tau u) & 0 \leq x \leq ut,\ 0 \leq t \leq w/u \\ c^{\mathrm{b}}\exp(-t/\tau) & ut \leq x \leq w,\ 0 \leq t \leq w/u \end{cases} \tag{3.8}$$

$$c(w+d,t) = \begin{cases} c^{\mathrm{b}} & 0 \leq t \leq d/u \\ c^{\mathrm{b}}\exp(-t/\tau) & d/u \leq t \leq (w+d)/u \\ c^{\mathrm{b}}\exp(-w/\tau u) & (w+d)/u \leq t \end{cases} \tag{3.9}$$

An evolution of the methanol concentration profile within the channel over the experimental duration is displayed in Figure 3.6. If the Raman sensitivity is ideal, the timespan d/u is from the beginning of the measurements to the point that a detectable change may be reflected in the spectra. On the other hand, the timespan w/u is from the point that the concentration change first appears to the point that steady state is achieved at the detection point. At the beginning of the reaction ($t = 0$), there

Table 3.2: Theoretical timeframes of fluid flowing towards the detection point from the upstream and downstream edges of the electrode

flow rate / μL min^{-1}	(d/u) / min	(w/u) / min	$((d+w)/u)$ / min
5	9.60	12.00	21.60
10	4.80	6.00	10.80
20	2.40	3.00	5.40

is no concentration gradient within the channel. As the reaction starts (with the pump driving the flow forward), a concentration gradient is formed as the electrode consumes some methanol in the electrode region. The concentration change increases as the fluid moves along the electrode from the upstream edge to the downstream edge of the electrode. For the first $t_1 = d/u$ seconds the concentration at the detection point has the bulk value. After that, the concentration is the same as at $x = w$, but just delayed by d/u seconds. For $t < w/u$, the liquid originally at the upstream edge at $t = 0$ has moved over the upstream part of the electrode up to $x = ut$. But downstream of that, the concentration is constant over the electrode surface, and is just changing with time according to the kinetics, *i.e.*, an exponential decay with time: $c^{\mathrm{b}} \exp(-t/\tau)$. So for a time w/u after the concentration starts to change at the detector, it decays with time exponentially. After that time, the concentration profile above the electrode has reached its steady state (exponential decay) profile and the concentration at the downstream edge doesn't change.

Comparison of the Theoretical Concentration Profile to the Experimental Results

Comparing the timeframes derived from Figure 3.5 to d/u and w/u shown in Table 3.2, two observations were made: (i) the time that a change in concentration is first observed at the detection point is shorter than d/u, and (ii) the experimental time to reach steady-state is longer than $(d + w)/u$. For the first observation, the slightly earlier appearance of the concentration changes may be due to diffusion towards the

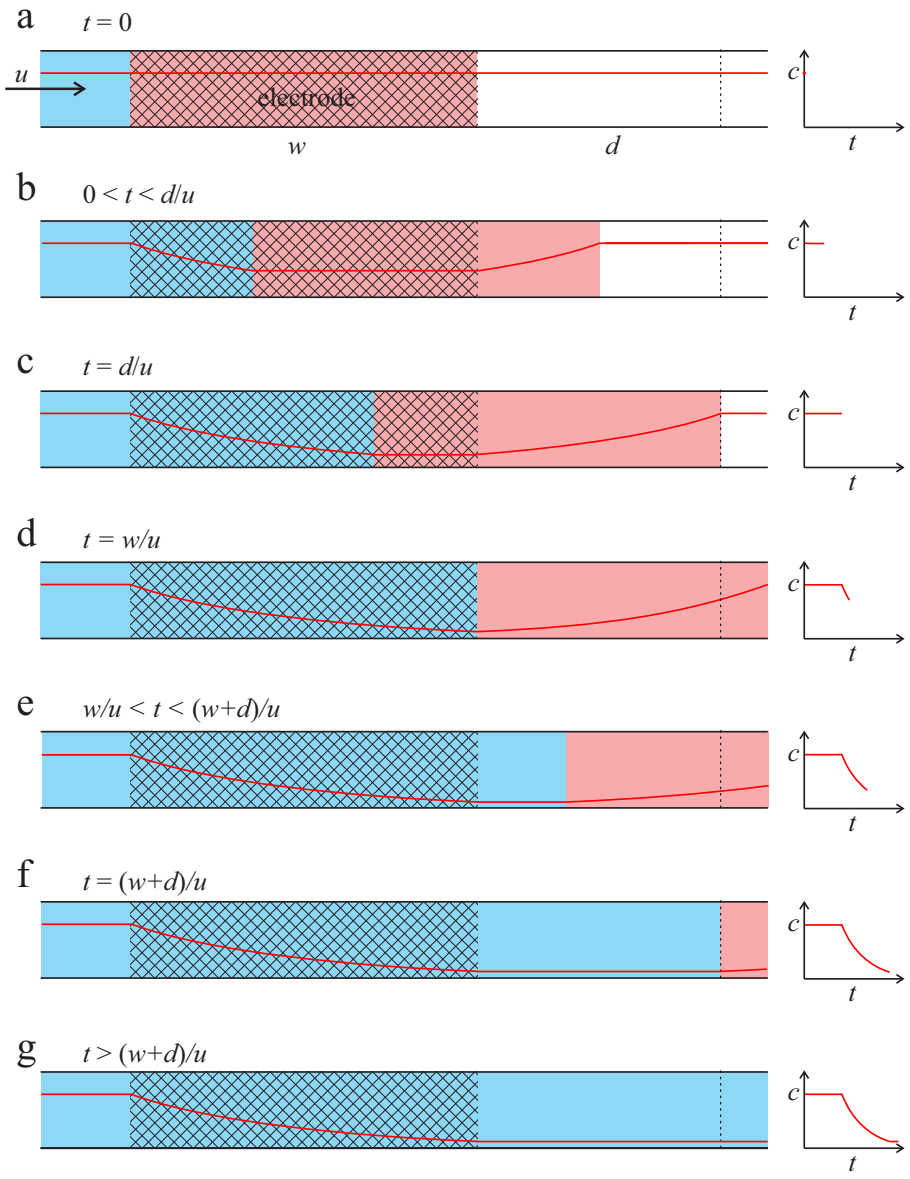

Figure 3.6: Schematic illustration of a 1D convection flow model applied to the microfluidic flow cell. Red lines are concentration profiles. Vertical dashed line is at the detection point. Fluid colours: pink - originally in the electrode region; blue - originally upstream of the electrode; white - originally downstream of the electrode.

Table 3.3: Calculated changes of methanol concentration for the cases of 5 μL per minute. Flow is in the electrode region for 12 min. Four electrons per methanol assumed.

E vs RHE / V	0.70	0.98	1.06
I / mA	14.22	22.87	37.98
$\Delta c = \frac{4uI}{FA_c}$ / M	0.442	0.711	1.181
Δc(measured) / M	0.64±0.15	0.93±0.13	1.29±0.12

detection point or uncertainty in the dimensions due to imprecise assembly.

The second observation is probably due to the perturbation of the flow pattern by the electrode. As the mesh electrode is placed in the middle of the channel, flow velocity above and below the electrode may be slightly faster than at the electrode region. Thus, less volume of the fluid that has larger reaction extent is brought forward, leading to a delay in the concentration profile.

However, as shown in Figure 3.5, most of the exponential concentration evolutions occurred within the first one third of the experimental durations, which are comparable to the timeframes of $(d + w)/u$. It is therefore suggested that for the fluid originally moving from the downstream edge of the electrode, the kinetics of methanol electrooxidation to formate is approximately first-order.

For steady state, Table 3.3 displays the calculated changes of methanol concentration that the cases of 5 μL min^{-1} over the 12 minutes over the electrode would lead to (assuming 4e/MeOH). It is found that the calculated Δc for the three overpotentials are close to the changes in methanol concentration by the end of the measurements as displayed in Figure 3.5a, which supports the delay of the concentration changes appearing on the Raman spectra.

3.4.2 Criteria to Quantitatively Determine Electrooxidation Products

In light of the reported results, it is clear that quantitative product analysis using Raman spectroscopy is possible for electrochemical systems. This makes it a useful tool in the effort to find more efficient electrocatalysts. Electrochemical microfluidic systems have different demands from purely chemical systems, mainly that the conductivity of the electrolyte in the channel is sufficient to carry the current produced. There are several criteria for successful determination of product distribution using Raman spectroscopy. These are i) the oxidation products have unique peaks and can either be determined directly by their peaks or through peak deconvolution, ii) high conversion rate that produces sufficient amounts of products above the detection limits, and iii) high conductivity to carry the current. The cell design suggested in this work serves as a practical compromise for these criteria. In this section, each of these criteria are discussed in detail, and suggestions are made on possible improvements, and in *Section 3.4.3*, the methanol oxidation results are discussed in light of these criteria.

Unique and Detectable Products

The value of the cell made at low cost (less than 10 US dollars) and easy handling of materials is embodied in the transferability to a large number of electrochemical reactions. This depends on two things: (i) each product has to have a strong enough signal above the detection limit, and (ii) the peaks of products are different enough so that they can be distinguished. For (i), it is well-known that molecules with higher polarizability are more Raman active as external electric field can induce dipole moments more easily. For example, vibrations of C-O bonds, C=O bonds and C-C bonds, nearly always have suitable Raman features.

Regarding the distinguishability of peaks, the amount of all products can be fully

determined if the reactant is a simple molecule. However, for organic molecules with more structural complexity, fully quantification may only be possible for some of the products. For example, glycerol gives up to 8-10 types of oxidation products [50] where many have similar bonding structure, making the detection of individual products a challenge.

In addition to this, the evolution of gaseous products should be avoided as it can affect the cell resistance or even block the channel. Also, care should be taken when studying highly volatile reactants to ensure a constant concentration, especially when comparing results at different flow rates.

High Conversion Rate

High conversion rate means that the rate of oxidation leads to a concentration at the detection point above the detection limit. Simply stated, the rate of production can be designated as the current divided by the amount of electrons per molecule reacted, while the rate of removal is the concentration that is flowing downstream at the average flow rate. In equation form, this can be given as in Eq. 3.10.

$$\frac{I}{zFA_{\mathrm{c}}} \gg c_{\mathrm{min}}u \tag{3.10}$$

Here, I is the partial current, z is the number of electrons necessary to produce the molecule, F is the Faraday constant, and c_{min} is the concentration detection limit. In general, if one wants to modify the system to achieve this condition, one can try to increase the current, either by changing catalyst, adding more electrode area, or increasing the overpotential. Similarly, one uses a lower flow rate to ensure that most of the products are detected.

In this work, the detection limit of formate based on S/N ratio (S/N ratio ≥ 3), c_{min}, was 0.05 mol dm^{-3}, the highest volumetric flow rate was 20 μL min^{-1}, and the average electrons needed can be estimated to be 6 (production of carbonate from

methanol). Thus, a current of at least 10 mA is necessary for quantitative detection. Besides, the actual concentration should be higher than $c_{\min}$ to ensure a higher peak intensity to enable the integration and enhance the accuracy. At the highest flow rate, we measured steady-currents above 14 mA, *i.e.*, an amount that ensures enough products.

However, in a system with multiple products (as illustrated in this work), the conversions from a reactant to different products should be considered separately. For example, re-adsorption of partial oxidation products may lead to larger fractions of complete oxidation products. Thus, to remove this influence and generate more kinds of products, an electrode that spans the channel and is perpendicular to the flow direction is desirable as it leads to least re-adsorption in the flow direction. However, the cross-sectional area of 6 mm^2 used here is not large enough to give sufficient current. The compromise made in our work is filling the end of channel with 6 mm $\times$ 10 mm Pt mesh that allows currents up to 2.67 mA cm^{-2} to be measured at high overpotential. More readsorption in this case leads to higher overall conversion rate to CO_2, and is one of the possible mechanisms why lower flow rate gives higher conversion efficiency.

High Conductivity

Conductivity is another factor that determines the general performance of the cell. Ideally, the cell should be able to carry the current downstream to a counter electrode without influencing the measured potential at the working electrode. A criterion can be deduced from this demand, *i.e.*, that the IR loss in the measurements is much smaller than the kinetic overpotential at the electrode so that the measured potential is realistic. In setting this demand, a suggested limit is that the IR loss is less than 10% of the kinetic overpotential. This is given in equation form in Eq. 3.11.

$$\eta_{\text{kin}} \gg 10 I \rho \frac{d_{\text{WE-CE}}}{A_{\text{c}}} \tag{3.11}$$

Here, η_{kin} is the kinetic overpotential, ρ is the electrolyte resistivity, $d_{\text{WE-CE}}$ is the distance between the working and the counter electrode, and A_{c} is the cross-sectional area of the channel. The kinetic overpotential can be estimated from the difference between the reversible potential and the potential for the reaction. The demand highlights the necessity of a highly conductive electrolyte. In our case, assuming an overpotential, η_{kin}, of 2 V and a current of at least 20 mA, and a distance, $d_{\text{WE-CE}}$, of 2 cm, the resistivity should be less than 0.03 Ω m. 5 M KOH has a resistivity of about 0.015 Ω m. This is very close to the limiting value and the sample voltammogram in Fig. S1 shows significant IR resistance during the measurements.

To ensure that the criteria in Eq. 3.11 are met, there are two main solutions. One is changing the geometry to make sure that the counter electrode is sufficiently large and not too far away from the working electrode. In addition, it is desirable that the reference electrode is outside the current path between the working and counter electrode. Otherwise, the measured potential is shifted because the RE is too close to the counter electrode. However, this is not easy for our cell as the reservoir accommodating the reference electrode would affect the pressure, and subsequently affect the flow pattern if located upstream. A suggested geometry is to have an integrated reference electrode upstream in a side channel as suggested by Fanavoll et al [51] in a recent work. The conductivity can be modified somewhat by changing the electrolyte. However, the electrolyte used here, 5 M KOH, is among the most highly conductive aqueous electrolytes as K^+ has higher ionic mobility (7.62×10^{-8} $m^2s^{-1}V^{-1}$) compared to Na^+ (5.19×10^{-8} $m^2s^{-1}V^{-1}$). Also, a higher electrolyte concentration (too alkaline) is not necessarily relevant for fuel cell systems. Therefore, the main option is to change the geometry, for example, one could envision having a narrow channel around the electrodes that widens out after the electrode to both lower the flow rate, and ensure that the current can be carried downstream. Another possible improvement is to have a side channel with frits (no flow) so that current can be transported outside of the channel without actually transporting the products.

Homogenized Concentrations at the Detection Point

One of the key assumptions behind being able to detect the products quantitatively is that the concentration at the detection point accurately reflect the product distribution. Thus, diffusional mass transport need to homogenize any concentration gradients perpendicular to the flow rate by the time the flow has reached the detection point. A rough estimate of the diffusion time is to assume that a molecule should be able to diffuse half the width of the channel within the time it takes to move downstream, *i.e.*, $t_{\text{diff}} < t_{\text{flow}}$, or as in given in Eq. 3.12.

$$\frac{h^2}{4D} \ll \frac{d}{u} \tag{3.12}$$

Here, h is the thickness of the channel, and therefore $h^2/4D$ is about 4 minutes. Putting this in the form of the flow rate, *i.e.*, $u < 4Dd/h^2$, and assuming D to be 10^{-9} m^2 s^{-1}, this gives a maximum flow rate for our system of 1.2 μL min^{-1}. This is lower than the flow rates used in our experiments. However, the actual diffusion rate is smaller as our working electrode covers a large fraction of the volume. Therefore, the criteria outlined here is stricter than necessary. In addition, our electrode has meshes that helps mixing close to the electrode as it influences the flow just downstream of the mesh.

To ensure that the criteria are met in a real system, the focus should be on reducing the diffusion length in the direction perpendicular to the flow, either by filling the channel with the electrode or by making the channel smaller overall. In addition, a longer distance down to the detection point will give more time for mixing. Another option is also to have a micromixer downstream of the electrode that ensures a more homogenized solution. It is assumed that at the point of detection, the electrolyte is perfectly mixed, which means that there are no concentration gradients, so that the measurements are a true reflection of the net change in concentration. To achieve this, one should: i) give sufficient mixing time (slow flow and high conversion rate),

or ii) introduce mixers. A hole with diameter less than 1 mm located downstream but upstream of the detection point could be taken as simplest way of creating mixing effect. The flow will be forced to go through the hole and mix more evenly. However, building such a hole within the channel will significantly increase the electrical resistance.

Thermal Stability

The influence of the reaction enthalpy, resistive heating, or heating due to absorption of the laser on the temperature of the system can be calculated for the respective flow rates from Eq. 3.13. Here, Q_{i} is a heating source (in W), U_{j} is the radiation efficiency (in W) including the heat conduction rate of teflon and solution, C_{p} is the heat capacity of water (75.3 J mol^{-1} K^{-1}), ΔT is the temperature change, ρ_{w} is the density of water (997 kg m^{-3}), and M_{w} is the molar mass of water (18.02 g mol^{-1}).

$$\sum_{\mathrm{i}} Q_{\mathrm{i}} - \sum_{\mathrm{j}} U_{\mathrm{j}} = C_{\mathrm{p}} \Delta T V_{\mathrm{f}} \frac{\rho_{\mathrm{w}}}{M_{\mathrm{w}}} \tag{3.13}$$

The calculated reaction enthalpy of methanol oxidation to formate was 1720 kJ mol^{-1}. In this calculation, the conventional enthalpies of formation of the anions OH^- and $HCOO^-$ were converted to absolute values by subtracting the absolute enthalpy of formation of H^+(aq), 386.1 kJ mol^{-1}, which is the sum of the enthalpy of formation of H^+(g) (1536.202 kJ mol^{-1} [52]) and the hydration enthalpy of H^+ (-1150.1 kJ mol^{-1} [53]). With a current of 38 mA, this can act as (4 e/molecule) a cooling source (approximately -215 mW). The resistive heating considering 45 Ω channel resistance and 38 mA current gives 65 mW. Considering the fact that there was no noticable temperature change during the measurements and no change of the reactivity was observed, it is suggested that the heat radiation and dissipation is able to keep the temperature stable during the measurements.

Discussion of Combined Criteria for Quantitative Raman Measurements in a Microfluidic Flow Cell

The criterion of unique and detectable products make experimental assessment necessary. For the criteria dealt with in this subsection, mathematical criteria can be derived so that performance can be assessed prior to building a cell or choosing an electrolyte. It is noticeable that among them, many are contradictory so that a practical compromise is necessary. For example, conversion rate (less electrolyte and higher current are wanted) vs conductivity (more electrolyte and lower current are wanted), or perfect mixing (long distance between WE and detection point) vs steady-state conditions (faster traveling time, *i.e.*, short distance).

Note that the manipulation of experimental or geometric parameters can have positive and negative effects, for example, higher flow rate is detrimental for most of these criteria, *e.g.*, need longer wait for steady-state and need a higher current to achieve high conversion rate, but it helps with the removal of excess heat. The system designed and used in this work represents a practical starting point and can be further optimized based on the system parameters when other electrochemical reactions than methanol oxidation are studied.

3.4.3 Discussion on the Difference Between the Amounts of Methanol Consumption and Formate Production

The product distribution of methanol electrooxidation is listed in Table 3.4. It is noticeable that at 5 μL min^{-1} and 10 μL min^{-1}, the sum of the concentrations of all products and the rest of the methanol is less than 5 mol dm^{-3}. In other words, some oxidation products remain undetected from Raman spectra. At low flow rate (5 μL min^{-1}), the concentration of undetected products is approximately equal to that of formate. Also, at moderate flow rate (10 μL min^{-1}) but high overpotentials (0.98 V

Table 3.4: Product Distribution of Methanol Electrooxidation. Uncertainties were determined using the standard deviation of the peak fitting propagated with the uncertainty of regression lines.

Flow rate / μL min^{-1}	E **vs RHE** / **V**	c**(methanol)** / **M**	c**(formate)** / **M**	[c**(carbonate)** + c**(undetected)**] / c**(formate)**
5	0.70	4.36±0.15	0.28±0.03	1.28±0.14
5	0.98	4.07±0.13	0.39±0.03	1.38±0.11
5	1.06	3.71±0.12	0.65±0.03	0.98±0.06
10	0.70	4.83±0.16	0.21±0.03	0±0.03
10	0.98	4.58±0.15	0.29±0.03	0.45±0.05
10	1.06	4.37±0.14	0.45±0.03	0.40±0.03
20	0.70	4.87±0.15	0.14±0.04	0±0.07
20	0.98	4.85±0.19	0.16±0.04	0±0.02
20	1.06	4.77±0.19	0.31±0.04	0±0.03

and 1.06 V), the ratio of undetected products to formate lowers to around 0.4-0.45. As flow rate increases to 20 μL min^{-1}, there is no undetected product as the sum of the concentrations of formate and methanol is within the error of 5 mol dm^{-3}. The ratio of (carbonate + undetected product) / formate shows that lower flow rates and higher potentials lead to a larger fraction of the undetected product.

The oxidation of methanol proceeds through a dual-pathway mechanism in alkaline systems as illustrated above. Based on a number of previously reported works [24,28,30,54,55], carbonate or CO_2, the complete oxidation product of methanol electrooxidation, can be preferentially produced in acidic solutions and high temperatures, due to the possibility of re-adsorption of the oxidation products for further oxidation. Considering that formate, CO_2 and carbonate are the only final products in this system for both pathways of methanol oxidation, a hypothesis made here is that the undetected product is CO_2, as the chemical equilibrium of dissolved CO_2 towards bicarbonate and eventually carbonate in strong basic electrolyte is not reached, although the chemical equilibrium constants of these two reactions are so high that all dissolved CO_2 would eventually become carbonate. To be more specific, the rate

of CO_2 production may be higher than the rate of its conversion into carbonate under some experimental conditions. Therefore, when the amount of CO_2 (aq) exceeds its solubility in water, gaseous carbon dioxide starts to evolve and escapes through the walls, which matches the observation from many *in-situ* FTIR studies of glycerol electrooxidation, *i.e.*, the presence of the CO_2 characteristic peak at 2343 cm^{-1} under alkaline conditions [56–59].

To test this hypothesis, the cell was immersed in saturated $Ca(OH)_2$ solution to detect CO_2 that escapes through the channel walls. The amount of escaped CO_2 can be calculated by weighing out the amount of $CaCO_3$ produced after filtration and air-drying of the $Ca(OH)_2$ solution. It was found that when the cell was operating at 1.06 V at 5 μL min^{-1}, 2.1 mg of $CaCO_3$ was produced within 80 minutes, after subtracting the amount of CO_2 captured from the atmosphere (about 4.0 mg). This test suggested that some CO_2 escapes through the walls. Another fact is that the calculated electron balance (Eq. 3.14) using average current over the measurement (I_{ave}) and volumetric flow rate (V_{f}) is under 100%, which also suggests the same conclusion. Assuming the presence of CO_2 production from methanol electrooxidation, it is shown that if all the undetected product is CO_2 ($c_{\text{ds,CO}_2}$ from carbon balance (Eq. 3.15)), the electron balance (Eq. 3.14) are estimated to be around 105%-137% for 5 μL min^{-1}, 97%-107% for 10 μL min^{-1}, and 99%-130% for 20 μL min^{-1}.

$$I_{\text{ave}} = FV(4c_{\text{ds,FA}} + 6c_{\text{ds,CO}_3} + 6c_{\text{ds,CO}_2}) \tag{3.14}$$

$$c_{\text{us,MeOH}} = c_{\text{ds,MeOH}} + c_{\text{ds,FA}} + c_{\text{ds,CO}_3} + c_{\text{ds,CO}_2} \tag{3.15}$$

(Here, the subscript us notes upstream and ds notes downstream, the species are denoted as MeOH = methanol, FA = formate, CO_3 = carbonate, and CO_2 = carbon dioxide).

Our results are consistent with methanol reacting through direct pathway in our selected range of overpotentials to give formate which could be further reacted to

CO_2, in accordance with previously reported results.

3.5 Conclusion

In this work, a method combining Raman spectroscopy and a microfluidic cell was demonstrated by studying methanol oxidation on platinum in alkaline solution. The reaction products found were formate, carbonate, and CO_2. Three main conclusions are presented:

- A method for quantitative Raman spectroscopy detection of oxidation products in a microfluidic cell was developed. The yield of each oxidation products could be determined quantitatively with little uncertainty ($\leq$ 0.1 mol dm^{-3}).

- The criteria for successful quantification were determined and these were i) quantitative analyses with Raman spectroscopy in electrochemical system is definitely feasible, ii) unique products, high conversion and conductivity, perfect mixing, and steady-state conditions must be met, iii) a practical solution for methanol oxidation is presented, and iv) this microfluidic system can likely be further modified to study other systems as long as the criteria in point ii) are met.

- Based on a carbon and electron balance, it was found that low flow rate / high overpotentials yields more carbonate and that high fow rate / low overpotentals yields more formate.

References

[1] M. E. Snowden, P. H. King, J. A. Covington, J. V. MacPherson, and P. R. Unwin, *Analytical Chemistry*, 2010.

[2] L. P. Zaino, N. M. Contento, S. P. Branagan, and P. W. Bohn, *ChemElectroChem*, 2014.

[3] E. Ko, V. K. Tran, Y. Geng, W. S. Chung, C. H. Park, M. K. Kim, G. H. Jin, and G. H. Seong, *Journal of Electroanalytical Chemistry*, 2017.

[4] N. I. Andersen, K. Artyushkova, I. Matanović, D. P. Hickey, S. D. Minteer, and P. Atanassov, *ChemElectroChem*, 2019.

[5] Z. Wang, Y. Zhang, B. Liu, K. Wu, S. Thevuthasan, D. R. Baer, Z. Zhu, X. Y. Yu, and F. Wang, *Analytical Chemistry*, 2017.

[6] X. Yue, Y. Su, X. Wang, L. Li, W. Ji, and Y. Ozaki, *ACS Sensors*, 2019, **4**(9), 2336–2342.

[7] J. H. Lim, D. Bae, and A. Fong, *Journal of Agricultural and Food Chemistry*, 2018, **66**(51), 13533–13540.

[8] Z. Gu, W. Zhu, M. Zhu, D. Wu, J. Zhou, J. Wang, Q. Zhu, and W. Chen, *ICHVE 2018 - 2018 IEEE International Conference on High Voltage Engineering and Application*, 2019, pp. 2018–2021.

[9] M. Kögler, B. Zhang, L. Cui, Y. Shi, M. Yliperttula, T. Laaksonen, T. Viitala, and K. Zhang, *Sensors and Actuators, B: Chemical*, 2016, **230**, 411–421.

[10] W. Chen, J. Cai, J. Yang, M. M. Sartin, and Y.-X. Chen, *Journal of Electroanalytical Chemistry*, 2017, **in press**.

[11] P. J. Larkin, *Infrared and Raman Spectroscopy: Principles and Spectral Interpretation*, 2017.

[12] A. F. Chrimes, K. Khoshmanesh, P. R. Stoddart, A. Mitchell, and K. Kalantarzadeh, *Chemical Society Review*, 2013, **42**, 5880.

[13] S. E. J. Bell, J. N. Mackle, and N. M. S. Sirimuthu, *Analyst*, 2005, **130**, 545–549.

[14] Z.-S. Wu, G.-Z. Zhou, J.-H. Jiang, G.-L. Shen, and R.-Q. Yu, *Talanta*, 2006, **70**, 533–539.

[15] K. R. Ackermann, T. Henkel, and J. Popp, *ChemPhysChem*, 2007, **8**, 2665–2670.

[16] L. X. Quang, C. Lim, G. H. Seong, J. Choo, K. J. Do, and S.-K. Yoo, *Lab on a Chip*, 2008, **8**, 2214–2219.

[17] S. E. J. Bell and N. M. S. Sirimuthu, *Chemical Society Reviews*, 2008, **37**, 1012–1024.

[18] X. Yang, A. Y. Zhang, D. A. Wheeler, T. C. Bond, C. Gu, and Y. Li, *Analytical & Bioanalytical Chemistry*, 2012, **402**, 687–691.

[19] Y. P. Sun, L. Xing, and K. Scott, *Journal of Power Sources*, 2010, **195**(1), 1–10.

[20] I. Danaee, M. Jafarian, A. Mirzapoor, F. Gobal, and M. G. Mahjani, *Electrochimica Acta*, 2010, **55**(6), 2093–2100.

[21] L. W. Liao, S. X. Liu, Q. Tao, B. Geng, P. Zhang, C. M. Wang, Y. X. Chen, and S. Ye, *Journal of Electroanalytical Chemistry*, 2011, **650**(2), 233–240.

[22] T. Iwasita and W. Vielstich, *Journal of Electroanalytical Chemistry*, 1986, **201**, 403–408.

[23] T. Iwasita and W. Vielstich, *Journal of Electroanalytical Chemistry*, 1988, **250**, 451–456.

[24] J. Rodriguez and E. Pastor, *Electrochimica Acta*, 1998, **44**, 1173–1179.

[25] H. Baltruschat, *Journal of the American Society for Mass Spectrometry*, 2004, **15**(12), 1693–1706.

[26] H. Wang, T. Löffler, and H. Baltruschat, *Journal of Applied Electrochemistry*, 2001, **31**, 759–765.

[27] T. H. M. Housmans, A. H. Wonders, and M. T. M. Koper, *The Journal of Physical Chemistry B*, 2006, **110**(20), 10021–10031.

[28] H. Wang and H. Baltruschat, *Journal of Physical Chemistry C*, 2007, **111**, 7038–7048.

[29] M. Heinen, Y.-X. Chen, Z. Jusys, and R. J. Behm, *ChemPhysChem*, 2007, **8**, 2484–2489.

[30] M. Chojak-Halseid, Z. Jusys, and R. J. Behm, *The Journal of Physical Chemistry C*, 2010, **114**(51), 22573–22581.

[31] B. Beden, M. C. Morin, F. Hahn, and C. Lamy, *Journal of Electroanalytical Chemistry*, 1987, **229**(1-2), 353–366.

[32] B. Beden, F. Hahn, S. Juanto, C. Lamy, and J.-M. Leger, *Journal of Electroanalytical Chemistry and Interfacial Electrochemistry*, 1987, **225**(1-2), 215–225.

[33] D. Kardash, J. Huang, and C. Korzeniewski, *Journal of Electroanalytical Chemistry*, 1999, **476**(2), 95–100.

[34] D. Kardash, J. Huang, and C. Korzeniewski, *Langmuir*, 2000, **16**(4), 2019–2023.

[35] Y. X. Chen, S. Ye, M. Heinen, Z. Jusys, M. Osawa, and R. J. Behm, *Journal of Physical Chemistry B*, 2006, **110**, 9534–9544.

[36] M. Heinen, Y. X. Chen, Z. Jusys, and R. J. Behm, *Electrochimica Acta*, 2007, **52**, 5634–5643.

[37] M. Heinen, Y. X. Chen, Z. Jusys, and R. J. Behm, *Electrochimica Acta*, 2007, **53**, 1279–1289.

[38] K. Kunimatsu, H. Hanawa, H. Uchida, and M. Watanabe, *Journal of Electroanalytical Chemistry*, 2009, **632**, 1090–119.

[39] S. X. Liu, L. W. Liao, Q. Tao, Y. X. Chen, and S. Ye, *Physical Chemistry Chemical Physics*, 2011, **13**, 9725–9735.

[40] T. Iwasita, *Electrochimica Acta*, 2002, **3663-3674**.

[41] J. L. Cohen, D. J. Volpe, and H. D. Abruna, *Physical Chemistry Chemical Physics*, 2007, **9**, 49–77.

[42] M. Kubler, T. Jurzinsky, D. Ziegenbalg, and C. Cremers, *Journal of Power Sources*, 2017, **375**, 320–334.

[43] M. Osada, M. Watanabe, K. Sue, T. Adschiri, and K. Arai, *The Journal of Supercritical Fluids*, 2004, **28**, 219–224.

[44] A. V. Tripkovic, K. D. Popovic, B. N. Grgur, B. Blizanac, P. N. Ross, and N. M. Markovic, *Electrochimica Acta*, 2002, **47**, 3707–3714.

[45] R. L. Sobocinski, M. A. Bryant, and J. E. Pemberton, *Journal of the American Chemical Society*, 1990, **112**, 6177–6183.

[46] Y. Zhang and M. J. Weaver, *Langmuir*, 1993, **9**, 1397–1403.

[47] G. J. Millar, J. B. Metson, G. A. Bowmaker, and R. P. Cooney, *Journal of the Chemical Society Faraday Transactions*, 1995, **91**, 4149–4159.

[48] B. Ren, X. Q. Li, C. X. She, D. Y. Wu, and Z. Q. Tian, *Electrochimica Acta*, 2000, **46**, 193–205.

[49] R. F. B. D. Souza, E. T. Neto, M. L. Calegaro, E. A. Santos, H. S. Martinho, and M. C. dos Santos, *Electrocatalysis*, 2011, **2**, 28–34.

[50] M. Y.Kwon, *Anal. Chem.*, 2010, **82**, 5420–5424.

[51] S. S. G. S. E.V. Fanavoll, D.A. Harrington and F. Seland, *Electrochimica Acta*, 2016, **225**, 69–77.

[52] D. D. Wagman, W. H. Evans, V. B. Parker, R. H. Schumm, I. Halow, S. M. Bailey, K. L. Churney, and R. L. Nuttall, The NBS Tables of Chemical Thermodynamic Properties, 1982.

[53] M. D. Tissandier, K. A. Cowen, W. Y. Feng, E. Gundlach, M. H. Cohen, A. D. Earhart, J. V. Coe, and T. R. Tuttle, *Journal of Physical Chemistry A*, 1998, **102**(40), 7787–7794.

[54] V. Rao, C. Cremers, U. Stimming, L. Cao, S. Sun, S. Yan, G. Sun, and Q. Xin, *Journal of The Electrochemical Society*, 2007, **154**(11), B1138–B1147.

[55] Z. Jusys, J. Kaiser, and R. J. Behm, *Langmuir*, 2003, **19**(17), 6759–6769.

[56] R. M. L. M. Sandrini, J. R. Sempionatto, E. Herrero, J. M. Feliu, J. Souza-Garcia, and C. A. Angelucci, *Electrochemistry Communications*, 2018, **86**(November 2017), 149–152.

[57] A. C. Garcia, E. B. Ferreira, V. V. Silva de Barros, J. J. Linares, and G. Tremiliosi-Filho, *Journal of Electroanalytical Chemistry*, 2017, **793**, 188–196.

[58] R. S. Ferreira, M. Janete Giz, and G. A. Camara, *Journal of Electroanalytical Chemistry*, 2013, **697**, 15–20.

[59] Y. Holade, C. Morais, K. Servat, T. W. Napporn, and K. B. Kokoh, *ACS Catalysis*, 2013, **3**(10), 2403–2411.

A Supporting Information

The datapoints and error bars of Figure 3.5 were calculated using Eq. S1 and S2. The standard deviation (σ_1) of the peak area $S_{t,i}$ is denoted as $\delta S_{t,i}$. The concentration and its uncertainty of the organic species shown in 3.5 (*i.e.* methanol or formate) and denoted as $c_{t,i}$ and $\delta c_{t,i}$. The uncertainties (68% confidence interval) of the slope m_i and intercept b_i derived from the regression lines (as shown in Table 3.1) are denoted as δm_i and δb_i.

$$c_i = \frac{S_{t,i} - b_i}{m_i} \tag{S1}$$

$$\delta c_{t,i} = c_{t,i}\sqrt{\frac{(\delta S_{t,i})^2 + (\delta b_i)^2}{(S_{t,i} - b_i)^2} + (\frac{\delta m_i}{m_i})^2} \tag{S2}$$

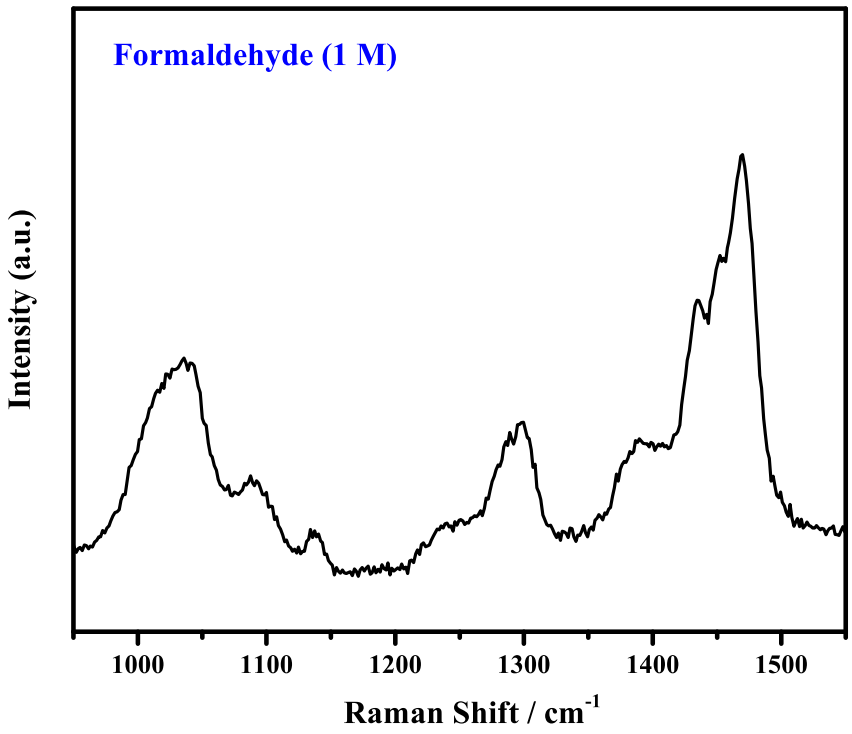

Figure S1: Raman spectrum of 1 M formaldehyde. (Acquisition time: 40 seconds, laser wavelength: 633 nm.)

Table S1: Fitting output of the decrease of methanol concentration with expoenential decay curve

Flow rate / μL min^{-1}	E **vs RHE** / **V**	$\mathbf{y_0}$	A_1	t_1	R^2
	0.70	4.461	0.457	17.900	0.940
5	0.98	4.050	0.819	29.049	0.994
	1.06	3.318	1.565	56.751	0.998
	0.70	4.815	0.294	20.454	0.986
10	0.98	4.360	0.602	39.158	0.982
	1.06	4.345	0.581	13.900	0.970
	0.70	4.866	0.124	7.929	0.949
20	0.98	4.875	0.123	2.548	0.726
	1.06	4.810	0.167	4.904	0.897

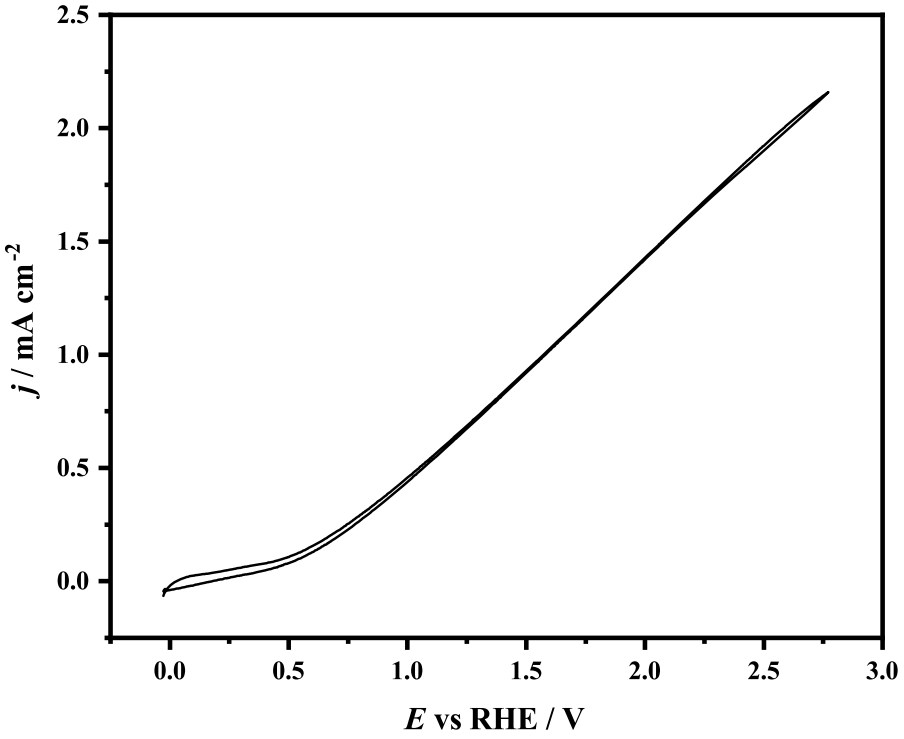

Figure S2: Cyclic voltammogram of methanol electrooxidation in the Raman electrochemistry flow cell (solution: 5 M CH_3OH + 5 M KOH, flow rate: 200 mV s^{-1}). Potentials here are not IR-corrected.

Table S2: Fitting output of the increase of formate concentration with expoenential decay curve

Flow rate / μL min^{-1}	E **vs RHE** / **V**	$\mathbf{y_0}$	A_1	t_1	R^2
	0.70	0.261	-0.208	11.398	0.967
5	0.98	0.398	-0.239	28.797	0.965
	1.06	0.676	-0.579	31.291	0.993
	0.70	0.214	-0.187	16.900	0.913
10	0.98	0.311	-0.263	15.697	0.940
	1.06	0.477	-0.407	12.676	0.960
	0.70	0.179	-0.173	4.248	0.970
20	0.98	0.173	-0.173	2.627	0.987
	1.06	0.305	-0.283	2.804	0.995

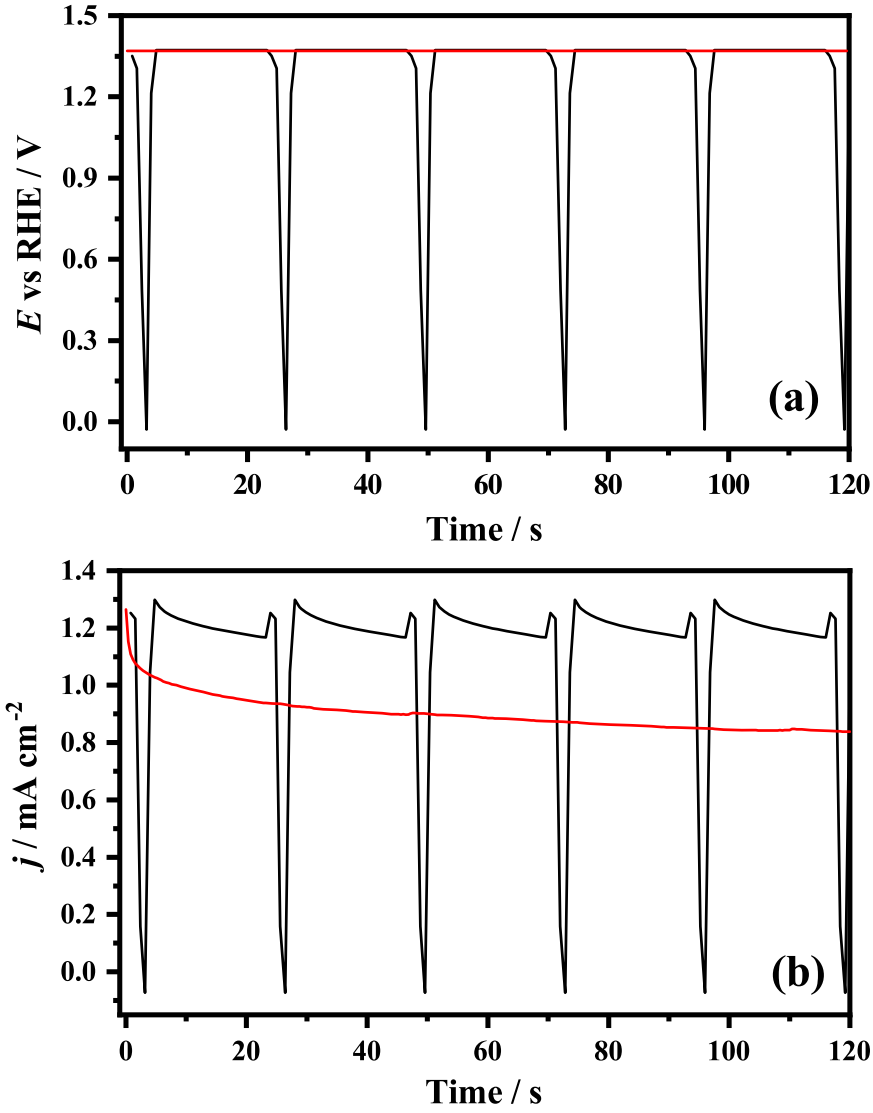

Figure S3: Example of chronoamperometry with short time holding (black) and general chronoamperometry data (red). (a) potential vs time and (b) current vs time during methanol electrooxidation.

Chapter 4

Comparative Studies of the Reactions of Small Alcohol Oxidation with Ni-based Electrocatalysts

Abstract

The cleavage of C-C bonds of polyols like glycerol can lead to more electron transfer and highly oxidized products (*e.g.* CO_2). Nickel, as a metal with natural abundance and decent catalytic activity, has the potential to be developed into a low-cost electrocatalyst for direct alcohol fuel cells (DAFC), which could fully dissociate polyols like glycerol for power generation. However, the mechanism for this bond dissociation has not yet been fully elucidated. This work presents a comparative study of ten different alcohols (methanol, ethanol, ethylene glycol, 1-propanol, 2-propanol, 1,2-propanediol, 1,3-propanediol, glycerol, 2-butanol and 1,4-butanediol) using cyclic voltammetry, potentiostatic electrochemical impedance spectroscopy and online Ra-

man spectroscopy, aiming at revealing how the reactivity and reaction pathway of an alcohol are subjected to its molecular structure, by showing the similarity and difference between their oxidation processes and product distributions. The results show that having hydroxyl groups on adjacent carbon atoms leads to the dissociation of alcohols through the production of carboxylate (*e.g.* formate for ethylene glycol oxidation).

4.1 Introduction

As a growing economy demands massive production of energy, the oxidation of small alcohols has been proved as a way to resolve the energy crisis by providing a more sustainable and green energy. Direct alcohol fuel cells (DAFCs) are being developed to industrialize this chemical process. Nickel (Ni), a transition metal with high natural abundance and high catalytic activity, is quickly becoming a research hotspot in the area of DAFCs [1, 2]. Currently, Ni is very commonly used as a co-catalyst to improve the catalytic efficiency of platinum (Pt), palladium (Pd), and gold (Au) by mitigating the poisoning effect during alcohol oxidation, exemplified by Pt-Ni nanoparticles [3], Pd-Ni nanorods [4], Pd-Ni nanoparticles [5,6], and Ni-Au foams [7]. Recently, the performance of Ni alone as an electrocatalyst for alcohol oxidation is being investigated by researchers worldwide to further lower the cost of fuel cells [8–13].

So far, the fuels for most of the reported DAFCs are methanol [4, 14, 15] and ethanol [16–19], because of their high energy density output, being 6.09 kWh $kg^{-1}$and 8.00 kWh kg^{-1}, respectively [20]. For different reasons such as lower toxicity, mono-alcohols with longer chains and more complicated structures, such as 1-propanol [5, 21], 2-propanol [2, 22], 1-butanol [8], 2-butanol [3], propargyl alcohol [23] and cyclohexanol [24,25] are also used. Glycerol, a common byproduct of biodiesel, which can be massively produced from the transesterification of triglycerides with alcohols, has received increasing research interest due to its reproducibility, low toxicity and volatility, high energy density (6.26 kWh L^{-1} [26]) and potential to be oxidized into many kinds of value-added chemicals [1, 27].

With Ni catalysts, the dissociation of the C-C bonds of glycerol is observed [26, 28–30], whereas acetate is reportedly to be the major product of ethanol fuel cells [10, 20, 27]. To theoretically explain these observations, a reaction mechanism proposed by Fleischmann et al [31,32] in the 1970s (Eq. (4.1) and Eq. (4.2)) has been

widely adopted. As shown in these equations, a surface layer of β-NiOOH from the electrooxidation of β-$Ni(OH)_2$ is believed to be the reactive species that facilitates the deprotonation and oxidation of hydroxyl groups. In constrast, there is much less progress in elucidating the reaction mechanism of C-C bond cleavage of polyols like glycerol.

$$\beta\text{-NiOOH} + R - CH_2OH + OH^- \rightarrow \beta\text{-Ni(OH)}_2 + H_2O + R - CHO + e^- \quad (4.1)$$

$$R - CHO + 3OH^- \rightarrow R - COO^- + 2H_2O + 2e^- \quad (4.2)$$

Apart from kinetic studies attempting to reveal the rate constants of alcohol oxidations [2,14,33,34], relatively few comparative studies of different alcohols have been conducted to show the effect of different molecular structures on the reactivity and reaction pathways. Bott-Neto et al. [27] compared the oxidation products of methanol, ethanol and glycerol with poly[Ni(*salen*)] films, and found the production of carboxylates at low overpotentials and conversion towards carbonate for all three alcohols at high overpotentials. Research conducted by Jafarian et al. [2] using nickel-modified graphite electrodes compared the onset potentials and products of methanol, ethanol, 1-propanol and 2-propanol, and concluded that reactivity of short-chain alcohols (*e.g.* methanol) is higher than longer-chain alcohols (*e.g.* 1-propanol). Also, Vijayabarathi et al. [35] presented a cyclic voltammetry study using a nickel hydroxide electrode involving eleven aromatic and aliphatic alcohols. However, it is still very rare to see work that measures the electrooxidation of both mono-alcohols and polyols to find out how the position of hydroxyl groups on carbon atoms affects the reaction pathway.

This work presents a comparative study in strong base of ten different alcohols (*i.e.,* methanol, ethanol, ethylene glycol, 1-propanol, 2-propanol, 1,2-propanediol, 1,3-propanediol, glycerol, 2-butanol and 1,4-butanediol). These were oxidized at an electrode made with electrodeposited Ni on carbon paper, which is similar to the

electrode used by Lee et al. [8]. Reactivity was estimated by cyclic voltammetry, and electrochemical impedance spectroscopy was used to measure the adsorbed species and poisoning effects during the oxidation of these alcohols. Moreover, online Raman spectroscopy was used for product identification in real time, which used a microfluidic flow device to facilitate the capture of spectra (a modified version of the device described in the previous chapter). This technique replaced the more traditional online IR spectroscopy, as water is a weak Raman scatterer that does not inhibit the monitoring of alcohol conversion.

4.2 Experimental

4.2.1 Chemicals and Materials

Nickel sulfate ($NiSO_4$, Matheson-Coleman & Bell), nickel chloride ($NiCl_2$, BDH Chemicals Ltd.), and boric acid (H_3BO_3, Bio Basic Canada Inc.) were used to make Ni electroplating solution, *i.e.*, a Watt's Bath without organic additives [36]. Methanol (99.9%, Fisher Chemical), ethanol (95%, Commerical Alcohols), 1-propanol (reagent grade, Bio Basic Canada Inc.), 2-propanol (99.5%, VWR Analytical), ethylene glycol (99%, VWR Analytical), 1,2-propanediol (99.5%, Sigma-Aldrich), 1,3-propanediol (98%, Sigma-Aldrich), glycerol (99.5%, Anachemia), 2-butanol (99%, Sigma-Aldrich), and 1,4-butanediol (99%, Sigma-Aldrich) were used to make alcohol solutions for electrochemistry studies (0.5 M alcohol + 5 M KOH). Solutions with 5 M KOH and 0.5 M different alcohols (*i.e.* methanol, ethanol, 1-propanol, ethylene glycol, 1,2-propanediol and glycerol) were made for online Raman spectroscopic studies. All solutions are purged with N_2 for 20 minutes before measurements.

Toray paper 090 (10 cm $\times$ 10 cm $\times$ 280 μm), used as the carbon support for electrodeposition of Ni, was purchased from Fuel Cell Store. The porosity ($\frac{V_{\text{fiber}}}{V_{\text{bulk}}}$) of Toray paper 090 and the thickness of the carbon fibers (D_{fiber}) are estimated to be

78% and 8 μm, as reported by the supplier. The bulk density of Toray paper (ρ_{bulk}) is 0.44 g cm^{-3}, therefore the density of carbon fiber (ρ_{fiber}) is calculated to be 2.0 g cm^{-3}, with Eq. (4.3). The total length of carbon fiber (L_{fiber}) in a unit volume of carbon paper can be calculated from the fiber thickness and V_{fiber} (Eq. (4.4)), which is further used to calculate the specific surface area (S_{fiber}) by Eq. (4.5). For every square centimeter of Toray paper 090, the specific surface area is calculated to be 29.9 cm^2.

$$\rho_{\text{bulk}} \times V_{\text{bulk}} = \rho_{\text{fiber}} \times V_{\text{fiber}} \tag{4.3}$$

$$V_{\text{fiber}} = L_{\text{fiber}} \times \frac{\pi D_{\text{fiber}}^2}{4} \tag{4.4}$$

$$S_{\text{fiber}} = L_{\text{fiber}} \times \pi D_{\text{fiber}} \tag{4.5}$$

The Toray paper was cut into pieces (1 cm $\times$ 5 cm per piece) using a ceramic knife. One end of each piece (an area about 1 cm $\times$ 1 cm) was flamed to remove the PTFE protective coating before electrodepositing Ni at approximately 65 °C. The current density for electrodeposition was 3.35 mA cm^{-2}, and therefore the charge transferred and catalyst loading were 1.00 C cm^{-2} and 9.1 mg cm^{-2}, respectively. As only 4.8% of the pores are filled with Ni, therefore S_{fiber} is used for normalizing the current, charge and impedances given below. Eight pieces of 1 cm $\times$ 1 cm Ni-on-Carbon paper (NiCP) electrodes prepared this way were used to study the alcohol oxidation in the microfluidic flow cell monitored by online Raman spectroscopy.

4.2.2 Measurements

All electrochemistry experiments used NiCP working electrodes, a mercury mercury oxide (Hg|HgO, in 20% KOH) reference electrode (0.93 V vs RHE) and a Pt wire counter electrode. All potentials measured versus Hg|HgO were converted to RHE. A Gamry Reference 600 potentiostat was used for all electrochemical measurements. In a conventional electrochemical cell, one NiCP electrode was used for cyclic voltamme-

try (CV), and potentiostatic electrochemical impedance spectroscopy (EIS) studies, after cycling 500 times from -0.05 V to 1.6 V in 5 M KOH solution to stabilize the amount of β-$Ni(OH)_2$ on the electrode surface. The frequency range for the EIS studies was from 100 kHz to 0.1 Hz, with 10 frequencies tested per decade. The obtained impedance data was fitted by complex nonlinear least squares as implemented in a publicly available Maple program [37]. The "magnitude experimental" weighting scheme was used and the quality of the fits was determined by the Akaike Information Criterion (AIC) [38]. For impedance data forming two semicircles in the Nyquist plots, the RQRCR (called "QC model" in this chapter) or RQRQR models (called "QQ model" in this chapter) were chosen. These circuits allow for inductive behaviour by fitting with negative R_{ads} and negative C_{ads} or Q_{ads}. The circuit of RQR is denoted as "Q model" and was used for fitting data sets with only one semicircle. The three equivalent circuits are shown in Figure 4.1. The assignment of fitting models is listed in Table S1. Fitting results are plotted in Figure S1-S4, with error bars indicating the standard deviation (σ_1) of $R_{\text{ct\_eff}}$, $C_{\text{dl\_eff}}$, $R_{\text{ads\_eff}}$, and $C_{\text{ads\_eff}}$. The percent errors of EIS fits are shown in Figure S5. CV and EIS measurements were done repetitively for three times, and the results were validated by their consistency.

The microfluidic flow cell for online Raman measurements is shown in Figure 4.2, which was based on the microfluidic flow cell reported in Chapter 3. The thickness and width of the channel are 2 mm and 1 mm to accommodate the NiCP electrodes. A PTFE tube (1 mm O.D.) connected to Harvard PHD 2000 syringe pump with preset flow rate was placed at one end of the channel. As the pump was set to work in withdrawing mode, the fluid enters the cell from the reversoir (1 cm wide) and exits through the PTFE tube. All edges of the device were sealed by Epoxy. A confocal Raman spectrometer (Renishaw InVia Raman Microscope) was used with a Nd:YAG laser (532 nm), and a Renishaw (horizontal) camera for detection. Prior to each experiment, the Raman spectrometer was calibrated with a Si wafer to ensure similar conditions. A 50 times magnification lens for long working distances (Olympus IC50,

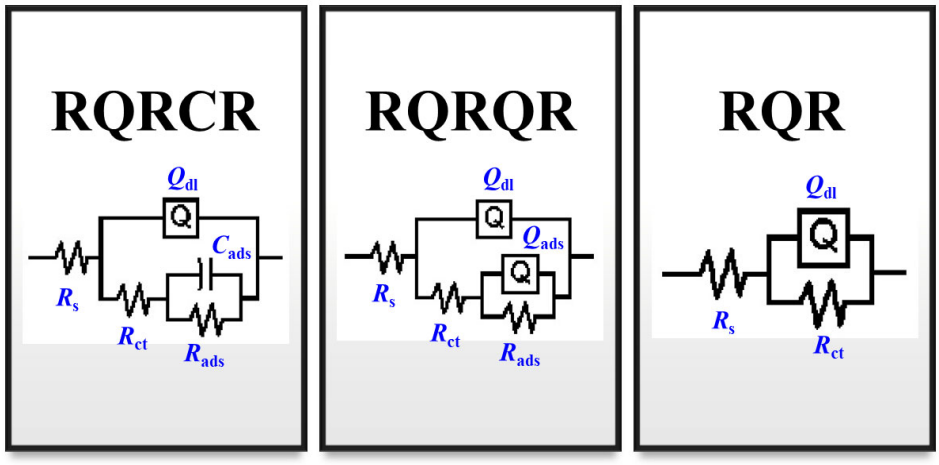

Figure 4.1: Equivalent circuits used for the fitting EIS data. Q denotes a constant phase element (CPE).

N.A.=0.55, laser power = 50 mW, and laser power density = 3.2 W μm^{-3}) focused the laser beam at the center of the channel (8 mm downstream of the edge of WE), and the height of the sample stage was adjusted until the S/N ratio was optimized. Each spectrum was collected for a total of 200 s in static mode from 630 cm^{-1} to 1800 cm^{-1}. As a high impedance induced by the channel can drift the overpotential, readings of the potentials for oxidation are corrected with the current and measured solution impedance (around 2 ohms). This device was resistive to 5 M KOH and 0.5 M alcohols over the duration of the experiment.

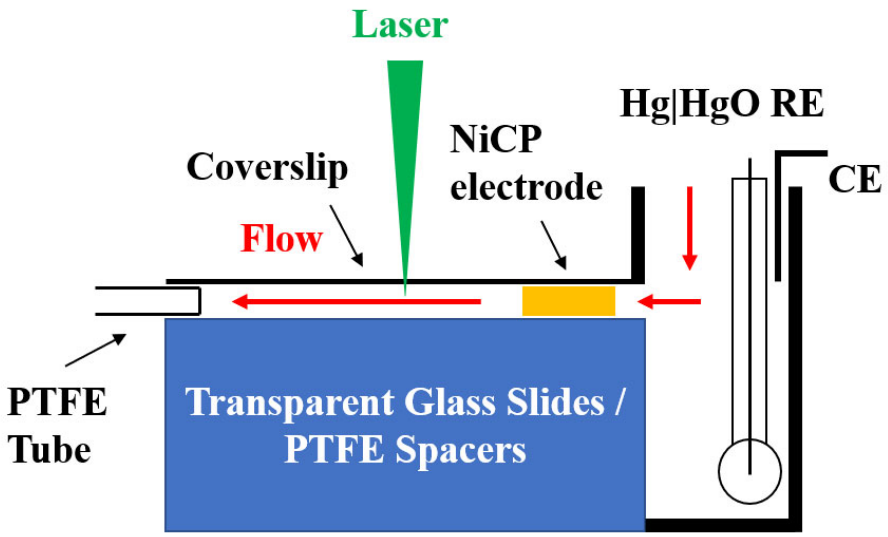

Figure 4.2: The Raman electrochemistry flow cell (not to scale). Liquid enters through the reservoir (on the right) and flows to the left (as indicated by the red arrow), exiting through the Teflon tube (1 mm O.D.). The thickness and width of the channel are 2 mm and 10 mm. The length and width of the working electrode are 1 cm and 1 cm. Laser was focused at 8 mm downstream of the electrode. A 1 cm wide glass reservoir was connected to the channel, accommodating a Hg|HgO reference electrode and a Pt wire counter electrode.

4.3 Results

4.3.1 Cyclic Voltammetry Studies of Small Alcohols with Ni-based Electrocatalyst

Figure 4.3 shows the cyclic voltammograms of NiCP in 5 M KOH without and with 0.5 M methanol. As displayed in Figure 4.3a (the first cycle), Ni is first electrochemically oxidized into α-$Ni(OH)_2$ (Eq. (4.6)), which is later converted to β-$Ni(OH)_2$ (Eq. (4.7)). Above 1.25-1.35 V, β-$Ni(OH)_2$ was completely and electrochemically oxidized into β-NiOOH (Eq. (4.8)). In the absence of alcohol, β-NiOOH is electroreduced back to β-$Ni(OH)_2$ during the cathodic scan. The ratio of the peak area of β-NiOOH formation to its reduction is 1.15, indicating that oxygen evolution reaction (OER) is involved in the anodic scan.

$$Ni + 2OH^- \rightarrow \alpha - Ni(OH)_2 + 2e^- \tag{4.6}$$

$$\alpha - Ni(OH)_2 \rightarrow \beta - Ni(OH)_2 \tag{4.7}$$

$$\beta - Ni(OH)_2 + OH^- \rightarrow \beta - NiOOH + H_2O + e^- \tag{4.8}$$

$$\beta - NiOOH + H_2O + e^- \rightarrow \beta - Ni(OH)_2 + OH^- \tag{4.9}$$

With the presence of alcohol, as exemplified by methanol in Figure 4.3b, β-NiOOH catalyzes the electrooxidation of alcohols into aldehyde (then to carboxylate in alkaline conditions), while reducing itself to β-$Ni(OH)_2$, as proposed by Fleischmann in Eqs. (4.1) and (4.2) [31, 32]. This electrocatalytic process consumes a portion of the β-NiOOH, therefore the cathodic peak indicating the reduction charge of the rest of the β-NiOOH is smaller. From Figure 4.3b to Figure 4.7, the cyclic voltammograms showing the oxidation of ten different alcohols are displayed. The amount of unconsumed β-NiOOH was estimated by integrating the cathodic peak (the reduction of

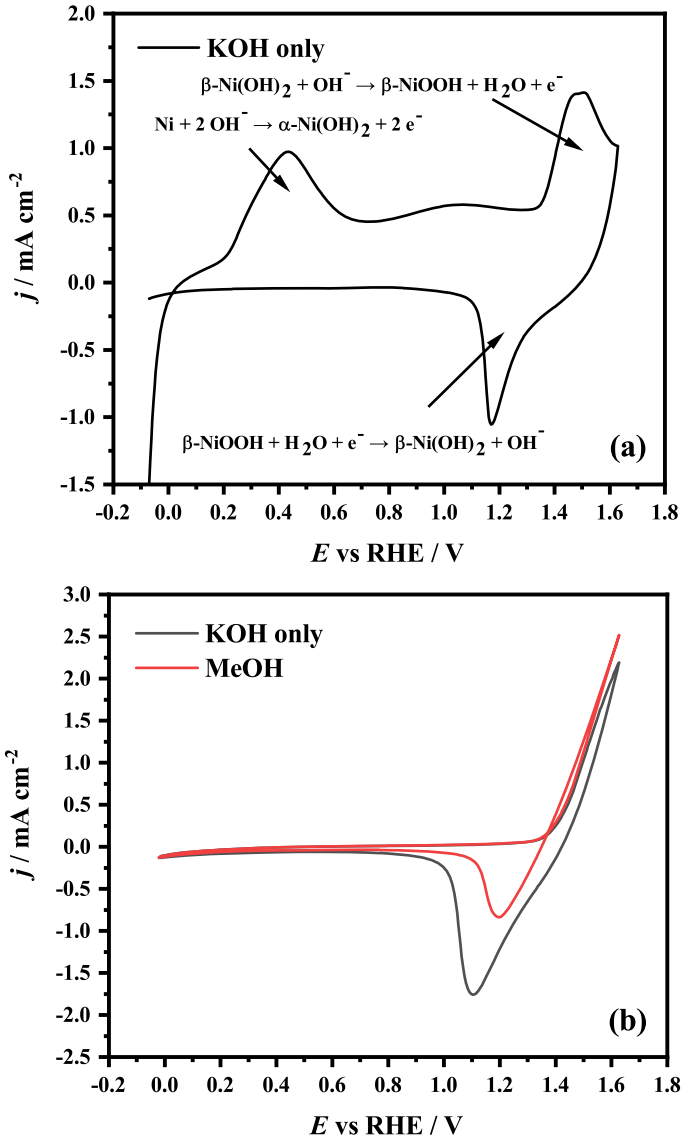

Figure 4.3: Cyclic voltammograms of electrodeposited Ni on Toray paper 090 in 5 M KOH. (a) KOH only (first cycle) and (b) KOH only (black curve, after 500 cycles in 5 M KOH) and with 0.5 M methanol (red curve). Sweep rate: 200 mV s^{-1}.

β-NiOOH), which is illustrated in Figure 4.8(a). The integrated cathodic peak area for β-NiOOH in 5 M KOH without alcohol oxidation was estimated to be around 1.81 mC cm^{-2}. For ethanol and 1-propanol, the charges were 0.59 mC cm^{-2} and 0.60 mC cm^{-2}, respectively (see Figure 4.4), less than that of methanol (0.78 mC cm^{-2}). Secondary alcohols (displayed in Figure 4.5) were the least electrochemically reactive alcohols with β-NiOOH, in which case the charges are 1.08 mC cm^{-2} for 2-propanol and 1.54 mC cm^{-2} for 2-butanol. A charge density of 0.04 mC cm^{-2} of β-NiOOH reduction was found for the case of glycerol oxidation, while the charges in the cases of 1,2-propanediol and ethylene glycol were close to 0.10 mC cm^{-2} (see Figure 4.6). Oxidation of 1,3-propanediol consumed less β-NiOOH than 1,2-propanediol, which shows the transferred charge to be 0.31 mC cm^{-2}. A similar peak area of 0.41 mC cm^{-2} was obtained from the oxidation of 1,4-butanediol (Figure 4.7).

The onset potential for the oxidation of each alcohol is revealed in Figure 4.8b by differentiating the anodic voltammetry current with respect to potential. In the absence of alcohol, β-NiOOH formation starts from 1.30 V, as can be seen from the curve of KOH only, which matches the oxidation curves of seven alcohols with only one hydroxyl group, or with two hydroxyl groups not on neighboring carbon atoms. By constrast, it can be clearly seen that the glycerol electrooxidation catalyzed by NiCP started from 1.20 V, which is the lowest among all alcohols. Ethylene glycol and 1,2-propanediol share a very similar onset potential for the electrooxidation, which is approximately 1.25 V. It is very interesting that all these three alcohols show a lower onset potential than the formation of β-NiOOH in 5 M KOH without alcohol.

4.3.2 Raman Spectroscopy Studies of Small Alcohols with Ni-based Electrocatalysts

Online Raman Spectroscopy was used to monitor the reaction processes by showing the characteristic peaks of alcohols and their oxidation products. The electrooxidation

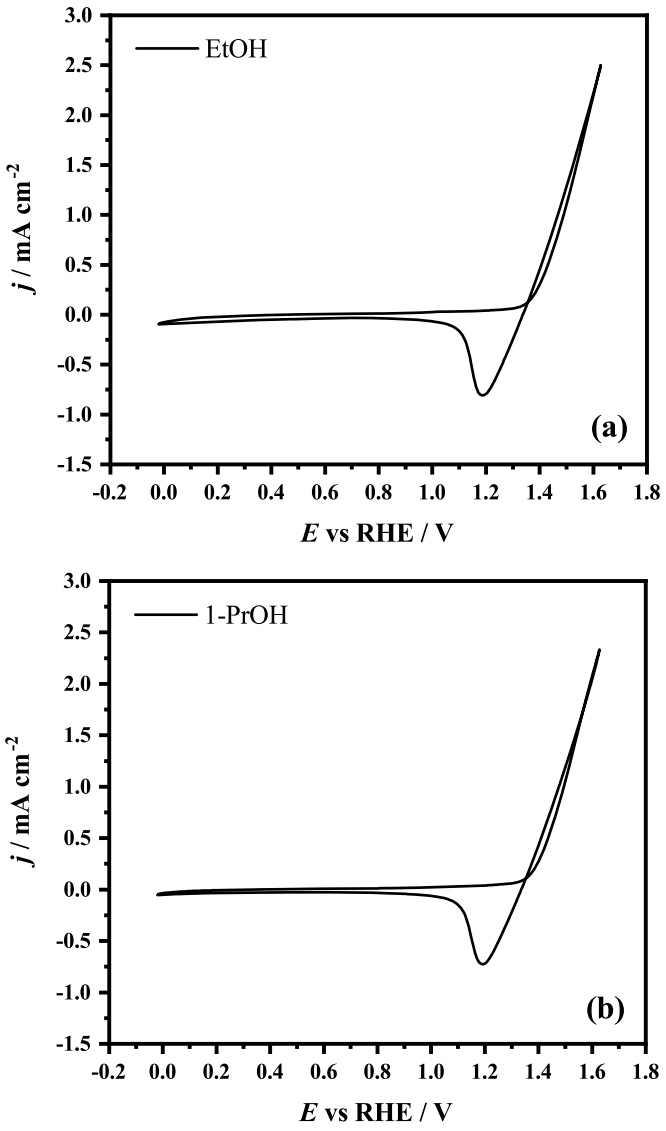

Figure 4.4: Cyclic voltammograms of electrodeposited Ni on Toray paper 090 in 5 M KOH. (a) with 0.5 M ethanol and (b) with 0.5 M 1-propanol. Sweep rate: 200 mV s^{-1}.

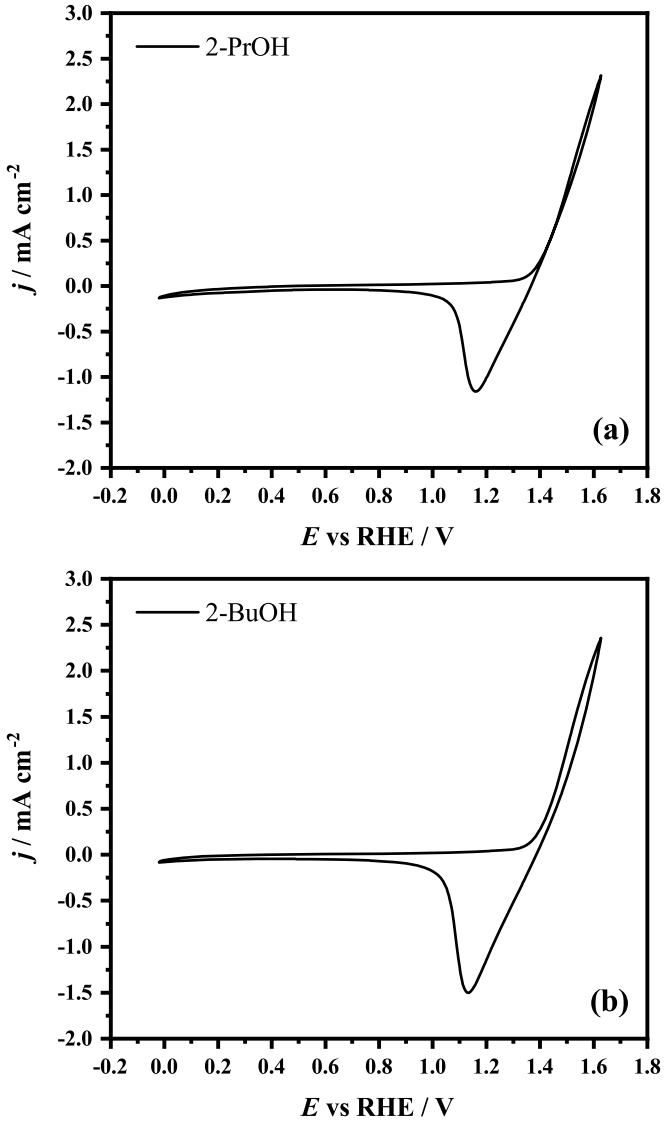

Figure 4.5: Cyclic voltammograms of electrodeposited Ni on Toray paper 090 in 5 M KOH. (a) with 0.5 M 2-propanol and (b) with 0.5 M 2-butanol. Sweep rate: 200 mV s^{-1}.

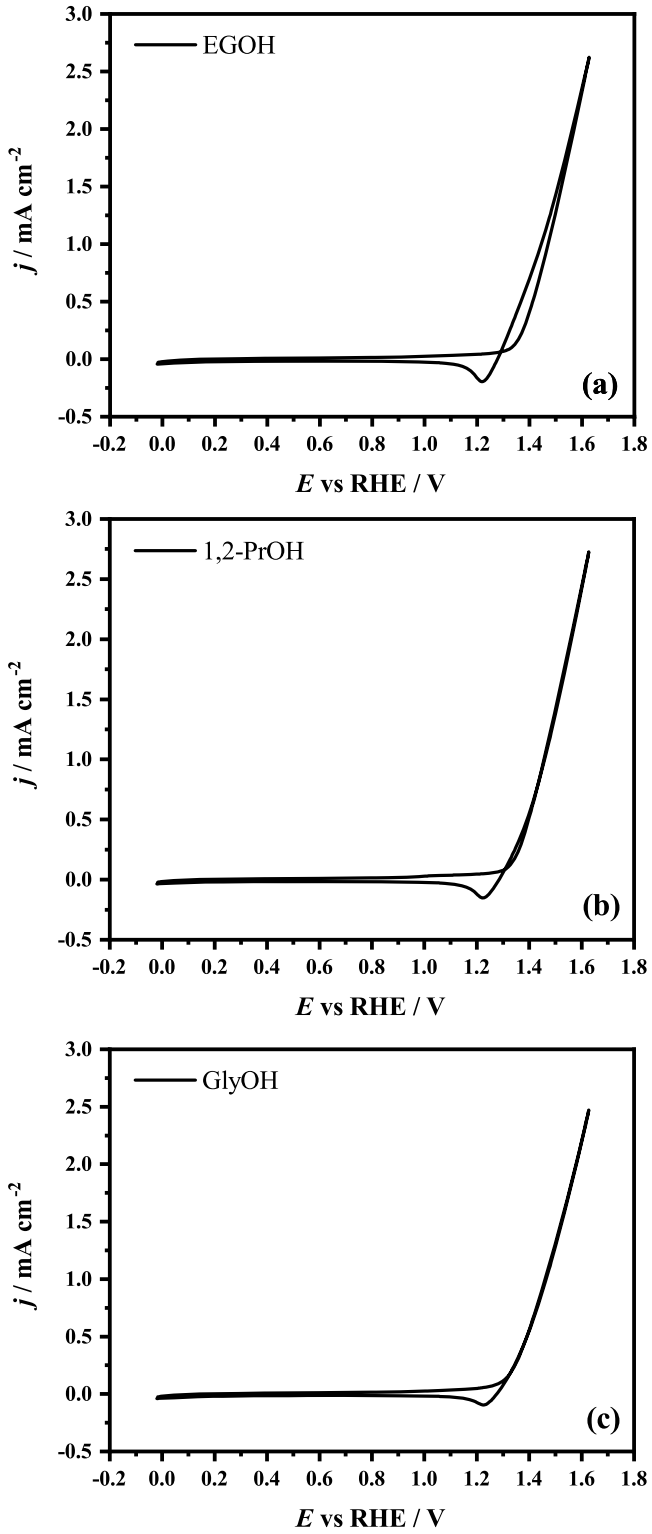

Figure 4.6: Cyclic voltammograms of electrodeposited Ni on Toray paper 090 in 5 M KOH. (a) with 0.5 M ethylene glycol, (b) with 0.5 M 1,2-propanediol and (c) with 0.5 M glycerol. Sweep rate: 200 mV s^{-1}.

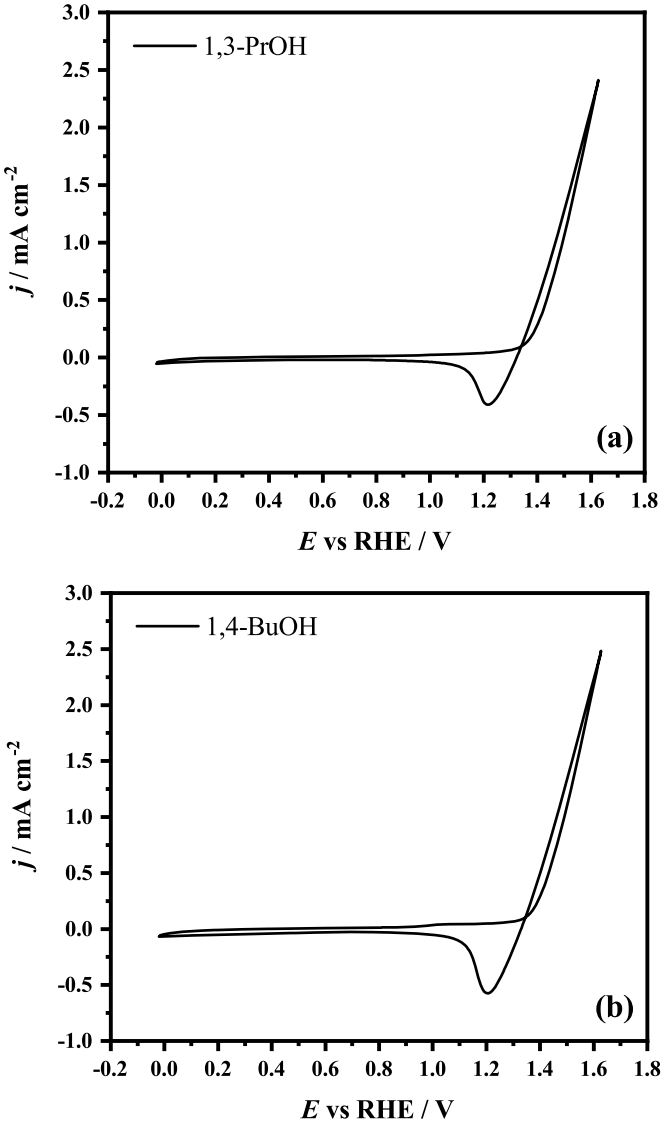

Figure 4.7: Cyclic voltammograms of electrodeposited Ni on Toray paper 090 in 5 M KOH. (a) with 0.5 M 1,3-propanediol and (b) with 0.5 M 1,4-butanediol. Sweep rate: 200 mV s^{-1}.

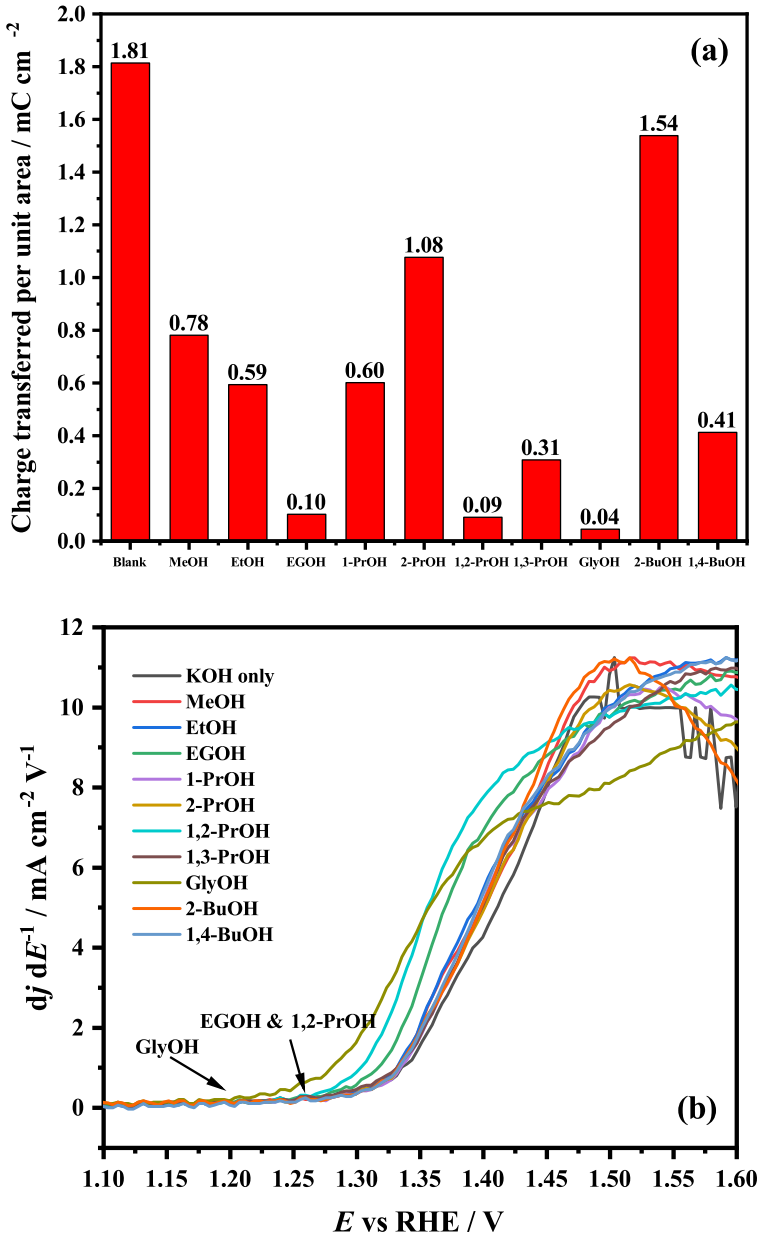

Figure 4.8: Analysis of cyclic voltammograms of alcohol oxidation with NiCP. (a) Bar graph showing the charge per unit area for the reduction of β-NiOOH after the electrooxidation of ten alcohols. (b) Derivative of the current density during the anodic scan of the electrooxidation of ten alcohols. Arrows show the onset potentials.

of six alcohols (methanol, ethylene glycol, 1,2-propanediol, glycerol, ethanol, and 1-propanol) were examined by online Raman spectroscopy, as shown in Figure 4.9.

As can be seen in Figure 4.9a, methanol is electrooxidized to formate (major product) and carbonate (minor). Also, as revealed by Figure 4.9b-d, it is noteworthy that the major oxidation product for ethylene glycol, 1,2-propanediol and glycerol is formate, indicating that the C-C bond dissociation between vicinal hydroxyl groups is the major oxidation pathway. However, for primary alcohols like ethanol (Figure 4.9e), acetate is the major electrooxidation product, with no formate produced. Similarly, the electrooxidation of 1-propanol did not produce any formate, which means that the oxidation pathway for primary alcohols are the conversion of hydroxyl groups to carboxylate groups. No detectable amount of oxalate, glycolate, tartronate and mesoxalate was found during the measurements.

As the Raman spectra taken during the electrooxidation of methanol, ethylene glycol, glycerol and ethanol were not affected by fluorescent products, the peak area of alcohols and carboxylates (*i.e.* formate and acetate) were quantified with calibration curves to verify that they are the major oxidation products (Figure S6). Additionally, various overpotentials and flow rates were conducted to the electrooxidation of ethanol (Figure S7), ethylene glycol (Figure S8), and glycerol (Figure S9). No other oxidation product was discovered. Online Raman Spectroscopy was not applied to other 3C and 4C-alcohols due to fluorescence originating from their oxidation products.

4.3.3 Potentiostatic Electrochemical Impedance Spectroscopy (EIS)

Potentiostatic EIS was conducted to study the oxidation of ten different alcohols varying from 1C-alcohol to 4C-alcohol, with NiCP. The steady state current changed by less than 5% during collection of the data, and validity of the results was confirmed by Kramers-Kronig tests.

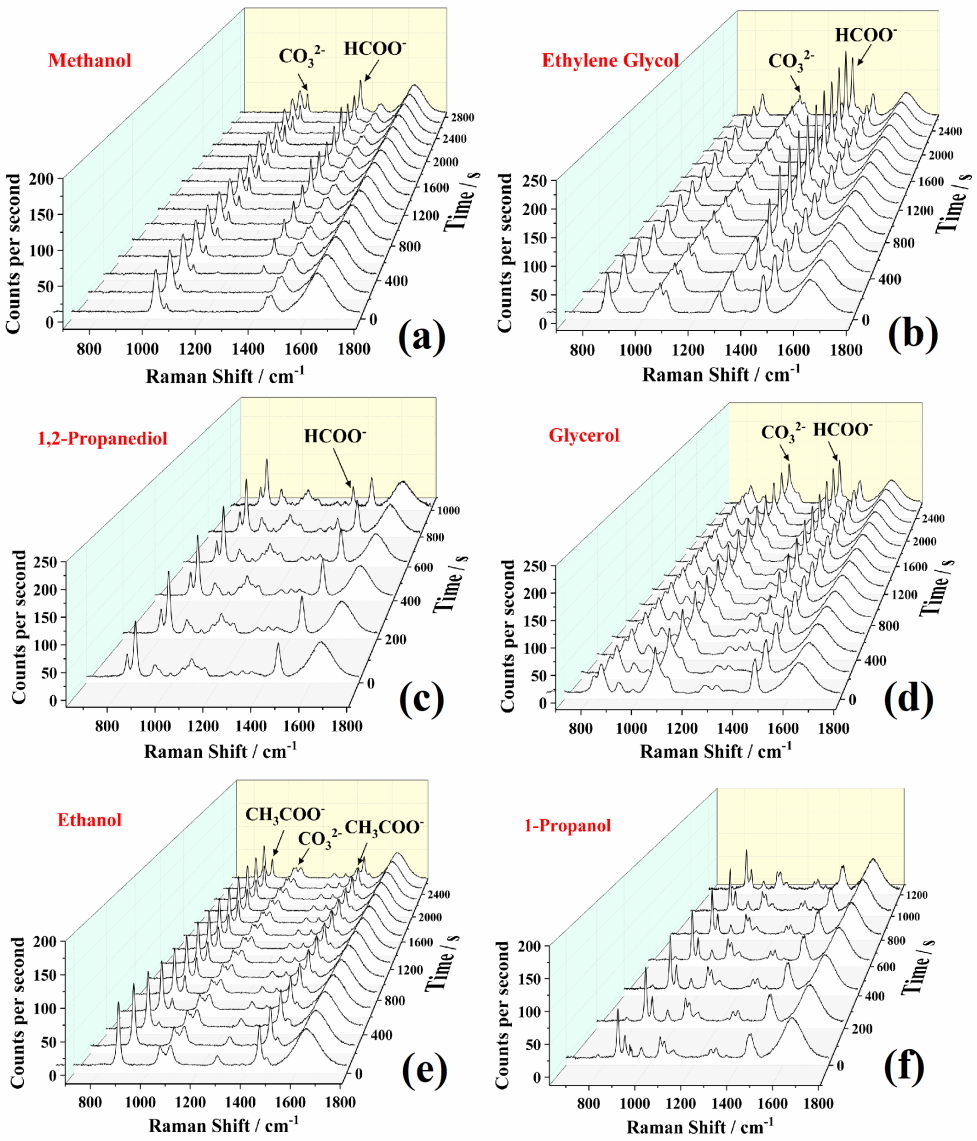

Figure 4.9: Time-dependent Raman spectra showing the electrooxidation of 0.5 M alcohol in 5 M KOH. (a) Methanol, (b) ethylene glycol, (c) 1,2-propanediol, (d) glycerol, (e) ethanol, and (f) 1-propanol. (Baseline subtracted. Flow rate: 50 μL min^{-1})

As shown in Figure 4.10(a-c), two semicircles were found in the potentiostatic EIS measurements (Nyquist plots) for methanol, ethanol and 1-propanol, which consisted of one large semi-circle (called the "first semicircle" in this section) with negative imaginary parts ($Z_{\text{imag}} < 0$), and one small semi-circle (called the "second semicircle" in this section) with positive imaginary parts. The two semi-circles indicate the presence of two processes with different time constants, which are calculated by the product of an effective resistance and an effective capacitance and displayed in Figure 4.11. For the first semicircle, the resistance is the effective charge transfer resistance ($R_{\text{ct\_eff}}$) and the capacitance is the effective double-layer capacitance ($C_{\text{dl\_eff}}$) derived using the Brug equation (Eq. S1) [39]; for the second semicircle, the resistance and capacitance (or inductance) are associated with adsorption. No Warburg element was found in all these spectra, which indicates that solution diffusion is not involved at 0.5 M concentration in the ranges of overpotentials tested, which matches the observation by Simpson et al [33].

One feature that the three alcohols have in common is that the first semicircle shrank (to around 25-30 ohm cm^2) with increasing potential, but expanded at higher overpotentials. As the size of the first semi-circles represents the charge-transfer resistance, the expansion of the first-semicircles means that charge transfer is hindered by a process happening at such overpotentials, which is attributed to poisoning species. The turning points were found to be 1.530 V for methanol, 1.480 V for ethanol and 1.455 V for 1-propanol. For these primary alcohols, the poisoning effect is more severe as the carbon chain length increases.

Also, when the overpotentials go above 1.555 V for ethanol and 1.530 V for 1-propanol, semicircles that go into the second and third quadrants have been found (exemplified by Figure S10). This very uncommon feature was found at onset potentials of OER. As the real part of the impedance is negative at intermediate frequencies but tends towards a positive intercept at zero frequency this indicates a hidden negative differential resistance, and may be associated with some types of inhibition which

is not strong enough to cause the current-potential slope (inverse of zero frequency intercept) to become negative. As OER competes with alcohol oxidation for the available β-NiOOH [33], the current is affected by both the poisoning effect reducing the current (negative resistance) and the OER boosting the current, with the OER dominating.

In constrast, for 2-propanol and 2-butanol, only one semicircle was found in the range of potentials and frequencies tested (see Figure 4.12(a-b)). The expansion of the semicircle was still found, starting from 1.405 V for 2-propanol, and 1.380 V for 2-butanol. However, after the expansion, the semicircles start shrinking above 1.480 V for 2-propanol and 1.455 V for 2-butanol, indicating another reaction (OER) takes place at higher overpotentials. No second semicircle was found for this new electrochemical reaction, suggesting that adsorption did not play a controlling role in the mechanism. As can be seen in Figure 4.13, the time constants of secondary alcohol oxidation is larger than primary alcohols.

The oxidation of vicinal diols and glycerol were examined with potentiostatic EIS as well, as shown in Figure 4.14(a-c). Similar to methanol, ethanol and 1-propanol, one large and one small semicircle are seen for ethylene glycol and 1,2-propanediol. For glycerol, second semicircles with negative Z_{imag} values were found at the potentials below 1.455 V, while positive Z_{imag} values were found at potentials above 1.480 V. One adsorbed species (*i.e.*, two semicircles) (inductive behaviour) is found for the oxidation of the three alcohols with neighboring hydroxyl groups. As the impedance spectra of glycerol were fitted with the QQ model, the effective capacitance of the adsorbed species ($C_{\text{ads\_eff}}$) was derived from Eq. S2. The second time constants are much larger than that of primary alcohols (see Figure 4.15). One major difference between Figure 4.10 and Figure 4.14 is that the first semicircle only shrinks as the potential increases to 1.630 V, *i.e.*, there is very little poisoning effect. Moreover, for different alcohols, the sizes and shapes of the second semicircles are different from each other, implying different kinetics of these adsorbed species. For the adsorbed

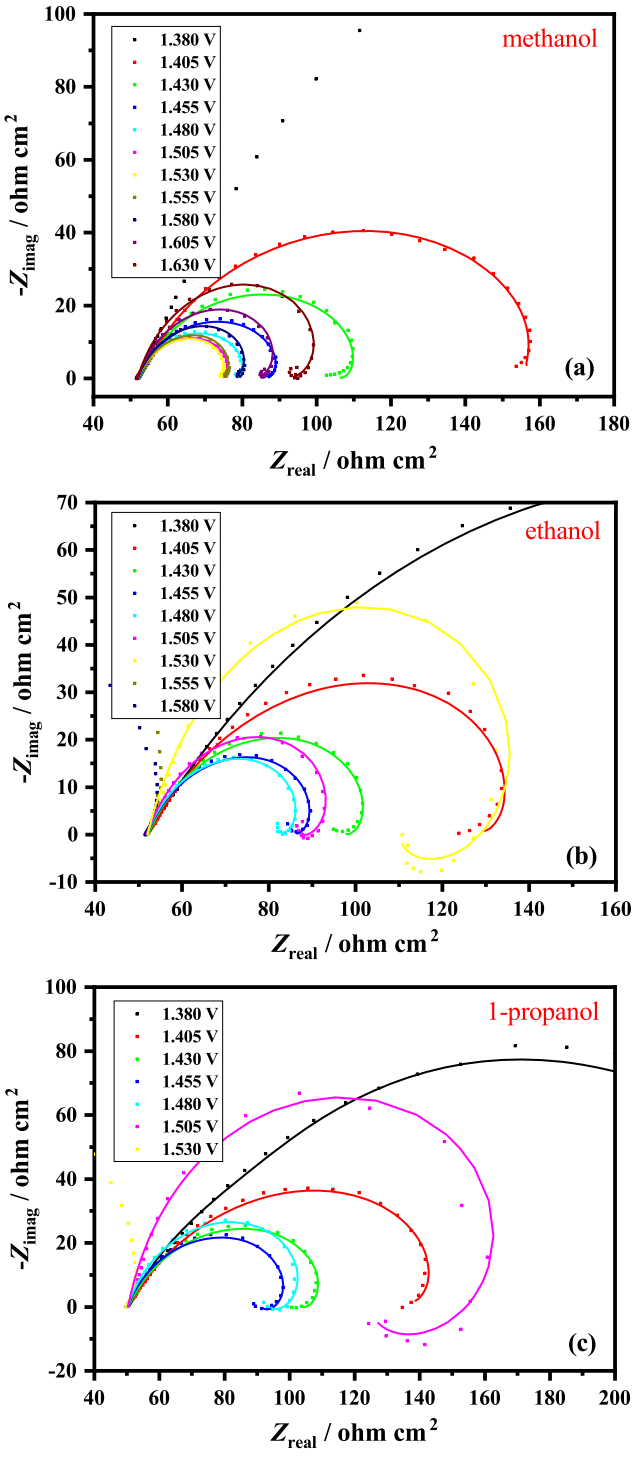

Figure 4.10: Potentiostatic EIS measurements of NiCP oxidizing 0.5 M (a) methanol, (b) ethanol and (c) 1-propanol in 5 M KOH. Solid curves indicate the fitting results.

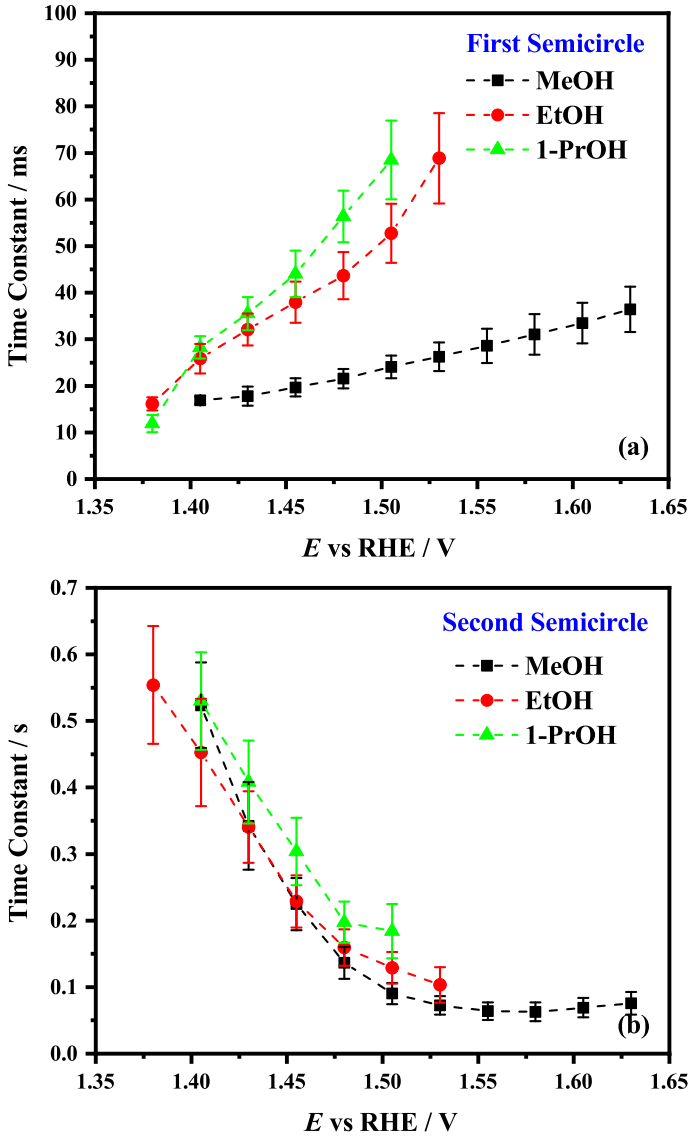

Figure 4.11: Time constants of the two processes during the oxidation of methanol, ethanol and 1-propanol. Error bars are calculated based on the error propagation from the standard deviation (σ_1) of $R_{\mathrm{ct\_eff}}$, $C_{\mathrm{dl\_eff}}$, $R_{\mathrm{ads\_eff}}$, and $C_{\mathrm{ads\_eff}}$.

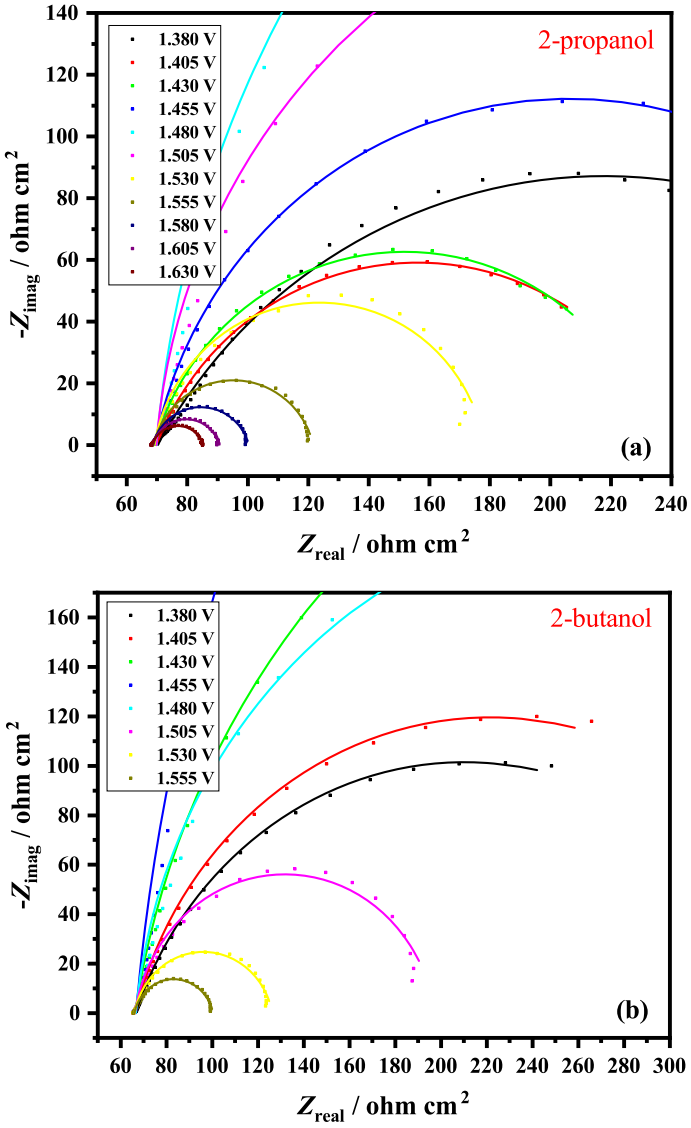

Figure 4.12: Potentiostatic EIS measurements of NiCP oxidizing 0.5 M (a) 2-propanol and (b) 2-butanol in 5 M KOH. Solid curves indicate the fitting results.

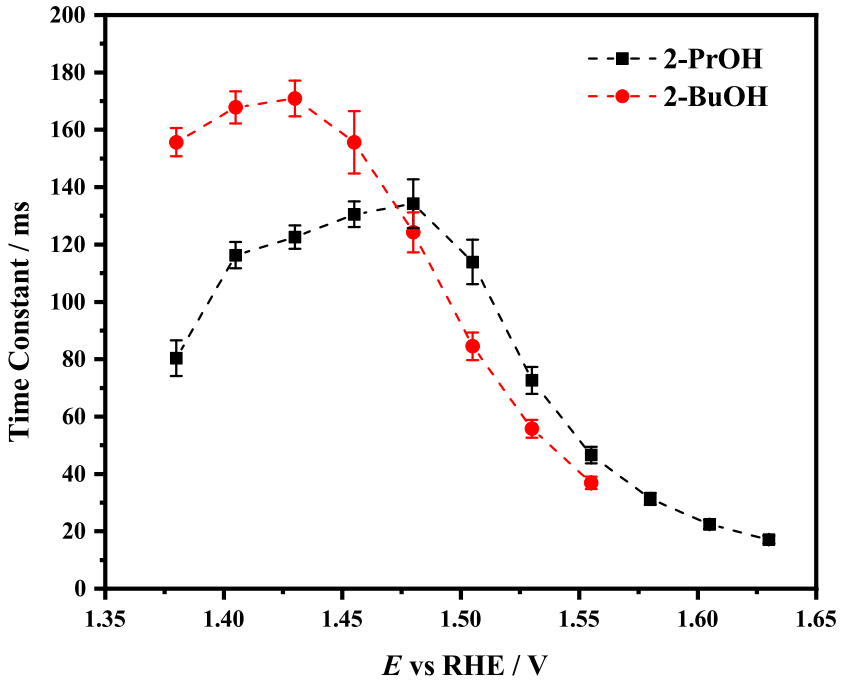

Figure 4.13: Time constants of the process during the oxidation of 2-propanol and 2-butanol. Error bars are calculated based on the error propagation from the standard deviation (σ_1) of $R_{\mathrm{ct\_eff}}$, and $C_{\mathrm{dl\_eff}}$.

Table 4.1: Features of Nyquist Plots for Different Alcohols

	Primary Monoalcohols	**Secondary Monoalcohols**	**Polyols with Vicinal OH Groups**	**Polyols with Two Terminal OH Groups**
Second Semicircle	Yes	No	Yes	Yes
Poisoning Effect	Yes	Yes	No	Yes
Convergence of Curves	No	No	No	Yes

species of glycerol oxidation above 1.530 V, its resistance is much smaller than other vicinal diols at the same overpotential, as represented by a much smaller second semicircle. However, its capacitance is one order of magnitude larger as is consistent with adsorption, and therefore it has the largest time constant.

The Nyquist plots and time constants of 1,3-propanediol and 1,4-butanediol oxidation can be found in Figure 4.16 and 4.17. Similar to primary monoalcohols, one adsorbed species was produced during the oxidation of alcohols, and a strong poisoning effect which expands both the first and second semicircles as the potential increases was identified. One unique feature for these diols with two terminal hydroxyl groups is that all semicircles converged into one point at 0.1 Hz in the range of overpotentials from 1.505 V to 1.630 V. The features presented in this section are summarized in Table 4.1.

4.4 Discussion

4.4.1 Reaction Mechanisms of Different Alcohols

Reaction mechanisms of ten different alcohols catalyzed by NiCP were revealed by CV, online Raman and EIS measurements. For polyols with vicinal hydroxyl groups,

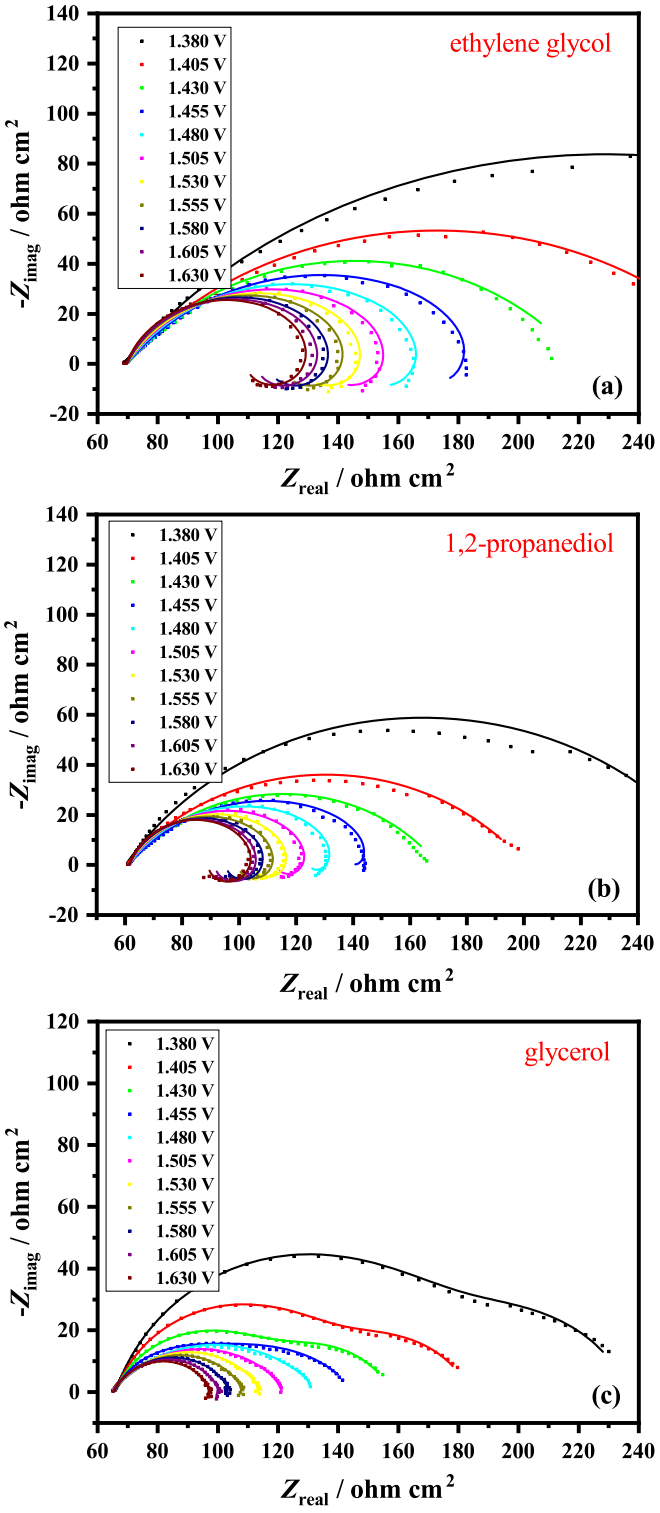

Figure 4.14: Potentiostatic EIS measurements of NiCP oxidizing 0.5 M (a) ethylene glycol, (b) 1,2-propanediol, and (c) glycerol in 5 M KOH. Solid curves indicate the fitting results.

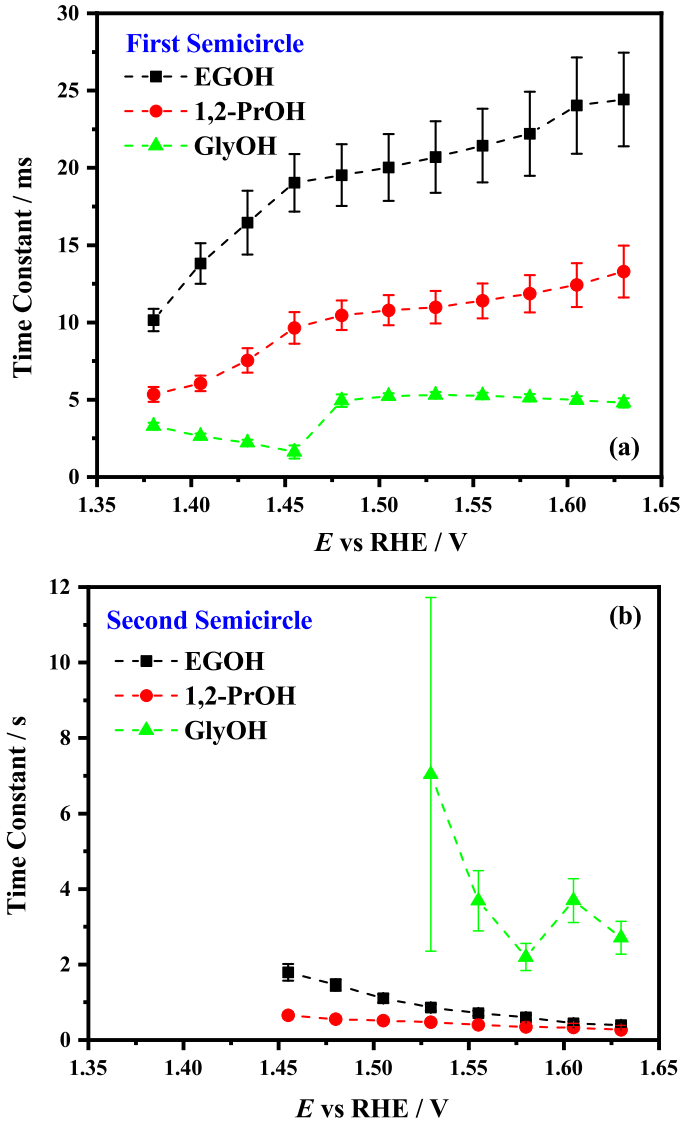

Figure 4.15: Time constants of the two processes during the oxidation of ethylene glycol, 1,2-propanediol and glycerol. Error bars are calculated based on the error propagation from the standard deviation (σ_1) of $R_{\mathrm{ct\_eff}}$, $C_{\mathrm{dl\_eff}}$, $R_{\mathrm{ads\_eff}}$, and $C_{\mathrm{ads\_eff}}$.

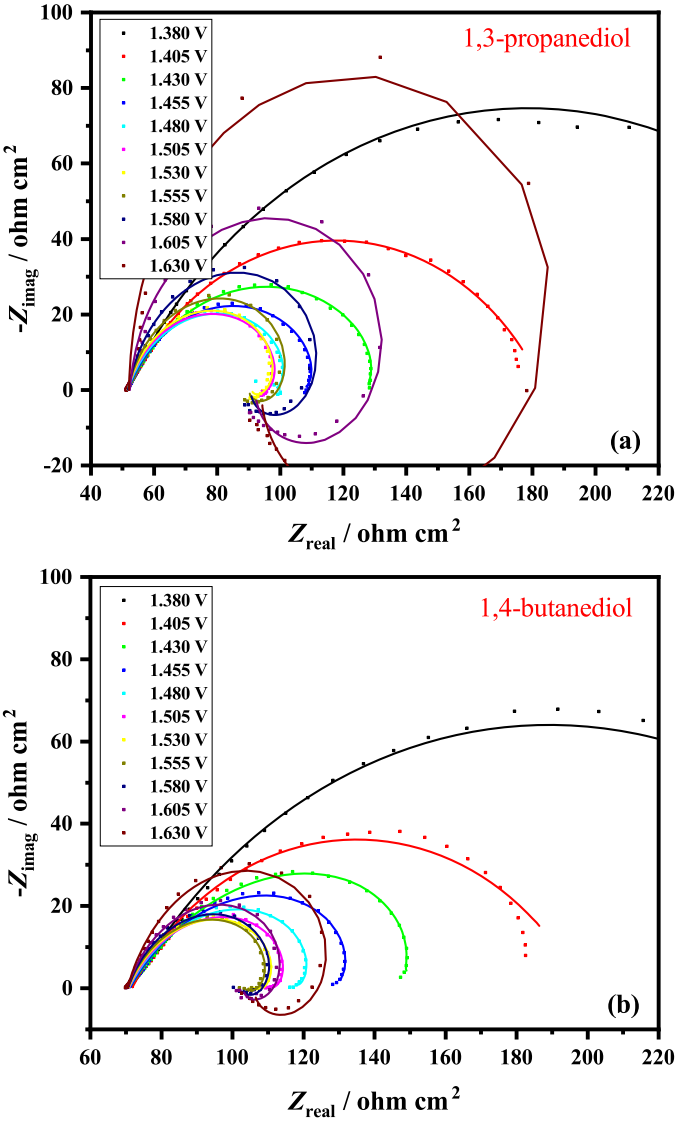

Figure 4.16: Potentiostatic EIS measurements of NiCP oxidizing 0.5 M (a) 1,3-propanediol and (b) 1,4-butanediol in 5 M KOH. Solid curves indicate the fitting results.

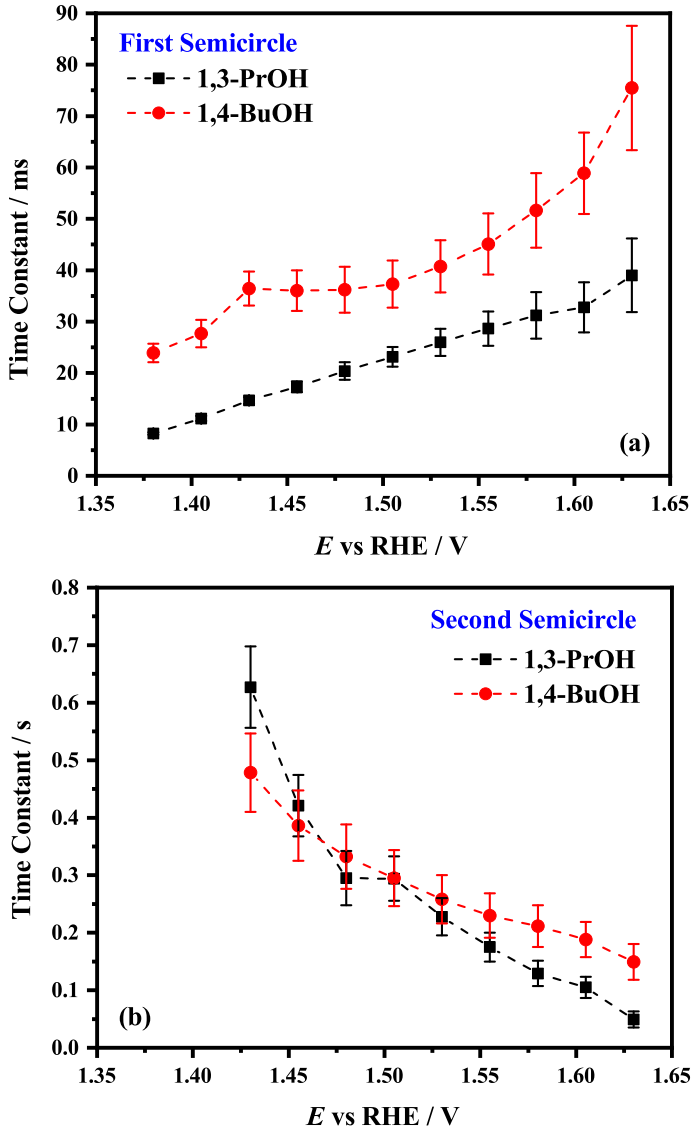

Figure 4.17: Time constants of the two processes during the oxidation of 1,3-propanediol and 1,4-butanediol. Error bars are calculated based on the error propagation from the standard deviation (σ_1) of $R_{\mathrm{ct\_eff}}$, $C_{\mathrm{dl\_eff}}$, $R_{\mathrm{ads\_eff}}$, and $C_{\mathrm{ads\_eff}}$.

Figure 4.8a shows that very little β-NiOOH (0.04-0.10 mC cm^{-2}) is left after the oxidation of these alcohols, which implies a highly efficient reaction process transferring charges to reduce β-NiOOH. Also, as the charges of other polyols bearing two separated hydroxyl groups (*i.e.*, 1,3-propanediol and 1,4-butanediol) are 0.31 and 0.41 mC cm^{-2}, the presence of vicinal OH groups leads to a much smaller charge, indicating a new reaction pathway involving this vicinity, which is different from the conventional pathway in which C-OH group is electrooxidized to C=O and later to carboxylate. This new reaction pathway is confirmed by the discovery of massively produced formate during the oxidation of ethylene glycol, 1,2-propanediol and glycerol from online Raman spectra, showing that the C-C bonds between carbonyl groups are dissociated. This observation is consistent with a weaker C-C bond energy (around 280 kJ mol^{-1}) between two carbonyl groups than between CH_3CO (around 343 kJ mol^{-1}) [40]. Moreover, as the potential increases, no negative slope (decrease of reactivity) or expansion of the semi-circles (increase of impedance) is identified in Figure 4.8b and 4.14, meaning that the whole oxidation process of these polyols with vicinal OH groups is not hindered by any poisoning effect. Another important discovery from Figure 4.8b is that the onset potential of these polyols is much lower than other alcohols, and lower than the formation of β-NiOOH in KOH solution without alcohol. It implies that the vicinal hydroxyl groups coordinate with Ni, change the surface environment and therefore shift the onset potential of oxidation downward.

A proposed mechanism of this whole oxidation process is schemed in Figure 4.18a, and consists of two sub-processes. The first sub-process (steps 1-2) involves the dissociative adsorption of alcohols onto the electrode surface via deprotonation of OH groups by the attack of OH^-. The following deprotonation of the C-H bond and the dissociation generate an intermediate with vicinal carbonyl groups, which is later re-adsorbed onto the surface, with two OH groups bonded to the carbon atoms separately (step 4). The breaking of the C-C bond and two O-Ni bonds (step 5) regenerate C=O and dissociate the molecule into two mono-carboxylates (*e.g.*

formate for ethylene glycol oxidation). It is implied that the oxidative removal of the intermediate of the second sub-process requires no other reactive species as this sub-process involves no deprotonation. No adsorbed species is left on the surface to poison the catalyst. The general reaction equations for ethylene glycol (Eqs. (4.10)-(4.11)) and glycerol electrooxidation (Eqs. (4.12)-(4.13)) follow:

$$2\beta\text{-NiOOH} + CH_2OHCH_2OH + 2OH^- \rightarrow 2\beta\text{-Ni(OH)}_2 + HCOCOH + 2H_2O + 2e^- \quad (4.10)$$

$$HCOCOH + 4OH^- \rightarrow 2HCOO^- + 2H_2O + 2e^- \quad (4.11)$$

$$3\beta\text{-NiOOH} + CH_2OHCHOHCH_2OH + 3OH^- \rightarrow 3\beta\text{-Ni(OH)}_2 + HCOCOCOH + 3H_2O + 3e^- \quad (4.12)$$

$$HCOCOCOH + 5OH^- \rightarrow 3HCOO^- + 2H_2O + 2e^- \quad (4.13)$$

By constrast, the oxidation of primary alcohols have the same onset potential with β-NiOOH formation. It partially consumes β-NiOOH but leaves 0.59-0.78 mC cm^{-2}. Based on the online Raman spectra of methanol and ethanol, C-OH group is preferentially oxidized into formate for methanol or acetate for ethanol, respectively. The results here match the mechanism proposed by Fleischmann and the observation by many other groups.

Figure 4.18b illustrates the major reaction mechanism of primary alcohol oxidation with NiCP generating carboxylate. Similar to the polyols mentioned above, dissociative adsorption (step 1-2) happens first, which involves the deprotonation of the OH group by OH^- from the electrolyte. Subsequently, the C-H bond is deprotonated, and the electrons from the bond are transferred towards Ni, producing RCHO as an intermediate (step 3). The conversion from RCHO to the final product ($RCOO^-$) can be either chemical or electrochemical (steps 4-5). In the electrochemical pathway, OH^- bonds to the carbon atom and transfers the electron to O, which is adsorbed

onto Ni. The last step before dissociation is another deprotonation of C-H bond and the corresponding electron transfer to remake C=O.

The oxidation of secondary alcohols is much simpler. They have the largest charge for the reduction of remaining β-NiOOH, meaning that the oxidation process consumes less β-NiOOH than all other alcohols. However, the current densities measured from CV (Figure 4.5) are comparable with other cases, implying that a large OER current is involved in the anodic scan, which is supported by a shrinking semi-circle from 1.480 V to 1.630 V in Figure 4.12 for 2-propanol (1.430 V to 1.555 V for 2-butanol). Unfortunately no Raman spectra were taken for the oxidation of secondary alcohols due to the fluorescent products. The oxidation process is depicted in Figure 4.18c. The experimental results are reproducible if the NiCP is not kept for a long time in the very high overpotential where oxygen evolution reaction can occur, otherwise the evolved oxygen would make the kinetics uncertain by bringing more fresh Ni from the bulk to the surface.

The oxidation of 1,3-propanediol and 1,4-butanediol are similar to primary alcohols. From Figure 4.8a, the charges (0.31 mC cm^{-2} for 1,3-propanediol and 0.41 mC cm^{-2} for 1,4-butanediol) are nearly half that for the primary alcohols, indicating that more hydroxyl groups are electrooxidized by β-NiOOH. Additionally, the charge for 1,4-butanediol is more than for 1,3-butanediol, which leads to the argument that longer carbon chains disfavor the oxidation process, possibly due to the difficulty in surface diffusion and adsorbing both terminal hydroxyl groups at the same time. The convergence of impedance curves at 0.1 Hz shown in Figure 4.16 still lacks a good interpretation and should to be investigated in future work.

4.4.2 Comparative Interpretation of Nyquist Plots

Comparing Nyquist plots (Figure 4.10-4.16) for all four types of alcohols, secondary alcohols (*i.e.* 2-propanol and 2-butanol) display one semi-circle representing a single

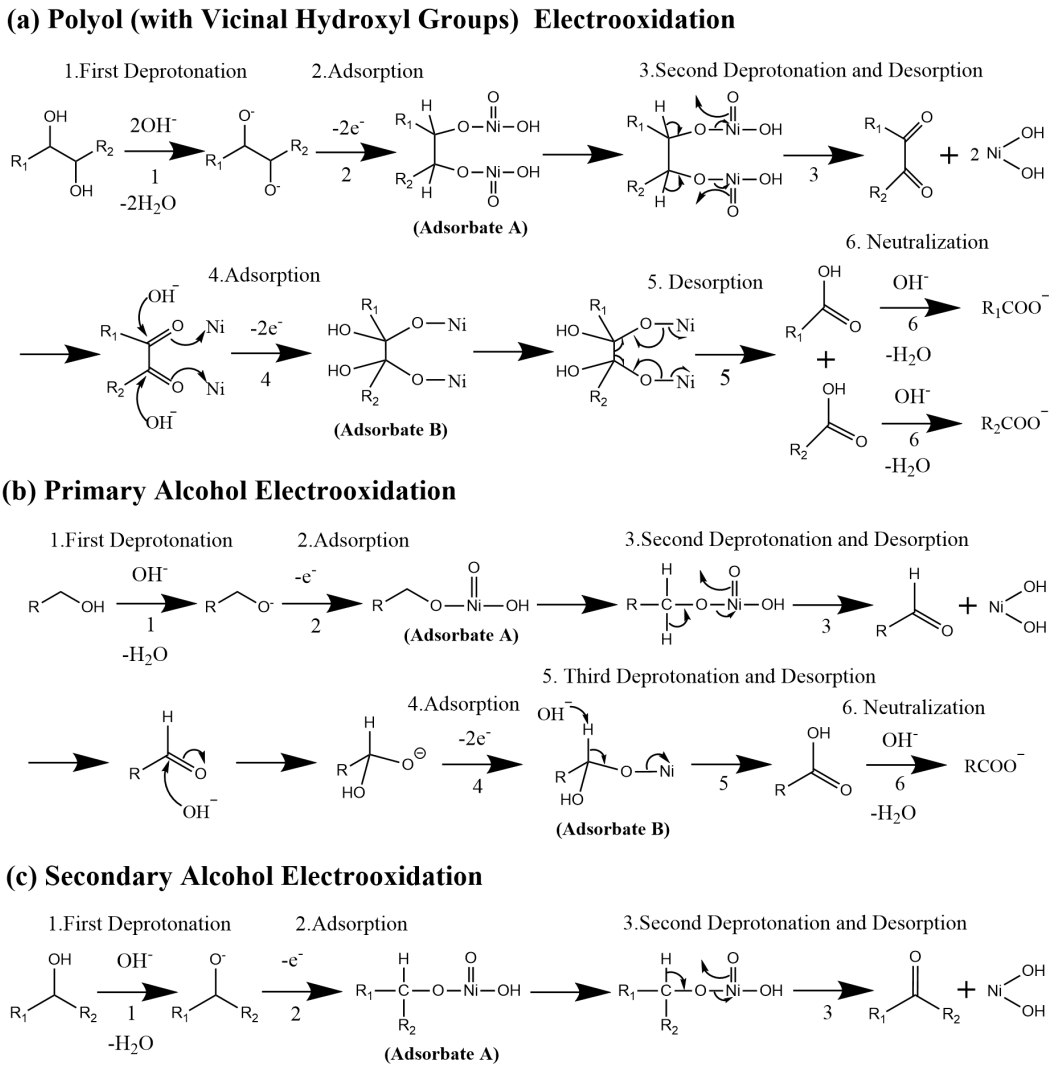

Figure 4.18: Schematic illustration of electrooxidation of different alcohols with NiCP electrodes. (a) Polyols with vicinal hydroxyl groups, (b) Primary alcohols and (c) Secondary alcohols. Arrows indicate electron transfer.

rate-determining step (*i.e.* all other steps involved in the oxidation are much faster) [41], while the other alcohols show two semi-circles. The presence of two semicircles suggest that: (i) two (or more) steps partially control the rate and (ii) one adsorbed species is involved in the kinetics. This observation matches a potentiostatic EIS study by Danaee et al. on the electrooxidation of glucose [42] and methanol [43] at a NiCu electode, where the two semi-circles were interpreted as a pseduo-inductive behavior, which is due to the desorption of intermediates reactivating the sites of Ni for the further adsorption of reactants.

Considering the reaction process proposed by Fleischmann [31, 32], the oxidation of alcohols first leads to the production of RCHO (for primary alcohols) or R_1COR_2 (for secondary alcohols), which goes through the generation of a surface adsorbate (product of steps 1-2 in Figure 4.18a-c, denoted as Adsorbate A) during the electrocatalysis. Later, the intermediates R_1COR_2 is not able to be further electrooxidized, but faces a chemical conversion to other products in basic electrolyte, while RCHO is further electrooxidized to $RCOO^-$, going through another surface adsorbate (Adsorbate B) generated in step 4 (and removed in step 5) for polyols in Figure 4.18a and primary alcohols in Figure 4.18b. If steps 2 and 3 (associated with Adsorbate A) are both partially rate limiting, *i.e.*, all other steps are faster, then presumably two semi-circles would be seen from the case of secondary alcohols as well. Therefore, Adsorbate B is more likely to be controlling the kinetics. For the cases of polyols with vicinal OH groups, the C-C bond dissociation is suggested to be the rate-determing step. As shown in Eq. 4.14-4.16, Γ_m is the number of sites for reaction on the surface of Ni, θ is the coverage of Adsorbate B and 1-θ represents all other adsorbates. Comparing the time constants of primary alcohols (Figure 4.11) with polyols (Figure 4.15), it can be found that polyols have larger time constants for the second semi-circles than primary alcohols, and therefore the C-C bond cleavage is a much slower process than the cleavage of C-H bonds towards the generation of $RCOO^-$.

$$\Gamma_{\mathrm{m}} \mathrm{d}\theta/\mathrm{d}t = v_4 - v_5 = k_4(1-\theta) - k_5\theta \tag{4.14}$$

$$j/F = 2v_2 + 2v_4 \text{ (for polyols with vicinal OH groups)} \tag{4.15}$$

$$j/F = v_2 + 2v_4 \text{ (for primary mono-alcohols)} \tag{4.16}$$

4.5 Conclusion and Future Works

In this work, electrochemical and Raman spectroscopic investigations were conducted on ten different alcohols (from 1C to 4C), from which four conclusions are obtained. Firstly, it is shown that the vicinal diols and triols coordinated to Ni can lower the onset potential of β-NiOOH formation from β-$Ni(OH)_2$, therefore improving the efficiency of the electrooxidation. Secondly, it is confirmed by Raman spectra that the dissociation of C-C bonds of neighboring carbon atoms bearing hydroxyl groups can occur, which produces formate as the major oxidation product. Thirdly, a poisoning effect is extensively seen in primary alcohols, secondary alcohols and polyols with separated hydroxyl groups, which implies reaction pathways towards poisoning species. Lastly, based on the size of the second semi-circles from EIS measurements, it is revealed that the cleavage of C-H bonds to produce $RCOO^-$ is much efficient than the cleavage of CO-CO bonds.

Several thorough investigations should be conducted in future work. For example, online UV-Vis spectroscopy can be developed to monitor the oxidation process of 3C and 4C alcohols, which avoids the issue of fluorescence emission. Besides, the use of microfluidic flow devices also allows the studies of the effects of external conditions (*e.g.* temperature) on the reactivity and reaction pathways of these alcohols.

References

[1] N. R. Stradiotto, K. E. Toghill, L. Xiao, A. Moshar, and R. G. Compton, *Electroanalysis*, 2009, **21**(24), 2627–2633.

[2] M. Jafarian, A. Mirzapoor, I. Danaee, S. A. Shahnazi, and F. Gobal, *Science China Chemistry*, 2012, **55**(9), 1819–1824.

[3] B. Habibi and E. Dadashpour, *Electrochimica Acta*, 2013, **88**, 157–164.

[4] F. Gao, Y. Zhang, T. Song, C. Wang, C. Chen, J. Wang, J. Guo, and Y. Du, *Journal of Colloid and Interface Science*, 2020, **561**, 512–518.

[5] Q. Yi, L. Sun, X. Liu, and H. Nie, *Fuel*, 2013, **111**, 88–95.

[6] A. Manzo-Robledo, N. J. Costa, K. Philippot, L. M. Rossi, E. Ramírez-Meneses, L. P. Guerrero-Ortega, and S. Ezquerra-Quiroga, *Journal of Nanoparticle Research*, 2015, **17**(12), 1–8.

[7] A. Hatamie, E. Rezvani, A. S. Rasouli, and A. Simchi, *Electroanalysis*, 2019, **31**(3), 504–511.

[8] G. G. Lee, J. Leddy, and S. D. Minteer, *Chemical Communications*, 2012, **48**(98), 11972–11974.

[9] M. P. Salinas-Quezada, D. A. Crespo-Yapur, A. Cano-Marquez, and M. Videa, *Fuel Cells*, 2019, **19**(5), 587–593.

[10] A. Cuña, C. Reyes Plascencia, E. L. da Silva, J. Marcuzzo, S. Khan, N. Tancredi, M. R. Baldan, and C. de Fraga Malfatti, *Applied Catalysis B: Environmental*, 2017, **202**, 95–103.

[11] N. A. Barakat, H. M. Moustafa, M. M. Nassar, M. A. Abdelkareem, M. S. Mahmoud, A. A. Almajid, and K. A. Khalil, *Electrochimica Acta*, 2015, **182**, 143–155.

[12] A. T. Shah, M. I. Din, U. Farooq, M. T. Z. Butt, M. Athar, M. A. Chaudhary, M. N. Ahmad, and M. L. Mirza, *Colloids and Surfaces A: Physicochemical and Engineering Aspects*, 2012, **405**, 19–21.

[13] F. Muench, M. Oezaslan, M. Rauber, S. Kaserer, A. Fuchs, E. Mankel, J. Brötz, P. Strasser, C. Roth, and W. Ensinger, *Journal of Power Sources*, 2013, **222**, 243–252.

[14] K. Rahmani and B. Habibi, *RSC Advances*, 2019, **9**(58), 34050–34064.

[15] D. Yu, X. Zhang, K. Wang, L. He, J. Yao, Y. Feng, and H. Wang, *International Journal of Hydrogen Energy*, 2013, **38**(27), 11863–11869.

[16] T. S. Almeida, Y. Yu, A. R. de Andrade, and H. D. Abruña, *Electrochimica Acta*, 2019, **295**, 751–758.

[17] J. B. Raoof, A. Omrani, R. Ojani, and F. Monfared, *Journal of Macromolecular Science, Part A: Pure and Applied Chemistry*, 2013, **50**(5), 541–546.

[18] Y. Yi, S. Uhm, and J. Lee, *Electrocatalysis*, 2010, **1**(2-3), 104–107.

[19] L. Shabnam, S. N. Faisal, A. K. Roy, and V. G. Gomes, *ChemElectroChem*, 2018, **5**(23), 3799–3808.

[20] N. A. Barakat, M. Motlak, A. A. Elzatahry, K. A. Khalil, and E. A. Abdelghani, *International Journal of Hydrogen Energy*, 2014, **39**(1), 305–316.

[21] S. Amin, A. Tahira, A. R. Solangi, R. Mazzaro, Z. H. Ibupoto, A. Fatima, and A. Vomiero, *Electroanalysis*, 2020, pp. 1–9.

[22] J. Van Drunen, T. W. Napporn, B. Kokoh, and G. Jerkiewicz, *Journal of Electroanalytical Chemistry*, 2014, **716**, 120–128.

[23] L. García-Cruz, A. Sáez, C. O. Ania, J. Solla-Gullón, T. Thiemann, J. Iniesta, and V. Montiel, *Carbon*, 2014, **73**, 291–302.

[24] Q. Yi, W. Huang, J. Zhang, X. Liu, and L. Li, *Journal of Electroanalytical Chemistry*, 2007, **610**(2), 163–170.

[25] Q. Yi, J. Zhang, W. Huang, and X. Liu, *Catalysis Communications*, 2007, **8**(7), 1017–1022.

[26] V. L. Oliveira, C. Morais, K. Servat, T. W. Napporn, G. Tremiliosi-Filho, and K. B. Kokoh, *Journal of Electroanalytical Chemistry*, 2013, **703**, 56–62.

[27] J. L. Bott-Neto, T. S. Martins, S. A. Machado, and E. A. Ticianelli, *ACS Applied Materials and Interfaces*, 2019, **11**(34), 30810–30818.

[28] M. Xiao, Y. Miao, W. Li, Y. Yang, and X. Liang, *Electrochimica Acta*, 2015, **178**, 209–216.

[29] V. L. Oliveira, C. Morais, K. Servat, T. W. Napporn, G. Tremiliosi-Filho, and K. B. Kokoh, *Electrochimica Acta*, 2014, **117**, 255–262.

[30] X. Liang, M. Xiao, M. Xu, D. Yang, Y. Yan, Y. Tian, and Y. Miao, *Journal of Applied Electrochemistry*, 2016, **46**(1), 1–8.

[31] M. Fleischmann, K. Korinek, and D. Pletcher, *Journal of Electroanalytical Chemistry*, 1971.

[32] M. Fleischmann, K. Korinek, and D. Pletcher, *Journal of the Chemical Society, Perkin Transactions 2*, 1972.

[33] D. E. Simpson, K. E. Juda, and D. Roy, *Electrocatalysis*, 2018, **9**(1), 86–101.

[34] R. Ojani, J. B. Raoof, M. Goli, and A. Alinezhad, *Journal of Applied Electrochemistry*, 2013, **43**(9), 927–937.

[35] T. Vijayabarathi, K. Vijayarani, and M. Noel, *Indian Journal of Chemical Technology*, 2010, **17**(6), 411–418.

[36] A. Saraby-Reintjes and M. Fleischmann, *Electrochimica Acta*, 1984.

[37] Complex Nonlinear Least Squares Fitting of Immittance Data, available at the Maple Applications Center, url = https://www.maplesoft.com/applications/view.aspx?SID=154540,.

[38] M. Ingdal, R. Johnsen, and D. A. Harrington, *Electrochimica Acta*, 2019, **317**, 648–653.

[39] B. Hirschorn, M. E. Orazem, B. Tribollet, V. Vivier, I. Frateur, and M. Musiani, *Electrochimica Acta*, 2010, **55**(21), 6218–6227.

[40] T. L. Cottrell, The Strengths of Chemical Bonds, 2nd Ed., 1966.

[41] D. A. Harrington, *Journal of Electroanalytical Chemistry*, 2015, **737**, 30–36.

[42] I. Danaee, M. Jafarian, F. Forouzandeh, F. Gobal, and M. G. Mahjani, *Journal of Physical Chemistry B*, 2008, **112**(49), 15933–15940.

[43] I. Danaee, M. Jafarian, F. Forouzandeh, F. Gobal, and M. G. Mahjani, *International Journal of Hydrogen Energy*, 2009, **34**(2), 859–869.

A Supporting Information

$$C_{\text{eff}} = (Y_0(R_{\text{s}}^{-1} + R_{\text{ct}}^{-1})^{n-1})^{1/n} \tag{S1}$$

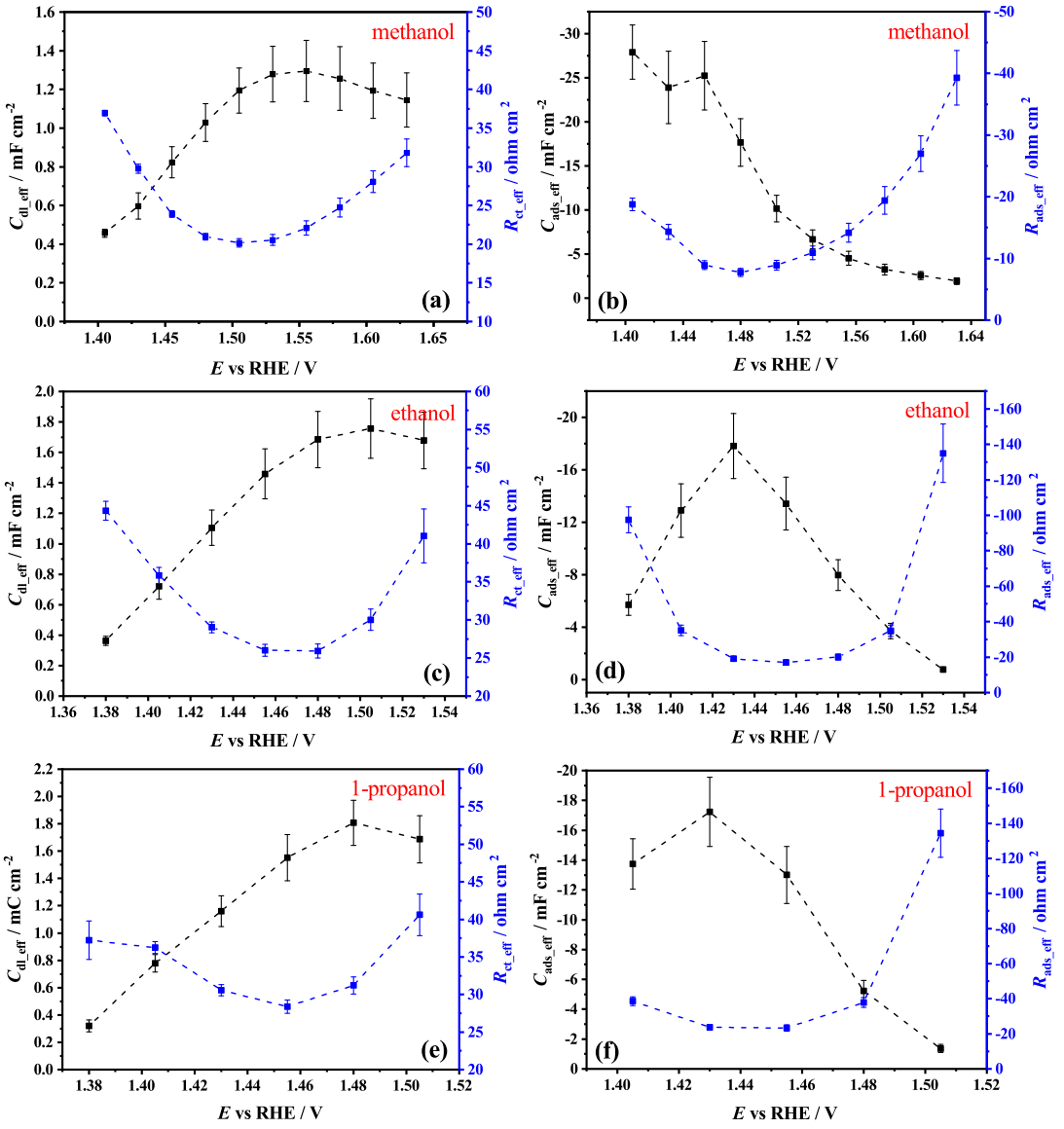

Figure S1: EIS fitting results (C_{dl}, R_{ct}, C_{ads}, R_{ads}) of Figure 4.10. (a-b) The first and second semicircles of methanol oxidation measurements. (c-d) The first and second semicircles of ethanol oxidation measurements. (e-f) The first and second semicircles of 1-propanol oxidation measurements. Error bars are calculated based on the error propagation from the standard deviation (σ_1) of R_{s}, R_{ct}, R_{ads}, Y_{dl}, Y_{ads}, and n.

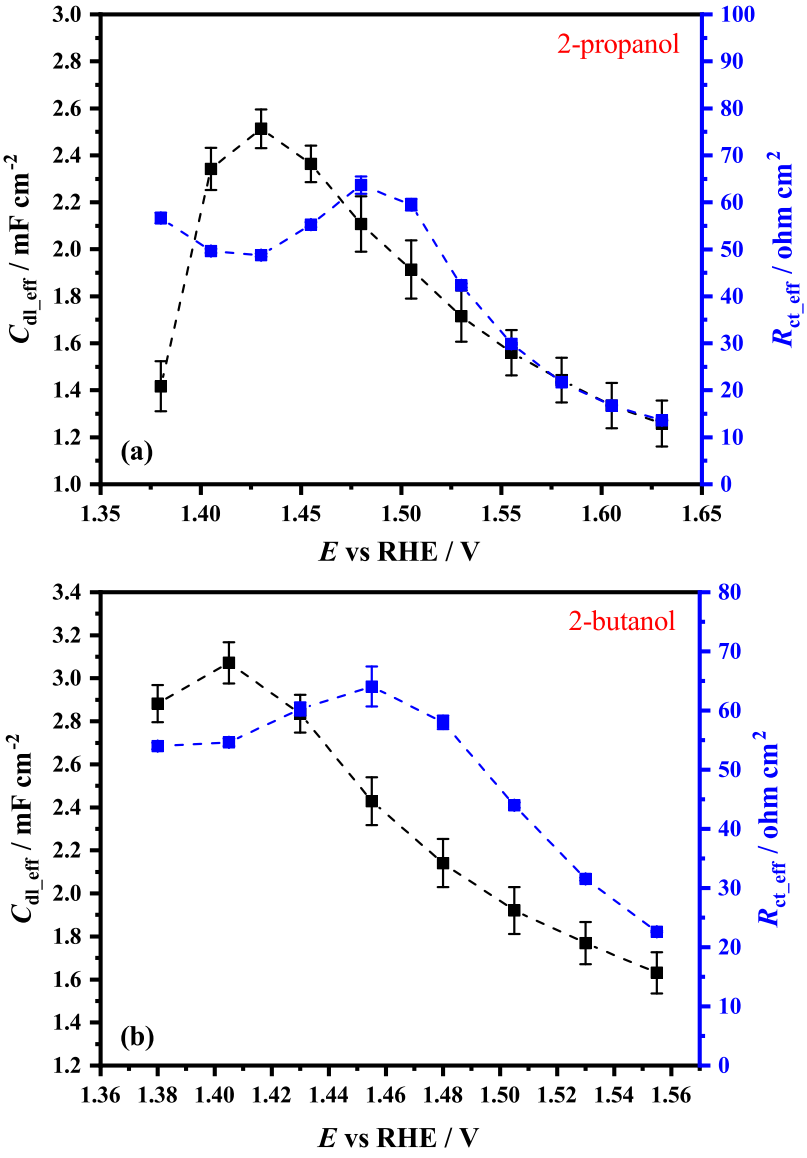

Figure S2: EIS fitting results (C_{dl} and R_{ct}) of Figure 4.12. (a) The semicircles of 2-propanol oxidation measurements. (b) The semicircles of 2-butanol oxidation measurements. Error bars are calculated based on the error propagation from the standard deviation (σ_1) of R_{s}, R_{ct}, Y_{dl}, and n.

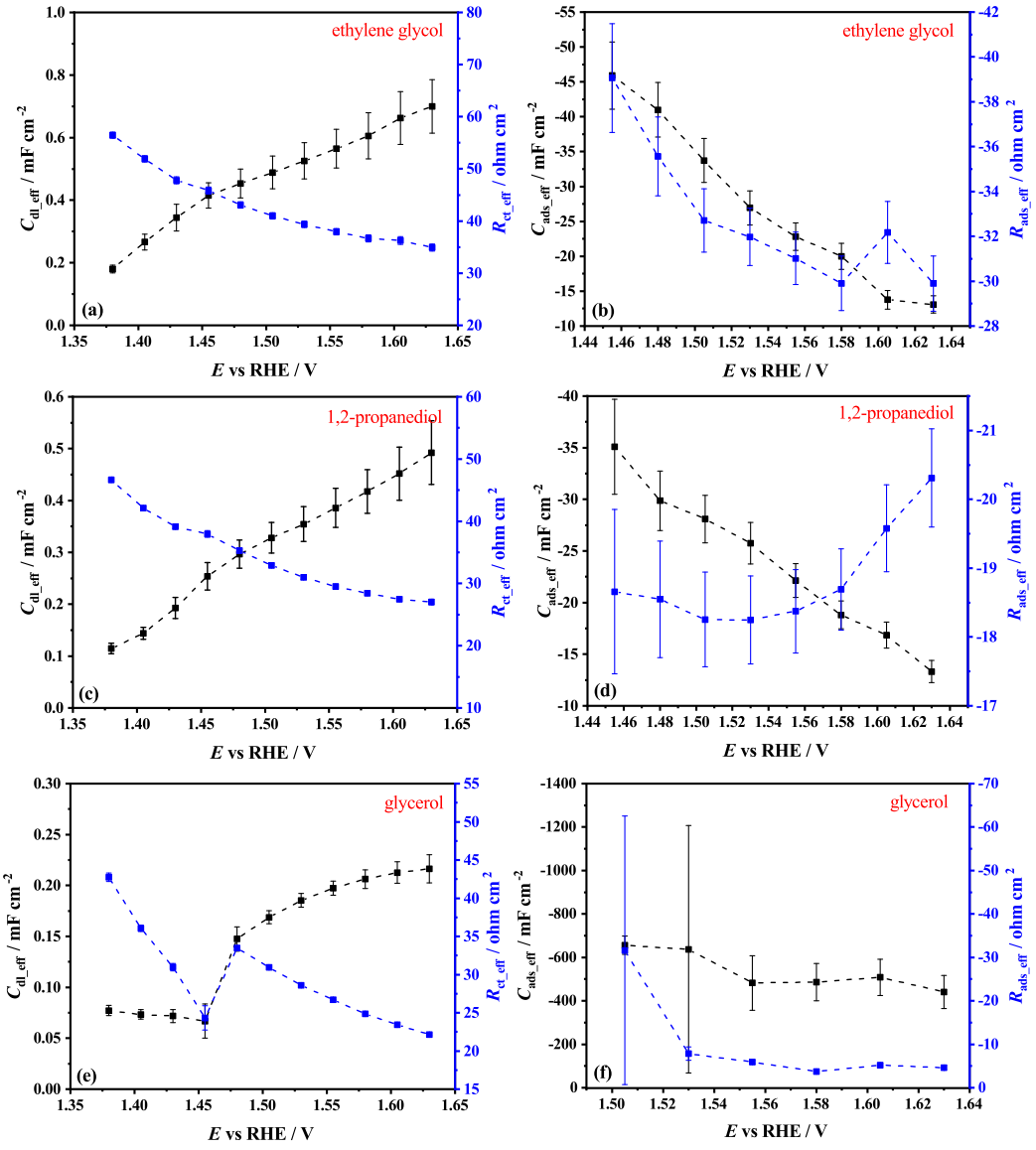

Figure S3: EIS fitting results (C_{dl}, R_{ct}, C_{ads}, R_{ads}) of Figure 4.14. (a-b) The first and second semicircles of ethylene glycol oxidation measurements. (c-d) The first and second semicircles of 1,2-propanediol oxidation measurements. (e-f) The first and second semicircles of glycerol oxidation measurements. Error bars are calculated based on the error propagation from the standard deviation (σ_1) of R_{s}, R_{ct}, Y_{dl}, R_{ads}, Y_{ads}, and n.

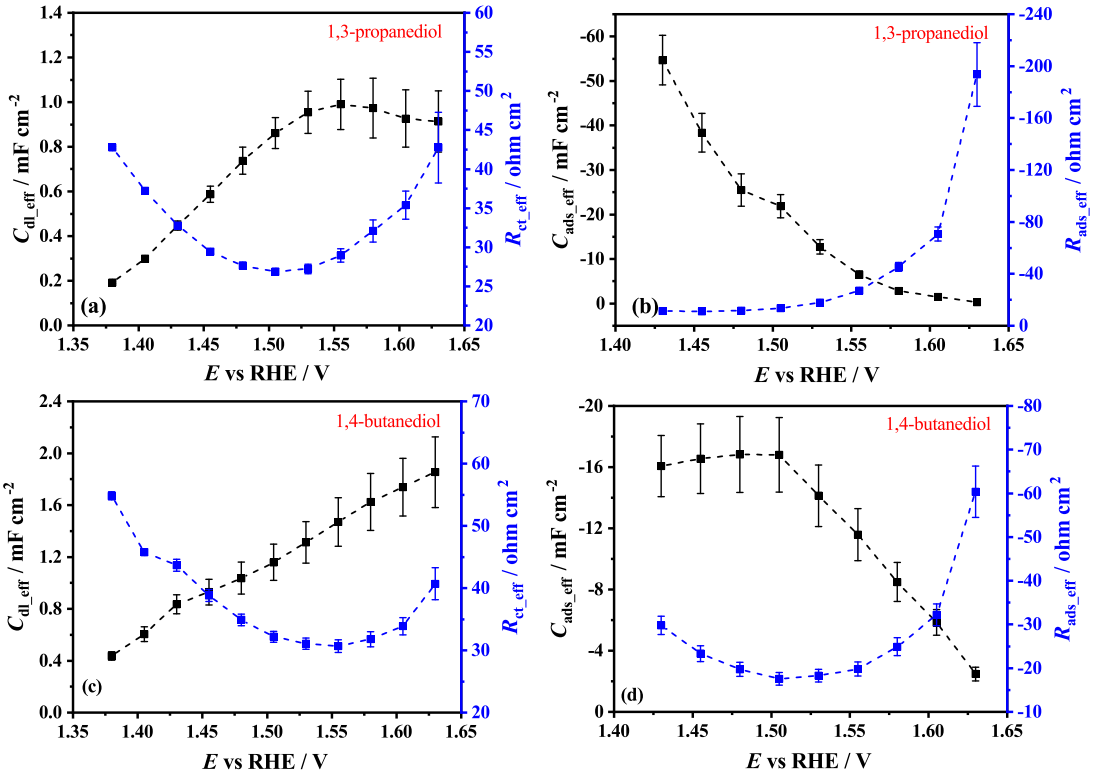

Figure S4: EIS fitting results (C_{dl}, R_{ct}, C_{ads}, R_{ads}) of Figure 4.16. (a-b) The first and second semicircles of 1,3-propanediol oxidation measurements. (c-d) The first and second semicircles of 1,4-butanediol oxidation measurements. Error bars are calculated based on the error propagation from the standard deviation (σ_1) of R_{s}, R_{ct}, Y_{dl}, R_{ads}, Y_{ads}, and n.

Table S1: Equivalent Circuits Used for Fitting Potentiostatic EIS Results

E vs RHE / V	MeOH	EtOH	1-PrOH	2-PrOH	2-BuOH	EGOH	1,2-PrOH	GlyOH	1,3-PrOH	1,4-BuOH
1.380	N/A	QC	QC	Q	Q	Q	Q	QQ	Q	QC
1.405	QC	QC	QC	Q	Q	Q	Q	QQ	Q	QC
1.430	QC	QC	QC	Q	Q	Q	Q	QQ	QC	QC
1.455	QC	QC	QC	Q	Q	QC	Q	QQ	QC	QC
1.480	QC	QC	QC	Q	Q	QC	QC	Q	QC	QC
1.505	QC	QC	QC	Q	Q	QC	QC	QQ	QC	QC
1.530	QC	QC	N/A	Q	Q	QC	QC	QQ	QC	QC
1.555	QC	N/A	N/A	Q	Q	QC	QC	QQ	QC	QC
1.580	QC	N/A	N/A	Q	N/A	QC	QC	QQ	QC	QC
1.605	QC	N/A	N/A	Q	N/A	QC	QC	QQ	QC	QC
1.630	QC	N/A	N/A	Q	N/A	QC	QC	QQ	QC	QC

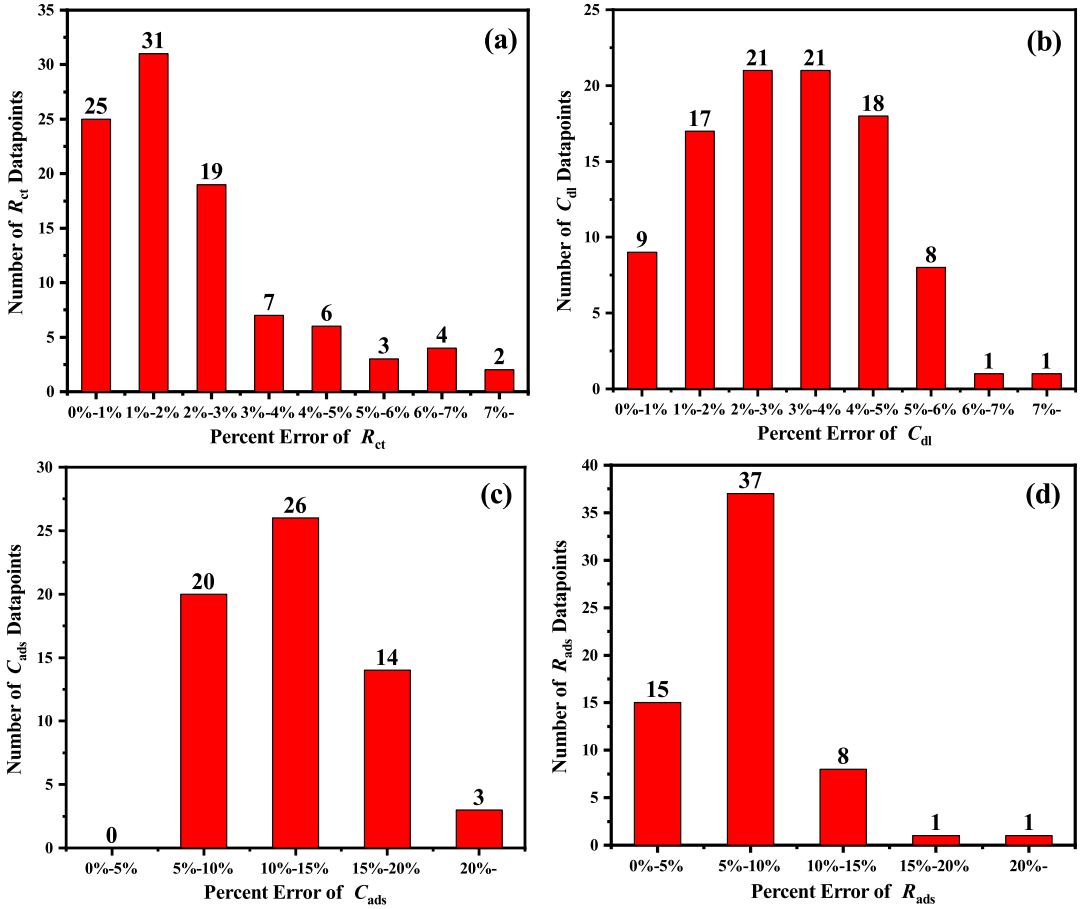

Figure S5: Percent Errors of EIS fits.

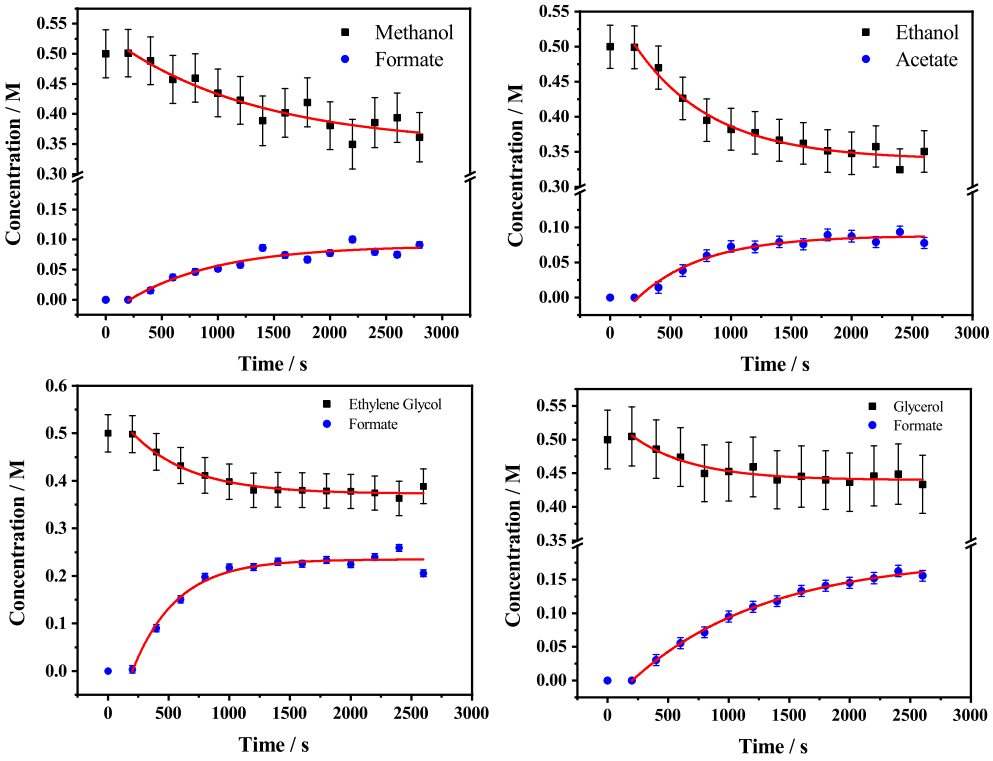

Figure S6: The evolution of the concentration of alcohol and carboxylate during the electrooxidation of 0.5 M (a) methanol, (b) ethanol, (c) ethylene glycol, and (d) glycerol in 5 M KOH. (Potential was held at 1.53 V. Flow rate: 50 μL min^{-1}. The calculation procedure of error bars can be found in the supporting information of Chapter 3.)

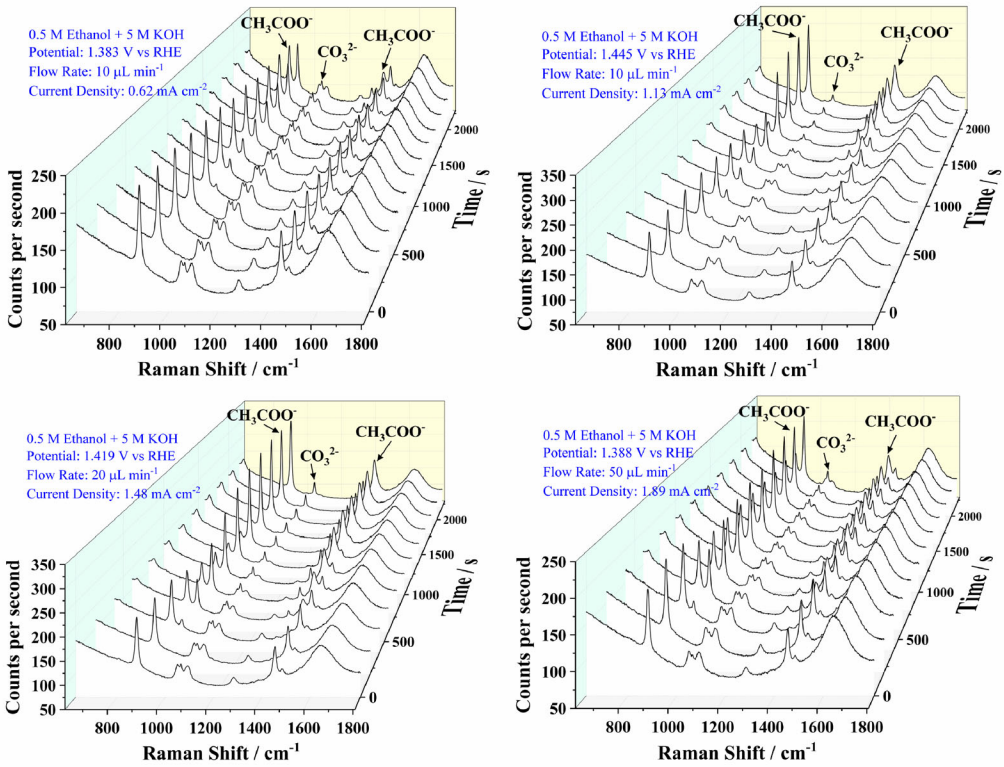

Figure S7: Time-dependent Raman spectra showing the oxidation of 0.5 M ethanol with NiCP in 5 M KOH.

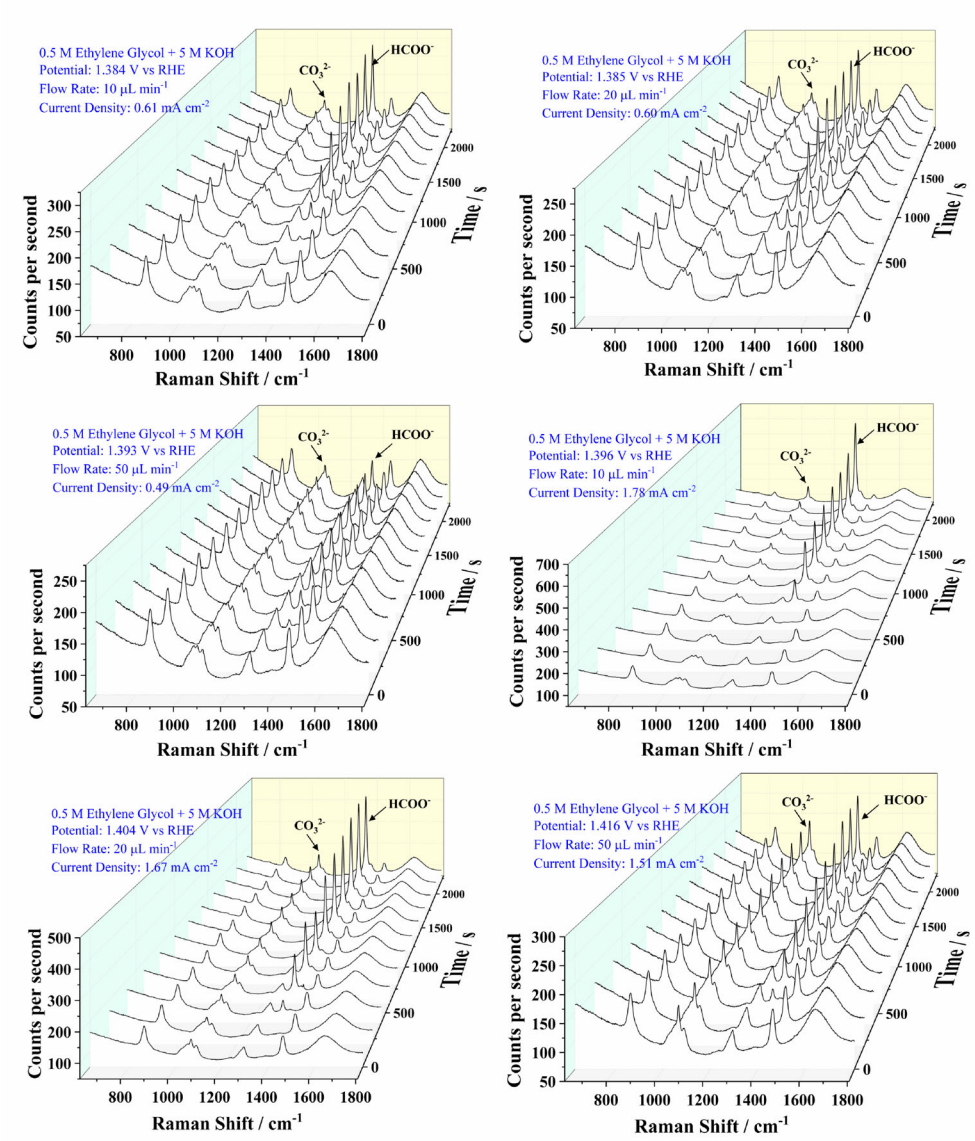

Figure S8: Time-dependent Raman spectra showing the oxidation of 0.5 M ethylene glycol with NiCP in 5 M KOH.

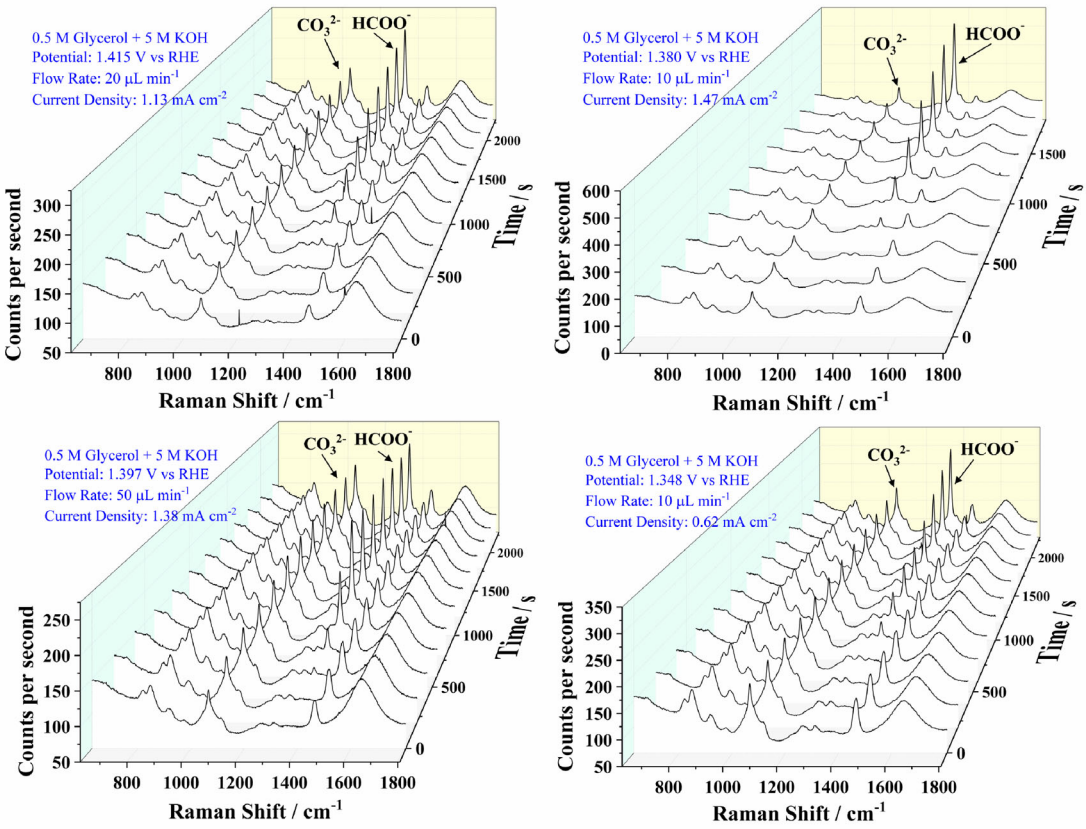

Figure S9: Time-dependent Raman spectra showing the oxidation of 0.5 M glycerol with NiCP in 5 M KOH.

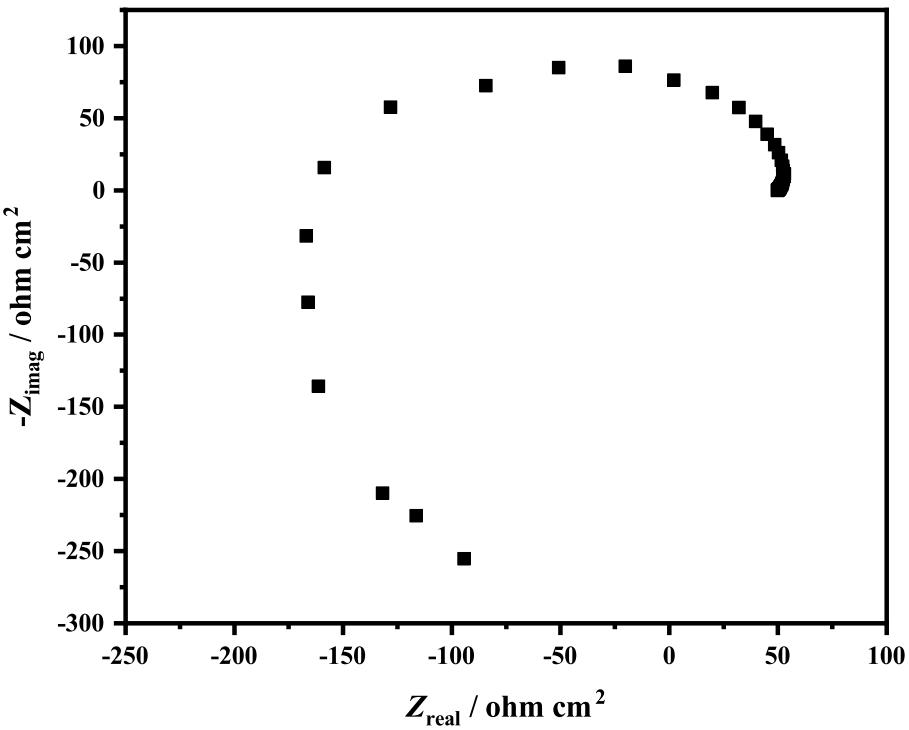

Figure S10: Potentiostatic EIS measurements of NiCP oxidizing 0.5 M 1-propanol in 5 M KOH at 1.530 V.

$$C_{\text{eff}} = (Y_0({R_{\text{ads}}}^{-1})^{n-1})^{1/n} \tag{S2}$$

Chapter 5

Design of Printed Circuit Boards (PCBs) for the Fabrication of Electrochemical Microfluidic Devices

Abstract

As a chemically resistant hard substrate with surface-mounted metal pads, Printed Circuit Boards (PCBs) have the potential to be utilized as substrates for building electrochemical microfluidic devices. Compared with regular electrochemical microfluidic substrates made with glass slides or filter papers, PCBs-based substrates have electrode pads with customized size, shape and position, and more wiring layers. Previous works have shown that the PCBs-based electrochemical microfluidic devices can be used as biosensors, electrochemical impedance cytometers, and electrochemical imaging platforms, while their workability as a platform for electrocatalysis has not yet been presented. This work presents a method to develop PCBs into mi-

crofluidic substrates for alcohol electrocatalysis. The copper pads are pretreated and electrodeposited with nickel (Ni), silver (Ag), palladium (Pd), and platinum (Pt) for various electrocatalytic purposes. Four types of PCBs-based microfluidic devices are presented, each designed with PCB software KiCAD and fabricated by PCB manufacturers. In the second, third and fourth designs, devices are built up with multi-layers of PCBs.

5.1 Introduction

Lab-on-printed-circuit-board (PCB) technology can integrate multi-functional electronic components and is regarded as a quick prototyping and cost-saving method (around less than 3 US dollar per square inch) [1–3]. In the most recent decade, microfluidic designs developed on printed circuit boards have been extensively used in many fields including digital microfluidic biochips [4, 5], electrophoresis devices for sorting microparticles [6, 7], and interdigitated microchannel patterns [8]. Advantages of PCBs, for example, accurate positioning of electrodes at the micrometer scale [9], and easy combination of microfluidic networks with electronic circuits [3], make electrochemistry studies with PCBs-based microfluidic devices very promising.

Currently, flow-over designs are very commonly seen in microfluidic devices for electrocatalysis. Lithography is one of the most widely used techniques that can apply thin and smooth layers of metal with customized patterns on a hard substrate for flow-over experiments [10, 11]. Although it has well-developed protocols, this technique is hard to utilize as it requires special facilities with ultra-clean environments, not to mention the cost and complexity of the operations. Inspired by the technology of PCBs that allow the easy customization of the shapes of copper pads mounted on a hard substrate (made of glass fibers and epoxy resistive to chemicals), this unique advantage can be developed into fabricating microfluidic devices [9]. Compared with photolithography, working electrodes that are directly electroplated on the copper pads for functionalization enjoy a much simpler experimental procedure, higher efficiency, and broader applicability. Also, it can be done in a regular lab environment. Besides, making alloys is possible by co-depositing metals with multi-metallic precursor solutions.

Moreover, microfluidic devices made of PCBs have two other great advantages over current devices. Primarily, PCBs allow a multi-layer wiring configuration [9], which can support a more complicated electrode pattern by having wires going inside the

boards for electrical connections, contrasted by regular microfluidic substrates having wires only on top of the substrates, which limits the number and size of electrodes they can contain. Secondly, PCB technology simplifies the fabrication of internal reference electrodes (IREs) on the microfluidic substrates. For most of the current microfluidic designs, external reference electrodes (*e.g.* Ag|AgCl) are used, accommodated in a downstream reservoir where the fluid exits [12,13], which is undesirable because of the size limit and ohmic loss. These issues can be resolved by having internal reference electrodes (*e.g.* PdH [14]) including pseudo-reference electrodes (a small metal pad undisturbed by the current flowing through the channel) [15–17] located either in a side channel or in the main channel upstream of the working electrode, which can be much closer to working electrodes.

However, previously published works applying PCB technology to electrochemical microfluidic devices only presented PCBs-based electrochemical sensors, which outperform optical sensors as they are not influenced by the turbidity of samples or the optical path length. Therefore, microfluidic impedance cytometers [18–20], electrochemical imaging systems [9], heavy metal sensors [21], and electrochemical biosensors [22–24] were invented, but so far there is no application of PCB-based microfluidic devices for studying electrocatalytic reactions. The development of electrochemical microfluidic devices with PCB technology is very promising and worthy of investigation.

Herein, initial studies of PCBs-based microfluidic devices for electrocatalysis are reported. Electrode pads were mounted on printed circuit boards in a pre-designed pattern, followed by the electrodeposition of nickel (Ni), silver (Ag), palladium (Pd) and platinum (Pt). Channels were made using PDMS (in the first design) and PCBs (in the second, third and fourth designs). Two types of internal pseudo reference electrodes were fabricated, and the electrocatalysis of methanol and glycerol at Ni and Pd electrodes are investigated.

Sealing of microfluidic devices with electronics is vital as the leaking triggers many

problems, such as short circuits. In most of the reported works, polydimethylsiloxane (PDMS) with plasma-activation makes a durable and hydrophobic seal. Alternatively, epoxy is often applied to the edges to prevent leaking of corrosive electrolytes. Nevertheless, PDMS is not considered a proper material for electrocatalytic devices for alcohol oxidations, as PDMS significantly absorbs small alcohol molecules ranging from methanol to glycerol. Also, both PDMS and epoxy bond tightly to substrates, making it hard to dissemble, recycle or reuse the devices afterwards. To address these issues, polytetrafluoroethylene (PTFE) tape is utilized to seal the edges of PCBs in the second, third and fourth designs since they show a strong hydrophobicity and moderate adhesivity. Combined with screws or binder-clips applying forces evenly along the microfluidic channel that mechanically clamp the boards together, these PCBs-based microfluidic devices can be kept watertight during the period of measurements.

5.2 Experimental

5.2.1 PCB General Design Rules

PCB designs were conducted with the open-source software KiCAD. The first, second and third designs of PCBs (one wiring layer) were sent to OSH Park for printing and Bittele Electronic Inc. printed the fourth PCB design (two wiring layers). All designs had gold-protected copper pads (one ounce copper per square foot). The board thickness is 1.6 mm (one wiring layer and spacer boards) and 0.8 mm (two wiring layers). All pin headers (2.5 mm $\times$ 2.5 mm) are positioned on the board edges. Some PCBs contain holes for electrolyte infusing, which are 1.2 mm wide. All printed PCBs were wrapped by PTFE tape before use to avoid any scratches on the pads. Wires for working electrodes and counter electrode were 2 mm wide and wires for reference electrodes are set to be 0.5 mm wide. Sample boards were made to test

the pretreatments and electrodeposition procedures. All PCBs are resistive to 0.5 M KOH over the duration of the experiment.

5.2.2 Designs of PCB-Based Electrochemical Microfluidic Devices

Three-dimensional schemes of several designs of PCB-based devices are introduced in this section. These 3D schemes are generated by 3D Viewer of KiCAD. In the schemes, purple area indicates the top side of PCB and yellow area indicates the bottom side. The traces of wires are shown in the color of dark purple (top) and green (bottom), respectively. Electrode pads are displayed in the color of red and cyan. The edges of PCBs and electrodes are marked by golden lines. All the components are shown proportionally in the 3D schemes. For the devices which involve multiple PCBs, PTFE tape are positioned between the boards on the edges.

PCB Samples for Electrodeposition

Two kinds of small PCBs (as shown in Figure 5.1) are designed for practicing the electrode preparation by electrodeposition. The size of them is 20 mm × 35 mm, with a 15 mm × 15 mm square Cu pad (on the left) or a circular Cu pad of 10 mm wide (on the right). The width of the Cu wires is 2 mm.

The First Design

In the first design of PCB-based microfluidic substates (see Figure 5.2 and 5.3), the board outline was set to be identical to a 3-inch by 2-inch glass slide, to simulate regular electrochemical microfluidic substrates (usually made with glass microscope slides). Eight rectangular pads (25 mm × 8 mm) were used as working electrodes, one square pad (15 mm × 15 mm) was used as counter electrode, one small rectangular

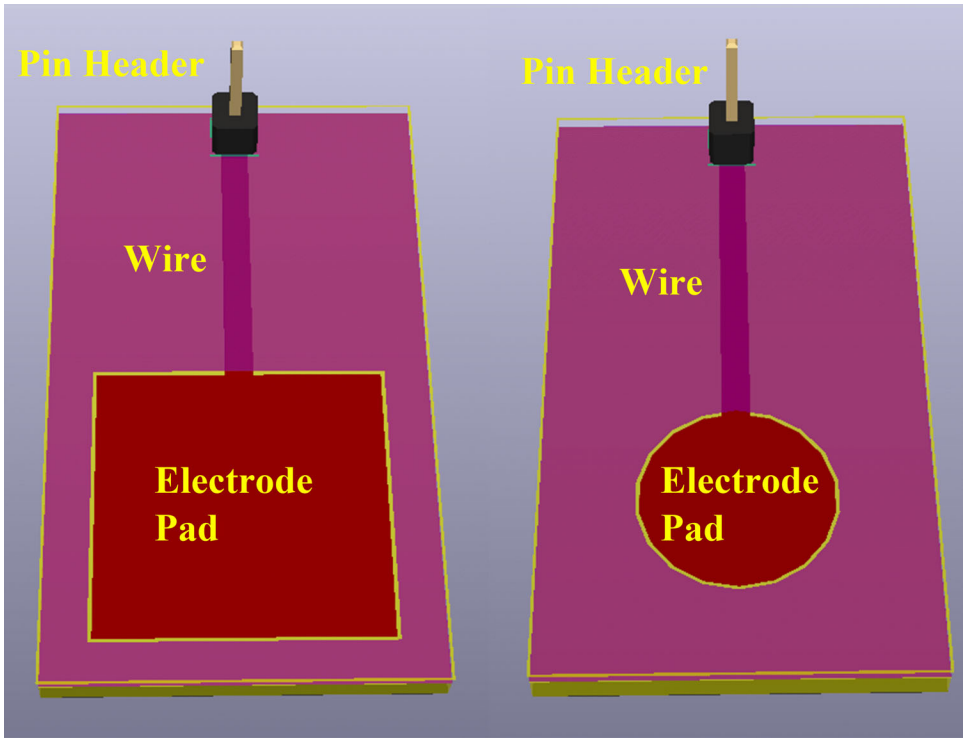

Figure 5.1: Two kinds of printed circuit boards for practicing electrode preparation by electrodeposition. Board dimensions: 35 mm × 20 mm × 1.6 mm. Square electrode pad: 15 mm × 15 mm. Round electrode pad: 10 mm (diameter). The width of the Cu wires is 2 mm.

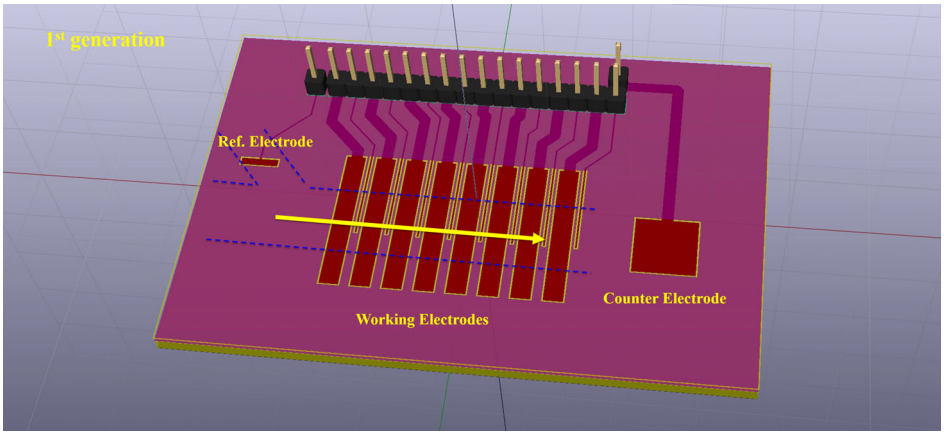

Figure 5.2: The first generation of PCB-based microfluidic device. Board dimensions: 75 mm × 50 mm × 1.6 mm. The shape of the channel (1.5 mm wide) is marked by the blue dashed lines. The flow direction is indicated by the yellow arrow. Working electrode pads: 25 mm × 8 mm (each). Sensing electrode pads: 15 mm × 1 mm (each). Reference electrode pad: 2 mm × 8 mm. Counter electrode pad: 15 mm × 15 mm. The width of Cu wires: 2 mm (for working and counter electrodes) and 1 mm (for reference and sensing electrodes). PTFE tube (1 mm O.D.), PDMS channel (1 mm thick) and cylindrical glass reservoir (1 cm wide and 2 cm high) are not shown in this figure.

pad (2 mm × 8 mm) was used as the reference electrode and 8 pads (15 mm × 1 mm) were placed next to each working electrode pad and used as sensing electrodes. The wiring for the working electrodes and the counter electrode is 1.5 mm thick, while the wiring for the reference electrode and the sensing electrodes is 0.2 mm thick. PDMS blocks were placed on top of the board to build the sides of the channel (1 mm thick). The width of the channel was 1.5 cm. The exit reservoir was a cylindrical glass tube, 1 cm wide and 2 cm high.

The Second Design

Figure 5.4 and Figure 5.5 present the second generation of the PCB-based microfluidic substrate design. Three layers of PCBs were used for making the microfluidic device: (i) a top layer (layer A) with several working electrode pads (10 mm × 6 mm) mounted

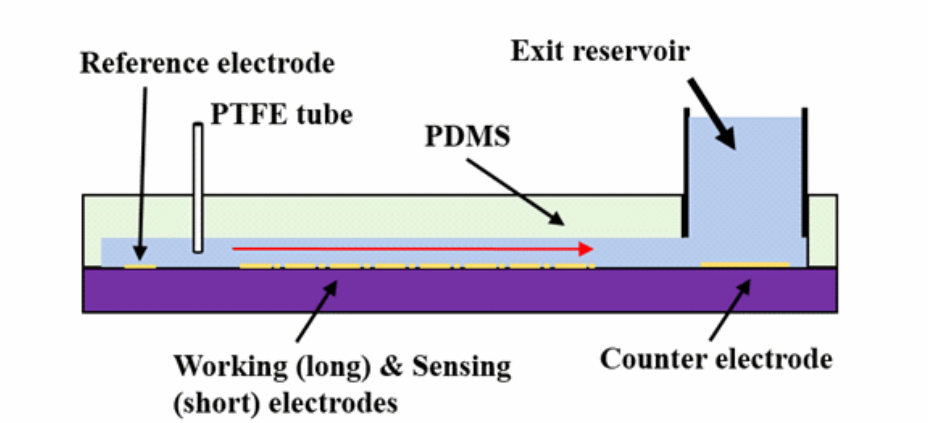

Figure 5.3: Side view of the first generation of PCB-based microfluidic device. Liquid enters via the PTFE tube. Red arrow indicates the flow direction. Blue area indicates the electrolyte.

on the bottom, facing downward, (ii) a channel layer (layer B), and (iii) a bottom layer (layer C) with a number of working electrode pads (10 mm × 6 mm), one sensing electrode (5 mm × 1 mm), one reference electrode (5 mm × 3 mm) at the corner and one counter electrode (20 mm × 20 mm). The wiring track width is 2 mm for the WE and CE, and 1 mm for the RE. Figure 5.4 shows the integration of the three PCBs, with the channel (10 mm wide) cut open on layer B, and with an area (25 mm × 25 mm) cut open on both layers A and B to make a reservoir. A detection hole (4 mm dia.) was drilled at the same position through all three boards for laser penetration. Layer D, made of PTFE, is optional, and can be replaced by a coverslip covering the detection hole. Two more holes (1.2 mm dia.) were drilled through layer A for supplying different electrolytes to the working electrodes and the reference electrode. A major improvement made by this design is that the thickness of the channel can be customized.

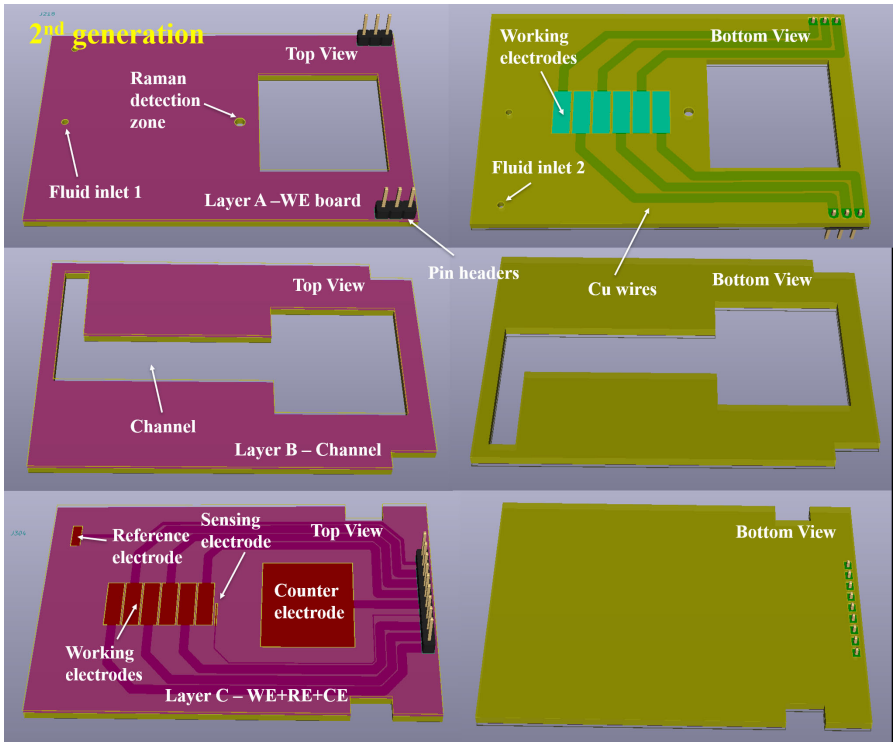

Figure 5.4: The second generation of PCB-based microfluidic device. Board dimensions: 75 mm × 50 mm × 1.6 mm (each). The thickness of the channel is 1.6 mm. The width of the channel is 5 mm (for reference electrode) and 1 cm (for working electrodes). The flow direction in Layer B was from left to right. Working electrode pads: 10 mm × 6 mm (each). Sensing electrode pad: 5 mm × 1 mm. Reference electrode pad: 5 mm × 3 mm. Counter electrode pad: 20 mm × 20 mm. The width of Cu wires: 2 mm (for working and counter electrodes) and 1 mm (for reference and sensing electrodes). Drilled holes (diameter): 1.2 mm (fluid inlets) and 4 mm (for Raman detection). PTFE tubes (1 mm O.D.) and PTFE sheet/coverslip covering the Raman detection hole are not shown in this figure.

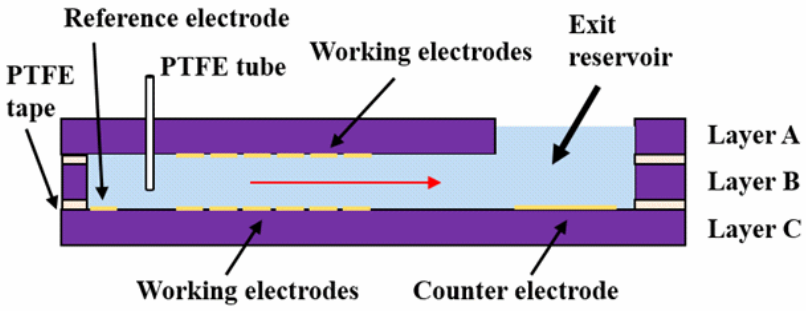

Figure 5.5: Side view of the second generation of PCB-based microfluidic device. Red arrow indicates the flow direction. Blue area indicates electrolyte.

The Third Design

The third generation of PCB-based microfluidic substrates are shown in Figure 5.6 and Figure 5.7. Five PCBs were integrated to make one device, with a detection zone (8 mm × 10 mm) cut open on layers A, C, D, and E for layer penetration. Working, reference, and counter electrodes were placed on the bottom of layer A, the bottom of layer C and the top of layer E, respectively. The counter electrode was resized to 20 mm × 15 mm, and the number of reference electrode pads (5 mm × 3 mm) were increased to 8 to enable a longer period of stable operation. The track width for copper wires was the same as the second design. There are three advantages of this design. Firstly, the WEs, REs and CE are mounted separately on different boards, which means the electrodeposition of one metal for making certain electrodes does not contaminate other electrodes. Moreover, if one electrode is damaged, the board can simply be replaced, instead of trashing all electrodes. Secondly, since the electrolytes with alcohol and without alcohol have different densities, layers A+B (WEs with channel) and layers C+D (REs with channel) can exchange their positions to make sure the one with a higher density is always placed lower than the other one to better maintain the laminar flows. Lastly, the liquid impermeability of the PCB-based

device is achieved by having hydrophobic materials applied to the regions outside the channels, and by applying forces with machine screws via the holes drilled on the boards.

The Fourth Design

The fourth generation of PCB-based microfluidic devices was aimed at improving the liquid impermeability. As shown in Figure 5.8 and Figure 5.9, the device consists of three layers and one pair of reference electrode pads. Two rectangular regions (8 mm $\times$ 20 mm) were cut open on layer A, which is used as two small reservoirs for the electrolyte for the reference electrodes. In the side view, please note that only the reversoirs are shown in Layer A. The area between the two reservoirs is therefore not shown. Working electrodes (10 mm $\times$ 6 mm) were placed on the bottom of layer A, which are connected separately to four specially-drilled holes (named "vias") filled with non-conductive epoxy. The wires (1 mm wide) go through vias to the top surface of the board and then to the pin headers. Similarly, the counter electrode pad on layer C has a via at the center of it, which leads to the bottom of the board and connects to the pin header. The wiring thickness for CE is 1.5 mm. Each circular reference electrode (5 mm dia.) was mounted on the bottom of a small board that covers one small reservoir in layer A. A via beside the circular pad is used for linking the wire (2 mm dia.) to the top of the board. For all filled vias, the diameter is 2 mm with drilled holes of 0.6 mm diameter. All vias are "tented" with solder mask. The purpose of using filled and tented vias is to reroute the wires to make the regions around the channels completely flat for a better sealing, otherwise the electrolyte tends to leak from the seam between the two uneven board surfaces.

Figure 5.10 and 5.11 are photographs of the PCBs printed from factory (unseparated), and Figure 5.12 is a photograph of the made-up device with fluid flowing into the device.

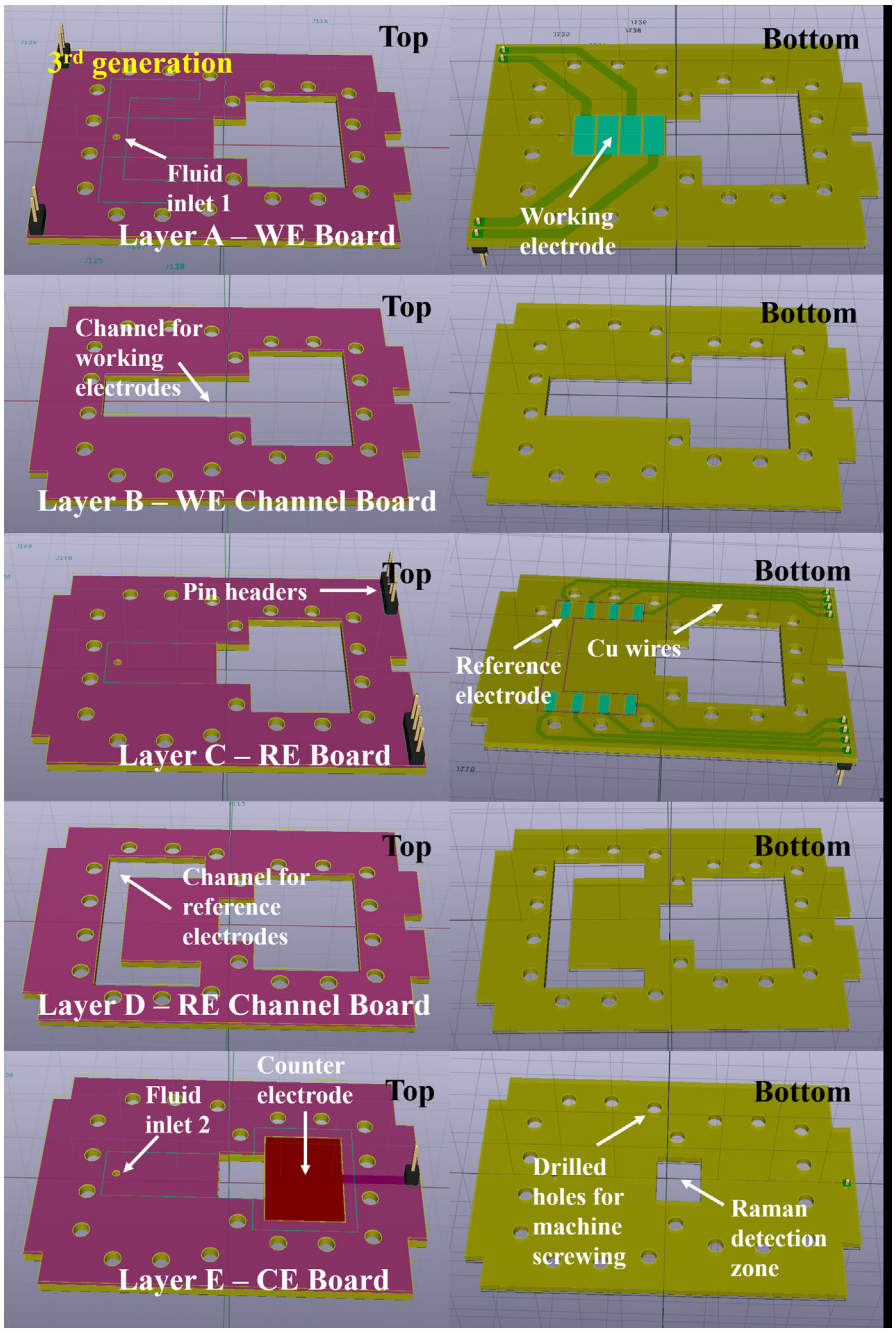

Figure 5.6: The third generation of PCB-based microfluidic device. Board dimensions: 75 mm × 50 mm × 1.6 mm (each). The thickness of the channel is 1.6 mm. The width of the channel is 5 mm (for reference electrode) and 1 cm (for working electrodes). The flow direction in Layer B was from left to right. Working electrode pads: 10 mm × 6 mm (each). Reference electrode pad: 5 mm × 3 mm. Counter electrode pad: 20 mm × 15 mm. Raman detection zone: 1 cm × 8 mm. The width of Cu wires: 2 mm (for working and counter electrodes) and 1 mm (for reference electrodes). Drilled holes (diameter): 1.2 mm (fluid inlets). PTFE tubes (1 mm O.D.) and coverslip covering the Raman detection zone are not shown in this figure.

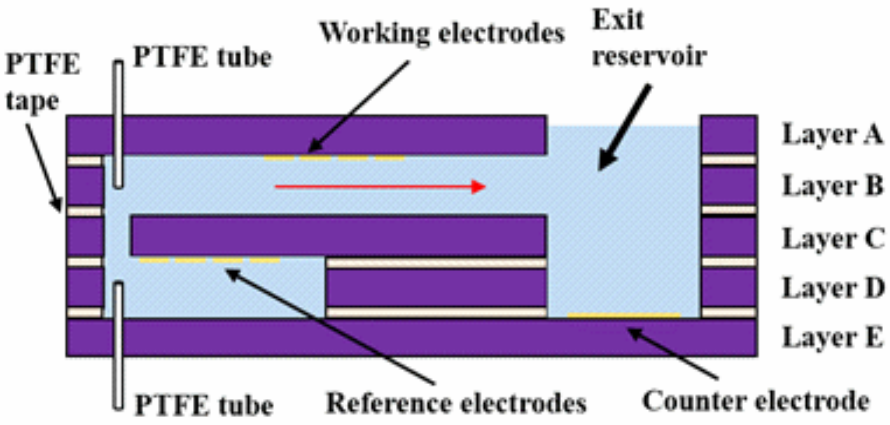

Figure 5.7: Side view of the third generation of PCB-based microfluidic device. Red arrow indicates the flow direction. Blue area indicates electrolyte.

5.2.3 Precursor Solutions and Current Densities Used for Electrodeposition of Nickel, Silver, Palladium and Platinum

A Gamry REF600 Potentiostat was used for conducting electrochemical pretreatment, electrodeposition and testing.

Watt's bath (pH=3-4) Without Organic Additives for Ni Electrodeposition	
Concentration of $NiSO_4 \cdot 6H_2O$ / g L^{-1}	330.00
Concentration of $NiCl_2 \cdot 6H_2O$ / g L^{-1}	45.00
Concentration of H_3BO_3 / g L^{-1}	37.00
Temperature / degree C	60-70
Current density for deposition / A cm^{-2}	0.0538
Duration of electrodeposition / s	200

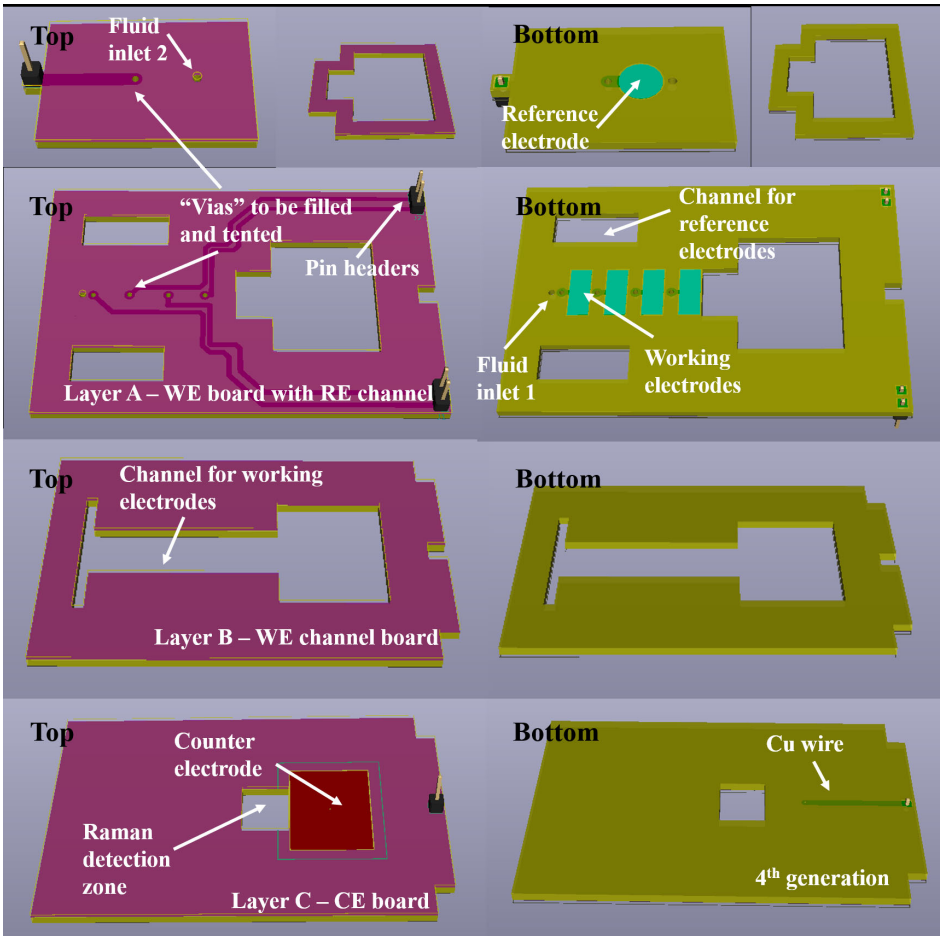

Figure 5.8: The fourth generation of PCB-based microfluidic device. Board dimensions: 75 mm × 50 mm × 0.8 mm (for Layer A and C) or 1.6 mm (for Layer B). Two rectangular regions (8 mm × 20 mm) were cut open on Layer A. The thickness of the channel for WE (Layer B) is 1.6 mm. The width of the channel is 1 cm (for working electrodes). The flow direction in Layer B was from left to right. Working electrode pads: 10 mm × 6 mm (each). Reference electrode pad: 5 mm (dia.). Counter electrode pad: 20 mm × 15 mm. Raman detection zone: 1 cm × 8 mm. The width of Cu wires: 2 mm (for working electrodes), 1.5 mm (for counter electrode) and 1 mm (for reference electrodes). Diameter of circular vias: 2 mm ("tented"). Drilled holes (diameter): 0.6 mm (for vias, filled with epoxy) and 1.2 mm (fluid inlets). PTFE tubes (1 mm O.D.) and coverslip covering the Raman detection zone are not shown in this figure.

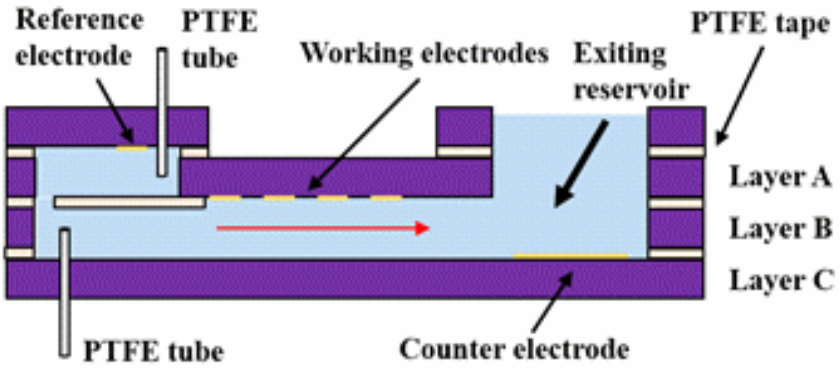

Figure 5.9: Side view of the fourth generation of PCB-based microfluidic device. Red arrow indicates the flow direction. Blue area indicates electrolyte.

Cyanide-free Solution for Ag Electrodeposition (pH=4-4.5)	
Concentration of AgCl / g L^{-1}	30.00
Concentration of $Na_2S_2O_3$ / g L^{-1}	500.00
Concentration of $K_2S_2O_5$ / g L^{-1}	30.00
Temperature / degree C	r.t.
Current density for deposition / A cm^{-2}	0.00133
Duration of electrodeposition / s	600-1200

$PdCl_2$ Heavy Deposition Solution (pH=0.1-0.5) for Pd Electrodeposition	
Concentration of $PdCl_2$ / g L^{-1}	52.80
Concentration of concentrated HCl / g L^{-1}	50.00
Concentration of NH_4Cl / g L^{-1}	30.00
Temperature / degree C	37-48
Current density for deposition / A cm^{-2}	0.08
Duration of electrodeposition / s	180

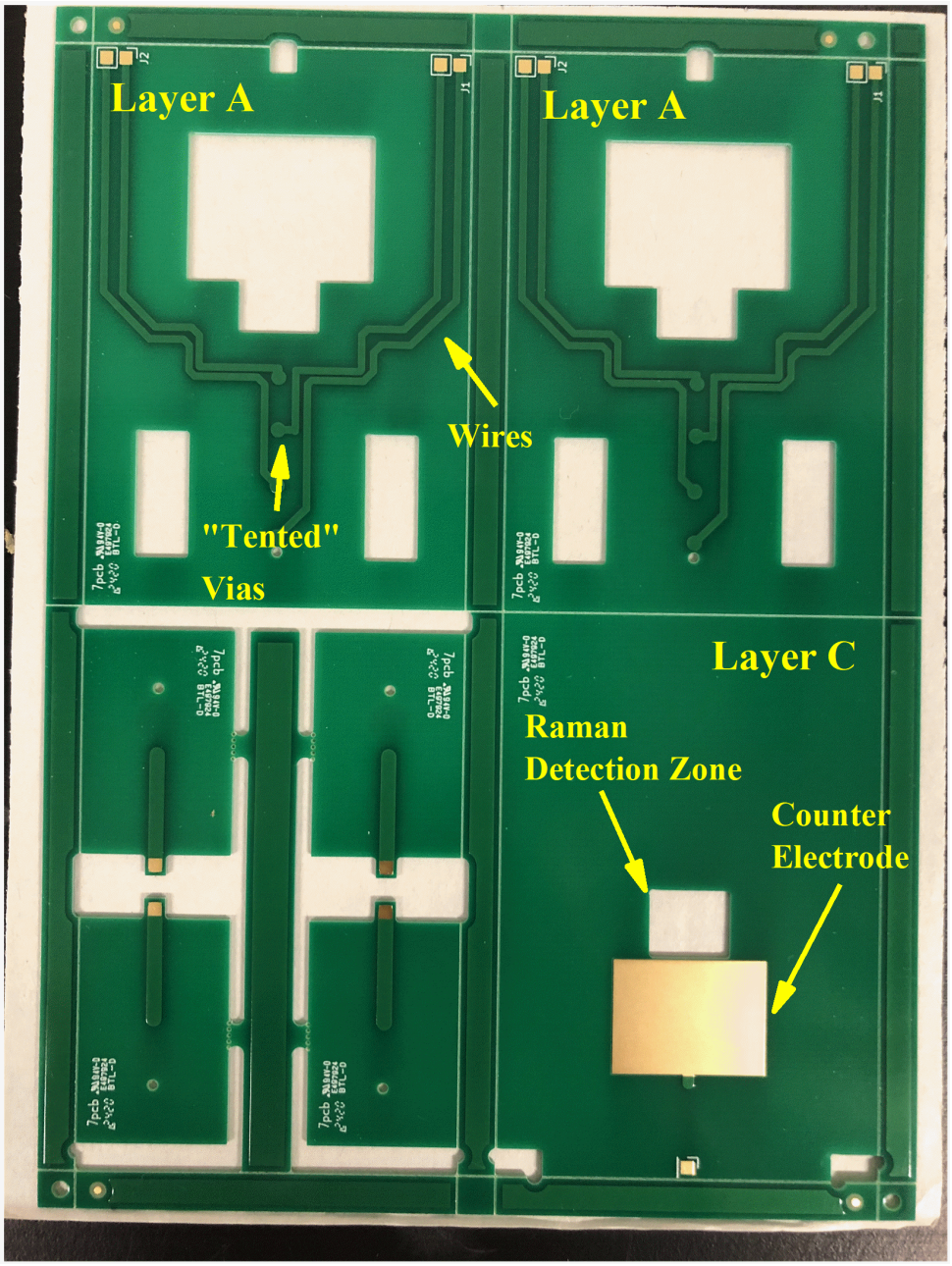

Figure 5.10: Photograph of PCBs for the fourth design of PCB-based microfluidic device. (The photograph shows the top of the boards.)

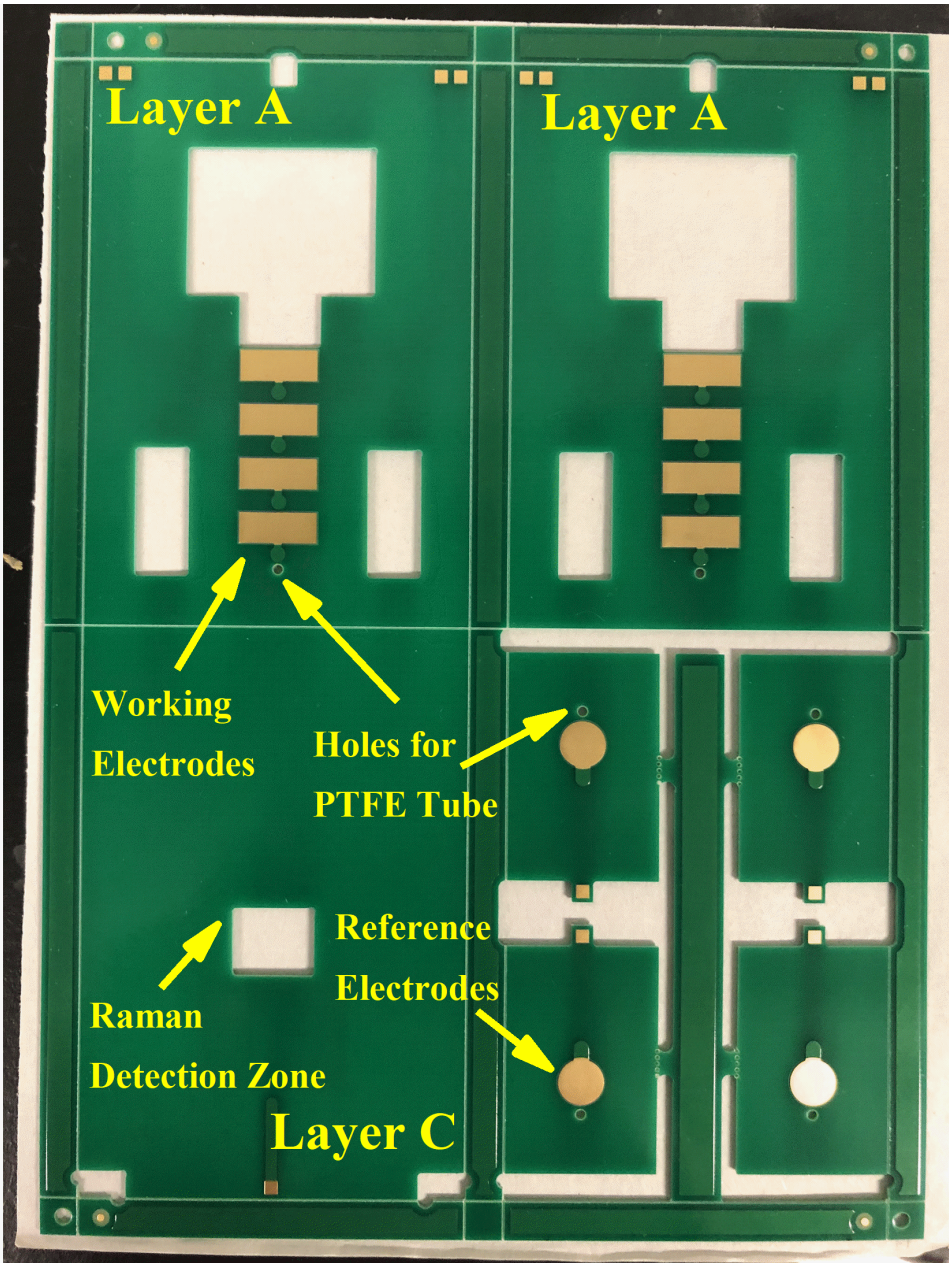

Figure 5.11: Photograph of PCBs for the fourth design of PCB-based microfluidic device. (The photograph shows the bottom of the boards.)

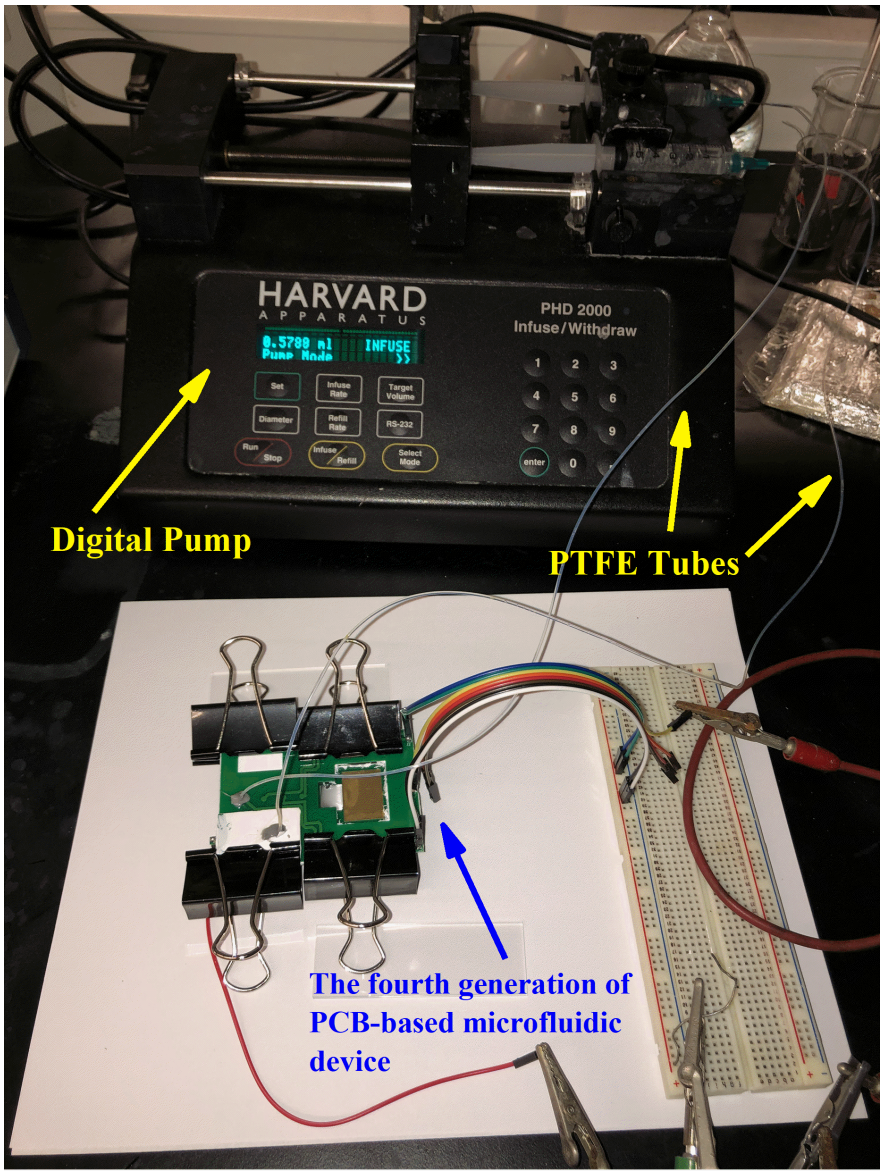

Figure 5.12: Photograph showing the fourth generation of the PCB-based microfluidic devices. Binder clips applied force to hold multiple boards (reference electrode board, Layer A, Layer B and Layer C) together. Teflon tubes were connected to the device and the flow rate was controlled by a digital pump.

H_2PtCl_6 Solution for Pt Electrodeposition	
Concentration of $H_2PtCl_6 \cdot 6H_2O$ / g L^{-1}	1.554
Concentration of H_2SO_4 / g L^{-1}	50.00
Current density for deposition / A cm^{-2}	0.00127
Duration of electrodeposition / s	3600-10800

5.3 Fabrication of PCB-based Electrodes on Test Boards

5.3.1 Pretreatment of Printed Circuit Boards (Test Boards)

PCBs are usually fabricated with a Au layer to minimize contact resistance and protect the copper pads underneath from corrosion. Ahead of electrodeposition, Au protective layers were removed to expose the Cu pads [9]. The Cu pads were immersed into 1 M HCl. Cyclic voltammetry was conducted repeatedly, with the upper and lower scan limits set to potentials at which oxygen and hydrogen evolution can happen rapidly (see Figure 5.13). Figure 5.13(a) shows the inital stage of the PCB pretreatment. The current of oxygen and hydrogen evolution increased over the first 30 cycles, indicating the roughening of the Au layer. In the second stage (Figure 5.13(b)), the cathodic peak between -0.2 V to 0 V vs Ag|AgCl (immersed in saturated KCl solution) kept growing during cycling with two small bumps appearing in the 60^{th} anodic scan at 0 V and 0.1 V vs Ag|AgCl, respectively, indicating the cracking and removal of the Au protection layer and the exposure of Cu. Meanwhile, the generation of oxygen and hydrogen started decaying. The pretreatment of PCBs was ceased in the middle of Stage 2, as the Au protection layer was almost fully removed and the Cu pad was ready. If cycling is continued (see Figure 5.13(c-d)), the Cu pad can be further roughened, as manifested by the expansion of the peaks for Cu oxidation and CuO reduction. Additionally, the oxygen and hydrogen evolution

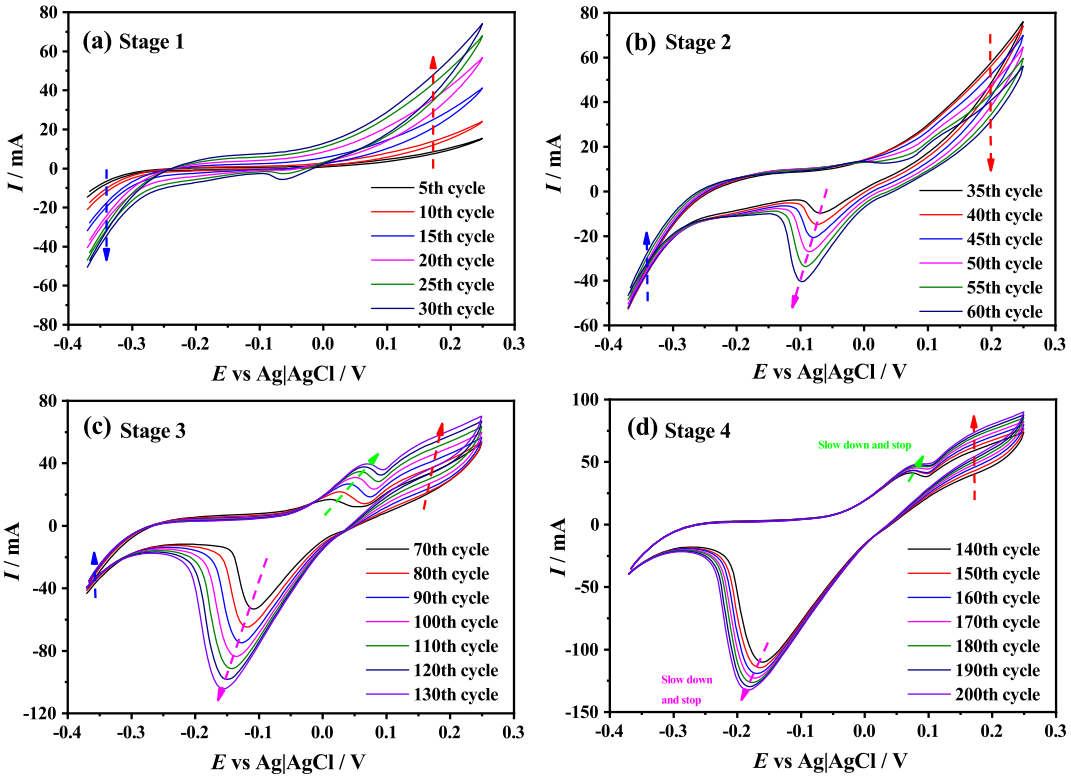

Figure 5.13: Cyclic voltammetry in 1 M HCl for the pretreatment of PCB test substrates.

currents were increased.

5.3.2 Electrodeposition of Nickel, Silver, Palladium, Platinum and Applications

The electrodeposition of Ni on Cu pads was conducted with a modified Watt's Bath as the precursor solution. Figure 5.14 is a photograph of a PCB with Ni deposited on the Cu pads. Cyclic voltammetry was conducted in 0.5 M KOH. It can be clearly seen from Figure 5.15 that α-Ni(OH)$_2$ can be produced from the electrooxidation of Ni. α-Ni(OH)$_2$ was converted later to β-Ni(OH)$_2$ at higher overpotentials, which was then electrooxidized into β-NiOOH. The reduction of β-NiOOH was also found in the

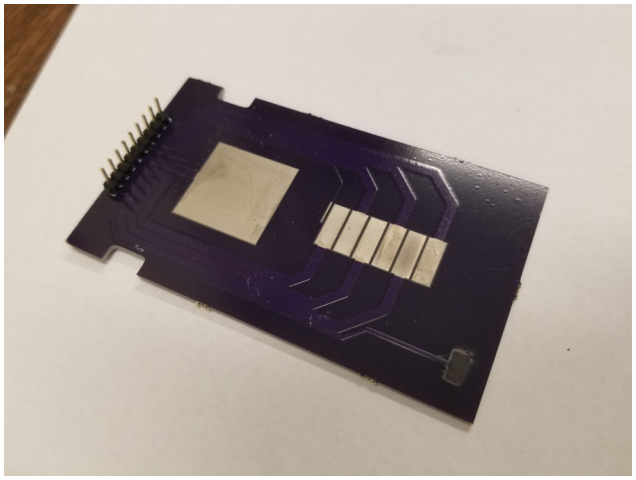

Figure 5.14: A photograph of a printed circuit board with electrodeposited Ni.

cathodic scan. Figure 5.16 presents a PCB with Ag deposited on Cu. The Ag layer was shiny when first deposited, however a heavy depositon makes the layer white. In Figure 5.15, an anodic peak and a cathodic peak in the range of 0.2-0.4 V vs Ag|AgCl indicate the formation and reduction of AgOH.

The deposition of Pd can be achieved using Pd precursor solution through the galvanic replacement reaction of Ni on the pads or electrochemically. The cyclic voltammograms of the Pd-covered pads obtained by these two methods are shown in Figure 5.17(a) and (b), respectively. The capability of electrodeposited Ni and Pd pads to catalyze the oxidation of alcohols was examined. Figure 5.18(a-b) are stable voltammograms. The electrochemical surface area (ECSA) of Ni and Pd was determined by integrating the charge for the formation of α-$Ni(OH)_2$ (up to 0.5 V vs RHE) and the reduction peak of PdO, normalized by 514 μC cm^{-2} [25–27] and 424 μC cm^{-2} [28, 29], respectively.

Figure 5.19 shows the cyclic voltammetry of electrodeposited Pt on Ni-coated pad. The Ni acts as an adhesion layer, and prevents Pt from making an alloy with Cu. The PCB with electrodeposited Pt was treated with 70% HNO_3 for 1-2 minutes to etch off any Ni exposed to the solution.

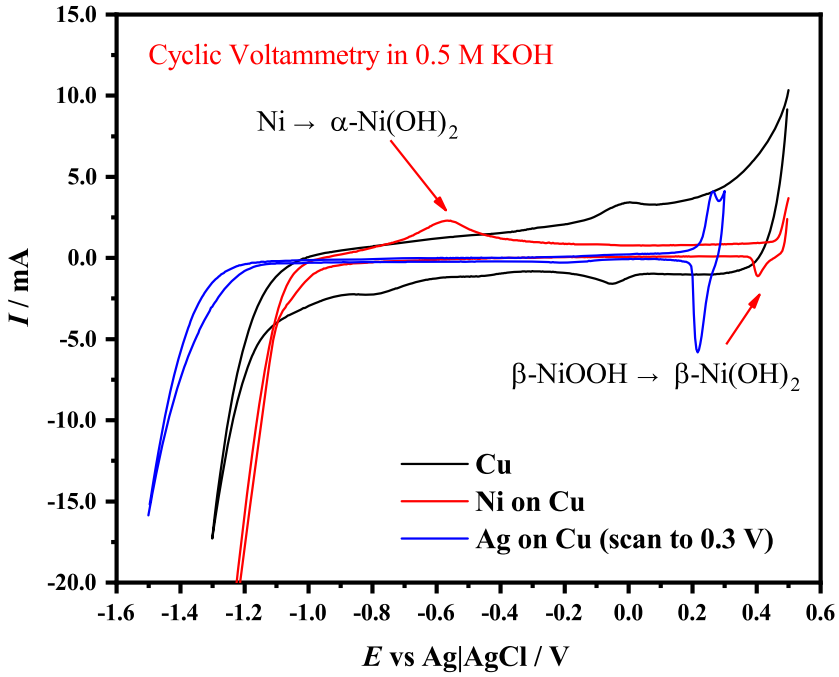

Figure 5.15: Cyclic voltammograms of a Cu pad after pretreatment, electrodeposition of Ni or Ag in 0.5 M KOH.

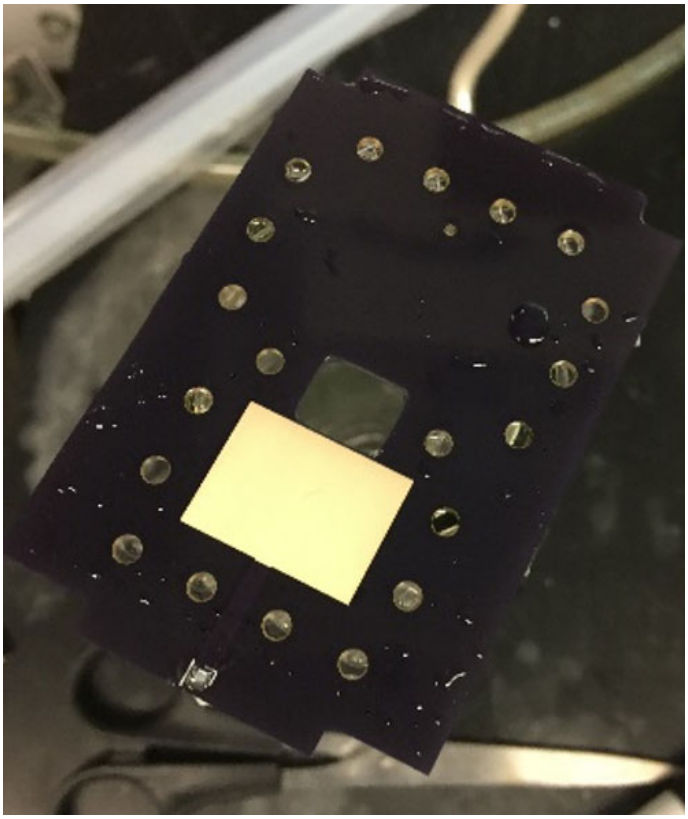

Figure 5.16: A photograph of a printed circuit board with electrodeposited Ag.

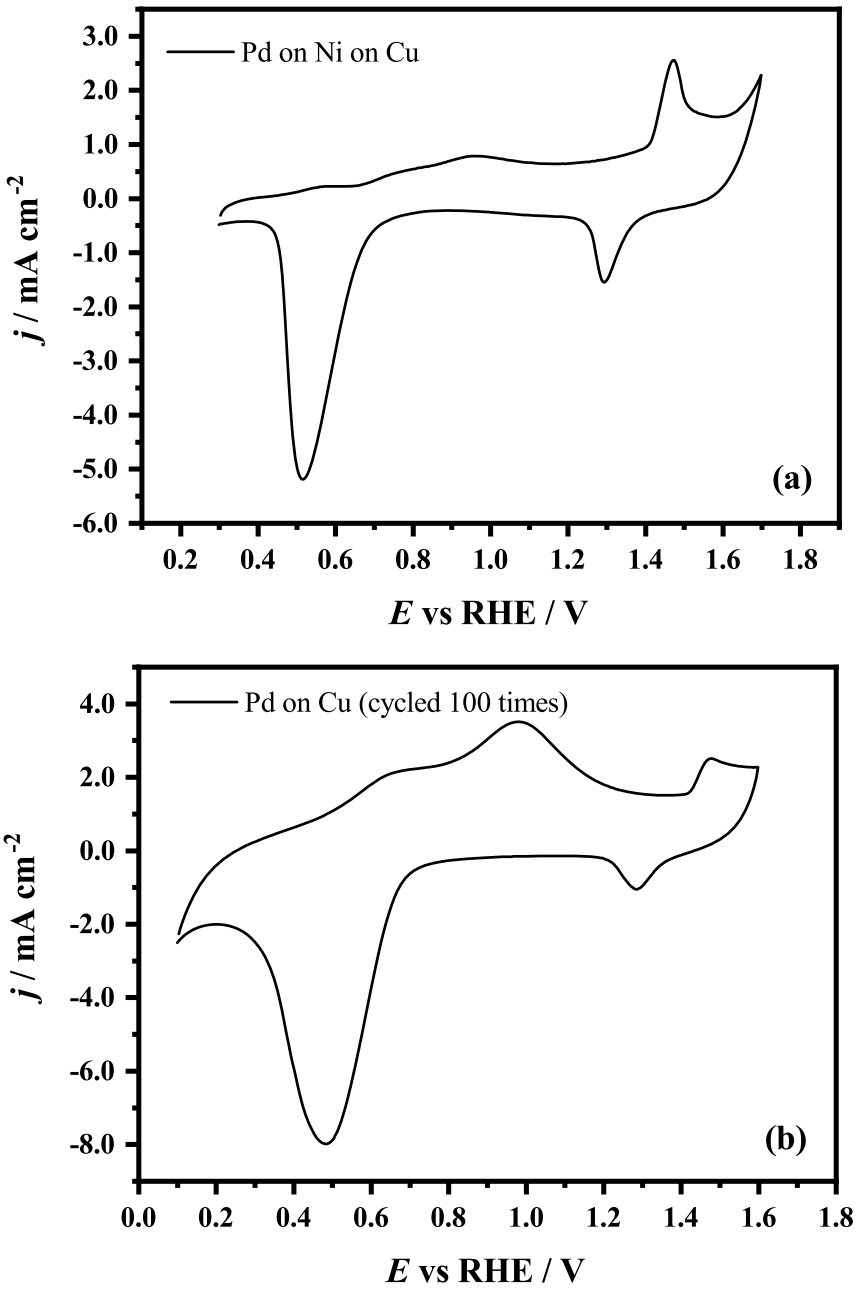

Figure 5.17: Cyclic voltammograms of PCB-based Pd electrodes. Measured in 0.5 M KOH and made by (a) electrodeposition on Cu and (b) replacing Ni adhesion layer on Cu.

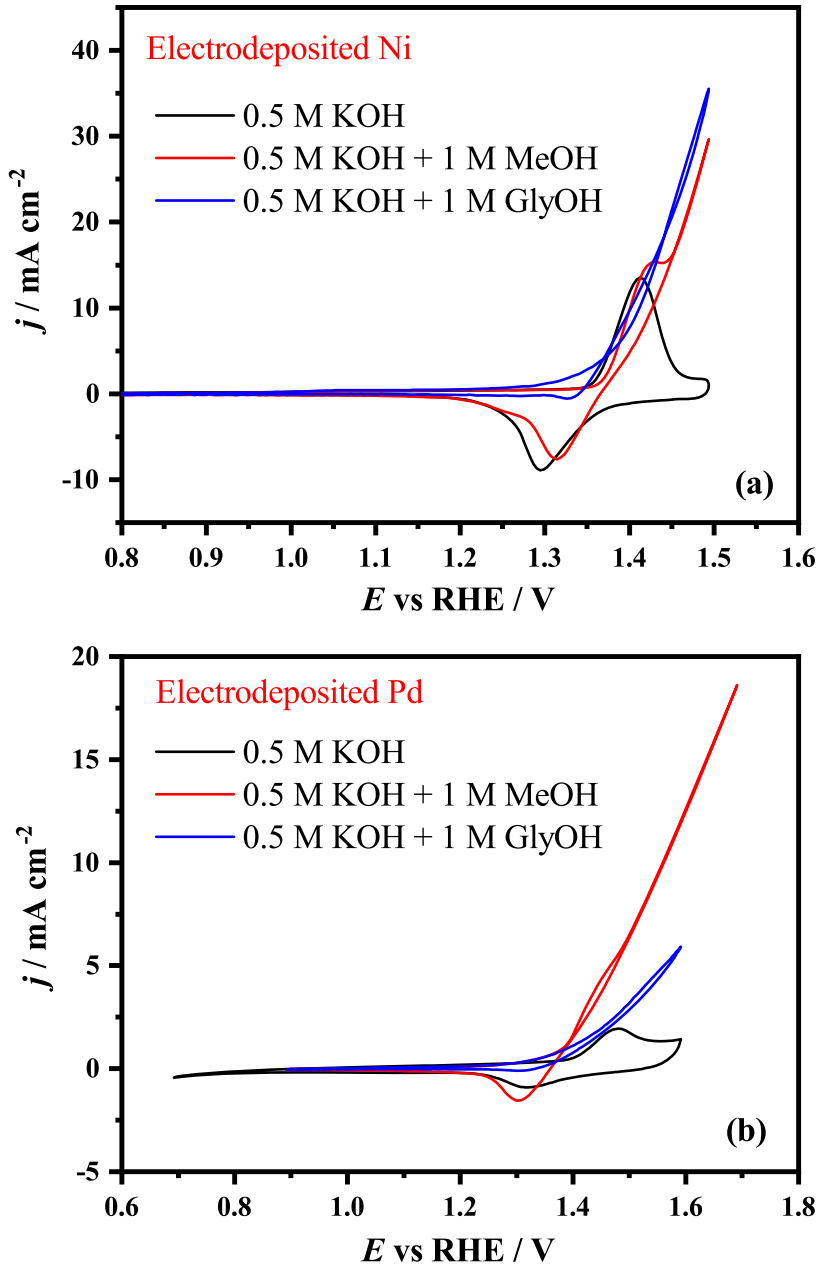

Figure 5.18: Cyclic voltammograms of PCB-based (a) Ni and (b) Pd electrode in 0.5 M KOH and the electrooxidation of 1 M methanol and glycerol.

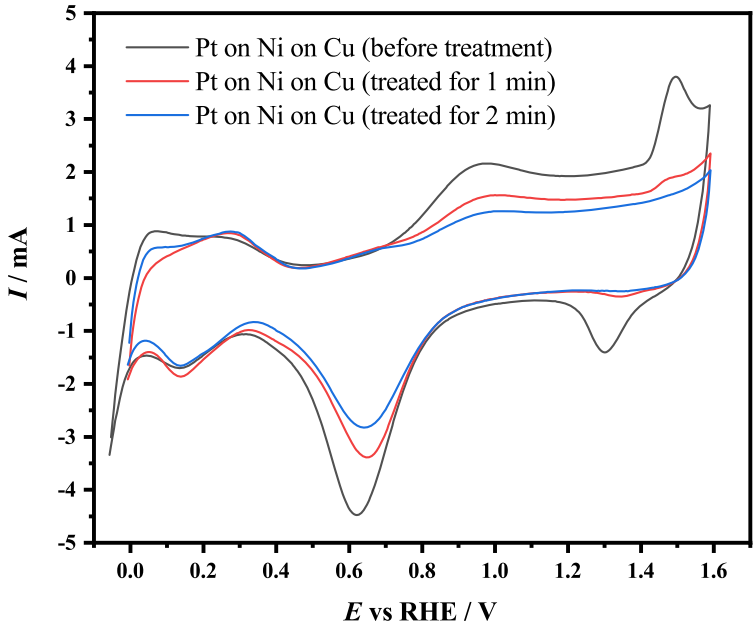

Figure 5.19: Cyclic voltammogram of a PCB-based Pt electrode (untreated and treated in 70% nitric acid) in 0.5 M KOH.

5.3.3 Internal Reference Electrodes

Using IREs in electrochemical microfluidic devices is a step forward compared with using external reference electrodes (*e.g.* Ag|AgCl or Hg|HgO) which are usually accomodated in a reservoir placed at the outlet, as IREs are more compatible with miniaturized electrochemical devices. There are two major types of IREs: pseudo reference electrodes and true reference electrodes. Pseudo reference electrodes are usually made with a layer of noble metal, such as Ag and Au, while the fabrication of true reference electrodes like PdH and Ag|AgCl needs modification of the metal pads. In this work, the preparation of IREs on PCBs is investigated, exemplified by a Ag|AgCl true IRE and a Pd pseudo IRE.

The fabrication of a Ag|AgCl IRE was done by electrooxidizing a Ag pad made as described in Subsection 5.3.2 at a potential which produces a decaying anodic current density starting from several 100 μA cm^{-2} for 30-60 minutes in 1 M HCl. Measured in a saturated KCl solution, the potential of this Ag|AgCl IRE is around 0.10-0.11 V versus a commerical Hg|HgO electrode sealed in a tube with a 20% KOH solution. As shown in Figure 5.20(a), the fabricated Ag|AgCl IREs can operate stably for several hours, and they are regenerable by repeating the electrooxidation procedure in 1 M HCl.

The tested stability of a Pd pseudo IRE is shown in Figure 5.20(b), by carrying out cyclic voltammetry overnight using a Pd wire as the working electrode and a Pd IRE as a reference electrode in 0.5 M KOH. The potential of this Pd pseudo reference electrode is around 40-50 mV versus the commercial Hg|HgO, and it was operated stably overnight.

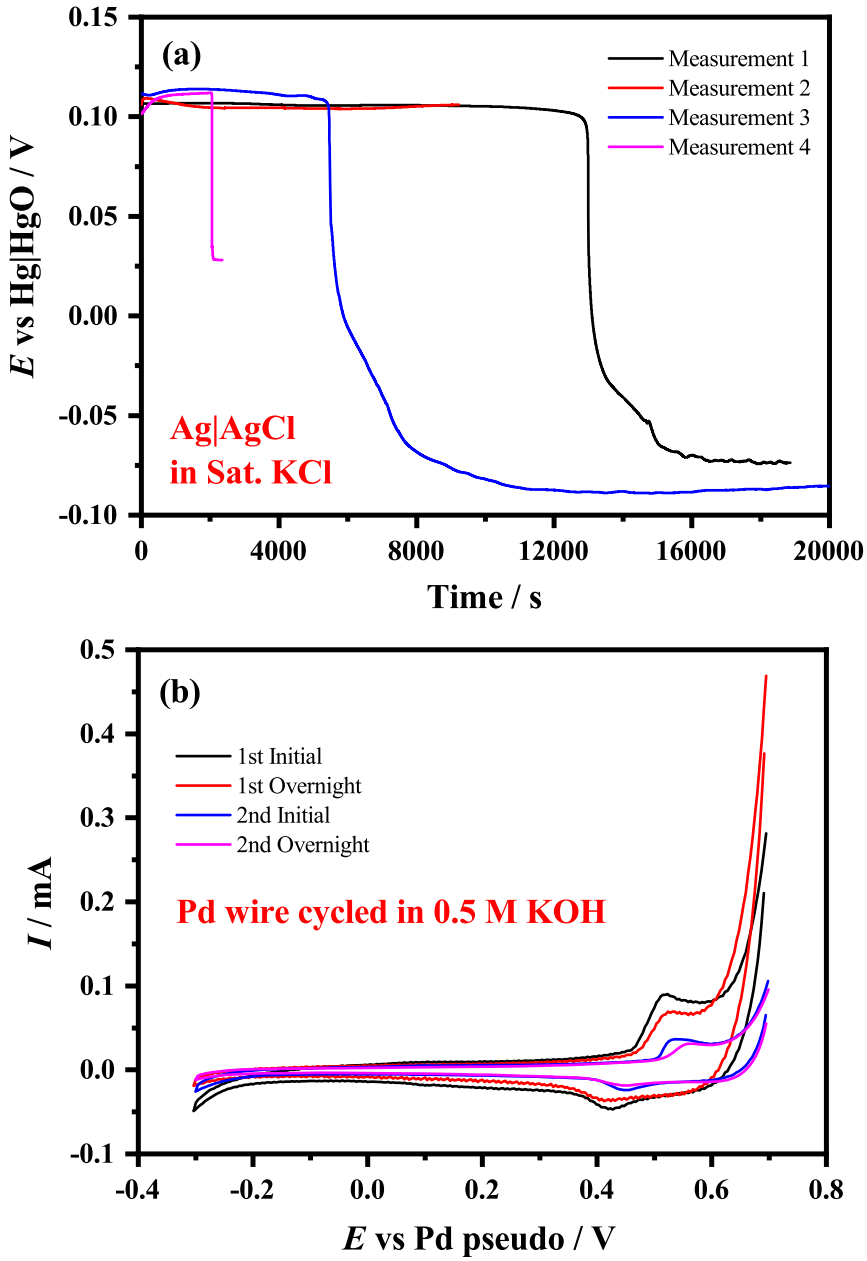

Figure 5.20: Electrochemical measurements showing the stability of an internal Ag|AgCl reference electrode and a Pd-pseudo reference electrode. (a) Open circuit potential of a PCB-based silver silver chloride electrode in saturated KCl solution versus a commercial Hg|HgO reference electrode, and (b) cyclic voltammetry of a Pt wire measured with a PCB-based Pd pseudo-reference electrode.

References

[1] S. Babikian, G. P. Li, and M. Bachman, *IEEE Transactions on Components, Packaging and Manufacturing Technology*, 2017, **7**(6), 846–854.

[2] H. Kim, H. Hwang, S. Baek, and D. Kim, *Sensors and Actuators, A: Physical*, 2018, **277**, 73–84.

[3] A. L. Zhang, X. Q. Zhang, W. Y. Hu, and X. T. Fu, *Ferroelectrics*, 2016, **502**(1), 69–75.

[4] S. Roy, D. Mitra, B. B. Bhattacharya, and K. Chakrabarty In *ACM Journal on Emerging Technologies in Computing Systems*, p. 8(3), 2012.

[5] D. Grissom, C. Curtis, S. Windh, C. Phung, N. Kumar, Z. Zimmerman, K. O'Neal, J. McDaniel, N. Liao, and P. Brisk, *Integration, the VLSI Journal*, 2015, **51**, 169–193.

[6] K. Park, H. J. Suk, D. Akin, and R. Bashir, *Lab on a Chip*, 2009, **9**(15), 2224–2229.

[7] W. K. Tomazelli Coltro, J. A. Fracassi Da Silva, and E. Carrilho, *Analytical Methods*, 2011, **3**(1), 168–172.

[8] J. Tu, Y. Qiao, H. Feng, J. Li, J. Fu, F. Liang, and Z. Lu, *RSC Advances*, 2017, **7**(50), 31603–31609.

[9] A. Kara, A. Reitz, J. Mathault, S. Mehou-Loko, M. A. Amirdehi, A. Miled, and J. Greener, *Lab on a Chip*, 2016, **16**(6), 1081–1087.

[10] A. Déctor, J. P. Esquivel, M. J. González, M. Guerra-Balcázar, J. Ledesma-García, N. Sabaté, and L. G. Arriaga, *Electrochimica Acta*, 2013, **92**, 31–35.

[11] C. J. Huang, J. L. Lin, P. H. Chen, M. J. Syu, and G. B. Lee, *Electrophoresis*, 2011, **32**(8), 931–938.

[12] E. Sinkala, J. E. McCutcheon, M. J. Schuck, E. Schmidt, M. F. Roitman, and D. T. Eddington, *Lab on a Chip*, 2012, **12**(13), 2403–2408.

[13] S. Gu, Y. Lu, Y. Ding, L. Li, H. Song, J. Wang, and Q. Wu, *Biosensors and Bioelectronics*, 2014, **55**, 106–112.

[14] E. V. Fanavoll, D. A. Harrington, S. Sunde, G. Singh, and F. Seland, *Electrochimica Acta*, 2017, **225**, 69–77.

[15] M. Fighera, P. D. Van Der Wal, and H. Shea, *Journal of the Electrochemical Society*, 2017, **164**(12), H836–H845.

[16] Y. Li, W. Van Roy, P. M. Vereecken, and L. Lagae, *Microelectronic Engineering*, 2017, **181**, 47–54.

[17] S. Kang, A. F. Nieuwenhuis, K. Mathwig, D. Mampallil, and S. G. Lemay, *ACS Nano*, 2013, **7**(12), 10931–10937.

[18] J. Guo, Y. Kang, and Y. Ai, *IEEE Transactions on Dielectrics and Electrical Insulation*, 2015, **22**(3), 1439–1443.

[19] J. Guo, C. M. Li, and Y. Kang, *Biomedical Microdevices*, 2014, **16**(5), 681–686.

[20] S. Emaminejad, M. Javanmard, R. W. Dutton, and R. W. Davis, *Lab on a Chip*, 2012, **12**(21), 4499–4507.

[21] B. B. Narakathu, S. G. R. Avuthu, A. Eshkeiti, S. Emamian, and M. Z. Atashbar, *IEEE Sensors Journal*, 2015, **15**(11), 6374–6380.

[22] H. Y. Y. Nyein, L. C. Tai, Q. P. Ngo, M. Chao, G. B. Zhang, W. Gao, M. Bariya, J. Bullock, H. Kim, H. M. Fahad, and A. Javey, *ACS Sensors*, 2018, **3**(5), 944–952.

[23] Y. H. Yun, Z. Dong, V. N. Shanov, and M. J. Schulz, *Nanotechnology*, 2007, **18**(46).

[24] K. Sanger, K. Zór, C. Bille Jendresen, A. Heiskanen, L. Amato, A. Toftgaard Nielsen, and A. Boisen, *Sensors and Actuators, B: Chemical*, 2017, **253**, 999–1005.

[25] B. Beden and D. J. M. L. Floner, 1985, **162**.

[26] J. Van Drunen, B. Kinkead, M. C. Wang, E. Sourty, B. D. Gates, and G. Jerkiewicz, *ACS Applied Materials and Interfaces*, 2013, **5**(14), 6712–6722.

[27] S. A. Machado and L. A. Avaca, *Electrochimica Acta*, 1994, **39**(10), 1385–1391.

[28] M. Lukaszewski, M. Soszko, and A. Czerwiński, *International Journal of Electrochemical Science*, 2016, **11**(6), 4442–4469.

[29] M. Simoes, S. Baranton, and C. Coutanceau, *Journal of Physical Chemistry C*, 2009, **113**(30), 13369–13376.

Chapter 6

Prospects

6.1 Conclusions

A literature review study on glycerol electrooxidation at Pt, Pd and Au electrodes summarized the experimental observations reported so far, and gave clarification of two arguments: (i) Pt is more active than Pd in dissociating C-C bonds of glycerol and (ii) high overpotentials lead to the C-C bond dissocation and the fast production of CO_2. The conclusions of that review are: (i) The inferior activity of cleaving C-C bonds of glycerol at Pd electrodes compared to Pt is due to the inferior deprotonation activity. (ii) The higher proportion of CO_2 generation is partially due to the fast depletion of hydroxide at the electrode which disfavors the carboxylation processes. Also, it is proposed that the reaction towards side products (carboxylates and carbonate) are dominated by parallel pathways.

A microfluidic flow device for electrocatalytic conversion of alcohols was developed, coupled with online and quantitative Raman spectroscopy. This device is used for studying the kinetics of methanol electrooxidation at a Pt mesh electrode. A simple model considering only one-dimensional convection was able to qualitatively explain the tine dependence of the detected species. Flow rate dependence was studied and

at higher flow rates there was quantitative conversion to formate.

A comparative study of the electrooxidation of different alcohols at Ni electrodes was conducted with an improved version of this device, together with electrochemical impedance spectroscopy. It was discovered that the vicinal diols and triols (*i.e.* ethylene glycol, 1,2-propanediol and glycerol) react with the dissociation of C-C bonds, which leads to the generation of formate as a major product. In contrast, the primary alcohols (*e.g.* ethanol) which bear only one terminal hydroxyl group are oxidized to carboxylate without C-C bond cleavage. This suggests that having vicinal hydroxyl groups lead to the cleavage of C-C bonds when electrocatalytically reacted at Ni electrodes.

A next generation of microfluidic devices for electrocatalytic studies was designed using printed circuit boards. These enable low-cost rapid prototyping and fabrication without clean-room conditions. Electrodeposition protocols were successfully developed for the fabrication of Ni, Ag, Pd and Pt electrodes on top of Cu pads. Four designs of PCB-based microfluidic devices were made, fabricated and validated under realistic conditions.

6.2 Future Work

6.2.1 Optimization of Electrocatalytic Microfluidic Devices

The electrocatalytic microfluidic devices presented in this work still have drawbacks which limit their use and wide applicability, and are still under optimizations. Several preliminarily tested and proposed optimization strategies are listed below:

(1) The evaluation of “withdrawing fluid” was investigated in this work but rarely studied before as most of the current microfluidic designs “infuse” fluid. In the "withdrawing" mode, the liquid enters the channel from the reservoir and exits through

the tube connected to the pump. The reverse flow direction maintains the downstream detection strategy but shifts the detection point to the region between the working electrode and the tube, which minimizes the ohmic loss by placing the working and reference electrodes much closer to each other and significantly reduces the internal pressure in the channel (which causes leaking). A careful selection of counter electrodes can effectively avoid getting electro-reduced products from the counter electrode into the main channel.

(2) The evaluation of channel dimensions. A tradeoff is that a thinner channel which betters the steady-state condition within the cross-sectional area also increases the internal pressure and ohmic resistance, therefore the ratio of current to lateral flow rate needs to be maximized.

(3) The use of side channels to minimize the resistance which affects the current if the "withdrawing mode" is disabled by the unavoidable electroreduction of reactants by counter electrode. A concern that is worth investigating is how to minimize the influence of side channels on the flow pattern in the main channel. A possible solution is to fill the side channels with electrolyte with a different density.

(4) The maximization of the surface area of deposited metallic catalysts per unit volume of carbon supports (*e.g.* carbon paper and carbon cloth). To enable quantitative detection by Raman spectroscopy, a high rate of downstream product generation is required to give enough Raman signal intensity. Therefore, a "flow through" design which provides a higher density of electrocatalysts is preferred.

6.2.2 Gas-Phase Reactants and Large Molecules

In future phases of this work, gas-phase reactants can be introduced into the device with corresponding improvements on the microfluidic device setup. The multi-phase microfluidic platform is aimed at converting gas phase reactants into aqueous species for downstream detection and kinetic studies (*e.g.* CO_2 electroreduction into valuable

products). Besides, large molecules with complicated structures may be studied using these devices, as they usually have stronger Raman signals compared with small molecules. However, the peak deconvolution of Raman spectra can be more challenging. The broad applicability of this device is to be tested to see whether it shows any possibility for commercialization.

6.2.3 Miniaturization and Material Substitution of the Electrocatalytic Microfluidic Devices

Preliminary work has shown that Raman spectra with a high S/N ratio can be obtained with a channel thickness around 0.3 mm or larger. In the current stage, our electrocatalytic microfluidic devices for Raman detection is an enlarged prototype at sub-milliliter scale for quicker fabrication, less complexity, lower cost of materials (10 US dollars for an online-Raman-compatible flow cell presented in Chapter 3 ann 4, and 25-100 US dollars for a PCB-based microfluidic device) and easier Raman detection. Once the proposed optimization is finished, miniaturization of both "flow through" and "flow over" designs will be started. Teflon spacers are to be replaced by thinner materials. For PCB-based "flow over" design, perfluoro rubber and polyimide have good chemical resistivity, hydrophobicity and flexibility for machine screwing and are ideal materials to replace PDMS.

A new branch of electrochemical microfluidic devices lies in the integration of components, as microstereolithography (MSL) was adopted by researchers to build microfluidic devices, however, it is at the expense of the transparent window on top of the channel / working electrodes. Upon the completion of the optimization of our microfluidic devices, efforts can be made toward the integration of all polymeric components to increase the durability, appearance and resistance to the internal pressure of the microfluidic devices, possibly using a 3D-printer. The compatibility of a printed device with a Raman detection window may be investigated to find a solution

for the optical transparency.